Molecular Dynamics Simulations of Material Assembly, Growth, and Transport

by

Pavel Ludwig Rehak
B. Sc. in Chemistry and Mathematics, State University of New York at Stony Brook, 2010
M. Sc. in Chemical Physics, University of Minnesota, Twin Cities, 2012

THESIS

Submitted as partial fulfillment of the requirements
for the degree of Doctor of Philosophy in Chemistry
in the Graduate College of the
University of Illinois at Chicago, 2021

Chicago, Illinois

Defense Committee:
Prof. Petr Král, Chair and advisor
Prof. Ksenija Glusac
Prof. Justin Lorieau
Prof. Ying Hu
Prof. Ehud Gazit, Tel-Aviv University

ACKNOWLEDGMENTS

I would like to acknowledge my advisor, Prof. Petr Král, for his constant guidance and support throughout my graduate studies at the University of Illinois at Chicago (UIC). He had spent enormous time with me to teach, guide, motivate and discuss research. Our discussions helped me to understand how to plan projects and use computational methods to approach and solve nanoscience problems. From his example, I learned how to be rigorous and always seek the scientific truth. He gave me the opportunity to work on many different projects requiring a diverse set of skills and background information. He taught me how to interact with collaborators who are not familiar with computational methods and interpret their data on the molecular level. He was always willing to discuss my weak points and lapses in understanding in the sciences and in life, in general. He gave me the opportunity to mentor graduate, undergraduate, and even high school students in nanoscience modeling. I have learned diverse branches of science and approached new problems. Most importantly, he was willing to tirelessly guide me through my shortcomings and personal struggles, while being understanding and patient.

I was privileged to work with numerous collaborators who provided me with problems and feedback for my simulations. I would like to thank Profs. Ehud Gazit, Vicki Colvin, Boris Rybtchinski, Alexander Spokoyny, Tianbo Liu, Reza Shahbazian-Yassar, Tolou Shokuhfar, Ruifeng Lu, Jerry Shan, and Sangil Kim.

I would like to sincerely thank to Prof. Lela Vuković, a former graduate student in our group, for guiding me in many projects that we published together and helping me in many other projects. I express gratitude to current group members and alumni, Dr. Henry Chan, Mrs. Yanxiao Han, Dr.

Soumyo Sen, Dr. Haiqi Gao, Mr. Sanoj, Mr. Michal Sawczyk, and Mrs. Alice Zeng for their support. Dr. Chan, and Dr. Sen helped me in constructing the systems and setting up the simulations.

I would also like to thank other faculties in the Department of Chemistry, UIC, especially Profs. Preston Snee, Duncan Wadrop, Luke Hanley, and Audrey Hammerich for their efforts to advise me. Finally, I would like to thank the staff, Dr. George Papadantonakis, Ms. Rhonda Staudohar (R.I.P), Ms. Silvia Solis, and Ms. Gloria Torres for their encouragement and indirect support.

I will never be able to thank enough my mother (R.I.P) for her enormous support on many facets in guiding me through life. She provided me with the emotional support and encouragement throughout my years as a graduate student. Her position as a research mechanical and computational engineer also helped me to navigate through difficult situations during my PhD, gave me an insight on how to approach problems, and even taught me technical skills, such as programming in FORTRAN, which many parents would not be able to provide. Most of all she had the right balance of nurturing and expectations for me. I dedicate this thesis in memory of my mother, Dr. Margareta Linda Francesca Rehak (1956-2020).

I would like to thank my neighbor and friend Mr. Edwin Nelson Folsom, who mentored me at both the personal and professional levels. He was a mechanical engineer who managed projects and people, so he taught me how to interact with people. At the same time, he helped me with avoiding many errors in the future.

I would like to thank my junior and senior high school math and science teachers who made math and science fun and interesting for me and ramped up my enthusiasm for modelling biological and physical sciences. They inspired and encouraged me to go into a career of science and held a level of rigor to prepare me and make me view the world as a scientist. In addition, I would

like to thank Profs. Anthony Phillips, Clare Grey, Miriam Rafailovich, Alfred Goldhaber, Peter van Nieuwenhuizen, and Thomas Kuo for letting me do independent research and studies as an undergraduate at SUNY Stony Brook. I thank Profs. Christopher Cramer and Jören Ilja Siepmann of University of Minnesota, for their insight and dedication to teach me computational chemistry. I would particularly like to thank Dr. Paul Ching for helping me to become a more effective instructor to students when I was having difficulty as a new TA.

Last but not least, I express gratitude to many friends and advocates I met throughout the years starting from junior high school and persisting to this day in helping me overcome difficult challenges during hard times. Ultimately, I would like to thank the countless medical professionals I met in my life who treated me for multiple conditions I had. They helped me feel better when I was severely ill and everything looked hopeless, thus ultimately allowing me to complete my PhD.

LIST OF ABBREVIATIONS

2D DOSY	2D Diffusion Ordered Spectroscopy
AA	All Atomistic
AAO	Anodized Alumina Oxide
ACO	Amorphous Calcium Oxalate
ADN	Adenine
AFM	Atomic Force Microscopy
AI	Ab Initio
AIB	Dialanine
ALA	Alanine
ANS	8-Anilino-1-Naphthalenesulfonic acid
AO	Atomic Orbital
ARG	Arginine
ASA	Acetylsalicylic Acid (aspirin)
ASN	Asparagine
ASP	Aspartic Acid
AUNP	Gold Nanoparticle
AUNR	Gold Nanorod
BNNP	Boron Nitride Nanopore
BNNT	Boron Nitride Nanotube
BO	Born-Oppenheimer
CaOx	Calcium Oxalate
CD	Circular Dichroism
CCSD(T)	Coupled Cluster Singly, Doubly, Triply Excited
CG	Coarse Grain
CGS	Critical Gelation Concentration

LIST OF ABBREVIATIONS (Continued)

CHARMM	Chemistry at Harvard Macromolecular Mechanics
CHELPG	Charges from Electrostatic Potentials using a Grid based method
CNT	Carbon Nanotubes
COD	Calcium Oxalate Dihydrate
COM	Calcium Oxalate Monohydrate
ConA	Concanavalin A
DLS	Dynamic Laser Light Scattering
DSCF	Double Self-Consistent Field
EGCG	Epigallocatechin Gallate
EM	Electron Microscopy
FTIR	Fourier Transform Infrared Spectroscopy
GLC	Graphene Liquid Cell
GLY	Glycine
GPC	Gel-Permeation Chromatography
GTO	Gaussian Type Orbitals
HF	Hartree Fock
HIS	Histidine
HRSEM	High-resolution Scanning Electron Microscopy
ITC	Isothermal Titration Calorimetry
LCAO	Linear Combination of Atomic Orbitals
LEU	Leucine
LJ	Lennard-Jones
MD	Molecular Dynamics
MO	Molecular Orbital
MOC	Metal-Organic Cages
MP2	2nd order Moller-Plesset Perturbation
NAMD	Nanoscale Molecular Dynamics
NMR	Nuclear Magnetic Resonance
NP	Nanoparticle

LIST OF ABBREVIATIONS (Continued)

NF-RED	Nano-Fluidic Reverse Electrodialysis
OCN	Organomimetic Cluster Nanomolecules
PC	Phosphatidylcholine
PBC	Periodic Boundary Conditions
PBS	Phosphate Buffer Solution
PEG	PolyEthylene Glycol
PES	Potential Energy Surface
PHE	Phenylalanine
PME	Particle Mesh Ewald
PS	Phosphatidylserine
PXRD	Powder X-Ray Diffraction
QM/MM	Quantum Mechanics/Molecular Mechanics
RED	Reverse Electrodialysis
RI	Refractive Index
RU	Response Units
SAOS	Small Amplitude Oscillatory Shear
SAXS	Small Angle X-ray Scattering
SASA	Solvent Accessible Surface Area
SEAD	Select-Area Electron Diffraction
SCF	Self-Consistent Field
SEM	Scanning Electron Microscopy
SLS	Static Laser Light Scattering
S_NAR	Nucleophilic Aromatic Substitution
SNT	Supramolecular Nanotubes
SP	Sugar-coated Particles
SPR	Surface Plasmon Resonance
STEM	Scanning Tunneling Electron Microscopy
STEM-EDS	Energy-Dispersive X-Ray Spectroscopy
STEM-EELS	Electron Energy Loss Spectroscopy

LIST OF ABBREVIATIONS (Continued)

STM	Scanning Tunneling Microscopy
STO	Slater Type Orbitals
TA	Tannic Acid
TEM	Transmission Electron Microscopy
TEPC	Track-Etched Polycarbonate
THF	Tetrahydrogen Furan
TRP	Tryptophan
TYR	Tyrosine
Uv-Vis	Ultraviolet-Visible Spctroscopy
vdW	van der Waals
VMD	Visual Molecular Dynamics
WAXS	Wide-Angle X-Ray Scattering
XRD	X-Ray Diffraction

SUMMARY

This thesis is devoted to computational studies of biomedical assemblies, material assemblies, and nanofluidics. The majority of projects involved collaborations with experimentalists as well as other computational groups. The thesis is based on 11 published papers and 4 submitted or in preparation.

In Chapter 1, we give a layout of the thesis. In Chapter 2, we present the theory and methods that we use in our projects. We start discussing quantum mechanics, classical atomistic simulations, and finally we explain how to collect the mean information using statistical mechanics.

In the Chapter 3, we present the formation and stability of biomedical assemblies, using atomistic molecular dynamics (MD) simulations. In sections 3.1-3.4, we start with simulating the assemblies of single amino acids and nucleobases. In sections 3.1 and 3.2, we study the stability of metabolite fibrils. In section 3.3, we study metabolites interacting with inhibitor molecules, in solvated and crystalline phases. In section 3.4, we study crystalline metabolites interacting with cellular membranes. In sections 3.5-3.7, we study polypeptides structural stability in solvated and assembled forms, as well as their interactions with gold nanoparticles. In section 3.5, we study the backbone conformations of a heptapetide in solvated and crystalline phases. In section 3.6, we study the same peptide in crystalline phase interacting with gold nanoparticles. Finally in section 3.7, we study the stability of a 20-peptide-long protein in solvated and fibrillar phases. We also study the same peptide in the same phases interacting with gold nanoparticles.

In Chapter 4, we model the formation and stability of supramolecular assemblies with applications to material sciences. In section 4.1, we start with the study of co-crystallization of proteins in the presence of gold nanoparticles with polyethylene glycol chains. Afterwards, in section 4.2, we discuss the formation and stability of supramolecular nanotubes in different solvent environments. In

section 4.3, we study nanomedicines, which are derived from decaborate clusters. In section 4.4, we also investigate the interactions of metabolite crystals, consisting of aromatic amino acids, with 2D nanosurfaces. In section 4.5, we discuss the self-assembly of complex cages, yielding gelation. Finally in section 4.6, we study the self-assembly of calcium oxalate with and without citrate inhibitors, resulting in different crystal structures.

In Chapter 5, we model nanofluidics. In section 5.1, we study the pressure of water in graphene liquid cells, with varying shapes of graphene cells and number of water molecules entrapped between those cells. In section 5.2, we also study power generation by osmotic diffusion of KCl through charged boron nitride nanotubes. Finally, we have studied some pumping phenomena, but these studies are in preparation.

CONTRIBUTION OF AUTHORS

This thesis is based on eleven papers that have been published, two under review, and two in preparation. All projects presented in this thesis, with the exception of section 4.4, were performed in collaboration with experimentalists. The computational works results performed by Pavel Rehak are presented in this thesis.

In Chapter 3, all sections were accomplished in collaboration with Prof. Ehud Gazit (Tel-Aviv University). In section 3.1, we observed the growth and stability of tryptophan fibrils. Fibrils were synthesized by Prof. Gazit's group. Spectroscopic data (TEM, HR-SEM, Confocal Flourescence Microscopy) and biological tests (Cytotoxicity tests and Apoptosis tests) were performed by Gazit's groups or collaborators. All experimental results were reported by the Gazit's group [1]. MD simulations that demonstrated the twisting of different tryptophan crystals were performed by Pavel Rehak, guided by Profs. Lela Vuković and Petr Král.

In section 3.2, we observed different material properties of enantiopure and racemic crystals of tryptophan and phenylalanine fibrils. Collaborators obtained all experimental results (Turbidity Analysis, SEM, TEM, Mass Spectroscopy, Wide-Angle X-Ray Scattering, Thermal Gravimetric Analysis, and NMR) reporting their results in the manuscript [2]. All MD simulations and enthalpy of crystal calculations on different enantiopure and racemic tryptophan and phenylalanine crystals were performed by Pavel Rehak under the guidance of Prof. Král.

In section 3.3, we investigated the inhibition mechanisms of fibrillar growth of metabolites tyrosine, phenylalanine, and adenine with inhibitors epigallocatechin gallate and tannic acid, as well as acetylsalicylic acid, as a negative control. Collaborators performed all experiments (ThT kinetics fluorescence assay, Turbidity measurements, DLS, TEM, HR-SEM, and Cell cyctotoxicity), report-

ing their results in the manuscript [3]. Pavel Rehak performed all MD simulations and enthalpy of binding calculations under the guidance of Profs. Lela Vuković and Petr Král.

In section 3.4, we studied the mechanism of adenine, tryptophan, and tyrosine fibrils interacting with model mamillian cellular mebranes. Collaborators performed all experiments (colorimetric response, fluorescence, and cell viability) and discussed their results in the manuscript [4]. All MD simulations and enthalpy calculations were performed by Pavel Rehak under the guidance of Prof. Král.

In section 3.5, we studied the backbone conformations of a model peptide in solvated, oligomeric, and crystalline environments as a model for various proteins involved in misfolding illnesses. Collaborators synthesized and crystallized the peptides and performed the experiments (structure determination Wide-Angle X-Ray Scattering, TEM, Powder X-Ray Diffraction, Optical Microscopy, Kinetic Assay, Ultraviolet-Visible spectroscopy, Fourier Transform Infrared spectroscopy) and reported their results in the manuscript [5]. All MD simulations and backbone RMSD calculations were performed by Pavel Rehak under the guidance of Prof. Král.

In section 3.6, we took one peptide backbone conformation in its crystalline phase and observed how gold nanoparticles and gold nanorods bounded to the crystal. Collaborators performed all experiments, including peptide synthesis, crystallization, STEM, nanpoarticle synthesis, and experiments with magnets and reported their results in the manuscript. Pavel Rehak performed all MD simulations and electrostatic potential calculations under the guidance of Prof. Král. This paper is currently under preparation.

In section 3.7, we looked at peptide fibril, inspired by naturally occurring peptide supramolecular structures, and examined its stability and interaction with a gold nanopartical. Collaborators per-

formed all of the experiments (electric characterization, NMR, peptide construction, supramolecular fibril construction, surface adhesion, chemical catalysis, charge detection, Cardiac patches, FTIR, EFM) and discussed their results in the manuscript [6]. All MD simulations were preformed by Pavel Rehak under the guidance of Prof. Král.

In section 4.1, we looked at the co-crystallization of lysozyme proteins in the presence of PEGylated gold nanoparticles, as a model to hasten protein crystallization, in collaboration with Prof. Vicki Colvin (Brown University). The Colvin group performed all the experiments, such as XRD and determination of unit cell parameters. Pavel Rehak performed all MD simulations, enthalpy calculations and electrostatic potential analysis, under the guidance of Prof. Král. This paper is currently under preparation.

In section 4.2, we looked at the self-assembly and stability of supramolecular nanotubes, less than 10 nm in diameters, in different solvent environments in collaboration with Prof. Boris Rybtchinski (Weizmann Institute). The collaborators performed all experiments (UV-vis absorption, cryo-TEM imaging, electron paramagnetic resonance spectra, transient absorption) as well as some computations, involving molecular mechanic geometry optimization to determine the supramolecular structure of the tubes [7]. Pavel Rehak employed the resulting obtained tube structure and even extended the tube in some cases for the simulations to follow. All MD simulations were preformed by Pavel Rehak under the guidance of Prof. Král.

In section 4.3, we studied a variety of different atomically precise NPs which can be used for medicine in collaboration with Prof. Alexander Spokoyny (UCLA). Experimentalists synthesized various nanoparticles from a dodecaborate cluster with atomically precise ligands. From our ability to design these NPs to such a precision, we have full control over their physical properties, sizes, and chemical properties. Collaborators performed the experimental measurements, such as ^{1}H NMR, ^{19}F

CONTRIBUTION OF AUTHORS (Continued)

NMR, ^{11}B NMR, TEM, SPR, and 2D DOSY [8]. Pavel Rehak examined 6 such NPs, with PEGylated ligands and determined their sizes in different solvents through MD simulations and analysis under the guidance of Prof. Král.

In section 4.4, we studied the properties, stability, and dynamics of hybridization of biomolecular crystals, (pure enantiomer TRP and PHE as well as racemic TRP) and low dimensional nanomaterials (graphene, phosphorene, and carbon nanotubes). Pavel Rehak performed all of the MD simulations and enthalpy calculations under the guidance of Prof. Král. This paper is currently under review.

In section 4.5 we examined the e self-assembly and gelation of platinum-based metal-organic cages, with different ligands bonding to the platinum metal centers, in collaboration with Prof. Tianbo Liu (University of Akron). Collaborators synthesized the cages, prepared the samples, performed NMR, SAXS, small amplitude oscillatory shear, static/dynamics light scattering (SLS and DLS), TEM, isothermal titration calorimetry, HRSEM, and XRD experiments [9]. Pavel Rehak performed all MD simulations and performed further simulations of cages that were not available for experiments, as well as MD analysis under the guidance of Prof. Král.

In section 4.6, we examined the self-assembly and crystallization processes of calcium oxalate (CaOx) in the absence and presence of the inhibitor citrate, which can influence the final crystal structure, in collaboration with Profs. Reza Shahbazian-Yassar and Tolou Shokuhfar (both at UIC). Collaborators performed SEM, XRD, STEM-EDS, STEM-EELS measurements and analysis. Pavel Rehak performed all MD simulations and analysis under the guidance of Prof. Král. This paper is currently under review.

In section 5.1, we studied the pressure of water entrapped in a graphene liquid cell. We also determine contributions of Laplace pressure versus pressure exerted the by vdW attractions between

the graphene membranes. The collaborators synthesized the graphene liquid cells, performed STEM images, and EELS analysis [10]. Pavel Rehak preformed all MD simulations and analysis under the guidance of Prof. Král.

In section 5.2, we studied the enhanced power output, of osmotic energy harvesting through boron-nitride nanotubes. The advantage is that the device ca be built on macroscopic scale and have an overall higher efficiency. The boron nitride tubes are charged with hydroxyl groups bounded to them, thus filtering cations and producing an osmotic current. The collaborators performed all the experimental work including membrane fabrication and characterization as well as ion exclusion, osmotic current, power density, and surface charge density measurements, in addition to numerical simulations. Dr. Haiqi Gao initiated the MD simulations and MD analysis under the guidance of Prof. Král. Pavel Rehak continued MD simulations and analysis to complete the work under the guidance of Prof. Král. This paper was accepted for publication.

TABLE OF CONTENTS

CHAPTER **PAGE**

CHAPTER **PAGE**

CHAPTER **PAGE**

LIST OF FIGURES

FIGURE **PAGE**

FIGURE **PAGE**

FIGURE **PAGE**

FIGURE **PAGE**

FIGURE **PAGE**

FIGURE **PAGE**

FIGURE **PAGE**

LIST OF TABLES

CHAPTER 1

INTRODUCTION

In the last two decades, interest in nanoscale sciences has exploded due to their relevance in everyday life, such as pharmacy, medicine, biochemistry, energy, environment, information technology, optics, and space exploration. Many experimental techniques, such as spectroscopy, X-Ray Diffraction (XRD), Electron Microscopy (EM), Transmission Electron Microscopy (TEM), Scanning Electron Microscopy (SEM), Scanning Tunneling Electron Microscopy (STEM), and Atomic Force Microscopy (AFM) have been developed to understand and observe material structures and study properties of nanoscale systems. Unfortunately, these experimental techniques are not effective enough for analyzing systems at the atomistic level. Atomistic simulations have been developed to complement experiments and enable researchers to fully understand these systems.

Quantum approaches yield the most rigorous results for all systems. In practice, most systems are too large to fully implement quantum methods and require further approximations. However, in systems that are designed to study quantum phenomena this description should be preserved to some extent. One usually has to balance rigor and efficiency when trying to solve realistic problems. We can use a whole spectrum of methods that can be ordered in decreasing precision (increasing scales) as: 1) *ab initio* calculations, 2) hybrid Quantum Mechanics/Molecular Mechanics (QM/MM) MD simulations, 3) all atomistic MD simulations, 4) coarse-grained (CG) MD simulations, and 5) mean-field simulations.

Atomistic simulations date back to the 1950's when Nicholas Metropolis developed the Monte Carlo algorithm and applied it to argon (monoatomic) atoms. The earliest systems were modeled

through hard sphere models. More complex models, such as the square potential well and the $12-6$ Lennard-Jones (LJ) potential, were subsequently used. In the 1970's, Martin Karplus pioneered protein folding simulations. Initially, such simulations were slow and could only yield one snapshot per day ($\approx$ 10ps). Eventually, the simulations have become much more efficient to implement. Today, depending on the machine power and system properties (e.g. number of atoms and rigor of calculations), it is possible to simulate 10^6 atoms for $1-10$ ns in one day on a personal workstation and perform a thousand times more demanding simulations on supercomputers. On specialized computers designed for MD simulations it is thus possible to simulate 10^8 atoms and reach simulation lengths ranging in the microseconds. In our systems, we must typically model 10^4-10^6 atoms, yet we do not need to model reactions using reactive force fields. Therefore, we use classical atomistic molecular dynamics simulations, but determine the parameters of the molecules through *ab initio* calculations.

1.1 Thesis organization

In this thesis, we examine the self-assembly and stability of biomolecular nanostructures, material growth, and nanofluidics. In Chapter 2, we discuss the theory and methodology behind the calculations performed. First, we discuss *ab initio* calculations (microscopic in scale and highest in rigor) that are used for parameter fitting in MD simulations. Then, we describe how we run the MD simulations. Finally, we discuss how to extract data from the MD simulations.

In Chapter 3, we discuss biomedical assemblies, studied in collaboration with Prof. Ehud Gazit (Tel-Aviv University). In sections 3.1 and 3.2, we discuss metabolite fibrils, consisting of a single amino acid or nucleobase molecular units. We discuss the stability of phenylalanine (PHE) and tryptophan (TRP) fibrils. We performed simulations of solvated crystals and facets in order to

explain an unidirectional fibrillar growth (for enantipoure crystals) and a broad 2D growth (racemic crystals).

In section 3.3, we examine the inhibition mechanisms in the formation of metabolite fibrils. We discuss tyrosine (TYR), adenine (ADN), and PHE in their crystalline and solvated phases, interacting with inhibitors epigallocatechin gallate (EGCG), tannic acid (TA), and the negative control aspirin (ASA). The binding enthalpies of each inhibitor and metabolite were calculated in order to predict the efficacy of each inhibitor.

In section 3.4, we determine orientations of metabolite crystals (ADN, TRP, and TYR) interacting with lipid bilayer membranes. These lipid bilayer membranes consist of phosphatidylcholine phospholipid (PC) and combination phosphatidylcholine and phosphatidylserine phospholipids (PC/PS).

In section 3.5, we study the folding of a polypeptide consisting of seven amino acids (SHR-FF) undergoing backbone conformational changes between α-helical and cross-β linker structures. The cross-β linker conformation represents the state at a global free energy minimum. We examine the root mean square displacement (RMSD) of backbone atoms of the peptides in solvated and crystalline phase.

In section 3.6, we discuss the crystalline form of SHR-FF in the cross-β linker conformation interacting with gold nanoparticles (AUNPs). Experimentalists saw that the AUNPs coalesced only on one side of the fibril. AUNPs are highly charged due to the citrate ligands binding to them. The peptides in the crystal are arranged such that there is a strong buildup of dipole moment in the crystal.

In section 3.7, we examine the fibrillar structure, self-assembly, and interactions with AUNP a polypeptide fibril. This polypeptide consists of 20 amino acids and was inspired by a peptide

produced by metal-reducing bacteria type IV pili. The fibrillar structure of this peptide is held together through β sheets, running antiparallel to each other. We simulated these peptides in the presence and absence of AUNP and examined their fibrillar stability in the presence and absence of AUNP.

In Chapter 4, we examine the self-assembly and growth of materials. In section 4.1, in collaboration with Prof. Vicki Colvin (Brown University), we discuss with co-crystallization of lysozyme protein and PolyEthylene Glycol (PEG) gold nanoparticles (AUNPs). The AUNP hastens the crystallization of proteins without changing the unit cell parameters of the crystal structure. The collaborators reported that AUNPs with long PEG chains (molecular weight $10kDa/chain$) could co-crystallize, but AUNPs with short chains ($1kDa/chain$) would not. We ran simulations to observe the co-crystallization mechanism of lysozyme proteins in the presence of both AUNPs. In addition, we also calculated electrostatic potential isosurfaces in order to predict how gold nanorods (AUNRs) would align themselves, when co-crystallizing with the lysozyme proteins.

In section 4.2, in collaboration with Prof. Boris Rybtchinski (Weizmann Institute), we discuss the self-assembly and stability of supramolecular nanotubes from PP2b derivatives in different solvent environments.

In section 4.3, in collaboration with Prof. Alexander Spokoyny (UCLA), we discuss the sizes of atomically precise PEGylated nanopatricles. We determine the sizes and flexibility of various nanomedicines with ligands containing polyethylene glycol chains of various lengths. We determine the sizes and flexibility of these nanomedicines in water and a phosphate buffer solution (pH = 7.4).

In section 4.4, we discuss the interactions between TRP (enantiopure and racemic) and PHE (pure enantiopure only) crystals and graphene, phosphorene, and carbon nanotubes (CNTs). The hybrid complexes had properties similar to those originating from individual crystal or nanosurfaces.

In section 4.5, in a collaboration with Prof. Tianbo Liu (University of Akron), we discuss the self-assembly of metal organic cages (MOCs). We ran simulations in order to predict gelation or precipitation of these MOCs. We saw that different interactions contribute to the self-assembly of the cages and their possible gelation.

In section 4.6, in collaboration with Prof. Reza Shahbazian-Yassar (UIC), we study the growth of calcium oxalate in the presence and absence of citrate inhibitor. In the absence of citrate, calcium oxalate monohydrate (COM) crystal forms, whereas in the presence of citrate calcium oxalate dihydrate (COD) crystal forms.

In chapter 5, we delineate our nanofluidics studies. In section 5.1, in collaboration with Prof. Reza Shahbazian-Yassar, we discuss the pressure of water with graphene liquid cells (GLCs). Water droplets were entrapped in square and circular GLCs, consisting of two sheets.

Finally, in section 5.2, in collaboration with Profs. Sangil Kim (UIC) and Jerry Shan (Rutgers), we discuss power generation by osmotic flow through a charged boron nitride nanotube (BNNT).

We complete the thesis with closing remarks.

CHAPTER 2

THEORY AND METHODS

In this thesis, we model nanoscale systems that have $10^4 - 10^6$ atoms. In this chapter, we discuss the theories and computational methods. We begin with quantum mechanics and *ab initio* calculations, which help us determine the forcefield parameters for MD simulations. Then we discuss the theory behind the simulations. We finish this chapter with the discussion on the analysis of the simulations, where we discuss how to prepare each system, calculate the trajectories, and extract observables.

2.1 Quantum Mechanics

Theory of *ab initio* calculations

In quantum mechanics all the information resides in the wavefunction of the system. We can determine this wavefunction by solving the Schrödinger equation:

$$i\hbar\frac{\partial\Psi(\vec{R_1},\ldots,\vec{R_M},\vec{r_1},\ldots,\vec{r_l},t)}{\partial t} = \hat{H}\Psi(\vec{R_1},\ldots,\vec{R_M},\vec{r_1},\ldots,\vec{r_l},t). \tag{2.1}$$

Here, nuclear coordinates for M nuclei are denoted as $\vec{R_i}$ and electronic coordinates for l electrons are denoted as $\vec{r_i}$, $\hbar$ is the reduced Plank's constant and $\hat{H}$ is the Hamiltonian operator, which has its classical analog in Equation 2.43. In time-independent problems (potentials), this Hamiltonian operator can give the eigenenergies of the system.

The full Hamiltonian of a molecular system is

$$\hat{H} = \sum_{j=1}^{M} \frac{\hat{p}_j^2}{2m_j} + \sum_{i=1}^{l} \frac{\hat{p}_i^2}{2m_e} - \sum_{j=1}^{M}\sum_{i=1}^{l} \frac{Z_j e^2}{\mid \vec{R_j} - \vec{r_i} \mid} + \sum_{q>i}^{l}\sum_{i=1}^{l-1} \frac{e^2}{\mid \vec{r_q} - \vec{r_i} \mid} + \sum_{s>j}^{M}\sum_{j=1}^{M-1} \frac{Z_s Z_j e^2}{\mid \vec{R_s} - \vec{R_j} \mid}. \quad (2.2)$$

The first term is the kinetic energy operator of the nuclei, the second term is the kinetic energy operator of the electrons, the third term is the nuclei-electron potential energy operator, the next term is the inter-electron potential energy operator, and the final term is the inter-nuclei potential energy operator.

The Born-Oppenheimer (BO) approximation assumes that nuclei are significantly more massive than electrons. Therefore, we can treat nuclei as fixed point masses, around which electrons are moving. Then the molecular wavefunction becomes separable with respect to electronic and nuclear coordinates as

$$\Psi(\vec{R_1}, \ldots, \vec{R_M}, \vec{r_1}, \ldots, \vec{r_l}) = \Psi(\vec{R}, \vec{r}) = \psi_{nuc}(\vec{R})\psi_{elec}(\vec{R}, \vec{r}). \quad (2.3)$$

Then the effective Hamiltonian of electrons can be described as

$$\hat{H} = \hat{H}_{elec} + V_{NN}(\vec{R}), \quad (2.4)$$

where

$$\hat{H}_{elec} = \sum_{i=1}^{l} \frac{\hat{p}_i^2}{2m_e} - \sum_{j=1}^{M}\sum_{i=1}^{l} \frac{Z_j e^2}{\mid \vec{R_j} - \vec{r_i} \mid} + \sum_{q>i}^{l}\sum_{i=1}^{l-1} \frac{e^2}{\mid \vec{r_q} - \vec{r_i} \mid} \quad (2.5)$$

and $V_{NN}(\vec{R})$ is constant since nuclei are fixed. This gives a simplified Schrödinger equation to solve for the electronic wavefunctions and electronic eigenenergies.

$$(\hat{H}_{elec} + V_{NN})(\vec{R})\psi_{s,elec}(\vec{R},\vec{r}) = U_s(\vec{R})\psi_{s,elec}(\vec{R},\vec{r}). \tag{2.6}$$

$U_s(\vec{R}) = E_{s,elec}(\vec{R}) + V_{NN}(\vec{R})$, where $U_s(\vec{R})$ is the electronic potential energy surface of the s^{th} excited state and $E_{s,elec}(\vec{R})$ is the related electronic energy parametrized by the nuclear coordinates $\vec{R}$.

After solving the electronic Hamiltonian, we can solve the nuclear Schrödinger equation.

$$\hat{H}_N(\vec{R})\psi_{nuc}(\vec{R}) = E_{mol}\psi_{nuc}(\vec{R}), \tag{2.7}$$

where $\hat{H}_N(\vec{R})$ is the nuclear Hamiltonian given by

$$\hat{H}_N(\vec{R}) = \sum_{j=1}^{M} \frac{\hat{p}_j^2}{2m_j} + U_s(\vec{R}), \tag{2.8}$$

and E_{mol} is the total energy of the molecule with all quantum numbers for the translational, vibrational, rotational and electronic degrees of freedom.

Electrons are Fermions, which means that the probability density does not change with the exchange of indistinguishable electrons. Consequently, acting with the permutation operator on the multi-electron wavefunction results in the negative of the original wavefunction.

$$\hat{P}_{ij}\Psi(1,\ldots,i,\ldots,j,\ldots,N) = \Psi(1,\ldots,j,\ldots,i,\ldots,N) = -\Psi(1,\ldots,i,\ldots,j,\ldots,N). \tag{2.9}$$

From this property, we can derive the Pauli Exclusion principle, where no two electrons can be in the same spatial and spin orbitals.

One way to construct a multi-electron wavefunction that yields its negative multiple after applying the permutation operator is by constructing as a superposition of Slater Determinants (SDs) (multi-electron complete basis set).

$$\Psi(\vec{r}) = \sum_{s_1,\ldots,s_l} c_{s_1}\ldots c_{s_l} \begin{vmatrix} \phi_1(\vec{r_1}) & \phi_2(\vec{r_1}) & \ldots & \phi_l(\vec{r_1}) \\ \phi_1(\vec{r_2}) & \phi_2(\vec{r_2}) & \ldots & \phi_l(\vec{r_2}) \\ \vdots & \vdots & \ddots & \vdots \\ \phi_1(\vec{r_l}) & \phi_2(\vec{r_l}) & \ldots & \phi_l(\vec{r_l}) \end{vmatrix}. \tag{2.10}$$

If we describe a multi-electron atom, then ϕ_i can be atomic orbitals (AO), which need to be optimized (depending on method). If we describe a multi-electron molecule, then ϕ_i can be molecular orbitals (MO). Each column in the matrix (Equation 2.10) represents the same orbitals and each row represents the j^{th} electron, where $\vec{r_j}$ is its position. The exact solution of the Schrödinger equation can be described as a linear combination of infinite number of SDs (complete basis set), giving also the exact eigenenergies. In practice, we need to truncate this linear combination in number of terms or types of summed series, so we only obtain approximate eigenfunctions and possibly eigenenergies.

Electronic structure calculations

The simplest multi-electron electronic structure calculations use the Hartree-Fock (HF) (mean field) theory, where the multi-electron wavefunction is represented by one optimized SD. Its form can be found in the variational solution, yielding HF equations (Equation 2.12). In the HF theory, the HF Hamiltonian is the sum of the individual Fock operators for each electron electrons, represented by $\hat{f}_i$,

$$\hat{H} = \sum_{i}^{l} \hat{f}_i = \sum_{i=1}^{l} -\frac{\nabla_i^2}{2} - \sum_{j=1}^{M}\sum_{i=1}^{l} \frac{Z_j}{\mid \vec{R_j} - \vec{r_i} \mid} + \sum_{q>i}^{l}\sum_{i=1}^{l-1} 2J_{iq} - K_{iq}, \tag{2.11}$$

which becomes equivalent to solving for a series of one-electron wavefunctions, $\phi_\alpha(i)$

$$\hat{f}_i \phi_\alpha(i) = \varepsilon_\alpha \phi_\alpha(i), \tag{2.12}$$

where ε_α is the eigenenergy of ϕ_α. The first two terms in the Fock operator represent the kinetic energy of electrons and attractive potential energy of electrons to nuclei. The last two terms give the inter-electron repulsion space. The expectation value of the Coulomb integral is

$$\langle \phi_i(1) | J | \phi_i(1) \rangle = \int_{allspace} \phi_q^*(2)\phi_q(2) \frac{1}{\mid \vec{r_q} - \vec{r_i} \mid} \phi_i^*(1)\phi_i(1) dV. \tag{2.13}$$

The number in the parenthesis labels individual electrons. The Coulombic integral can be viewed as the mean-field analog of the classical repulsion of two electrons. The expectation value of the exchange integral is

$$\langle \phi_i(1) | K | \phi_i(1) \rangle = \int_{allspace} \phi_q^*(2)\phi_i^*(1) \frac{1}{\mid \vec{r_q} - \vec{r_i} \mid} \phi_q(1)\phi_i(2) dV. \tag{2.14}$$

This integral has no classical analog and vanishes when there are two electrons in opposite spin-orbitals.

The HF theory provides a starting point for calculating the electronic structure of multi-electron systems. However, in the HF method, we are missing electron correlations. To include them, we can add more SDs. For example, we can use a perturbation theory, where we split the Hamiltonian

by having the original Hartree-Fock Hamiltonian, $\hat{H}^0$ (explicitly expressed in Equation 2.11) and a perturbation, $\hat{V}$ in

$$\hat{H} = \hat{H}^0 + \hat{V}, \tag{2.15}$$

known as Møller-Plesset perturbation theory. The perturbation is the correction term formed by the exact electron-electron coupling term minus the HF electro-electron coupling term.

$$\hat{V} = \sum_{q>i}^{l} \sum_{i=1}^{l-1} \frac{1}{\mid \vec{r_q} - \vec{r_i} \mid} - (2J_{iq} - K_{iq}). \tag{2.16}$$

For optimal compromise between rigor and computational effort, we use the second order Møller-Plesset (MP2) level of theory. In the first order correction, $E_0^{(1)}$ given in

$$E_0^{(1)} = \langle \Psi_{HF}(\vec{r}) \mid \hat{V} \mid \Psi_{HF}(\vec{r}) \rangle, \tag{2.17}$$

we still use the HF single SD wavefunction, $\Psi_{HF}(\vec{r})$, thus MP1 is equivalent to HF theory. In the second order correction, $E_0^{(2)}$ given in

$$E_0^{(2)} = \sum_{s \neq 0} \frac{\mid \langle \Psi_s^{(0)} \mid \hat{V} \mid \Psi_{HF} \rangle \mid^2}{E_0^{(0)} - E_s^{(0)}}. \tag{2.18}$$

The exact HF method provides a complete basis set of MOs from, which N are occupied and the other unoccupied. Replacing the occupies MOs in the HF SD by one or more unoccupied MOs gives eventually a complete N electron basis set. We usually pick only singly or doubly excited SDs, i.e. SDs with one or two unoccupied MOs.

Basis sets

AOs are derived from the one-electron solution of the Schrödinger equation, where we obtain STOs, with the radial dependence, $R(r) \propto e^{-\zeta' r}$. When calculating inter-electron repulsions (such as evaluating Coulombic and exchange integrals in Equation 2.13 and Equation 2.14) we need to integrate a product four such functions, which have no analytical solution. We approximate these STOs with Gaussian Type Orbitals (GTOs), with the functional form of

$$\Psi(x, y, z) = N(x - x_0)^n (y - y_0)^m (z - z_0)^j e^{-\zeta(r - r_0)^2}. \tag{2.19}$$

In this function form, the nucleus is at the origin (x_0, y_0, z_0). N in Equation 2.19 is the normalization constant. The sum of the pre-factor exponents equals the angular momentum quantum number, i.e. $n + m + j = l$. When $l = 0$, there is an s-type orbital and there are no pre-factor variables; when $l = 1$ there is a p-type orbital and we have x, y or z as a pre-factor variable; when $l = 2$ there is a d-type orbital and we have a possible linear combination of variable pre-factors, whose exponents sum to 2. Unlike STOs, GTOs are differentiable at the origin and decay more rapidly.

When applying GTOs in the calculations, we split the ζ and obtain a linear combination of Gaussian functions. A typical basis set could be labelled as $6 - 31G^*$. Here the core and valence electrons have a split ζ. The core electrons are represented as a linear combination of six Gaussian functions. The valence electrons are split even further with two different ζ, one with 3 Gaussian functions and a second with only one Gaussian function. It is possible to have another split of ζ, such as the basis set represented by $6 - 311G^*$. The $*$ represents the fact that we use d-orbitals for the heavy atoms, C, N, and O, due to polarization effects in a chemical bond. If there is a second $*$ then we use p-orbitals for H atoms.

2.2 Molecular Dynamics Simulations

We can describe system fluctuations, dynamics, and conformational changes on the microscopic level through MD simulations. These microscopic processes can ultimately influence what experimentalists see on the macroscopic level. As we discussed earlier, the classical MD simulations describe the motion of molecules by classical Newtonian or Langevin equations, where the inter- and intramolecular forces can be obtained from force fields, extracted from more precise quantum mechanics calculations. The nuclear dynamics usually proceeds on the ground state potential energy surfaces (PES) obtained from the calculations. We will clarify this more in the following sections.

Potential energy surface

The potential energy is essential to determine forces and acceleration of bodies in the system as shown in Equation 2.44. Then we can numerically integrate the acceleration to determine atomic velocities, which then can be integrated to determine their positions. First we need to know the functional form of the PES, which best approximates the electronic PES derived from *ab initio* calculations. Most classical PES used in molecular mechanics have the functional form, in the form of

$$U_{MM}(\vec{R}) = \sum_{Bonds} K_b(r_b - r_{b0})^2 + \sum_{Angles} K_\theta(\theta - \theta_0)^2 + \sum_{Dihedrals} V_i(1 + \cos(n\phi + \phi_0)) + \sum_{j>i}^{N} \sum_{i=1}^{N-1} \left\{ \frac{q_i q_j}{4\pi\epsilon_0 r_{ij}} + 4\epsilon_{ij} \left[\left(\frac{\sigma_{ij}}{r_{ij}} \right)^{12} - \left(\frac{\sigma_{ij}}{r_{ij}} \right)^{6} \right] \right\} \quad (2.20)$$

and illustrated in Figure 1. The first three sums are performed over the internal degrees of freedom, which represent bond stretches ($1,2$ terms with only one bond separating the atoms), angle bends ($1,3$ terms with two bonds separating the atoms), dihedral rotations ($1,4$ terms with three bonds

separating the atoms). Other PES may have additional $1,3$ (such as Urey-Bradley) or $1,4$ (such as improper) terms. The external degrees of freedom, which apply to $1,4$ terms and beyond, are the electrostatic and dispersion interactions, determined in Equation 2.32 and Equation 2.39.

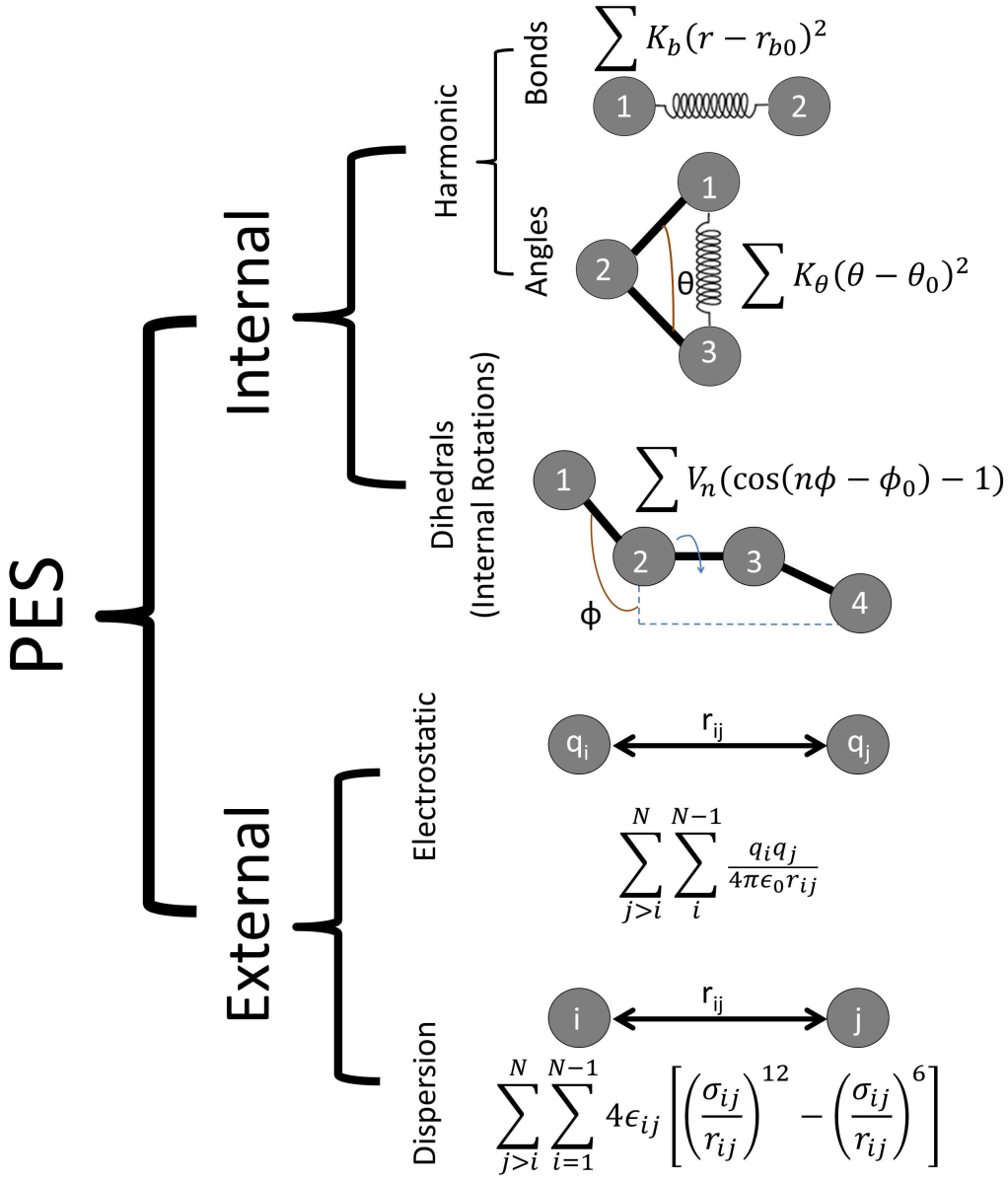

Figure 1: Internal degrees of freedom: (1) Bond Stretches $(1-2$ terms) (2) Angle Bends $(1-3$ terms) (3) Dihedral Rotation $(1-4$ terms). External degrees of freedom $(1-4$ terms and beyond) Electrostatic and Dispersion Interactions.

Bond stretches and angle bends originate from vibrational degrees of freedom. A molecule with N atoms has $3N$ total positional degrees of freedom. There are three degrees of translational freedom and either two for linear molecules (including diatomics) or three for nonlinear molecules degrees of rotational freedom. This yields $3N-5$ for linear and $3N-6$ for nonlinear molecules vibrational degrees of freedom. Vibrations are practically frozen at ambient temperatures. Calculated accelerations would be too large, due spikes in numerical differentiation of stiff bonds and angles. We model the vibrational degrees of freedom after Hooke's Law for the harmonic oscillator, due to the ease of differentiating quadratic functions.

The dihedral terms are a reflection of the molecule undergoing internal rotations. An atom or a group of atoms, separated by three bonds, rotate with respect to each other along the axis of the second bond separating the two groups. We describe the dihedral contribution to the PES as a linear combination of trigonometric functions due to the periodicity of complete rotations upon a bond.

We have an expense of $O(N^2)$, where N is the number of atoms, when modelling modelling non-bonded interactions using Equation 2.20. We only consider two atoms within a certain distance, as non-bonded terms decay with radial distance, in order to reduce cost. In order to have smooth differentiation, we use a switching function

$$f_{switch} = 1(r_{ij} < r_{on}) \tag{2.21}$$

$$f_{switch} = \frac{(r_{off} - r_{ij})^2(r_{off} + 2r_{ij} - 3r_{on})}{(r_{off} - r_{on})^3}(r_{on} \leq r_{ij} \leq r_{off}) \tag{2.22}$$

$$f_{switch} = 0(r_{off} \leq r_{ij}). \tag{2.23}$$

Usually we have $r_{on} = 10$ Å and $r_{off} = 12$ Å. We only consider atoms that are within 14 Å of each other for the evaluation of non-bonded interactions, with this list updated every 20 steps. This is a good approximation for dispersion interactions which decay as r^6, thus making them short ranged interactions. However, Coulombic interactions, which decay as r are long ranged, since they decay more slowly. We implement the Particle Mesh Ewald (PME) algorithm, which uses Fast Fourier Transform (expense $\mathrm{O}(N \log N)$) to calculate Coulombic contributions of atoms beyond the cutoff region (real space) and in image boxes (reciprocal space), in order to correct the errors from using a switching function. Usually it takes ≈ 500 image boxes for each PME implementation.

Parameterization of PES

Nuclei of atoms move through an electronic PES. It is possible to run MD simulations using the electronic PES directly to determine nuclear motions. Due to the expense of calculating these PESs, such calculations can be performed only on small systems with limited trajectories. Therefore, we use classical molecular mechanics to model larger systems with longer trajectories, which uses a PES that approximates the electronic PES, i.e. in Equation 2.20, we try to approximate $U_{MM}(\vec{R})$ to the electronic PES, i.e. $U_s(\vec{R})$ in Equation 2.6. For this PES in Equation 2.20, we obtain parameters determined from *ab initio* calculations, which best approximates the electronic PES. This method requires less effort to calculate.

Sometimes parameters for the PES can be obtained empirically or through previous studies. For example, parameters for biomolecules have been extensively derived through computational and experimental research over the years. For most other instances, these parameters are not so readily available, so we need to calculate them, using quantum mechanics.

When we use quantum calculations for parameter fitting in Equation 2.20, we try to obtain: (1) equilibrium geometries, (2) force constants (for harmonic terms), (3) energy profiles (for dihedral and dispersion interactions), and (4) partial charges (for electrostatic interactions).

In geometry calculations, we adjust nuclear positions until we obtain a minimal energy is obtained. Ideally, we try to search for the condition

$$\frac{\partial U_s(\vec{R})}{\partial \vec{R}_j} = 0, \tag{2.24}$$

where $\vec{R}_j$ is the position of the j^{th} nucleus. To obtain the optimal geometry we use double self-consistent field method (DSCF). In this method, we use a double iteration loop. First, we guess the nuclear coordinates, then we perform the SCF method, then we change the nuclear coordinates, and apply the SCF method again. We compare the energies obtained and determine whether they are within a threshold. If the new energy is within that, we finish the optimization calculation, otherwise we adjust the coordinates and repeat the procedure. This helps us determine the variable r_{b0} and θ_0 in Equation 2.20.

When determining the dihedral scan, we also perform geometric optimization calculations. We change the dihedral angle by steps and then constrain this dihedral angle and allow the remainder of the molecule to relax. Usually, we have two scans: (1) $-180^\circ \leq \phi \leq 0^\circ$ and (2) $0^\circ \leq \phi \leq 180^\circ$, and a step size $\Delta\phi = 10^\circ$.

In the calculation for the force constants, we use results from the quantum harmonic oscillator problem. We need to determine the Hessian matrix, labelled as D, whose elements are given in

$$D_{jk} = \frac{\partial^2 U_s(\vec{R})}{\partial \vec{R_j} \partial \vec{R_k}}. \tag{2.25}$$

There, we obtain the double derivative of the energy with respect to the nuclear coordinates ($\vec{R_j}$ and $\vec{R_k}$). From the quantum harmonic oscillator we have the relations

$$\omega_{jk} = \frac{1}{2\pi}\sqrt{\frac{K_{jk}}{\mu_{jk}}} \tag{2.26}$$

and

$$\mu_{jk}(2\pi\omega_{jk})^2 = \frac{\partial^2 U_s(\vec{R})}{\partial \vec{R_j} \partial \vec{R_k}}, \tag{2.27}$$

where ω_{jk} is the angular frequency of the vibrations between the j^{th} and k^{th} nuclei, K_{jk} is the force constant of the bond between the j^{th} and k^{th} nuclei, and μ_{jk} is the reduced mass of j^{th} and k^{th} nuclei, needed to describe the relative motion of two bodies

$$\mu_{jk} \equiv \frac{m_j m_k}{m_j + m_k}. \tag{2.28}$$

In order to determine force constants we need to diagonalize the Hessian, using the relation

$$det[\mu_{jk}(2\pi\omega_{jk})^2 - \delta_{jk}\lambda_j] = 0. \tag{2.29}$$

Then we can determine K_b and K_θ in Equation 2.20.

Parameter fitting

Internal parameter fitting

After computing optimal geometries and diagonalizing the Hessian we obtain a quantum PES. We then need to fit the constant molecular mechanics parameters (K_b, r_{0b}, K_θ, θ_0 in Equation 2.20), such that these parameters fit the quantum PES as closely as possible. We use the relation

$$F_{bond,angle} = \sum_{bond,angle} \left(\frac{r^{QM} - r^{MM}}{r_{scale}} \right)^2 + w \sum [U_s^{distort}(\vec{R}) - U_{MM}^{distort}(\vec{R})]^2 \tag{2.30}$$

to determine these parameters. When fitting the parameters we look at different distortions. The first term in Equation 2.30, represents the geometric values of the molecule. The second term represents the changes in energy upon distorting the molecule and determines the force constants. The pre-factor w is the weight we place on the energy values when fitting. When we increase w, we try to make a more precise calculation for force constants. Usually geometric value converge quickly, whereas force constants converge slowly.

When we fit dihedrals, we first obtain an energy scan and fit using the relation

$$F_{dihedral} = \sum_{i}^{scans} w_i (U_s(\vec{R}) - U_{MM}(\vec{R}) + c)^2. \tag{2.31}$$

Here we try to minimize the differences between the energy values obtained in the QM calculations and those values obtained through the parameters used in Equation 2.20 for each scan. The last term in the summation is the normalization $c = \overline{U}_{MM}(\vec{R}) - \overline{U}_s(\vec{R})$, so that $\frac{\partial F_{dihedral}}{\partial c} = 0$. $\overline{U}_{MM}(\vec{R})$ represents average molecular mechanics energy and $\overline{U}_s(\vec{R})$ represents average quantum mechanics

energy. In the dihedral fitting we adjust in Equation 2.20 the multiplicity, n and ϕ_0. The value of n can be integers ranging from 1 to 6. The phase angle $\phi_0 = 0°$ or $180°$.

External parameter fitting

At the nanoscale there are many intermolecular forces that affect how a system behaves. Electrostatic, dispersion, and hydrogen bonding interactions are the most important intermolecular forces that influence our systems.

The external terms are the most important parameters, when calculating self-assembly processes. In Equation 2.20, there are long-ranged Coulombic interactions and short-ranged dispersion interactions. In the Coulombic term only the distance between the i^{th} and j^{th} species (r_{ij}) and their charges (q_i and q_j) depend on the system, whereas all other terms are universal constants. The distances can be determined during the calculation of the trajectories. The molecule, on the other hand could be charged or neutral. The molecule exerts an electric field, even if it is neutral because it could have a dipole or quadrupole moment. We assign partial charges to the individual atoms within the molecule to best replicate the electric field exerted by this molecule. The sum of the partial charges of each atom must also be equal to the net charge of the molecule.

Electrostatic interactions are a combination of monopole, dipole, quadrupole, and higher order interactions. These interactions become weaker with higher order poles, due to more rapid decay with respect to distance, and have more complex orientation dependence. The exact dependence can be determined by solving the Poisson equation and applying the appropriate boundary conditions.

In solution environments, as opposed to vacuum, screening effects occur. When there are two charges in vacuum, the electrostatic interaction is determined through the Coulombic equation given by

$$U_{Coul}(r_{12}) = \frac{Q_1 Q_2}{4\pi\epsilon_0 r_{12}}, \tag{2.32}$$

where U_{Coul} represents the electrostatic potential energy between the two species, r_{12} is the distance between the two species, $Q_{1,2}$ are the charges of first and second species, and ϵ_0 is the vacuum permittivity.

When these charges are in a solvent with ions, oppositely charged ions are attracted to their respective charged particles and cancel the electric field. A large number of ions in the solution can cause more counterions to come closer to the charged particle. The net electric field this particle exerts decays more rapidly. If the concentration is lower, then there are less counterions to cancel the net electric field exerted by the particle and it decays more slowly. In addition, if temperature is increased, then the ions are more mobile and less likely to coalesce around the charged species. Therefore, the screening length would increase. The electrostatic interactions can be calculated after solving the Boltzmann-Poisson relation and the next result is

$$U_{Coul}(r_{12}) = \frac{Q_1 Q_2}{4\pi\epsilon\epsilon_0 r_{12}} e^{-\frac{r_{12}}{\lambda_D}}, \tag{2.33}$$

where λ_D is the Debye (screening) length is determined by

$$\lambda_D = \sqrt{\frac{\epsilon\epsilon_0 k_B T}{2 N_A e^2 I}}, \tag{2.34}$$

k_B J/K is the Boltzmann constant, T is the absolute temperature, N_A is Avogadro's number, e is the charge of one proton (i.e. elementary charge), and I is the ionic strength, given by

$$I = \frac{1}{2} \sum_{i=1}^{n=iontype} C_i z_i^2 \ . \tag{2.35}$$

In Equation 2.35, we perform a summation over the ion types and C_i is the concentration of the i^{th} species and z_i is the charge of the i^{th} ionic species. The Debye length, λ_D, is considered the distance in which the particle can exert its electric field on other particles. Beyond this length, the electric field of particle will affect very little other charged particles. In a physiological solution at T= 310 K ($[NaCl] = 0.15$M), $\lambda_D \approx 7$ Å. In a highly concentrated solution of $[NaCl] = 1.00$M, $\lambda_D \approx 3$ Å at the same temperature. When we model Coulombic interactions, the higher order poles, solvent, and screening effects are calculated implicitly through Equation 2.32.

There are many ways to determine partial charges of atoms, which give a wide variety of different results for the same molecule. Electrostatic Potential-based Charge fitting yields the most accurate results for systems not undergoing chemical reactions, because they are based on electric field calculations of the molecule. The energy obtained from quantum calculations is given

$$U_s^{Coul} = \int \frac{\rho(\vec{r})q}{\mid \vec{R} - \vec{R_q} \mid^2} d\vec{R} = qV_{QM}(\vec{R_q}). \tag{2.36}$$

Here, we take point charges, q at coordinates $\vec{R_q}$, which are in an electric field. The charge distribution is expressed as $\rho(\vec{r})$, and $\vec{R_q}$ is the distance of the point charge from the molecule. $V_{QM}(\vec{R_q})$ is the quantum potential. With the adjustment of the molecular partial charges we try to recreate this quantum potential.

We use the fitting weighted function

$$F_{elec} = \int W(\vec{R})[V(q(\vec{r}), \vec{R}) - V_{QM}(\vec{R})]^2 dV + \lambda(q_{tot} - \sum_{i=1}^{N_{atoms}} q_i). \tag{2.37}$$

We minimize this function under the Lagrangian constraint that the sum of the atomic partial charges needs to be equal to the net charge of the molecule. The weighting factor, $W(\vec{R})$ has the property that $\lim_{\vec{R}\to 0} W(\vec{R}) = 0$ and reaches a maximum value at $\mid \vec{R} \mid \approx 3 - 5$ Å away from the atom.

$$W(\vec{R}) = exp[-\beta\{log(\frac{\rho'(\vec{R})}{\rho_r})\}], \tag{2.38}$$

where $\rho'(\vec{R})$ is a predefined sum of atomic electron densities, ρ_r is a reference electron density, and β is an adjustment parameter to satisfy the limits of $W(\vec{R})$.

Dispersion occurs when the wavefunctions of two molecules are close enough, at a distance r, and their electrons become correlated, thus there is an attraction, which decays as r^6. The molecules cannot come too close due to the fact that electrons are Fermions, thus leading to the Pauli exclusion principle. This causes a repulsion, which decays as r^n, as an approximation. Usually the best average is $n = 12$. To model the electron correlation and the Pauli Exclusion principle, the $12 - 6$ Lennard-Jones (LJ) potential is used is

$$U_{LJ}(r_{ij}) = 4\epsilon_{ij}\left[\left(\frac{\sigma_{ij}}{r_{ij}}\right)^{12} - \left(\frac{\sigma_{ij}}{r_{ij}}\right)^{6}\right], \tag{2.39}$$

where r_{ij} is the distance between the i^{th} and j^{th} atoms, ϵ_{ij} is the strongest possible attraction (i.e. the energy well), and σ_{ij} is the finite distance, where potential energy, $U_{LJ}(r_{ij}) = 0$ (i.e. the van der Waals (vdW) radius). The strongest interactions occur at $r_{ij}^{min} = \sqrt[6]{2}\sigma_{ij}$, at which point the net

force would be 0. In order to calculate the dispersion interactions between two atoms (labelled as ii and jj), we take the geometric mean of their energy wells,

$$\epsilon_{ij} = \sqrt{\epsilon_{ii}\epsilon_{jj}}, \tag{2.40}$$

and the arithmetic mean of the vdW radii,

$$\sigma_{ij} = \frac{\sigma_{ii} + \sigma_{jj}}{2}. \tag{2.41}$$

Parameters for dispersion interactions can be obtained through rigorous calculations (usually density functional theory) of the energy profile between different atoms. In practice these type of calculations are intensive. Therefore we use analogy of similar atoms fitting from previously determined energy fitting studies or even based on empirical studies.

Hydrogen bonding occurs when there is a highly electronegative and relatively small atom (such as oxygen, nitrogen, or fluoride) bonded to a hydrogen atom within a molecule, causing this molecule to be a hydrogen bonding donor. Due to the small size of hydrogen it is possible for the hydrogen bonding donor to be attracted to a hydrogen bonding acceptor, which would also be a highly electronegative and relatively small atom. Once this bonding occurs the distance between the hydrogen atom and the acceptor's atom is smaller than the sum of their vdW radii. The distance for strongest attraction of hydrogen bonding is within the repulsive region of the LJ potential. In earlier versions of classical molecular dynamics hydrogen bonding was explicitly modelled, but since then has been abandoned. Today classical models describe hydrogen bonding implicitly through the combination of dispersion and electrostatic interactions, using Equation 2.39 and Equation 2.32.

System preparation

In order to calculate the trajectories of the system we need to integrate numerically Equation 2.45, with the PES in Equation 2.20. The size of systems we can simulate in a reasonable time is limited, due to computer capacity. Therefore we need to implement periodic boundary conditions (PBC). We replicate the simulation box in all directions to emulate macroscopic solvent environments.

We use the Nosé-Hoover method to keep pressure and temperature constant, when preparing a simulation. First we set up the system in VMD or CHARRMM GUI. Before running any equilibration we relax the system by minimizing it. Usually there is a high positive potential energy, mostly due to atoms being in the repulsive region of Equation 2.39 potential. Relaxing the system then prevents too large accelerations, thereby also velocities and temperatures becoming too large. Once we start pre-equilibration runs, we initially assign velocities as shown in

$$f_{MB}(\overrightarrow{p_{x,i}}) = \frac{1}{\sqrt{2\pi m_i k_B T}} e^{\frac{\overrightarrow{p_{x,i}}^2}{2m_i k_B T}}, \tag{2.42}$$

where $f_{MB}(\overrightarrow{p_{x,i}})$, is the Maxwell-Boltzmann distribution of the momenta of the atoms in a cardinal direction, m_i is the mass of the i^th atom, and T is the temperature at which we set our simulation. We would rescale $3N$ velocities of N atoms such that the net momentum is zero ($\overrightarrow{p_{tot}} = \sum \overrightarrow{p_i} = 0$). The Berendsen thermostat rescales velocities (thus kinetic energies) of the atoms so that they are representative of the translational kinetic energy at the desired temperature. Pressure is controlled by rescaling the atomic coordinates, thus controlling intermolecular forces inside the primary box and with other molecules in the image boxes. We stiffen bonds involving a hydrogen and a heavy atom through the SHAKE algorithm because that bond would have the highest frequency due to the significantly lower reduced mass.

Calculation of trajectories

We run our simulations in order to observe thermodynamic phenomena. We explore the ensemble of each system through time-dependent trajectories. In order to explore the ensemble, we need to calculate trajectories.

Newtonian mechanics

When using the MD approach, we need to calculate trajectories in order to understand the studied phenomena. According to Newtonian mechanics, linear momentum, angular momentum, and energy are conserved. The Hamiltonian is defined as

$$H \equiv \frac{\vec{p}^2}{2m} + U, \tag{2.43}$$

whose value is constant with respect to space and time. From this we can calculate forces in a system by

$$\vec{F} \equiv \frac{d\vec{p}}{dt} = -\frac{dU}{d\vec{r}}. \tag{2.44}$$

This system of equations to calculate MD trajectories.

Langevin dynamics

We use Langevin dynamics in order to keep temperature and pressure constant, which are subject to rounding errors in our numerical simulations. In Langevin dynamics, we couple our system to a thermal bath and the equation of motion is given by

$$\frac{d\vec{p}}{dt} = -\frac{dU}{d\vec{r}} - \gamma_{Lang}\frac{d\vec{r}}{dt} + \sqrt{\frac{2\gamma_{Lang}k_BT}{m}}\overrightarrow{G(t)}. \tag{2.45}$$

The first term is derived from Equation 2.44, the second term has a damping factor, γ_{Lang} multiplying the velocity, in the third term there is a random force acting on the particles, $\overrightarrow{G(t)}$, with a multiplying factor coming from the theory of Brownian motion, where k_B is the Boltzmann constant.

We can determine the acceleration of each atom from Equation 2.45. We use Velocity Verlet algorithm, to numerically integrate the acceleration.

$$\frac{d\overrightarrow{r_{n+\frac{1}{2}}}}{dt} = \frac{d\overrightarrow{r_n}}{dt} + \frac{d^2\overrightarrow{r_n}}{dt^2}\frac{\Delta t}{2} \tag{2.46}$$

$$\overrightarrow{r_{n+1}} = \overrightarrow{r_n} + \frac{d\overrightarrow{r_{n+\frac{1}{2}}}}{dt}\Delta t \tag{2.47}$$

$$\frac{d\overrightarrow{r_{n+1}}}{dt} = \frac{d\overrightarrow{r_n}}{dt} + \frac{d^2\vec{r_n}}{dt^2}\Delta t. \tag{2.48}$$

In this process, we determine a mid-point velocity of the atoms. Then we determine positions. This integration conserves linear momentum. Usually we have time steps $\Delta t = 1 - 2fs$.

2.3 Classical Statistical Mechanics

When setting up a system, we try to emulate experimental conditions as much as possible, when setting up a system. First, we need to choose ensembles, which place certain constraints on the system. In our simulations we have closed systems, which are not isolated. There is energy exchange between the system and the surroundings. Therefore temperature, rather than energy, is constant. The systems do not exchange particles with the surroundings. The two ensembles we use in our simulations are canonical (NVT) and isothermal-isobaric (NPT). In our trajectories we have a 6N

dimensional phase space of coordinates ($\vec{r}_i$) and momenta ($\vec{p}_i$) for N atoms. During our trajectories we explore different values of phase space. Each different value of phase space is a microstate.

Canonical ensemble

Because temperature is constant, the simplest ensemble we use is the canonical ensemble (NVT). In this ensemble the Helmholtz free energy is minimized. This ensemble describes a closed system, in which particles cannot enter or leave, but is coupled to a thermal bath, where we can have an exchange of energy. Temperature is held constant through a simulation thermostat, where velocities are rescaled. The probability of accessing a microstate is given by

$$w(\vec{r},\vec{p}) = \frac{e^{-\frac{E(\vec{r},\vec{p})}{k_B T}}}{\int\int e^{-\frac{E(\vec{r},\vec{p})}{k_B T}} d\vec{r}d\vec{p}} \tag{2.49}$$

and the continuous summation of all microstates (partition function) is given by

$$Q \equiv \int\int e^{-\frac{E(\vec{r},\vec{p})}{k_B T}} d\vec{r}d\vec{p}. \tag{2.50}$$

We now need to use Boltzmann weight to determine probabilities. We use this ensemble usually when we have a simulation with two phases.

Isobaric isothermal ensemble

Most experiments are performed in an open environment. Therefore pressure rather than volume is constant, thus we use the isobaric-isothermal ensemble (NPT). In this ensemble the Gibbs free energy is minimized. This system, like the canonical ensemble, is closed and coupled to a heat bath, but differ in that the volume is flexible. Pressure is held constant through a barostat, where the volume is changed by rescaling the positions of the atomistic coordinates. The potential energy of

the system changes through the rescaling of the atomistic coordinates, which then causes forces to also change. We try to scale the volume of the system such that we have a constant target pressure, P. The probability of accessing a microstate is given by

$$w(\vec{r},\vec{p}) = \frac{e^{-\frac{E(\vec{r},\vec{p})+PV}{k_B T}}}{\int\int\int e^{-\frac{E(\vec{r},\vec{p})+PV}{k_B T}} d\vec{r}d\vec{p}dV} \tag{2.51}$$

and the continuous summation of all microstates (partition function) is given by

$$Q \equiv \int\int\int e^{-\frac{E(\vec{r},\vec{p})+PV}{k_B T}} d\vec{r}d\vec{p}dV. \tag{2.52}$$

We use this ensemble usually when we have a simulation with one phase. This ensemble is used frequently in biological systems and systems where we model macroscopic solvent environments.

Extracting of observables from MD trajectories

When we want to calculate an observable property, A, in an isobaric isothermal ensemble, we can use

$$\langle A\rangle = \frac{\int\int\int A(\vec{r},\vec{p},V)e^{-\frac{E(\vec{r},\vec{p},V)}{k_B T}} d\vec{r}d\vec{p}dV}{\int\int\int e^{-\frac{E(\vec{r},\vec{p},V)}{k_B T}} d\vec{r}d\vec{p}dV}, \tag{2.53}$$

which integrates this observable with respect to the probabilities of the microstates. In practice we can allow the simulation to run until convergence and determine the average value of the observable in

$$\langle A\rangle = \lim_{\Delta t\to\infty} \frac{1}{\Delta t}\int_t^{t+\Delta t} A(\vec{r},\vec{p})dt' \approx \frac{1}{N}\sum_{t=1}^{N} A(\vec{r},\vec{p}), \tag{2.54}$$

where we look at individual snapshots and calculate the observable at that snapshot. Then we average the values of the observables amongst all selected snapshots.

Ergodic hypothesis

In a chemical system we define a state through phase space, which consists of the positions ($\vec{r_i}$) and momenta ($\vec{p_i}$) over N atoms, thus giving a total of 6N dimensional phase space. Each value of $\vec{r_i}, \vec{p_i}$ represents a unique microstate. The probability of accessing the microstate is given by the Boltzmann weight. Examples for the NVT and NPT ensembles are given in Equation 2.49 and Equation 2.51. In our trajectories we explore different phase spaces, which are changing throughout the simulation. Observing the entire trajectory is equivalent at looking at an ensemble, i.e.

$$\langle A \rangle_{ensemble} = \langle A \rangle_{time}, \tag{2.55}$$

where $\langle A \rangle_{ensemble}$ can be determined from Equation 2.53 and $\langle A \rangle_{time}$ can be determined from Equation 2.54.

Calculation of Gibbs free energy from MD trajectories

Spontaneity of any process can be determined through the change in Gibbs free energy of the system, given by

$$\Delta G = \Delta H - T\Delta S, \tag{2.56}$$

assuming constant pressure and temperature. ΔG represents the change in the Gibbs free energy, ΔH represents the change in enthalpy, which is equal to the heat released to the surroundings for an isobaric process, T is the absolute temperature at which the process occurs, and ΔS is the change

in entropy of the system. When there is a spontaneous and irreversible process at fixed pressure and temperature, $\Delta G < 0$. In a system at equilibrium $\Delta G = 0$. When there is a process that requires work from an outside source $\Delta G > 0$.

In a process of self-assembly, the entropy of the system decreases, i.e. $\Delta S < 0$, which would impede the spontaneity of the process. Therefore, the process needs to be exothermic, $\Delta H < 0$, according to Equation 2.56. If enthalpic driving forces are strong enough, they can overcome the loss in entropic contributions. Larger molecules can self-assemble more easily since there is less loss in entropy than if the molecules were smaller. A solution with high concentration also has less entropic losses than a solution with lower concentration. Therefore larger molecules and higher concentration create more favorable conditions for spontaneous self-assembly and crystallization. Molecules with stronger intermolecular attractions can assemble more easily, due to enthalpic contributions. Strong intermolecular interactions could also be achieved by having highly charged moments (such as monopole or dipole).

One way we can extract the Gibbs free energy profile is to use potential mean force. In this method, we do umbrella sampling of forces one body exerts on a particle. First, we constrain one particle at a certain distance away from a body through a harmonic potential. We allow this particle to diffuse within this potential. The distance the particle diffuses reflects the force the body exerts on the particle. Then, we place the harmonic potential at a different distance and repeat the procedure to obtain a profile of forces a body exerts on a particle versus distance. We can then integrate the force profile to obtain the Gibbs free energy profile.

Self-assembly of supramolecular structures

Self-assembly of suprastructures occurs when small units coalesce into a higher order structure. Self-assembly can occur at macroscopic or microscopic scales. Atoms, molecules, and nanoparticles (NPs) can be the unit building blocks for suprastructures. Examples of supramolecular structures in biology are lipid bilayer membranes, fibrils, and globular proteins. In material science, examples of supramolecular structures are superlattices, micelles, and other clusters.

The second law of thermodynamics states that for a spontaneous (and irreversible) process, the entropy of the universe (which is divided into system and surroundings) is increasing, and is represented as

$$\Delta S_{univ} = \Delta S_{sys} + \Delta S_{surr} > 0, \tag{2.57}$$

where ΔS_{univ} is the total change in entropy (i.e. entropy of the universe), ΔS_{sys} is the change of entropy of the system, and ΔS_{surr} is the change in entropy of the surroundings. For a process in equilibrium (and reversible) the entropy of the universe is constant, thus $\Delta S_{univ} = 0$. For a non-spontaneous process, the entropy of the universe decreases, and $\Delta S_{univ} < 0$. In a spontaneous self-assembly process, the sub-units coalesce. Therefore the entropy of the system decreases $\Delta S_{sys} < 0$. Heat is released to the surroundings ($\delta q_{sys} < 0$), because the building blocks of the suprastructure are attracted through forces. The heat released to the surroundings affects its entropy as

$$\Delta S_{surr} = \int_{initial}^{final} \frac{\delta q_{surr}}{T_{surr}} > \Delta S_{sys} = \int_{initial}^{final} \frac{\delta q_{sys}}{T_{sys}}. \tag{2.58}$$

The surroundings are usually solvent molecules, which have excited thermal motions, thus the entropy of the surroundings increases. This increase of entropy of the surroundings is greater than the decrease of entropy in the system, thus the entropy of the universe has a net increase, as described in Equation 2.58.

CHAPTER 3

BIOMEDICAL ASSEMBLIES

(Previously published as Shaham-Niv, S., Rehak, P., Vuković, L., Adler-Abramovich, L., Král, P., Gazit E. Formation of Apoptosis-Inducing Amyloid Fibrils by Tryptophan. *Israel Journal of Chemistry* **57**, 729 (2017); Bera, S., Xue, B., Rehak, P., Jacoby, G., Ji, W., Shimon, L. J. W., Beck, R., Král, P., Cao, Y., Gazit E. Self-Assembly of Aromatic Amino Acid Enantiomers into Supramolecular Materials of High Rigidity. *ACS Nano* **14**, 1694 (2020); Shaham-Niv, S., Rehak, P., Zaguri, D., Levin, A., Adler-Abramovich, L, Vuković, L., Král, P., Gazit, E. Differential Inhibition of Metabolite Amyloid Formation by Generic Fibrillation-Modifying Polyphenols. *Communications Chemistry* **1**, 1 (2018); Shaham-Niv, S., Rehak, P., Zaguri, D., Kolusheva, S., Král, P., Gazit E. Metabolite Amyloid-like Fibrils Interact with Model Membranes. *Chemistry Communications* **54**, 4561 (2018); Mondal, S., Jacoby, G., Sawaya, M. R., Arnon, Z. A., Adler-Abramovich, L., Rehak, P., Vuković, L., Shimon, L. J. W., Kraál, P., Beck, R., Gazit E. Transition of Metastable Cross-α Crystals into Cross-β Fibrils by β-Turn Flipping. *The Journal of American Chemical Society* **141**, 363 (2019); Mondal, S., Rehak, P., Král, Gazit, E. Anisotropic assembly of Metal Nanostructures onto an Asymmetric Peptide-Based Nanofibers. **in Preparation**; Guterman, T., Ing, N. L., Fleischer, S., Rehak, P., Basavalingappa, V., Hunashal, Y., Dongre, R., Raghothama, S., Král, P. Dvir, T., Hochbaum, A. I., Gazit E. Electrical Conductivity, Selective Adhesion, and Biocompatibility in Bacteria-Inspired Peptide–Metal Self-Supporting Nanocomposites. *Advanced Materials* **31**, 1807285 (2019).)

In this chapter, all papers were co-authored in collaboration with Prof. Ehud Gazit (Tel-Aviv University). We study the biological and material properties of biomolecular suprastructures. First, we examine single metabolites, such as amino acids and nucleobases. These are the simplest biomolecules. We examine the stability of enantiopure and racemic mixtures in biocrystals. Then, we study peptides, polymers of amino acids, inspired by nature. We study their conformation in different environments and their interaction with gold nanoparticles.

3.1 Formation of Apoptosis-Inducing Amyloid Fibrils by Tryptophan

Adapted from Ref. [1] (*Isr. J. Chem. 2016*, 57 DOI: 10.1002/ijch.201600076) with permissions from John Wiley and Sons Publishing Groups.

Introduction

Misfolding of proteins and peptides leads to the formation of amyloid fibrils. These amyloid fibrils have been associated with a wide range of notable human disorders with unrelated etiology, including Alzheimer's disease, Parkinson's disease, and type II diabetes [14–19]. Amyloid fibrils originate from diverse and structurally unrelated groups of proteins. However, they share a unique set of similar biophysical and structural properties. These fibrillar supramolecular assemblies have a diameter of $5-20$ nm and are predominantly rich in $\beta-$sheet secondary structure. They can specifically bind to dyes, such as thioflavin T (ThT) and Congo red [20–22]. Amyloid-forming proteins and polypeptides have a high frequency of aromatic residues [23] in their sequences. These aromatic residues most likely stabilize amyloidal structures by geometrically restricted interactions between planar aromatic chemical entities. These residues affect the morphology of the assemblies, accelerate their formation, improve their stability and reduce the minimal association concentration [24–27].

Trytpophan has the highest aggregation propensity of all 20 naturally occurring amino acids [28]. Tryptophan was found to have a high aggregation ability in the context of tripeptides, regardless of the position of the amino acid, (in the N-terminal, middle, or C-terminal positions) [29]. This aromatic amino acid (see Figure 2A) is rare, yet is essential for humans, playing a crucial role in protein stability and recognition [30]. Tryptophan is a critical component of numerous metabolic pathways, being a biochemical precursor for serotonin, melatonin, and niacin [31]. Accumulation of tryptophan can lead to pathological conditions. The accumulation of tryptophan has been reported

in autosomal recessive disorders, such as hypertryptophanemia and Hartnup disease. Hypertryptophanemia occurs due to the inability of the body to process tryptophan, leading to a massive buildup of tryptophan in the blood and urine that would not happen in a healthy patient. This results in musculoskeletal effects and to behavioral and developmental abnormalities [32–34]. Hartnup disease is caused by damage to a neutral amino acid transporter, limited to the kidneys and small intestine. The absorption of nonpolar amino acids, mainly tryptophan is decreased, in comparison to a healthy patient. The increased levels of tryptophan and indolic compounds are detected in the patients' urine. Common symptoms include the development of a rash on parts of the body exposed to the sun, mental retardation, headaches, collapsing and fainting [35].

Experimental results

Collaborators characterized the structure of tryptophan assemblies and examined whether they possess the hallmarks of ordered amyloid structures. As discussed above, amyloid fibrils share a set of biophysical properties, showing the morphology of elongated fibrils with a typical diameter of $5-20$ nm. In addition, they self-assemble to form ordered β-sheet secondary structures, which can be detected using the typical amyloid dye ThT. This amyloid-specific reagent changes its fluorescence upon interaction with ordered amyloid assemblies, which can be further monitored using fluorescence microscopy, measurements of ThT emission data at 480 nm (excitation at 450 nm) over time, and measurements of fluorescence emission spectra. Indeed, using transmission electron microscopy (TEM) and high-resolution scanning electron microscopy (HR-SEM), the tryptophan assemblies were found to present an elongated fibrillar morphology, similar to that observed for common amyloid aggregates, with a diameter of $15-75$ nm (see Figure 2B, C). Furthermore, a typical change in the ThT fluorescence signal was detected in the presence of these fibrils, as shown using confocal fluorescence microscopy, where a bundle of fluorescent fibrils was observed (see Figure 2D). In addition, these

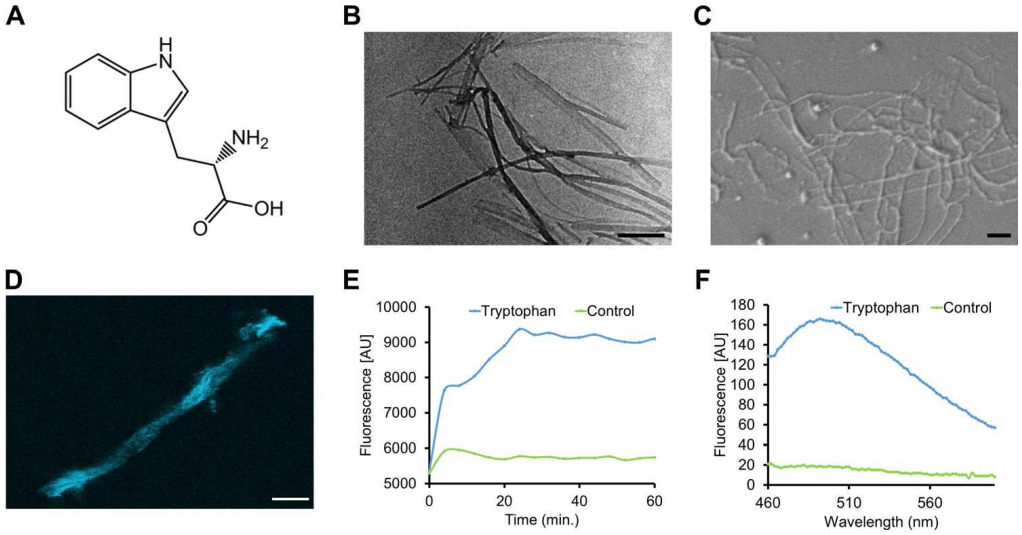

Figure 2: **Formation of amyloid-like structures by tryptophan self-assembly.** For all assays, tryptophan (4 mg/mL) was dissolved at 90° C in PBS and cooled down gradually for the formation of structures. (A) Tryptophan skeletal formula. (B) TEM micrograph of tryptophan assemblies. Scale bar is 500 nm. (C) HR-SEM micrograph of tryptophan assemblies. Scale bar is 500 nm. (D) Confocal fluorescence microscopy image of tryptophan assemblies stained with ThT. Images were taken immediately after the addition of the ThT reagent (final concentration 20μM ThT). Excitation and emission wavelengths were 458 and 485 nm, respectively. Scale bar is 20μm. (E) ThT fluorescence assay of tryptophan assemblies. Tryptophan (4 mg/mL) was dissolved in PBS at 90° C, followed by the addition of ThT to a final concentration of 20μM. ThT emission data at 480 nm (excitation at 450 nm) was measured over time. (F) ThT fluorescence emission spectra of tryptophan assemblies (4 mg/mL) following excitation at 430 nm. Aged samples were added to 40μM ThT in PBS to a final concentration of 20μM ThT. The control reflects addition of PBS to 40μM ThT in PBS to a final concentration of 20μM ThT.

fibrils presented a distinctive time-dependent fluorescence curve and emission fluorescence spectra correlating to those of amyloid assemblies (see Figure 2E, F).

MD simulations: methods and results

Two different tryptophan crystals [36] were modeled in all-atomistic simulations: (i) a small system of 288 molecules ($12 \times 12 \times 2$), which has only one layer of zwitterion aggregation in the crystal; and (ii) a large system of 1536 molecules ($16 \times 16 \times 6$), which has three layers of zwitterion aggregation. Both simulations were performed with the NAMD [37] package, using the CHARMM

force field [38–42]. Fibrils were placed in an aqueous environment, with [NaCl] = 0.15 M to emulate cellular (physiological) conditions. The Langevin dynamics with a damping coefficient of 1 ps^{-1} and a time step of 1 fs was used to describe systems in a NPT ensemble at a pressure of 1 atm and a temperature of 310 K. During production run equilibration simulations particle mesh Ewald [43] was used with a grid spacing of 1.0. The SHAKE algorithm was used for the hydrogen atoms. Non-bonded interactions were evaluated at every time step, and full electrostatics were evaluated at every second time step. The non-bonded interactions used the switching algorithm, with the switch on distance at 10 Å and the switch off at 12 Å. Non-bonded pair lists were 13.5 Å, with the list updated every 20 steps. During minimization and pre-equilibration runs, all the heavy atoms of amino acids were subjected to large constraints so that dissolution would not occur. During equilibration runs, all heavy atoms in one molecule within each crystal were subjected to 20% of the previous constraints, whereas the remaining molecules were not subjected to constraints. The constraint on a single molecule was applied to prevent the crystal as a whole from leaving the primary box. Data and snapshots were recorded every 10 ps.

To examine the possible structures of fibrils formed by tryptophan in its assembly process and the potential way in which tryptophan assemblies could exhibit a stable unidirectional growth, atomistic molecular dynamics (MD) simulations were used. [36] Figure 3 shows different tryptophan crystal assemblies that were simulated. In the simulations, we assumed that the molecular structure of the fibril is essentially based on the molecular structure of the bulk crystal, [36] in analogy to phenylalanine and diphenylalanine assemblies, which have related molecular structures in fibril and bulk crystal assemblies [44, 45]. However, the bulk structure in the experimentally observed linear fibrils might have some degree of folding or reorganization that allows it to maintain one dominant growth direction. For example, in many materials whose bulk structures are formed by relatively

weakly bound stacked layers (e.g., graphene organization of carbon), the individual layers can form kinetically stable nanotubes under suitable conditions. In a similar way, bulk tryptophan crystallizes in the form of bilayers, where the polar and nonpolar groups stay separated, and the polar zwitterionic groups stabilize the bilayers by hydrogen bonds and Coulombic interactions between zwitterion groups. Such tryptophan bilayers can undergo some sort of folding into nanotubes or related structures.

To examine this possibility in our MD simulations, we simulated a small tryptophan bilayer formed by 288 tryptophan molecules organized in a membrane-like structure with middle zwitterion groups bound by hydrogen bonds (Figure 3A, B), a small triple tryptophan bilayer formed by 1536 tryptophan molecules (Figure 3C, D), and three differently cut tryptophan bilayers formed by 640, 640, and 3200 tryptophan molecules (Figure 3F-H). The structures of tryptophan crystals were simulated in 0.15 M NaCl solution (corresponding to the ionic strength of the physiological solution).

Figure 3A-D presents the two smaller systems at initial times and after $100-200$ ns long simulations. The monolayer has great flexibility, with the crystal bending in and out of the plane, whereas the trilayer is significantly more rigid. In both cases, only molecules from the edges and corners are seen to leave the crystals, while the top and bottom parts of the layers and the bulk of the crystals remained intact throughout the simulations. With a larger surface to volume ratio, the monolayer released a considerable number of molecules, showing the stabilization trend of larger crystal nuclei. This can be partly due to increased bending of the monolayer, destabilizing the molecules at its surface (edges). The amphiphilic tryptophan molecules that leave the crystals may recombine with molecules at the crystal sides via zwitterion-zwitterion attraction (edges become rounded). Even though zwitterions are strongly attracted to the aqueous environment, their coupling to other zwitterions in the crystals is preferential, since it is supported and protected by a mutual coupling of

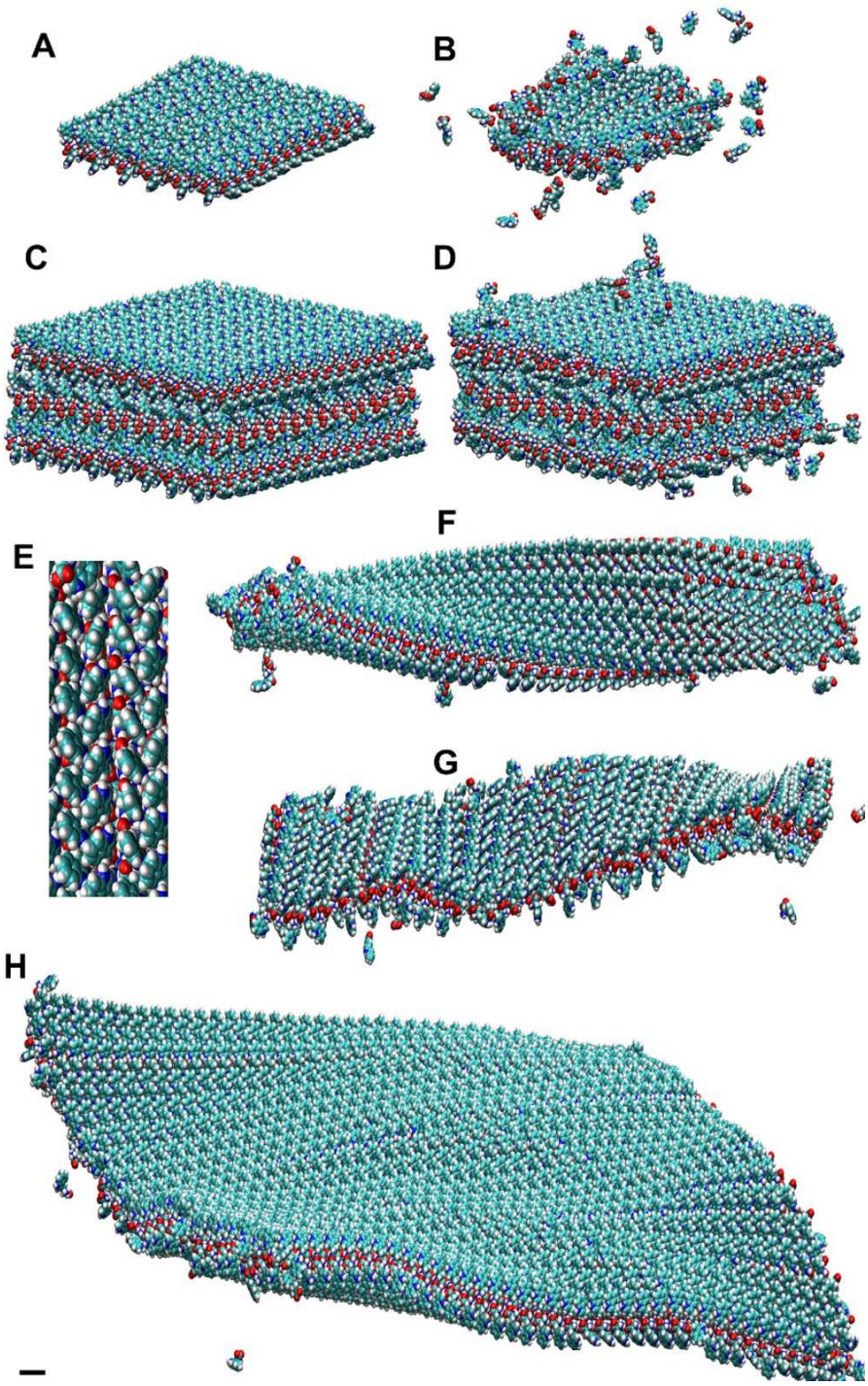

Figure 3: **Modeling of hydrated tryptophan fibrils.** (A,B) A tryptophan bilayer at times t = 0, 244 ns. (C,D) A triple tryptophan bilayer at times t = 0, 104 ns. All scale bars represent 10 Å. The bilayer bending fluctuates significantly over time, in contrast to the triple bilayer. The fluctuating bilayer also tends to release more molecules, but both systems remain mostly stable over time. (E) Detail of a tryptophan layer with exposed aromatic rings forming parallel 1D chains of paired rings. (F) An elongated tryptophan bilayer at the end of a 15 ns simulation. (G) Other tryptophan bilayers, cut along the orthogonal to parallel 1D chains of paired rings, after 12 ns, and (H) cut along both directions with respect to 1D chains of paired rings, after 6 ns.

apolar aromatic head groups within the crystals. At times, free molecules are also observed to adsorb at the crystal (apolar) surfaces, but they do not form further layers under the conditions of the simulations performed (observation time, number of free molecules in the simulation box). These simulations support the idea that the crystals grow in the direction of bilayers, which might be twisted or folded to protect their edges. To understand better the preference towards 1D growth, we present in Figure 3E a detailed structure of a tryptophan layer with exposed aromatic rings forming parallel 1 D chains of paired rings (six such parallel chains can be recognized in Figure 3A). Figure 3B shows that the chains of paired rings remain relatively rigid and stable during the simulations, while most of the layer bending proceeds in the direction orthogonal to these chains.

To further examine the hypothesis that the tryptophan layers may have a preference towards 1D growth, we simulated bilayers elongated in two separate directions (Figure 3F, G) and in both directions simultaneously (Figure 3H). All the bilayer structures fluctuate and bend. However, the fluctuations are mostly in the direction orthogonal to the chains of paired rings. Therefore, the structure that is cut along the chains (Figure 3F) is nicely twisted, while the orthogonally cut structure randomly fluctuates (Figure 3G). The large structure is twisted along the chains in an ambivalent manner at the two sides. These simulations demonstrate more clearly the possibility of tryptophan bilayer edges coming together to form a tubular structure in which chains of rings run parallel to the tube axis (Figure 3F). This tube could form the nucleus of a larger fibril, with the addition of new molecules occurring only at the tube edges along a single dimension or forming thicker multiwall tubular structures.

Conclusions

To conclude, in the current study we have presented the ability of the single tryptophan amino acid to self-associate into ordered supramolecular amyloid-like fibrils. Although many previous reports

predicted the important role of tryptophan in the amyloid aggregation process, this is the first time where the amino acid alone is described to self-assemble into amyloid ultrastructures. The biophysical properties of the tryptophan assemblies were characterized using different methods, including both transmission and scanning electron microscopy, as well as the use of amyloid-specific dyes. Molecular dynamics simulations were used to examine a potential molecular organization of the tryptophan fibrils and their growth and stability. The simulations reveal a possible tendency of tryptophan towards the formation of well-organized fibrils with twisted structures.

3.2 Chirality-induced self-assembly of aromatic amino acids into supramolecular materials

Adapted from Ref. [2] (ACS Nano *2020*, 14, DOI:10.1021/acsnano.9b07307) with permissions from ACS Publishing Groups.

Introduction

Metabolites are amino acids and nucleobases. They are biology's simplest building blocks and can perform a multitude of functions [46]. Metabolites can self-assemble into distinct nanostructures and display diverse material properties [47]. We strive to achieve revolutionary advances in the design and fabrication of attractive functional materials [46,48], inspired by nature. Single amino acids have been explored to design exciting biomaterials [49–51], similar to protein amyloids. Aromatic amino acids such as PHE, TRP, TYR, and histidine (HIS) can form a wide range of nanostructures, depending on the self-assembly conditions [50, 51]. The use of unimolecular amino acid assemblies to design attractive material has been limited by the lack of chemical diversity and functional complexity.

Chirality is a natural attribute of most biomolecules and possesses a universal significance for many fields [52–54]. Out of the 20 naturally occurring amino acids, 19 are left handed chiral and only glycine is achiral. We investigate the self-assembly kinetics and the mechanism of structure formation by enantipoure and racemic mixtures of PHE and TRP. The presence of racemate mixtures (by adding equimolar of non-natural right handed chiral amino acids) was found to significantly alter the self-assembly kinetics and the resultant nanostructure morphologies when compared to enantiopure mixtures.

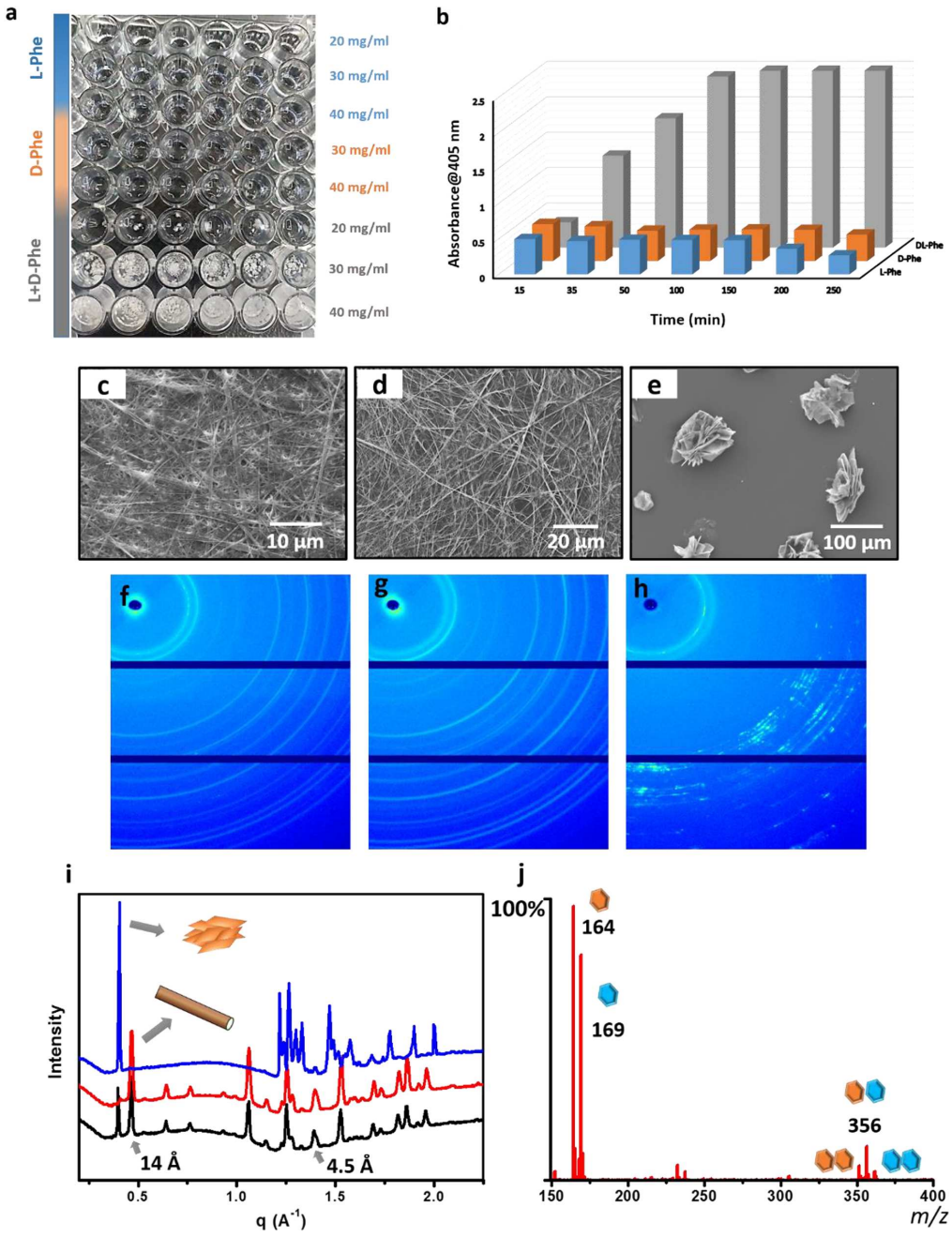

Figure 4: **Self-assembly of pure and mixed PHE enantiomers.** (a) Macroscopic visualization of the phase behavior after 24 h. (b) Kinetics of the 405 nm absorbance of the three systems (-L , -D and -DL) at 30 mg/mL over a period of 4 h. (c-e) HR-SEM images of (c) L-PHE, (d) D-PHE, and (e) DL-PHE. (f-h) X-ray scattering 2D patterns of (f) L-PHE, (g) D-PHE, indicating random orientation of structures in the plane of the film, and (h) DL-PHE, indicating the presence of polycrystalline assemblies. (i) Corresponding azimuthally integrated spectra of L-PHE, D-PHE, and DL-PHE shown in black, red, and blue, respectively. (j) Mass spectra of the noncovalent assemblies of the intermolecular complexes. Hexagons represent D-PHE (yellow) and L-PHE (blue).

Experimental results

To analyze the self-assembly of PHE, we first probed the phase behavior of the pure enantiomers (L and D) and their equimolar mixture at a wide range of concentrations up to 40 mg/mL. Dissolving either of the single enantiomers in double-distilled water by heating at 90° C produced a clear solution, which remained clear over time, while cooling to room temperature, even at the 40 mg/mL concentration (Figure 4a,b). However, the phase behavior of the mixed DL (1 : 1) system was completely different. Although upon heating, the equimolar mixture of up to 40 mg/mL of D and L isomers fully dissolved in water and produced a clear solution, the turbidity of the solution began to increase immediately after starting to cool (Figure 4b). Moreover, in very short time, large flake-like structures were found to precipitate out from the solution, indicating a faster rate of aggregation for the DL-system. Figure 4c-e shows high-resolution scanning electron microscope (HR-SEM) images of the self-assembled nanostructures formed by the pure enantiomers and their mixed systems. Both L- and D-PHE formed micrometer-long singular fiber structures similar to the previously reported amyloid-like assemblies (Figure 4c,d) [55]. However, the DL-system showed inhibition of fiber formation and fabrication of different types of aggregates, namely, crystalline flake-like structural assemblies (Figure 4e). The formation of different types of morphologies coincided with their optical appearances over time, as observed from their turbidity assay. The level of turbidity was low for the more compact nanofibrillar structures of pure L and D isomers, while increased turbidity was measured for the DL-system due to a higher degree of light scattering from the large flakes (Figure 4b).

To understand the effect of chirality on the self-assembly of L-TRP, we employed the D-TRP and thoroughly studied the effect in the racemic mixture. The phase behavior of pure D-TRP revealed to some extent different kinetics than that of L-TRP, as it did not show a change in turbidity

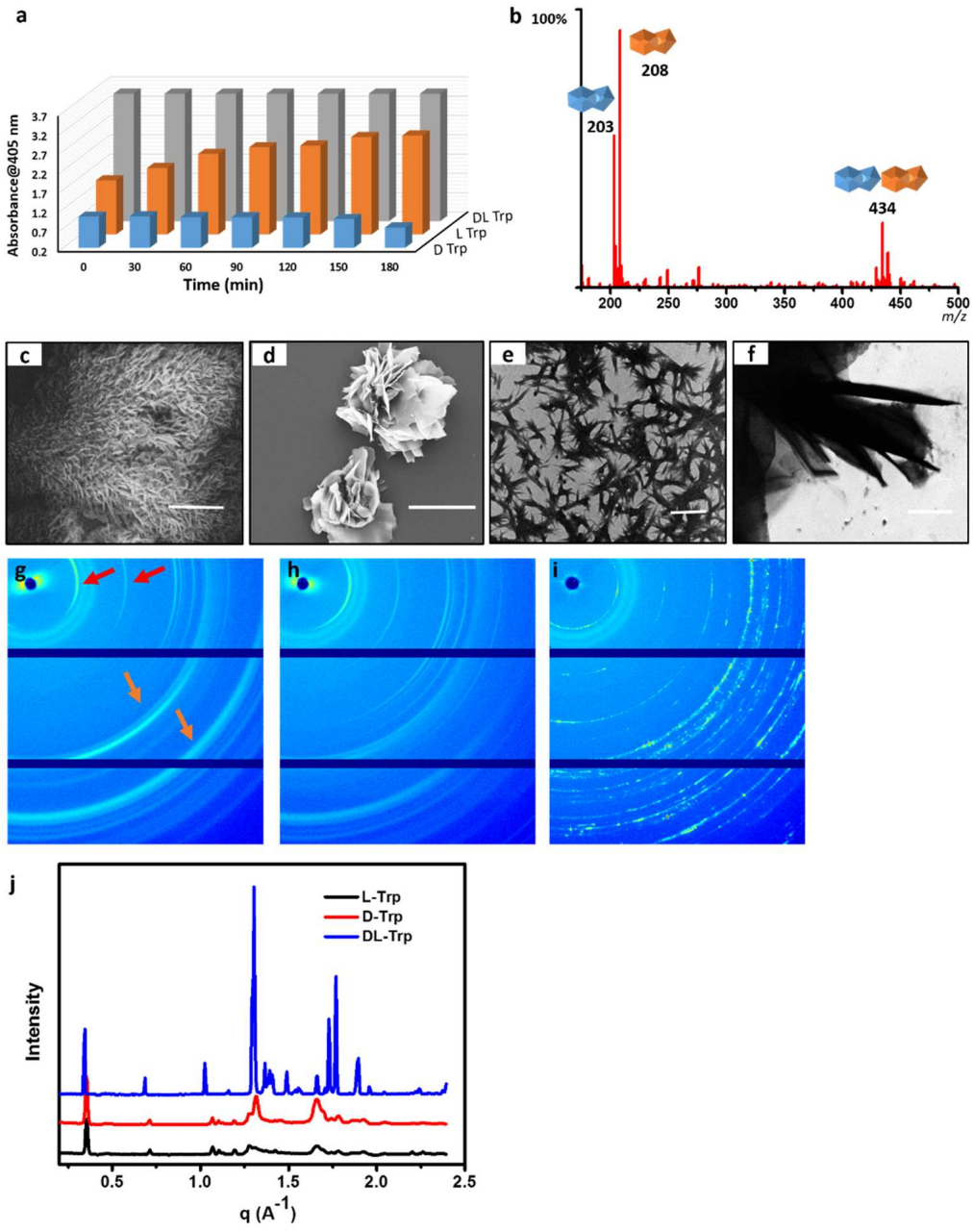

Figure 5: **Modulation of L-TRP self-assembly by incorporation of D-TRP.** (a) Kinetics of the 405 nm absorbance of the 30 mg/mL solutions over a time period of 3 h. (b) Mass spectra of the noncovalent assemblies of the intermolecular complexes. (c-f) HR-SEM and TEM images of (c and e) D-TRP and (d and f) DL-TRP. (g-i) X-ray scattering 2D patterns of (g) L-TRP, (h) D-TRP, and (i) DL-TRP. (j) Corresponding azimuthally integrated spectra. Scale bar for (c) and (d) is 50μm and for (e) and (f) is 1μm.

over time at the 30 mg/mL concentrations, but formed structures in solution at higher concentration (Figure 5a). ANS binding assay using D-TRP showed a similar change of environment from hydrophilic to hydrophobic, as also observed for L-TRP. The concentration-dependent NMR study also demonstrated a shift toward lower ppm values due to the screening of the aromatic proton as a result of $\pi - \pi$ stacking. The characteristics of an equimolar mixture of D- and L-TRP $(1:1)$ were completely different from those of their individual pure enantiomers.

MD simulations: methods and results

The MD simulations were performed with NAMD2.12 and NAMD 2.13 packages [37], using a CHARMM 27 force field [56]. Atomistic MD simulations were performed under physiological conditions, i.e., [NaCl] = 0.15 M, where the amino acids were in zwitterionic form. The TIP3P model was used for water molecules. The simulations were described by a Langevin dynamics in an NPT ensemble with P = 1 atm and T = 310 K. A Particle Mesh Ewald [57] summation was used to calculate long-range Coulombic interactions, with a grid spacing of 1.0. Short-range dispersion interactions used a switching algorithm, with an on/off distance of 10/12 Å. Pair lists were 13.5 Å, updated every 20 steps; $1-4$ interactions were not scaled.

Crystal Bending Simulations. Left-handed and mixed enantiomer crystals were constructed using crystal structures [36, 58]. Each crystal has one bilayer held together by hydrogen bonding between $40 \times 8 \times 2$ or $8 \times 40 \times 2$ amino acids. Left-handed crystals were minimized for $50,000$ steps and pre-equilibrated for 300 ps, with heavy amino acid atoms constrained. Then, these crystals were released and simulated for 20 ns, with a time step of 2 fs and $\gamma_{Lang} = 1.00 ps^{-1}$. Mixed enantiomer crystals were minimized for $20,000$ steps and pre-equilibrated for $1-1.6$ ns, with heavy amino acid atoms constrained. Then, the crystals were released and simulated for 100 ns.

Amino Acids Mobility Simulations. Here, the two types of crystals with dimensions of $12 \times 12 \times 12$ amino acids were in a physiological solution. First, the systems were minimized for 5000 steps, with heavy amino acid atoms constrained. Then, the systems were warmed for 2000 steps, with a time step of 1 fs, $\gamma_{Lang} = 1.00ps^{-1}$, and an increment of 1 K every 5 steps until the temperature reached 310 K. Then, the systems were pre-equilibrated with the same constraints for 1 ns and a time step of 1 fs. Afterward, the systems were further pre-equilibrated for 1 ns, a time step of 1 fs, and $\gamma_{Lang} = 0.01ps^{-1}$, while eliminating constraints on one side group of each amino acid of the central 10×10 amino acids on each facet. Finally, the central 10×10 amino acids were released, while all other heavy amino acid atoms were constrained and simulated for 30 ns at a time step of 2 fs.

Enthalpy of Binding Calculations. We calculated the enthalpy of amino acids binding to the crystal (described in the previous paragraph), using NAMD energy plugin version 1.4 [37] in VMD [59]. Enthalpies of binding were calculated: (1) between amino acids and facets within which they were present and (2) between those amino acids and the remaining (constrained) amino acids in the crystal, ignoring solvent effects in both calculations. Enthalpy of binding was the sum of electrostatic and dispersion interactions, assuming Coulombic and $12-6$ Lennard-Jones potentials, respectively. In the enthalpy calculations, the system parameters were kept the same as in the rest of the simulations. We calculated each enthalpy of binding every 10 ps for the entire 30 ns of simulation. We normalized the enthalpy terms with respect to the number of mobile amino acids (100 in each calculation) and averaged them over all snapshots.

We used atomistic molecular dynamics (MD) simulations to model PHE crystals. Since the structure of the racemic PHE crystal is not known, we simulated only one pure enantiomer, L-PHE crystal. First, we prepared small bilayer PHE crystals, with structures shown in Figure 6. These elongated crystals were cut either along the well-visible aromatic zipper or orthogonal to it, producing

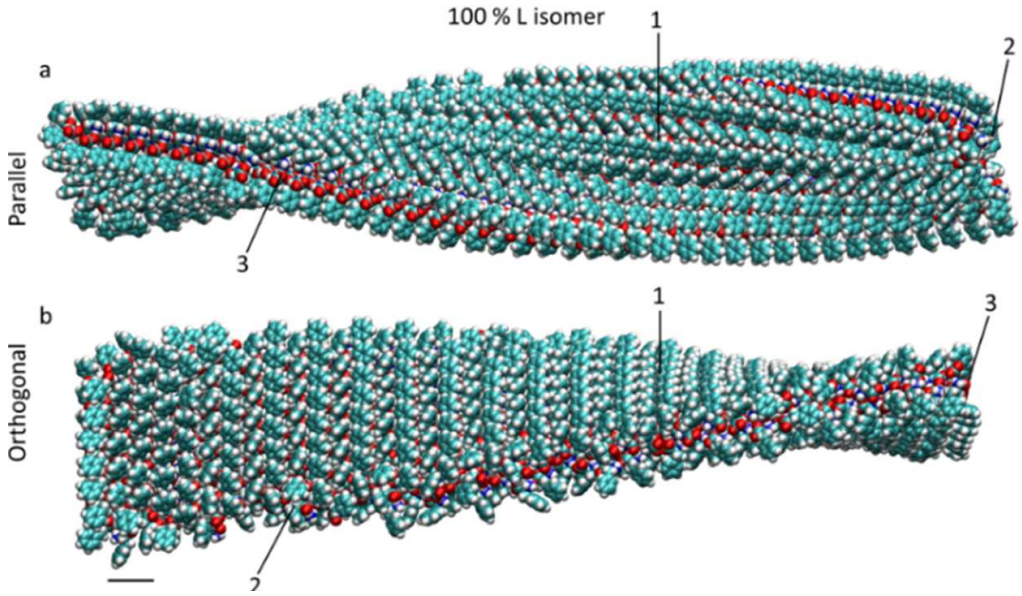

Figure 6: **MD simulations of pure L-PHE crystals.** (a) Pure L-PHE crystal cut along an aromatic zipper after 20 ns of simulation. (b) Pure L-PHE crystal cut orthogonally to the aromatic zipper after 20 ns of simulations. (1) Top bilayer facet, (2) the facet parallel to the aromatic zipper, and (3) the facet orthogonal to the aromatic zipper. Scale bar represents 1 nm.

two crystals of $40 \times 8 \times 2$ or $8 \times 40 \times 2$ amino acids, placed in physiological solutions under ambient conditions. Figure 6a,b reveal that after 20 ns of simulations, these L-PHE crystals had a tendency to fold in both parallel and orthogonal directions relative to the aromatic zipper. This tendency toward folding might promote the crystal to grow in a linear fashion, most likely along the zipper.

These simulations reveal that the chirality of amino acids and the lack of central symmetry in the crystals formed by these molecules promote crystal bending. Moreover, crystals formed by enantiomers of the same amino acid should be mirror images of each other. Therefore, their simple combination would give rise to flat racemic crystals. Real racemic crystals would contain the same number of both enantiomers suitably packed in their elementary cells, thus producing flat crystals.

Next, we simulated the dynamics of L-PHE on the surfaces of the crystals and calculated the binding energies of amino acids nested on the crystal facets. The results reveal that the top bilayer

(facet 1 in Figure 6) is highly stable, due to hydrogen-bonding networks between zwitterion groups of the amino acids, which keep the bilayers intact. Additional bilayers bind to the top bilayer through weaker $C-H-H-C$ dispersion interactions, which would slow down growth in this direction. The amino acids show a large mobility on the L-PHE crystal facets, which are parallel and orthogonal to the aromatic zipper (facets 2, 3, respectively, in Figure 6). The amino acids in the facet parallel to the aromatic zipper (facet 2 in Figure 6) show relatively strong binding with other amino acids in the same facet, but not with the remainder of the crystal. In the facet orthogonal to the aromatic zipper (facet 3 in Figure 6), the situation is opposite. These results show that growth on the facet parallel to the aromatic zipper is more likely to continue and produce twisted 1D crystals. The D-isomer is only a mirror image of the L-isomer. Thus, the evolutions of the D-isomer will be a mirror image of the L-isomer and will also grow into 1D twisted structures.

We simulated pure left-handed enantiomer crystal of $12 \times 12 \times 12$ amino acids to further examine a possible directionality in crystal growth of PHE. On each facet of the crystal, the central 10×10 amino acids in the first layer were free and amino acids in deeper layers were frozen. These facets (Figure 8) were denoted as 1) "top bilayer plane" (facet 1 in Figure 6 and colored yellow in Figure 7), it contacts the solvent through apolar aromatic side groups and when extended it forms additional bilayers, 2) "parallel to zipper plane" (facet 2 in Figure 6 and colored green in Figure 7), its normal vector is parallel to the aromatic zipper and when it is extended the aromatic zipper lengthens, and 3) "orthogonal to zipper plane" (facet 3 in Figure 6 and colored orange in Figure 7), its normal vector is at an angle with the aromatic zipper's direction (angle depends on unit cell parameters) and is orthogonal to a vector normal to the zwitterion layer. The results in Figure 8 reveal that PHE

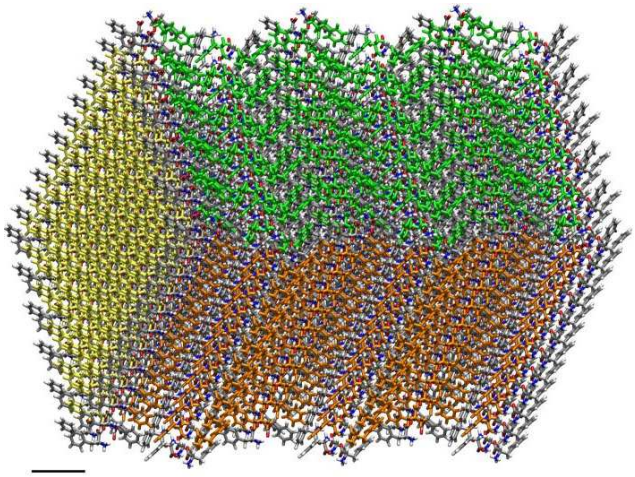

Figure 7: Definition of different facets for pure L-PHE crystals. Yellow amino acids are top bilayer; green amino acids are parallel to the aromatic zipper; orange amino acids are orthogonal to the aromatic zipper. Scale bar represents 1 nm.

Facet	100% L-isomer (kcal/mol)
Top Bilayer	-85.92
Parallel to Zipper	-73.06
Orthogonal to Zipper	-50.90

TABLE I. INTERACTION ENERGIES (PER MOLECULE) BETWEEN AMINO ACIDS WITHIN THE SAME FACET.

Facet	100% L-isomer (kcal/mol)
Top Bilayer	-58.36
Parallel to Zipper	-39.44
Orthogonal to Zipper	-64.39

TABLE II. INTERACTION ENERGIES (PER MOLECULE) BETWEEN AMINO ACIDS OUTSIDE THE SAME FACET.

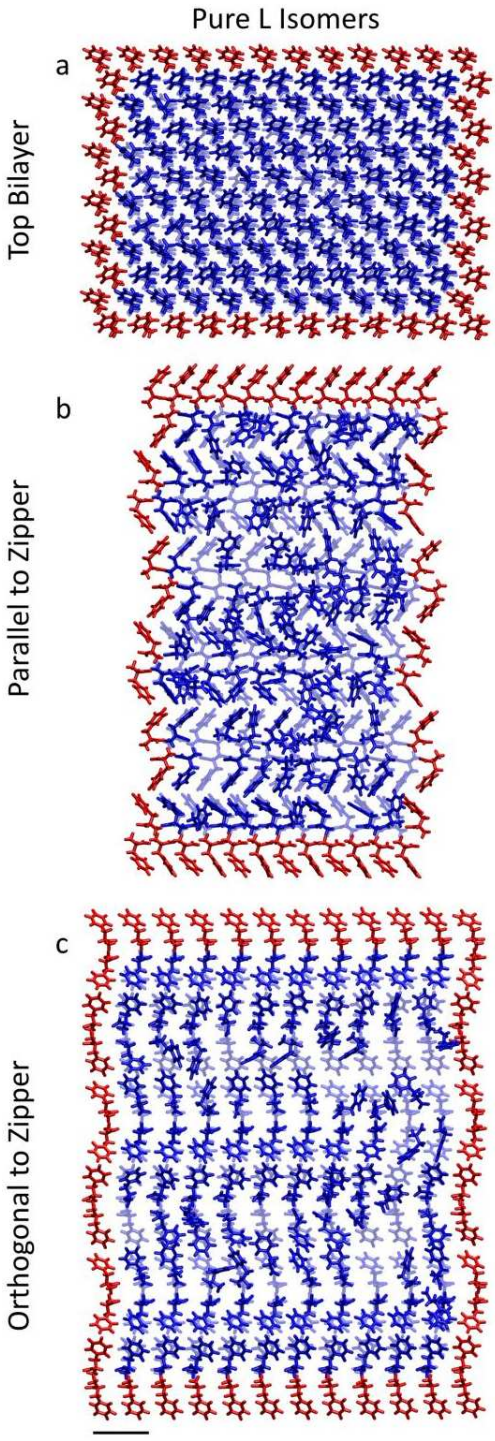

Figure 8: Motion of PHE amino acids in the first layer at different crystal facets. Red molecules in the first layer and all molecules below the first layer were constrained; dark blue molecules represent final positions of free peptides after 30 ns of simulations; light blue molecules represent their initial positions. Pure left-handed enantiomers: (a) Top bilayer; (b) Parallel to aromatic zipper; and (c) Orthogonal to the aromatic zipper. Scale bar represents 1 nm.

amino acids in the left handed crystal have significant mobility in facets both parallel and orthogonal to the aromatic zipper (facet 2 and 3 in Figure 6, respectively).

In order to quantify the strength of the PHE binding on each facet, we calculated nonbonding interaction energies of free amino acids 1) with other amino acids on the same facet (Table I) and 2) with the remaining amino acids in the crystal (Table II). In the left handed crystal, free amino acids in the top bilayer have strong interactions with other mobile amino acids as well as with the constrained amino acids, due to hydrogen bonding networks through zwitterions. Free amino acids in the facet parallel to the aromatic zipper are most mobile due to their relatively weak interactions with the constrained amino acids in the crystal. At the same time, free amino acids in the facet orthogonal to the aromatic zipper have the strongest interactions with the constrained amino acids. They have a significant mobility, due to their weak interactions with other mobile amino acids on the same facet. Once the crystal is forming, amino acids on the facet parallel to the aromatic zipper will most likely assemble and stay intact. Amino acids on the facet orthogonal to the aromatic zipper are less likely to assemble. Once they assemble, they will bind relatively strongly to the crystal, thus contributing to the stability of the crystal, though they would not tend to propagate in this direction.

The TRP systems were modeled like in Figure 6, including the racemic TRP crystal structure. The prepared small bilayer TRP crystals, with structures shown in Figure 9, consisted of either pure left-handed (L) isomers or from 50% left- and 50% right-handed (D) isomers. The crystals were again cut and simulated as before. Figure 9a,b reveal that after 20 ns the pure L-TRP crystal has a tendency to fold in a direction parallel to the aromatic zipper, but it undulates along the orthogonal direction [1]. Thus, L (D)-TRP crystals might grow along the zipper (1D), in analogy to L (D)-PHE crystals. On the other hand, the mixed DL-TRP crystals stay on average flat, as shown in Figure 9c,d,

since their possible twists are compensated by the presence of both enantiomers. The mixed DL-TRP crystals might grow in 2D or 3D. L-TRP crystals have similar stability of facets like L-PHE crystals. In particular, the amino acids on the facet parallel to the aromatic zipper (facet 2 in Figure 9) show small mobility and relatively strong binding energies. In combination with the observed bending, it is likely that the crystal would grow in this 1D direction. In the DL-TRP crystal, the facet orthogonal to the aromatic zipper (facet 3 in Figure 9) is more stable, while the facet parallel to the zipper is less stable. This could be understood from the binding energies (Table III and Table IV), showing that the same enantiomers have larger binding energies than opposite enantiomers. However, a flat racemic crystal should be able to easily grow in both directions.

We simulated two crystals (100% L TRP, 50/50% L/D TRP) of $12 \times 12 \times 12$ amino acids to further examine a possible directionality in crystal growth of TRP, using the same methods as with the PHE crystals. These facets (Figure 11) had the same nomenclature as the PHE crystal, i.e. 1) "top bilayer plane" (facet 1 in Figure 9 and colored yellow in Figure 10), it contacts the solvent through apolar indole side groups and when extended it forms additional bilayers, 2) "parallel to zipper plane" (facet 2 in Figure 9 and colored green in Figure 10), its normal vector is parallel to the aromatic zipper and when it is extended the aromatic zipper lengthens, and 3) "orthogonal to zipper plane" (facet 3 in Figure 9 and colored orange in Figure 10), its normal vector is at an angle with the aromatic zipper direction (angle depends on unit cell parameters) and it is normal to the zwitterion layer. The results in Figure 11 reveal that TRP in the left handed crystal has a significant mobility only in the facet orthogonal to the aromatic zipper (facet 3 in Figure 9 (top)), whereas in the mixed enantiomer crystal TRP, has a significant mobility only in the facet parallel to the aromatic zipper (facet 2 in Figure 9, bottom). The crystals should experience slower growth on these facets. However,

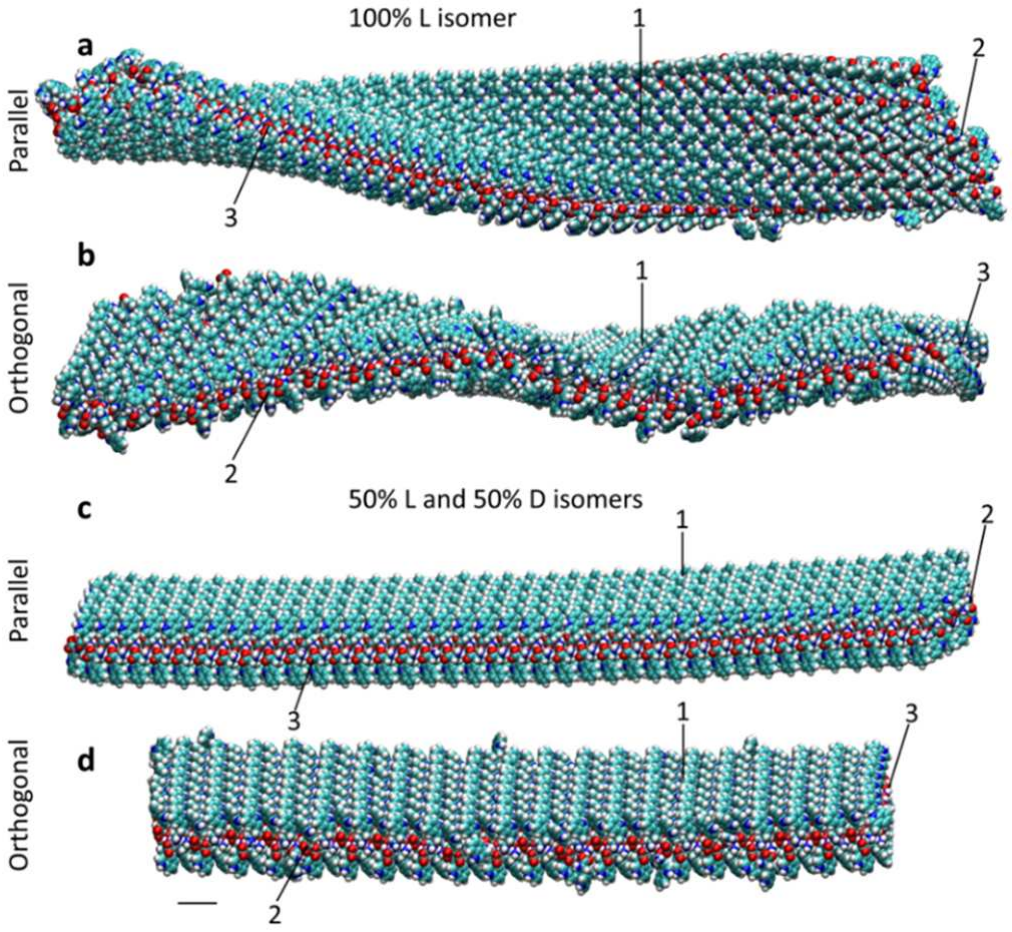

Figure 9: **MD simulations of TRP crystals.** L-TRP crystal cut (a) along an aromatic zipper and (b) orthogonally to the aromatic zipper after 20 ns. DL-TRP crystal cut (c) parallel to the aromatic zipper and (d) orthogonally to the aromatic zipper after 100 ns. Points showing (1) the top bilayer facet, (2) the facet parallel to aromatic zipper, and (3) the facet orthogonal to aromatic zipper. Scale bar represents 1 nm.

a pure enantiomer crystal becomes also twisted (Figure 9), which can prevent further crystallization in the folded directions.

We calculated nonbonding interaction energies of free amino acids in order to quantify the strength of TRP binding on each facet 1) with other amino acids on the same facet (Table III) and 2) with the remaining amino acids in the crystal (Table IV). In the left handed crystal, free amino acids in the top bilayer have strong interactions with other mobile amino acids and also with the constrained amino

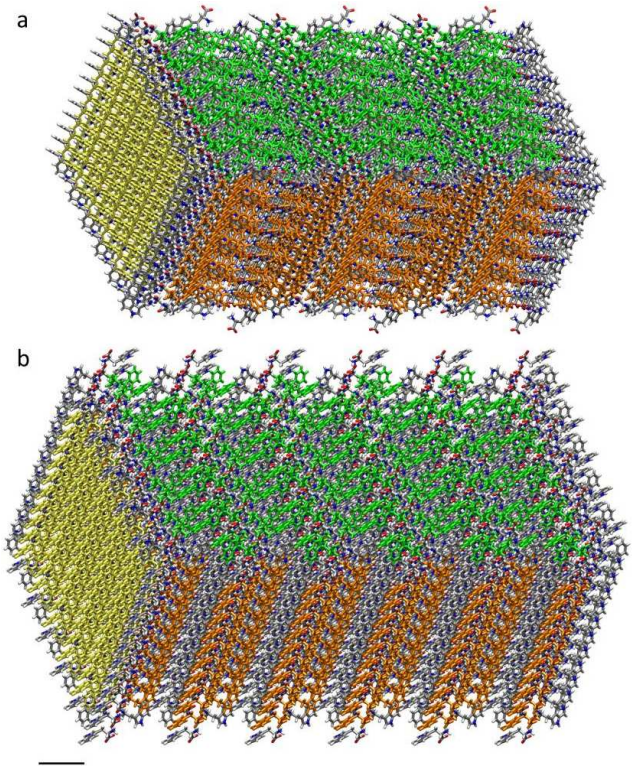

Figure 10: Definition of different facets for TRP crystals (a) pure left handed enantiomers and (b) mixed enantiomer. Yellow amino acids are top bilayer; green amino acids are parallel to the aromatic zipper; orange amino acids are orthogonal to the aromatic zipper. Scale bar represents 1 nm.

Facet	100% L-isomer (kcal/mol)	Mixed enantiomers (kcal/mol)
Top Bilayer	-78.09	-86.35
Parallel to Zipper	-65.34	-51.40
Orthogonal to Zipper	-68.38	-84.89

TABLE III. INTERACTION ENERGIES (PER MOLECULE) BETWEEN AMINO ACIDS WITHIN THE SAME FACET.

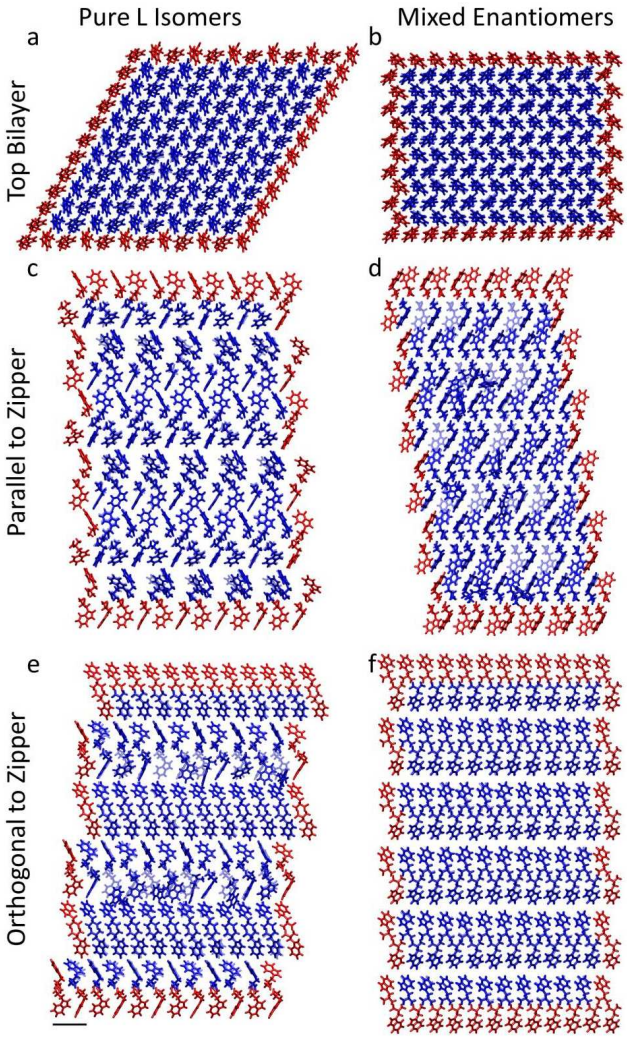

Figure 11: Motion of TRP amino acids in the first layer at different crystal facets. Red molecules in the first layer and all molecules below the first layer were constrained; dark blue molecules represent final positions of free peptides after 30 ns of simulations; light blue molecules represent their initial positions. Pure left-handed enantiomers (a, c, e): (a) top bilayer; (c) parallel to aromatic zipper; and (e) orthogonal to the aromatic zipper. Mixed enantiomers (b, d, f): (b) top bilayer; (d) parallel to aromatic zipper; and (f) orthogonal to aromatic zipper. Figures (b, d) have mixed chirality within each facet, whereas figure (f) has homogenous chirality. Scale bar represents 1 nm.

Facet	100% L-isomer (kcal/mol)	Mixed enantiomers (kcal/mol)
Top Bilayer	-76.15	-66.48
Parallel to Zipper	-64.48	-77.60
Orthogonal to Zipper	-59.31	-45.65

TABLE IV. INTERACTION ENERGIES (PER MOLECULE) BETWEEN AMINO ACIDS OUTSIDE THE SAME FACET.

acids, due to hydrogen bonding networks through zwitterions. At the same time, free amino acids in the facet orthogonal to the aromatic zipper have the weakest interactions with the constrained amino acids, thus they have a significant mobility. In the mixed enantiomer crystal, one side of a given aromatic zipper has one chirality and the other side has the opposite chirality. Table III to Table IV reveal that, due to steric effects, amino acids with the same chirality have a stronger affinity to each other, but amino acids with the opposite chirality have weaker affinities. Moreover, amino acids in the facet orthogonal to the aromatic zipper have strong interactions within the same facet and weak interactions with the remaining amino acids. The opposite is true for amino acids in the facet parallel to the aromatic zipper: they have weak affinities to other amino acids within the same facet and strong affinities to amino acids in the remainder of the crystal.

Conclusion

Aromatic amino acids play a crucial role in the formation of functional structures by the self-assembly of proteins and peptides, the major components of life. Our investigation of aromatic amino acid self-assembly together with the demonstration of the involvement of various interactions, such as electrostatic interactions, aromatic $\pi - \pi$ stacking, hydrogen bonding, etc., to drive the aggregation process provides the basis for understanding their self-assembly mechanism. Moreover, the experimental evidence presented here suggests different self-assembly kinetics and mechanisms for DL-composites of aromatic amino acids, allowing the fabrication of interesting materials with exciting

physical properties compared to the pure enantiomers. Previously reported protein crystallography revealed that a racemic mixture of the enantiomeric forms of a protein molecule can crystallize in ways not obtainable by natural proteins [60]. In addition, several experimental data support a theoretical prediction that racemic protein mixtures are highly amenable to crystallization due to the accessibility of several highly preferred achiral space groups. The high aggregation propensity of DL-amino acids to form self-assembled structures compared to the pure enantiomers, as observed in the current study, also supports a similar phenomenon for single amino acids. Moreover, the single-crystal structure analysis clearly demonstrated a favorable knob-to-hole packing of aromatic rings in the DL-mixture, which induced the easy growth of racemic crystals and the fabrication of self-assembled rigid materials. This study provides a different direction for chirality-induced tailor-made fabrication of futuristic functionalities based on natural systems for diverse nanotechnological applications.

3.3 Differential inhibition of metabolite amyloid formation by generic fibrillation-modifying polyphenols

Adapted from Ref. [3] (*Comm. Chem. 2018*, 1. DOI: 10.1038/s42004-018-0025-z) with permissions from Nature Publishing Groups.

Introduction

Small-molecule inhibitors are promising for ameliorating amyloidogenic diseases by inhibiting of amyloid formation. These small molecules specifically bind with amyloid assemblies and, thus, inhibit the self-assembly process [61–64]. Polyphenols, are found to be effective in the inhibition of amyloid structures formation. They are composed of one or more small aromatic phenolic rings that specifically and efficiently inhibit amyloid aggregation. Polyphenols represent the first generation of amyloid-based potential therapeutic agents. They cause a dramatic reduction in amyloidogenic-related cell death, and have been shown to efficiently inhibit the amyloid self-assembly in vitro. Dietary polyphenols have shown beneficial health-promoting effects in chronic and neurodegenerative diseases [65–67].

We investigate the inhibitory effect exerted on metabolite amyloid formation of the two polyphenolic compounds, epigallocatechin gallate (EGCG) and tannic acid (TA). They efficiently inhibit the formation of various protein amyloids and display beneficial preventive and therapeutic effects in neurodegenerative diseases [68–72]. We show that these two polyphenols successfully inhibit the self-assembly of adenine, phenylalanine, and tyrosine into amyloid-like fibrils that accumulate in adenine phosphoribosyltransferase deficiency, PKU and tyrosinemia metabolic disorders, respectively. Linking amyloid formation and metabolite amyloids in inborn error of metabolism disorders, and the inhibition of metabolite amyloids by natural small polyphenolic compounds as presented here, may lead to an innovative course of treatment for these disorders.

Experimental results

Spectroscopic monitoring of metabolite amyloid assembly inhibition.

Both EGCG and TA were found to inhibit adenine (8 mg/ml, ≈ 60 mM) fibrils in a dose-dependent manner, as demonstrated by the ThT fluorescence assay, presenting near complete inhibition of adenine aggregate formation at their higher concentrations. Some adenine aggregates could be observed only at the lowest inhibitor concentration, where EGCG and TA treatment resulted in a reduction of ca. 50% and 70% in ThT intensity, respectively, indicating a stronger inhibitory effect of TA. Similarly, in the case of phenylalanine (40 mg/ml, ≈ 242 mM) aggregates, both EGCG and TA inhibited the formation of the assemblies in a dose-dependent manner. EGCG presented a substantial inhibition at all concentrations, as reflected by the great reduction in the ThT fluorescence intensity curves, whereas TA presented a complete inhibition only at its highest concentration, a significant reduction in aggregation when applying the intermediate concentration and almost no effect using the lowest concentration. Finally, both inhibitors presented near complete inhibition of tyrosine (2 mg/ml, ≈ 10 mM) aggregates formation at their highest concentration and a significant reduction at the lower concentrations used, where nearly no formation of aggregates was detected, as reflected from the ThT fluorescence intensity assay. It should be noted that ThT was previously indicated to promote amyloid formation [73]. Thus, the clear inhibitory effect observed is even more notable.

Ultrastructural analysis of the effect of polyphenols on metabolite amyloid formation.

To gain insight into the morphological changes of the amyloid assemblies in the presence of the inhibitors, we employed transmission electron microscopy (TEM) and extreme high-resolution scanning electron microscopy (XHR-SEM), using the same concentrations of both metabolites and inhibitors as described above. As a control, TEM and XHR-SEM images of the polyphenolic inhibitors, at the

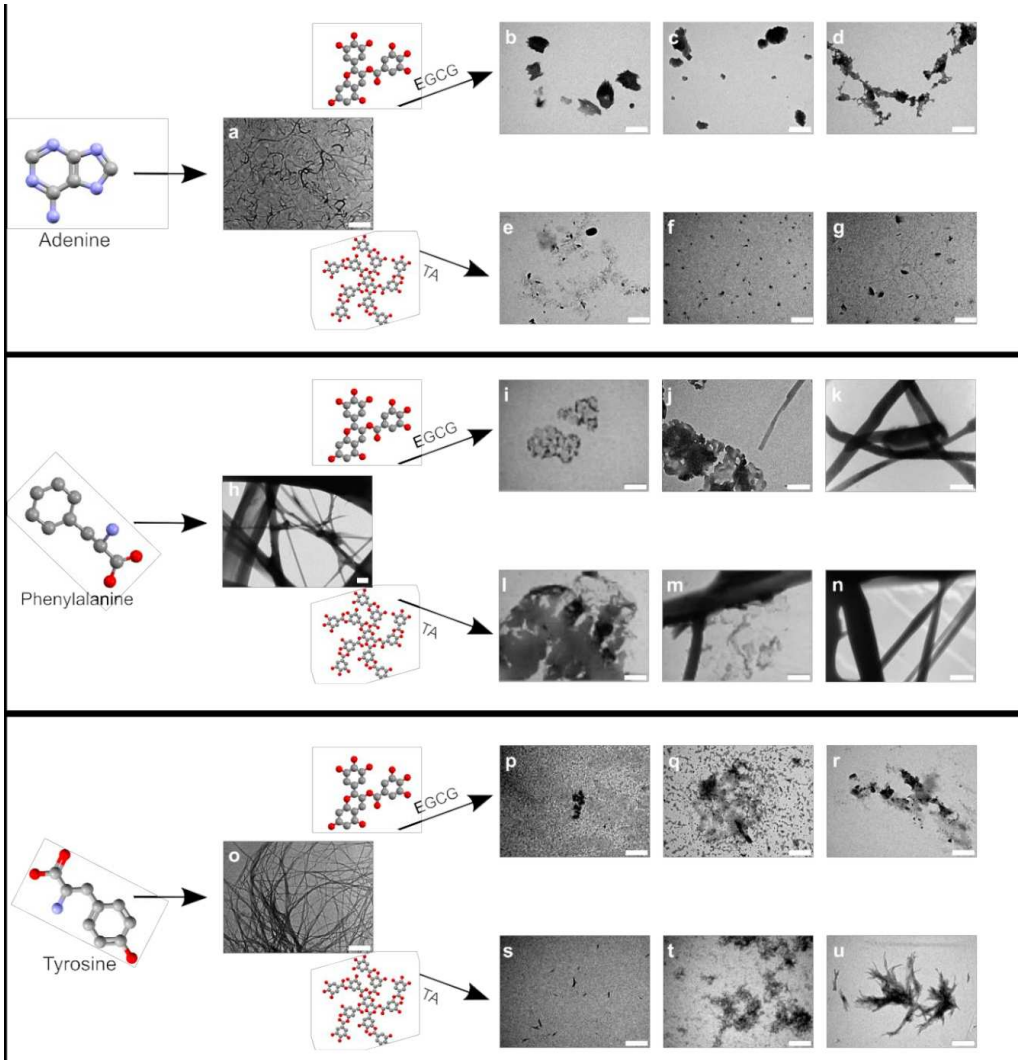

Figure 12: Inhibition of metabolite amyloid fibril formation by EGCG and TA. a-u Adenine, phenylalanine and tyrosine were dissolved at 90° C in PBS to a final concentration of 8 mg/ml, 40 mg/ml, and 2 mg/ml, respectively, mixed with PBS alone a, h, o or with the inhibitors, EGCG b-d, i-k, p-r, or TA e-f, l-n, s-u, at the concentrations stated below, and examined by TEM imaging. Scale bars 500 nm. The results represent three biological repeats. a Adenine. b Adenine + EGCG 1 mM. c Adenine + EGCG 0.5 mM. d Adenine + EGCG 0.05 mM. e Adenine + TA 0.1 mM. f Adenine + TA 0.01 mM. g Adenine + TA 0.0025 mM. h Phenylalanine. i Phenylalanine + EGCG 1 mM. j Phenylalanine + EGCG 0.5 mM. k Phenylalanine + EGCG 0.05 mM. l Phenylalanine + TA 0.1 mM. m Phenylalanine + TA 0.01 mM. n Phenylalanine + TA 0.0025 mM. o Tyrosine. p Tyrosine + EGCG 1 mM. q Tyrosine + EGCG 0.5 mM. r Tyrosine + EGCG 0.05mM. s Tyrosine + TA 0.1 mM. t Tyrosine + TA 0.01 mM. u Tyrosine + TA 0.0025 mM.

highest concentrations used, were acquired. In the absence of the inhibitors, adenine and tyrosine presented the typical fibrillar morphology of amyloid assemblies (Figure 12a, o), whereas in the presence of either EGCG or TA, inhibition of fibrils formation was observed in a concentration-dependent manner (Figure 12b-g, p-u). In the case of phenylalanine, lower metabolite concentrations resulted in the formation of a typical fibrillar amyloid morphology, yet at the higher concentration of 40 mg/ml, the concentration used in the ThT fluorescence assay, a different morphology was observed (Figure 12h). Both EGCG and TA hindered these structures in a concentration-dependent manner (Figure 12i-n). Notably, the TA concentrations employed in both ThT fluorescence assay and TEM imaging were at least an order of magnitude lower than those of EGCG, thus indicating a more potent inhibitory effect of TA. This is consistent with the relative inhibitory effect of the two compounds toward the formation of amyloids by protein and peptide building blocks [67]. In addition, for all metabolites, the lack of the formation of assemblies, as observed using TEM, correlates well with the results of the ThT fluorescence assay.

Analysis of the mechanism underlying the inhibition of metabolite amyloid formation.

In order to better understand the mechanism by which the polyphenol inhibitors affect the metabolite fibril formation, EGCG and TA were added to the system at different time points of the metabolite fibrillation process (after 0, 0.5, 1, and 2 h), and the kinetics of metabolite fibril formation was monitored using the ThT fluorescence assay. Both endpoint after overnight (Figure 13a-c) and kinetics data were recorded. Overall, EGCG inhibited metabolite fibril formation even when added at later stages of fibrillation. TA inhibited the formation when added at an earlier time point, while showing a much lower impact when added at the later stages of fibrillation.

Next, we examined whether the addition of inhibitors at later time points of metabolite fibrillation had an effect on their resulting cytotoxicity (Figure 13d). When EGCG was added after 2 hours, cell

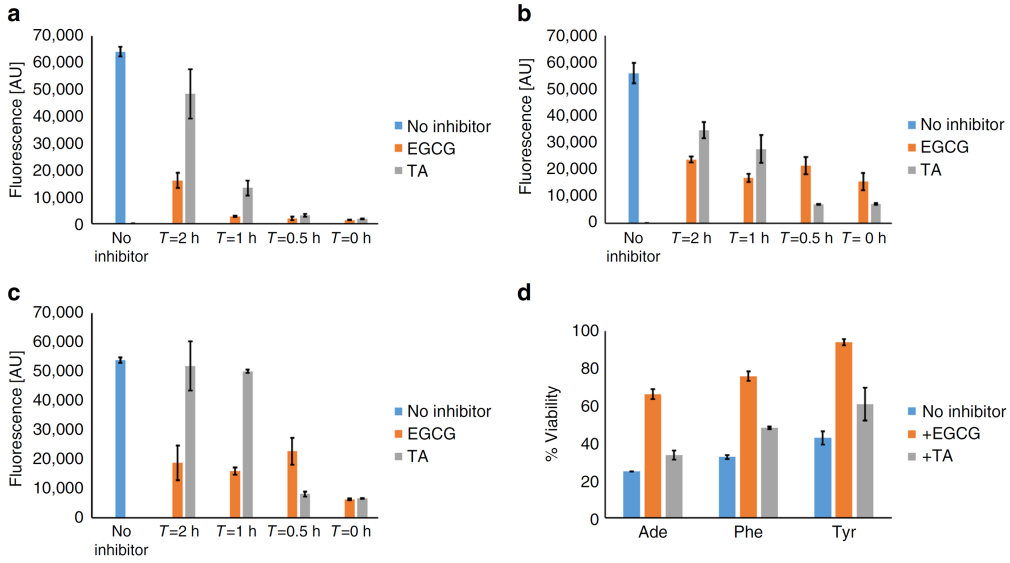

Figure 13: The effect of polyphenol inhibitors added at different time points on fibril self-assembly inhibition. All metabolites were dissolved at 90° C in PBS and ThT in PBS was added. The inhibitors, EGCG (1 mM, orange) or TA (0.1 mM, gray), or PBS (blue) as a control, were added at different time points (0, 0.5, 1, and 2 h). Following excitation at 450 nm, ThT emission data at 480 nm were measured over time for an overnight and endpoint fluorescence readings are presented. a Adenine 8 mg/ml. b Phenylalanine 40 mg/ml. c Tyrosine 2 mg/ml. d Adenine, phenylalanine, and tyrosine were dissolved at 90° C in DMEM/Nutrient Mixture F12 (Ham's) (1 : 1) without FBS, to a final concentration of 2, 4, and 2 mg/ml, respectively, and mixed after 2 hours with EGCG (orange, 0.1 mM) or TA (gray, 0.01 mM) following an overnight incubation. The samples to which no inhibitor was added were similarly mixed after 2 h with medium without FBS (blue). Then, SH-SY5Y cells were incubated with the metabolites in the absence or presence of the inhibitors for 24 h, followed by addition of MTT reagents. Following a 4 h incubation, extraction buffer was added and after an additional 0.5 h incubation, absorbance was determined at 570 nm. The data are presented as mean ± SD. The results represent three biological repeats.

viability was significantly restored. However, the addition of TA did not restore cell viability, which decreased to similar levels as the control without the inhibitor. These results are in agreement with the ThT fluorescence assay (Figure 13a-c), suggesting that TA mostly inhibits fibrilization at the early stages of nucleation, whereas EGCG acts both at the early and later stages of fibril formation. Taken together, the combination of results obtained via both the in vitro and neuronal cell model systems provides important insights into the differential mode of action of each inhibitor.

MD simulations: methods and results

Force field fitting.

The force field parameters for inhibitor molecules were calculated using Gaussian09 [74]. Owing to the large size of TA, this molecule was divided to two sections in the calculations: (1) an inner core, which is a beta-d glucose derivative, with each hydroxyl group being methylated; (2) ligands, with the ester group that is bonded to the core methylated. In the calculations of the EGCG core, the two main fused rings and the ester group were considered; the aromatic groups of EGCG were replaced with methyl groups. Force field parameters for aromatic groups used the results from TA calculations or were approximated with methyl groups. Geometries and force constants of inhibitors were determined using $MP2/6-31g(d)//MP2/6-31g(d)$ level for the EGCG core and TA core. Owing to the extent of ligand calculations, $MP2/6-31g(d)//MP2/6-31g$ methods were used instead. Force field fitting was performed using VMD Force Field Toolkit Plugin [75]. To determine dihedral parameters, MP2 level of calculations were also used to derive a quantum target, with the angle scanned six steps in both positive and negative directions at a step size of 15°. Charges were determined using the ChelpG algorithim [76].

Solvated metabolite simulations.

Systems formed by 288 ADN, PHE, and TYR freely solvated metabolite molecules were simulated in the presence of a small nucleation crystal of 125, 108, and 100 metabolite molecules, respectively. Each system consisted of 7 TA, 10 EGCG, or 15 ASA molecules. Systems with TA or EGCG were simulated for 20 ns, and those with ASA for 30 ns, using NAMD2 [37] and the CHARMM force field. The systems were simulated in [NaCl] = 0.15 M aqueous solution, in order to imitate physiological conditions. The Langevin dynamics with a damping coefficient of 1 ps^{-1} and a time step of 2 fs was used to describe systems in a NPT ensemble at a pressure of 1 atm and a temperature of 310 K.

During minimization, pre-equilibration, and equilibration, Particle Mesh Ewald [57] was used with a grid spacing of 1.0. The non-bonded interactions used the SHAKE switching algorithm with a switch on/off distance of 10/12 Å. Non-bonded pairs lists were 13.5 Å, with the list updated every 20 steps; $1-4$ non-bonded interactions were not scaled. There were $50,000$ steps of minimization followed by 2 ns of equilibration, after which the simulations were performed. The same approach was used in the simulations of inhibitors binding to metabolite crystals.

Crystalline metabolite simulations.

Simulated bulk-like crystals of ADN, PHE, and TYR had 564, 768, and 800 molecules, respectively, which were cut from their bulk crystal structures [44, 77, 78]. The solutions of simulated bulk crystals contained 25 TA, 50 EGCG, or 50 ASA molecules, and no free metabolite molecules. No specific fibril structures were considered.

Solvated metabolite interaction energies.

Average interaction energies between inhibitors and free metabolites or crystals were calculated from the simulated systems. The CHARMM force field [38–40, 79, 80] and NAMDenergy plugin in VMD [59] were used to determine the strength of total interaction energy for each inhibitor by calculating vdW and electrostatic interaction energies. Interaction energy between each inhibitor and any metabolite molecule, which had at least one atom within 3.5 Å of any atom of the selected inhibitor, was considered for the calculation. For each snapshot, the total energy and number of metabolites inter- acting with the inhibitor was recorded. Interaction energy per metabolite and inhibitor was determined at each snapshot. When averaging the interaction energy, only cases with at least one metabolite interacting with the inhibitor were included. The average number of free metabolites was

computed for the entire trajectory. The average number of interacting metabolites was normalized with respect to the concentrations of both inhibitors and solvated metabolites (Table V).

Crystalline metabolites interaction energies.

Similar to solvated metabolites, we chose one inhibitor for the crystal cases and evaluated its interaction energies with metabolites on the crystal. Metabolites on crystal, which were within 3.5 Å of the inhibitor, were considered. The average interaction energy was computed using the same procedure as for the solvated metabolites. The number of inhibitors interacting with the crystal was determined by calculating any inhibitor with at least one atom within 3.5 Å of the crystal. This number was averaged throughout the trajectory. Then, it was normalized with respect to the concentration of inhibitors and surface area of the crystal, obtained at the end of the trajectory (Table V), because some metabolite molecules dissolved from the crystals during the simulation.

	Solvated Metabolites		Crystal Metabolites	
System	Free Metabolite Concentration (M)	Inhibitor Concentration (M)	Surface Area (nm^2)	Inhibitor Concentration (M)
ADN-TA	0.313	0.005	154	0.010
ADN-EGCG	0.275	0.007	162	0.025
ADN-ASA	0.240	0.009	166	0.047
PHE-TA	0.200	0.005	304	0.009
PHE-EGCG	0.187	0.006	306	0.027
PHE-ASA	0.216	0.011	303	0.045
TYR-TA	0.173	0.004	345	0.010
TYR-EGCG	0.187	0.006	349	0.030
TYR-ASA	0.231	0.012	348	0.043

TABLE V. CONCENTRATIONS OF SOLVATED METABOLITES AND INHIBITORS IN EACH SOLVATED SYSTEM; CRYSTAL SURFACE AREA AND INHIBITOR CONCENTRATION IN CRYSTAL SYSTEM.

Figure 14 demonstrates representative binding modes of the inhibitors, TA, EGCG, and ASA, and free solvated adenine (ADN), phenylalanine (PHE), and tyrosine (TYR). Figure 15 to Figure 17

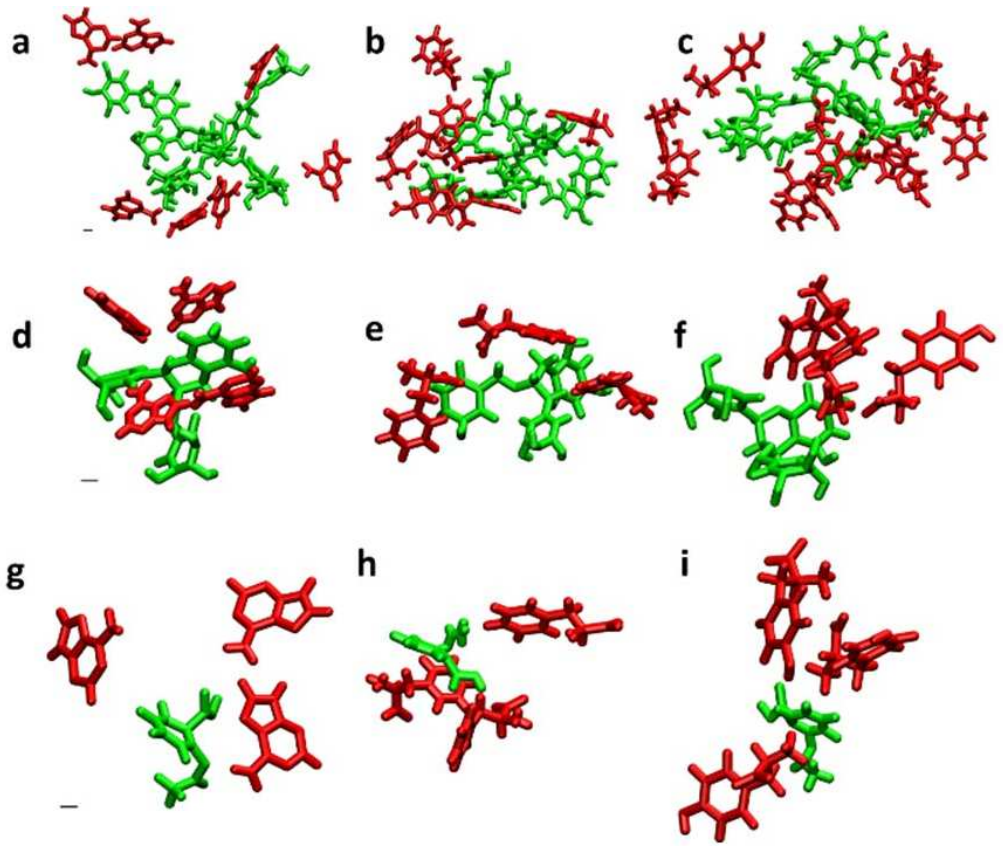

Figure 14: **Examples of simulated inhibitors coupling with freely solvated metabolite molecules.** (a-c) TA; (d-f) EGCG; (g-i) ASA. (a,d,g) Adenine; (b,e,h) Phenylalanine; (c,f,i) Tyrosine. Metabolite molecules are shown in red, inhibitor molecules are shown in green. Scale bar in each row represents 1 Å.

show TA, EGCG, and ASA inhibitors on each of the different facets of the ADN, PHE, and TYR crystals, respectively.

To gain further insight into the distinct inhibition mechanisms of the two inhibitors, we performed molecular dynamics (MD) simulations of the potential inhibition activity of EGCG, TA, and ASA during the formation of metabolites fibrillar assemblies. In particular, we examined the interactions between inhibitor molecules and both free solvated metabolite molecules and small metabolite fibril nuclei. Figure 18a-d presents the MD-simulation of phenylalanine coupled to TA and EGCG (see Figure 14 to Figure 17 for additional data). The interaction energy was determined by selecting an

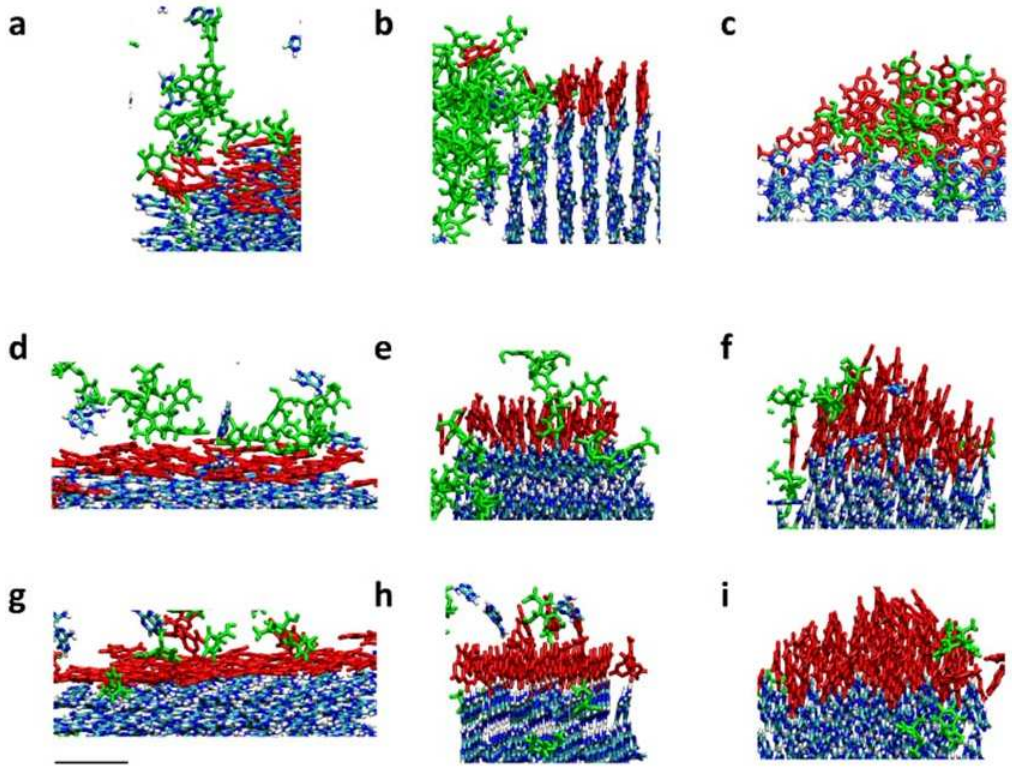

Figure 15: **Examples of inhibitors coupling to adenine metabolite crystal.** (a-c) TA; (d-f) EGCG; (g-i) ASA. (a,d,g) facet A; (b,e,h) facet B; (c,f,i) facet C. The interacting facets of metabolite molecules are shown in red, inhibitor molecules are shown in green, and the remaining metabolites are shown in blue/teal. Scale bar is 1 nm.

inhibitor and calculating the average binding energy per metabolite within 4.5 Å of that inhibitor molecule. We partitioned the trajectory into two sections and averaged the binding energy of each section. The midpoint between the averages was chosen as the final value. Error bars were determined from the deviation of the averages of each partition and the midpoint.

As revealed by the simulations, the average binding energies of the metabolites to both TA and EGCG are similar, whereas the binding energies to ASA are $2-3$ times lower. Moreover, there is a small variation of these energies between the studied metabolites, with the binding energy of adenine found to be $\approx 50\%$ of those of phenylalanine and tyrosine (Figure 18e).

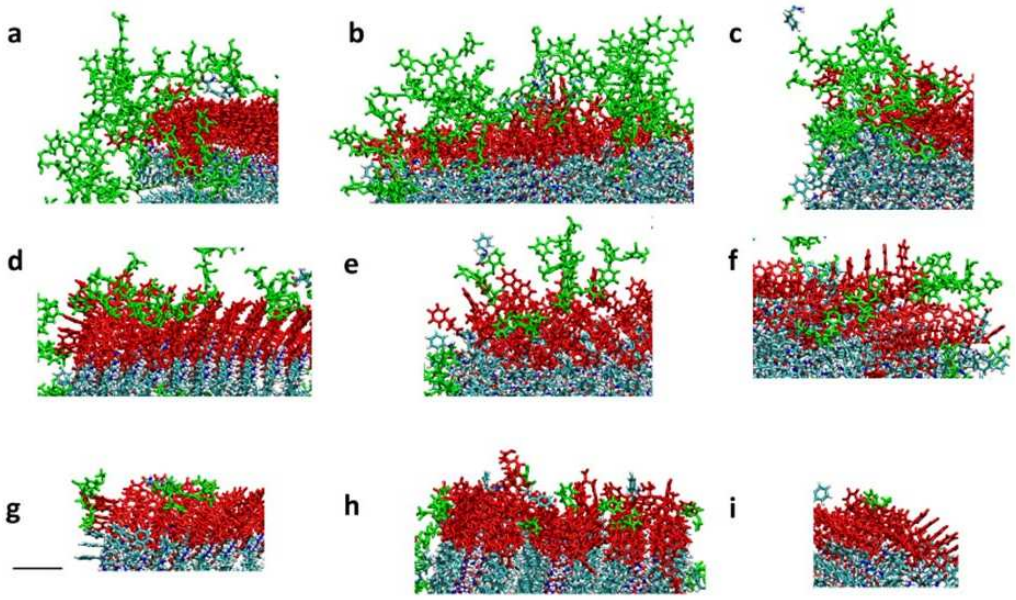

Figure 16: **Examples of inhibitors coupling to phenylalanine metabolite crystal.** (a- c) TA; (d-f) EGCG; (g-i) ASA. (a,d,g) facet A; (b,e,h) facet B; (c,f,i) facet C. The color scheme is the same as in Figure 15. Scale bar is 1 nm.

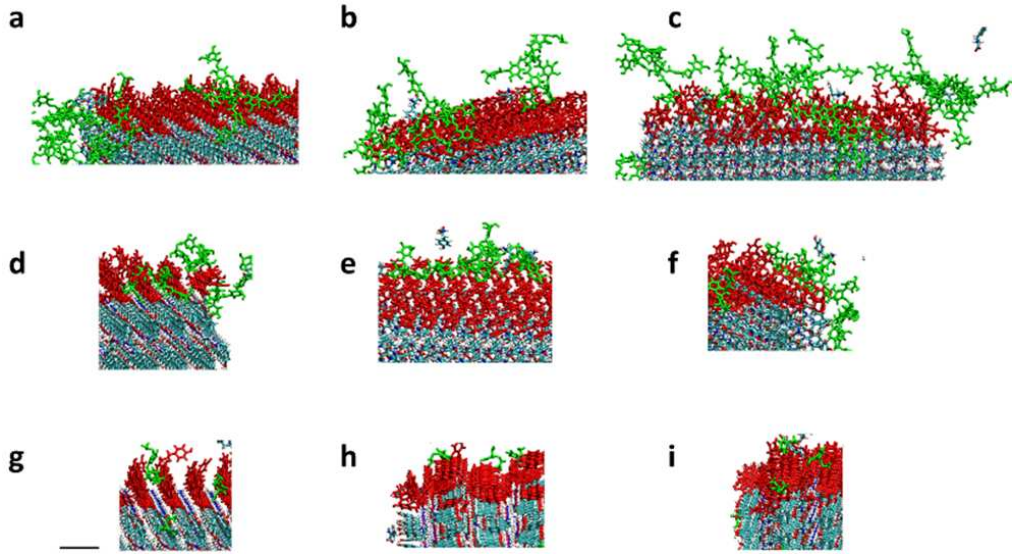

Figure 17: **Examples of inhibitors coupling with tyrosine metabolite crystal.** (a-c) TA; (d-f) EGCG; (g-i) ASA. (a,d,g) facet A; (b,e,h) facet B; (c,f,i) facet C. The color scheme is the same as in Figure 15. Scale bar is 1 nm.

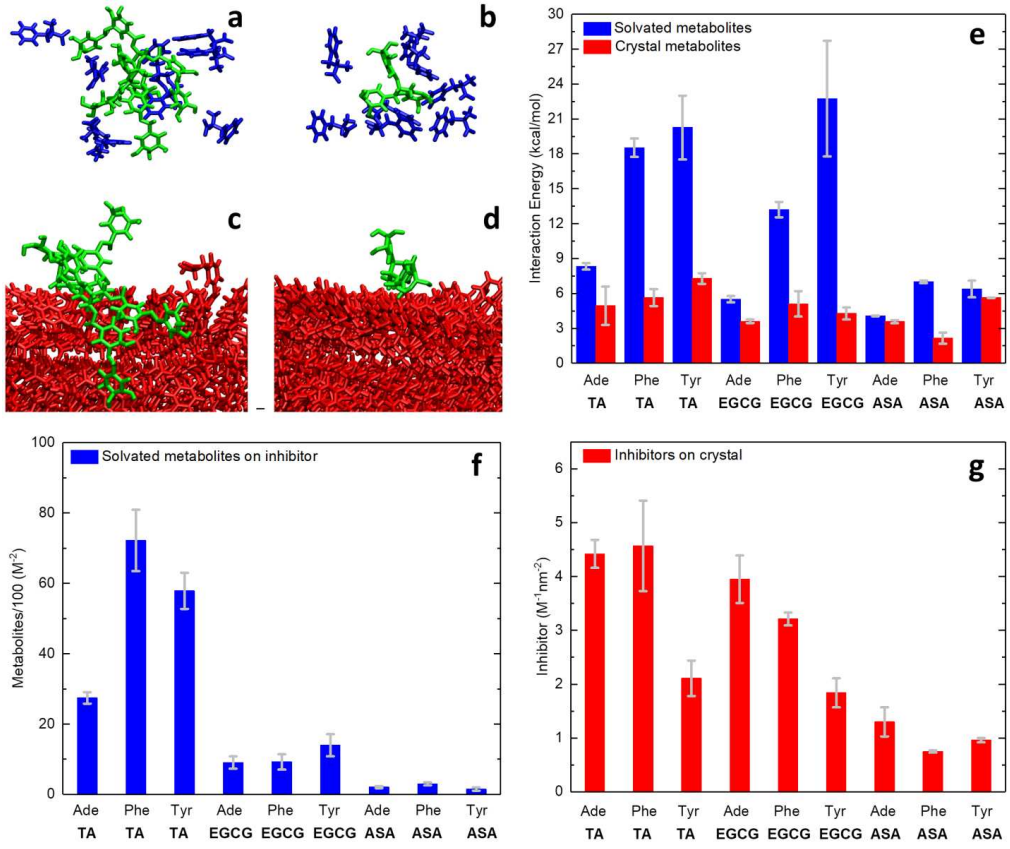

Figure 18: Simulations of metabolites and inhibitors coupling. a-d Snapshots of TA a, c and EGCG b, d coupling with PHE metabolites in free a, b and crystal c, d forms. Free metabolites are shown in blue; metabolite molecules in crystal are shown in red, inhibitor molecules are shown in green. Scale bars in a-b, c-d represent 1 Å. e The average total coupling energies between inhibitors and either free (blue) or crystalline (red) metabolites, within 3.5 Å of the inhibitor, normalized per inhibitor and metabolite. f The average number of free metabolites around inhibitors, normalized by the concentration of free metabolites and inhibitors in the system. g The average number of inhibitors adsorbed to metabolite crystals, normalized by the concentration of inhibitors and the surface areas of crystals. Column heights were determined by blocking the trajectory into two halves and calculating the midpoint between the averages of each block. Error bars are the deviation of the average of each half of the trajectory and the midpoint.

Next, we calculated the number of free metabolites coupled to inhibitors, normalized by the concentrations of metabolites and inhibitors (Figure 18f). We determined averages and uncertainties using the same procedure we used in determining the interaction energy. This analysis shows that a larger number of free metabolites can adsorb to TA as compared with EGCG or ASA, despite similar binding energies of these inhibitors to individual metabolites (Figure 18e). This difference results from the significantly larger surface area of TA, as compared with EGCG or ASA. These observations correlate well with the experimental results showing that TA efficiently binds free metabolites, whereas EGCG reaches the same efficiency only at about an order of magnitude higher concentration.

In addition, the number of inhibitors bound to the metabolites in their crystalline state and normalized to the concentrations of inhibitors and the surface areas of the metabolite crystals was calculated (Figure 18g). The data reveal that at the same concentrations, TA and EGCG have a similar propensity for binding to the ordered lattice, whereas ASA has a very low binding propensity. This explains the experimental observations showing that EGCG can block the growth of fibrils even when added at later stages, as it binds to the crystal at about an order of magnitude higher concentration. Given the relative dimensions of TA and EGCG, EGCG can cover the crystals to a larger extent at the higher concentrations used. Moreover, there is a twofold decrease of inhibitors bound to the tyrosine crystal, probably owing to the fact that the preferable binding sites are not fully exposed in this form as its facets are jagged, unlike adenine and phenylalanine surfaces, preventing the formation of $\pi - \pi$ stacking interactions (Figure 18g).

Conclusion

Here, we reveal that two aromatic polyphenolic compounds, EGCG and TA, which have been previously shown to generically inhibit the formation of protein and peptide-based amyloid struc-

tures, can also inhibit the formation of metabolite amyloid fibrils, even when applied at a very low molar ratio. The examined concentrations, resulting in the same end-effects, varied between the metabolites, as previously shown for different protein and polypeptide amyloid aggregates [81]. We demonstrated the activity of these inhibitors both in vitro, using ThT fluorescence assay and TEM analysis, and in vivo, using the 3-(4,5-dimethylthiazolyl-2)-2,5-diphenyltetrazolium bromide (MTT) cell viability assay preformed on a neuronal cell model. The addition of the polyphenols at different time points provided a key mechanistic information about the process of inhibition by EGCG and TA and its correlation to reduced cytotoxicity. We demonstrated that in spite of the generic inhibition, the compounds function via two different mechanisms. Although EGCG affects both early and later stages of fibrillation, TA is only effective in the early state. To gain further insights on these different inhibition mechanisms, we preformed MD simulations. The simple chemical composition of the metabolites and the information about their molecular packing allowed to decipher the mechanism of amyloid formation, making them a potential model for understanding and controlling protein amyloid formation. The simulation provided molecular details about the nature of the binding of the two inhibitors to the studied metabolites in both monomeric and crystalline forms. It appears that each metabolite binds to both inhibitors with similar energy. At the molarity experimentally used here, the two inhibitors also bind a comparable number of free metabolites. However, at this molarity, the number of EGCG molecules binding to the crystalline form is several fold higher than the TA molecules, providing a theoretical framework to understand the distinct effect of the inhibitors when added at different stages of amyloid self-assembly.

The metabolites studied in the scope of this work are known to accumulate in different inborn error of metabolism disorders and, as we have previously shown, can self-assemble and form supramolecular β-sheet-like amyloid structures. In protein and peptide-based amyloids aggregation, the core β-sheet

structure seems to be primarily stabilized by hydrogen bonds [82, 83]. Based on their structural resemblance and previous findings regarding phenylalanine and tyrosine assemblies' formation [84], we can speculate that the amyloid metabolite supramolecular structures are also stabilized via hydrogen bonds, which may support the findings derived from the simulations presented here regarding the nature of inhibitor-metabolite interactions. This was indeed the case for phenylalanine, for which the newly determined crystal structure of the zwitterionic state, that promotes fibrils formation, shows a clear hydrogen-bonding network as observed in peptides and proteins [44]. Moreover, the overlay of computer-generated putative poly-phenylalanine β-strands on the crystal structures resulted in remarkable superposition [55]. The use of known protein and peptide amyloid inhibitors in order to affect metabolite amyloid structure formation further supports the notion of an extended family of amyloid structures that includes protein, peptides, and metabolites. Finally, the less-explored concept of error of metabolism disorders as amyloid diseases may thus lead to the development of new therapeutic strategies, in addition to the current dietary restrictions.

3.4 Metabolite amyloid-like fibrils interact with model membranes

Adapted from Ref. [4] (*Chem. Comm. 2018*, 54. DOI:10.1039/c8cc01423j) with permissions from Royal Society of Chemistry Publishing Groups.

Introduction

Metabolite amyloid assemblies induce apoptotic cell death [1, 55], similar to protein amyloid structures [85,86]. Interactions of the amyloidogenic assemblies with the cell membrane is considered the most prevalent course of toxicity [87]. We investigate the possible interaction between metabolite amyloid assemblies and model membranes, as an insight into their cytotoxicity.

We used the highly-characterized chromatic biomimetic membrane system containing phospholipids and polydiacetylene (PDA). PDA is a lipid-like polymer, which forms vesicular bilayer structures that mimic membrane surfaces. It exhibits a rapid blue-red fluorescent chromatic response (FCR) transformations, induced by contact with external species [88,89], such as amyloidal assemblies produced by the IAPP polypeptide [18]. In addition to the PDA, we use combinations of vesicular bilayer phospholipid compositions, one containing only the phosphatidylcholine phospholipid (PC), a major component of cell membranes, and the other comprising a combination between PC and phosphatidylserine (PS). PS is known for its important role in cell cycle signalling, specifically in case of apoptosis [90]. We examined the interaction between these model membrane systems with tryptophan, tyrosine and adenine amyloid-like assemblies that accumulate in hypertryptophanemia and hartnup disease, tyrosinemia and adenine phosphoribosyltransferase deficiency, respectively [91, 92].

Experimental results

To gain further insight into the metabolites interaction with the model membrane systems, the fluorescence anisotropy of 1-(4-trimethylammoniumphenyl)-6-phenyl-1,3,5-hexatriene (TMA-DPH),

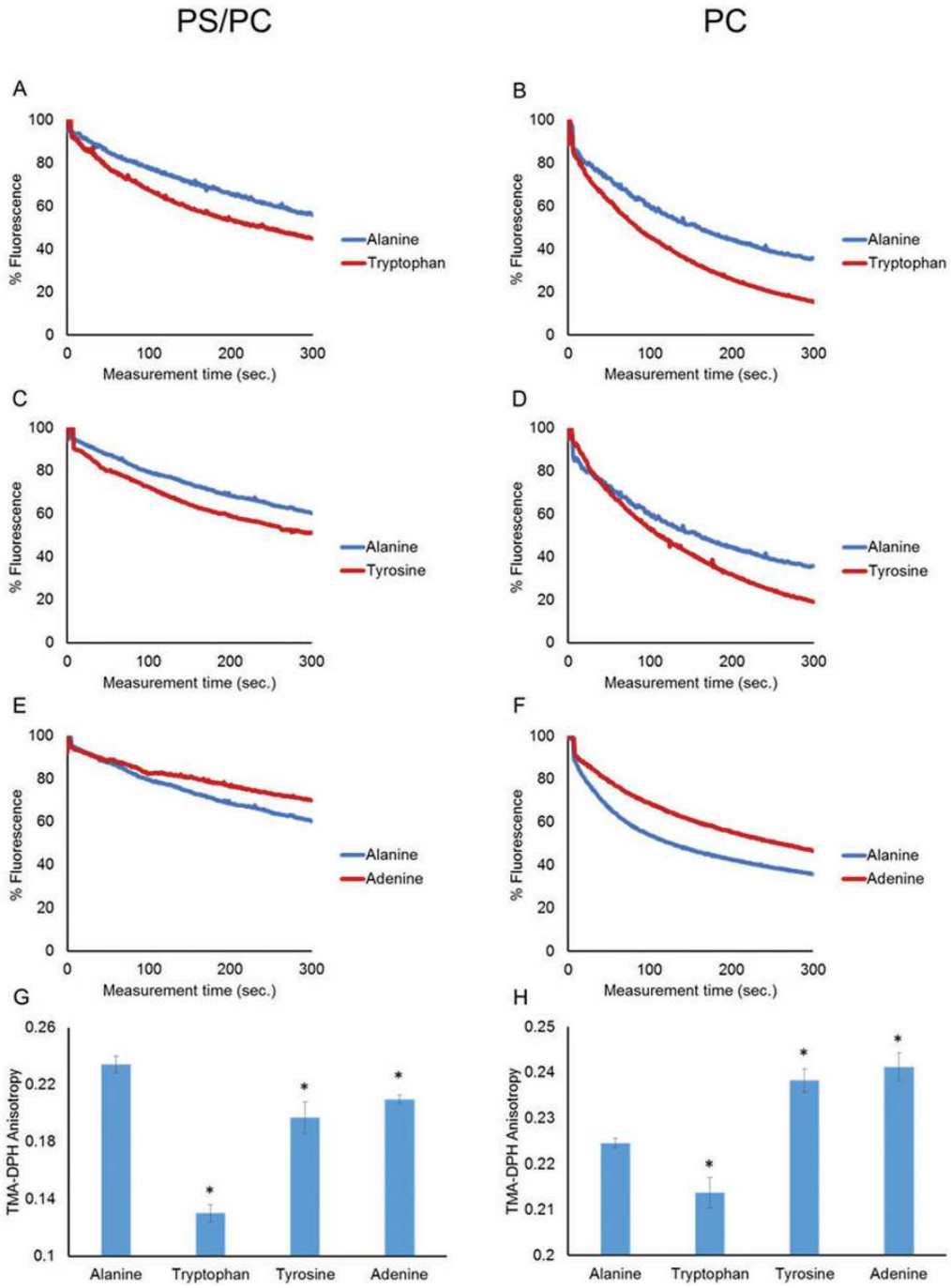

Figure 19: Metabolite assemblies' interaction with membrane model systems. Tryptophan (4 mg ml^{-1}), tyrosine (4 mg ml^{-1}) and adenine (2 mg ml^{-1}) metabolite assemblies' solutions were examined. Alanine (4 mg ml^{-1}) solution was examined as a control. Two phospholipid compositions of membrane model systems were examined, PC and a combination of PC with PS. (A-F) Quenching of NBD fluorescence as measured after a 24 h incubation with metabolite assemblies', or alanine solution as a control, following an addition of dithionite quencher. The Y-axes present the fluorescence values as a percentage of the initial emission reading. (G and H) Fluorescence anisotropy of TMA-DPH, incubated for 24 h with metabolite assemblies' solutions, or alanine solution as a control (*$p < 0.001$ compared to alanine).

a common sensitive probe which reacts to the dynamics of its lipid environment, was measured [93,94]. As in the FCR and quenching assays, the fluorescence anisotropy was measured after a 24 h incubation. Alanine presented same effect as the untreated control and thus served as a negative control. The tryptophan assemblies induced a significant decrease in TMA-DPH fluorescence anisotropy in both phospholipid compositions (Figure 19G and H), indicating a higher lipid mobility around the probe and an increase in membrane fluidity. Together with the FCR and quenching assays, these results imply the ability of tryptophan assemblies to fully penetrate the model membrane system. Both tyrosine and adenine assemblies induced a significant decrease in TMA-DPH fluorescence anisotropy when tested with the PS/PC lipid composition (Figure 19G), while in the PC lipid composition, an increase in the fluorescence was observed (Figure 19H). Overall, in the case of tyrosine amyloid-like fibrils, the results indicate a penetration ability of the assemblies. In the PC lipid composition the structures might be lodged between the lipids, increasing the membrane rigidity. In contrast, a better interaction with the PS/PC composition may allow for a deeper penetration of the tyrosine fibrils to the membrane, resulting in increased membrane fluidity. In the case of adenine amyloid-like fibrils, the assemblies appear to interact with the outer side of the membrane, resulting in an increase in membrane rigidity, while better interaction with the PS/PC composition might allow for a similarly slight increase in membrane fluidity.

MD simulations: methods and results

Simulations

Bulk crystal structures for tryptophan, tyrosine, and adenine [36,77,78] were chosen. Membranes were constructed using the CHARMM GUI software [95]. SOPC lipid molecules were chosen for the PC membrane, and 90% SOPC and 10% SOPS lipid molecules were chosen for the PC/PS combination membrane. Initially, three different orientations (facet A,B,C) were chosen for each

crystal structure. For tryptophan and tyrosine, the head groups were in direct contact with the membrane in facet A and perpendicular to the membrane in facets B and C. For both of these crystals, another orientation was chosen, such that the zwitterions were in direct contact with the membrane. In the case of the adenine crystal, facet A was determined such that the plane of the molecules in the crystal was parallel to that of the membrane. In facets B and C, the planes of the molecule were oblique to that of the membrane.

Simulations were performed using the NAMD2 [37] package, using the CHARM force field [38–40, 56, 79, 96, 97]. The systems were simulated in [NaCl] = 0.15 M aqueous solution, in order to imitate physiological conditions. The Langevin dynamics with a damping coefficient of 1 ps^{-1} and a time step of 2 fs was used to describe the systems in a NPγT ensemble at a pressure of 1 atm, surface tension of 40 dyne/cm, and a temperature of 310 K. During minimization, pre-equilibration, and equilibration, Particle Mesh Ewald [57] was used with a grid spacing of 1.0. The non-bonded interactions used the SHAKE switching algorithm with the switch on/off distance at 10/12 Å. Non-bonded pairs lists were 13.5 Å, with the list updated every 20 steps; $1-4$ non-bonded interactions were not scaled. There were $50,000$ steps of minimization. Production runs for each system lasted 30 ns.

Interaction energies

Average interaction energies between each crystal and membrane were calculated from the simulated systems. The CHARMM force field [38–40,56,79,96,97] and NAMDenergy plugin in VMD [59] were used to determine the strength of total interaction energy for each combination of metabolite crystal and membrane calculated as a sum of the electrostatic and van der Waals (vdW) interaction energies. Electrostatic interaction energies were calculated for a dielectric constant of 1 and disper-

sion interactions were approximated by the $12-6$ Lennard Jones potential. Long range electrostatic interactions were modeled by the Particle Mesh Ewald method [57].

In order to determine the crystal-membrane interactions, interaction energies per contact area were calculated. Throughout the simulations, a significant number of metabolites was found to dissociate from the crystal. Many of these molecules were later absorbed in the membrane. These free molecules had to be omitted from the calculations. Contact area between metabolite crystal and membrane was determined by calculating solvent accessible surface area (SASA) with command in VMD. Contact Area is given by Equation 3.1, where SASA is the solvent accessible surface area of the membrane, crystal, or the union of both species, as indicated. Interaction energy between metabolite crystal and membrane was normalized to the contact area in each snapshot.

$$ContactArea = \frac{SASA_{membrane} + SASA_{crystal} - SASA_{membrane+crystal}}{2} \tag{3.1}$$

By observing the trajectories and computing normalized interaction energies, the most stable orientations of each assembly with respect to the membrane were identified (Figure 20A-C, Figure 21, Figure 22, and Figure 23, ESI). The tryptophan crystal showed the most favourable interactions with the zwitterion in direct contact with the phospholipid membrane (Figure 20A and Figure 21, ESI), tyrosine showed the most favourable interaction with the polar head groups in direct contact with the membrane (Figure 20B and Figure 22, ESI), and adenine showed the most favourable contact when the plane of the crystalline molecules was parallel to that of the membrane (Figure 20C and Figure 23, ESI). The other orientations showed an unstable configuration. Furthermore, the corresponding interaction energy per contact area was calculated (Figure 20D). The interaction energy largely corresponded to the FCR experiments, when comparing the association of the individual metabolite

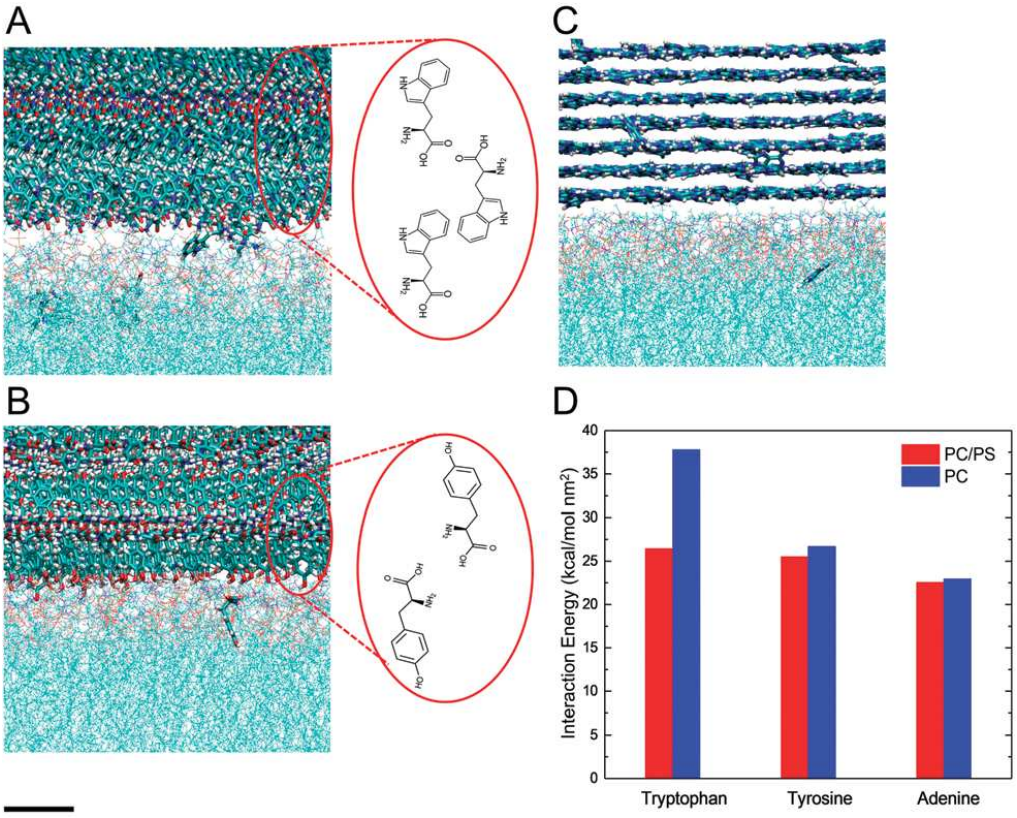

Figure 20: Molecular dynamic simulations of the interaction of metabolite assemblies with membrane systems. (A-C) Most stable orientations for (A) tryptophan in zwitterion layer, (B) tyrosine in facet A, and (C) adenine in facet A. (D) Interaction energies of tryptophan, tyrosine, and adenine with both membranes, normalized to the contact area.

crystalline systems with the two membranes. Since the MD simulations data cannot be normalized to the concentration, the comparison between the different metabolites is limited. The tryptophan assemblies showed a stronger binding to the PC phospholipid membrane as compared to a PS/PC membrane, at a ratio similar to that observed in the FCR experiments. The adenine crystalline systems bounded equally to both membranes, as also observed in the FCR analysis. However, in the case of tyrosine, the interaction energies of the crystalline systems are the same for both PC and PS/PC phospholipid membrane, although showing a higher FCR effect for the PC phospholipid.

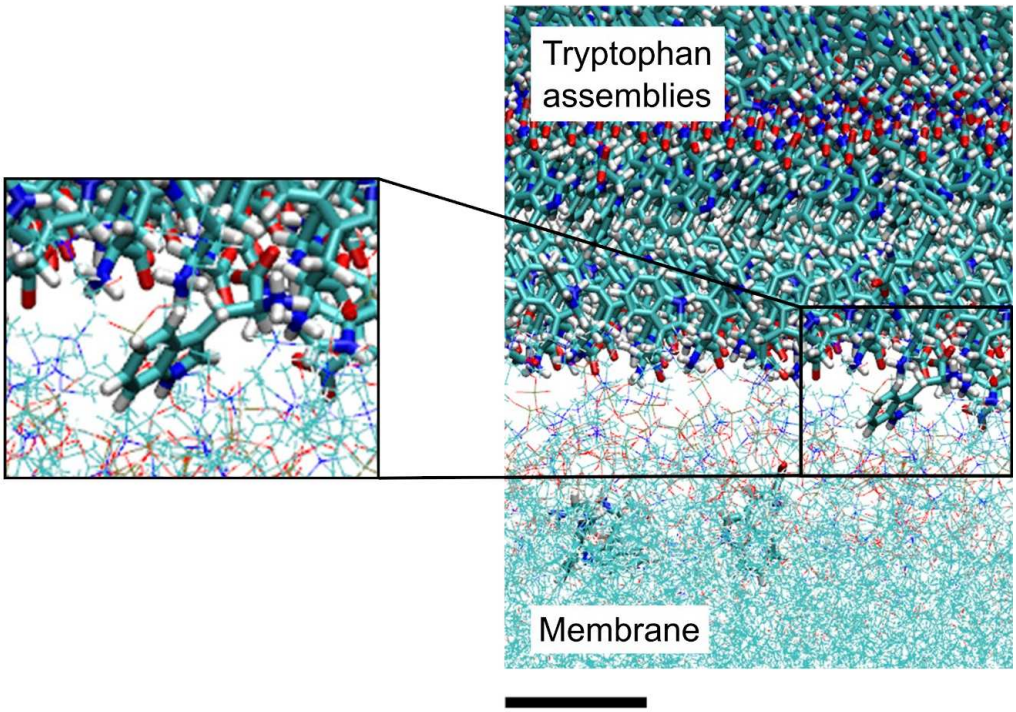

Figure 21: **Molecular dynamic simulations of tryptophan assemblies with membrane systems.** Enlarged figure taken from Fig. 3A. The most stable orientations of the tryptophan assemblies (zwitterion layer) are presented.

Smaller differences detected by the FCR analysis might require considerable time scales, and probably also more precise force fields, to be identified using MD simulations.

The most stable configuration for the tryptophan structures was driven by coulombic and hydrogen bonding interactions. Due to the bulky apolar head group of the tryptophan molecule, the tryptophan assemblies had maximum interactions with the zwitterion when contacting the membrane. When the apolar head group was in direct contact with the membrane, the structures torqued and changed orientation, thus resembling those of facets B and C, both of which had only a limited exposure of zwitterions to the membrane. Due to the higher exposure to the polar groups when the zwitterion layer was in direct contact to the membrane, it appears that it would bind in that orientation.

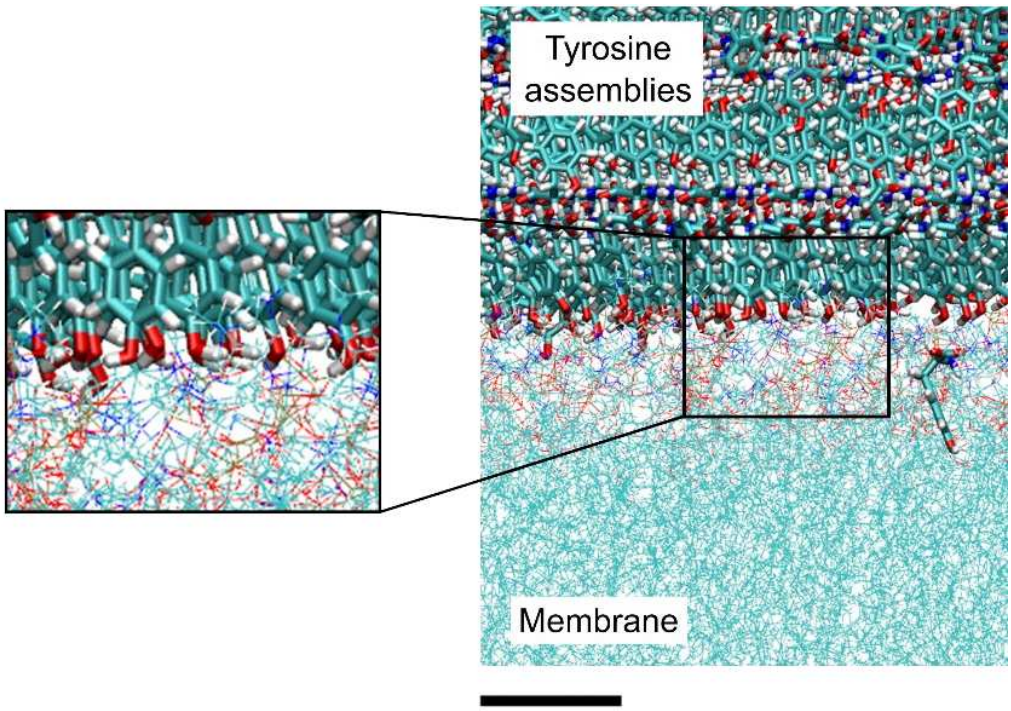

Figure 22: **Molecular dynamic simulations of tyrosine assemblies with membrane systems.** Enlarged figure taken from Fig. 3B. The most stable orientations of the tyrosine assemblies (facet A) are presented.

Tyrosine and adenine crystal orientations relative to the membrane were also determined by hydrogen bonding and coulombic forces. In case of the tyrosine crystalline systems, the polar phenol head group bound strongly to the membranes, as seen in facet A. When the zwitterion layer was in direct contact with the PC lipid membrane, the assemblies torqued away from the orientation, as observed in the case of facets B and C. Due to facet A stability, where no significant torqueing was observed, it can be determined that in the tyrosine structures, direct contact of the phenol groups with the membranes is preferable.

In case of the adenine assemblies, due to the quadrupolar structure of the molecule, there were significantly weaker coulombic interactions, with the stronger dispersion interactions compensating. In facet A, the dispersion and coulombic interactions were of the same magnitude, unlike the other

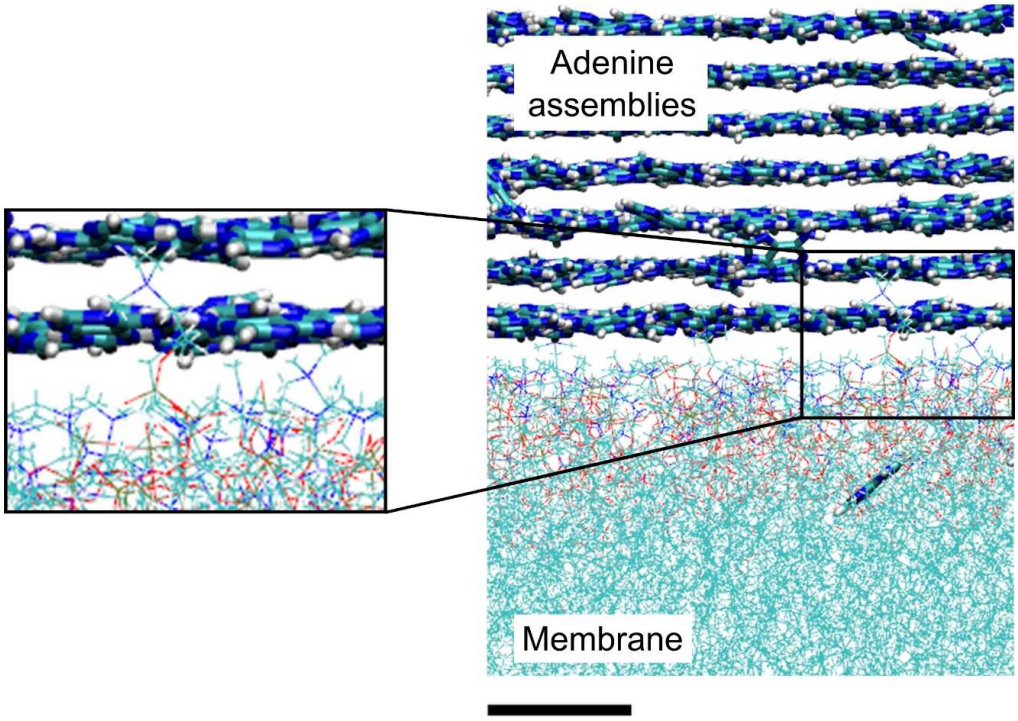

Figure 23: **Molecular dynamic simulations of adenine assemblies with membrane systems.** Enlarged figure taken from Fig. 3C. The most stable orientations of the adenine assemblies (facet A) are presented.

two orientations, where they were weaker. This was observed when the adenine molecules were most exposed to the membrane, attained only when the plane of the molecules was parallel to that of the membrane.

Conclusion

The experimental data here demonstrate the ability of metabolite amyloid assemblies to interact with phospholipid membranes, as previously shown in the case of their proteinaceous amyloid assemblies counterparts. Our results demonstrated the differential membrane binding ability of all three metabolite structures. We show that the tryptophan and tyrosine assemblies penetrate the membrane models, while the adenine structures bind parallel to the membrane. Similar to proteinaceous amyloids [98–101], distinctive mechanisms underlie the membrane interaction of metabolite

amyloids, while resulting in a comparable cytotoxic effect. Furthermore, molecular dynamics simulations provide a detailed atomistic information of the mechanism underlying the interaction of the metabolite assemblies with the membrane. The remarkable similarity between the mode of interaction of the metabolite amyloid assemblies and the protein ones further emphasizes the functional relationship between the two systems, supporting the definition of metabolite amyloids as an extension of the "amyloid hypothesis". We hope that the observations presented here will promote further exploration of the mechanism of interaction and the nature of the membrane-interacting species. As membrane interaction is assumed to play a key role in the apoptotic activity of metabolite and protein amyloids the targeting of these interactions may be an important therapeutic direction to the future treatment of various amyloid-associated disorders.

3.5 Transition of Metastable Cross-α Crystals into Cross-β Fibrils by β-Turn Flipping

Adapted from Ref. [5] (*J. Am. Chem. Soc. 2019*, 141 DOI:10.1021/jacs.8b10289) with permissions from ACS Publishing Groups.

Introduction

Aggregation of many intrinsically disordered or globular proteins into insoluble fibrillar deposits with cross-β structure causes many debilitating protein misfolding illnesses, such as Alzheimer's, Parkinson's, and Huntington's diseases [102–105]. It has been shown that natively unfolded sequences aggregate and populate an intermediate oligomeric state rich in helix-helix associations. The intermediate state of globular proteins proceeds the partially unfolded native-like structures in the assembly process. Many protein structures in the globular state have helical conformation [106–109]. Myoglobin, a predominantly α-helical globular protein, not related to any known disease conditions, converts to amyloid-like fibrillar aggregates with cross-β structure at high pH and elevated temperature [110]. Above a critical concentration the natively folded soluble proteins may be metastable in nature and its corresponding Gibbs free energy may represent a local minimum in the energy profile. Amyloid fibrils are lower in energy (and thus more favorable) and may actually represent the global minimum [111, 112]. Amyloid states can populate different energy levels with new structural features and have polymorphism within amyloid species [113]. Proteins can also assemble into crystal lattices composed of native metastable conformations [114, 115]. In situ characterization of the conformational conversion between the native crystalline and cross-β ensembles can provide important atomic-level insights into the structural factors affecting the relative stability of the metastable and amyloid states and the nature of the transition state [11,116,117]. The inability of intrinsically disordered pathologically relevant sequences to form metastable crystalline assemblies has so far hindered

such deliberation. The different conditions required for in vitro fibril formation and crystallization of natively folded proteins, [102, 108, 110] in contrast to the constant physiological conditions under which amyloidogenesis progresses in vivo, [12, 116] also comprise a major obstacle.

Experimental results

Recently, we have demonstrated the ability of a short seven-residue sequence, SHR-FF, to self-assemble into crystalline supramolecular fibrillar structures [118]. To gain further insight into the atomistic features of the SHR-FF fibrillar assembly, we performed X-ray powder diffraction (PXRD) analysis of the lyophilized fiber assemblies. Furthermore, to eliminate the possibility of structural reorganization during drying, the wide-angle X-ray scattering (WAXS) spectra of the self-assembled nanofibers were also recorded in their original mother liquor without lyophilization. The PXRD and WAXS analyses revealed the same diffraction profiles, both distinctly different from the predicted PXRD pattern of the reported X-ray crystal structure [118]. The SHR-FF crystal was regrown under conditions native to fibril assemblies.

Single-crystal X-ray structural analysis revealed that the peptide adopted an amphiphilic helical conformation, with adjacent helical molecules interacting through π-stacking and hydrophobic interactions, as reported earlier [118]. These columnar helical dimeric associations propagated along the c-axis and were positioned perpendicular to the length of the crystal (along the a-axis), revealing distinct cross-α architecture, as determined by face indexing of the single crystal. This architecture is similar to a recently reported cross-α structure, though comprised of much shorter peptides [119,120]. The Fourier-transform infrared spectroscopy (FTIR) signal of the dried crystals at 1658 cm^{-1} also supported the helical conformation. Since a cross-α structure cannot account for the observed X-ray scattering profile, it was concluded that SHR-FF could adopt two distinct higher order self-assembled

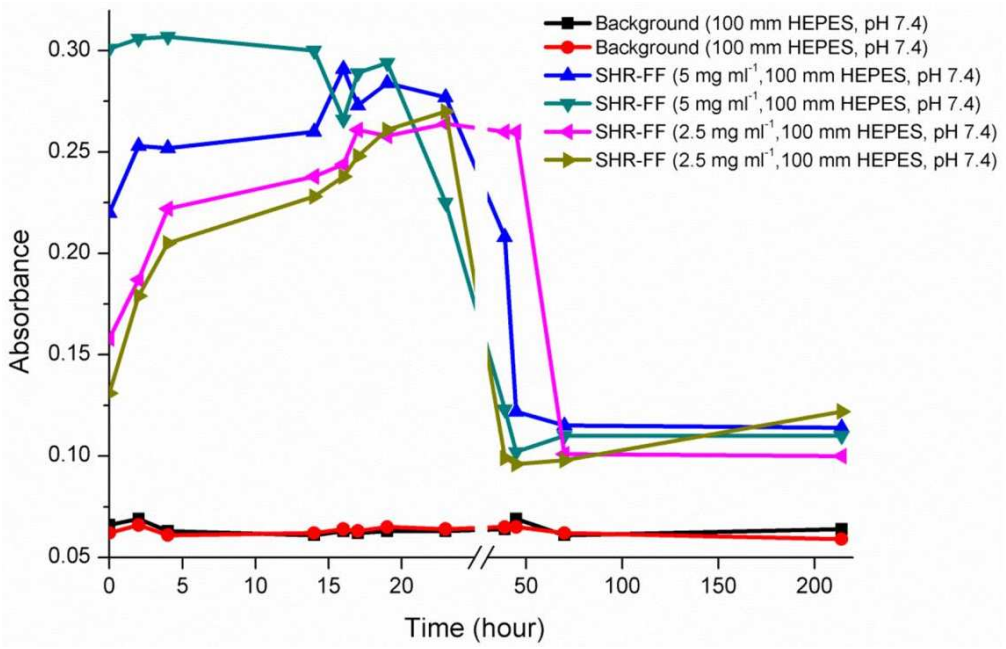

Figure 24: Analysis of the variation of SHR-FF monomer concentrations as the cross-α crystals converts to cross-β-fibrils. Two different plateaus regions provided the information about the equilibrium peptide concentrations in solution in presence of cross-α or cross-β-phases. These equilibrium concentrations [C] can be converted to the Gibbs free energy ΔG of each of the phases, through following chemical thermodynamics [11, 12]. $[C_{eq}] = exp(-\beta\Delta G)$ where, $\beta = (\mathrm{k}_B\ \mathrm{T})^{-1}$, T is the absolute temperature, k_B is the Boltzmann constant. The elongation free energies per residue of heptapeptide SHR-FF cross-β fibrils (2.5 kJ mol^{-1}) showed excellent correlation with the reported values for heptapeptide GNNQQNY from Sup35 sequence (2.0 kJ$\cdot\mathrm{mol}^{-1}$) and decapeptide TTR $(105-115)$ from Transthyretin (TTR) protein (2.12 kJ $\cdot$ mol^{-1}) [13].

states. Additional WAXS analysis established that the formation of a noncross-α fibrillar state does not depend on the cosolvent or buffer compositions.

The finding that SHR-FF can alternatively exist as cross-α or cross-β-like ensembles separated only by a thermal energy barrier could serve as a paradigm for delineation of assembly kinetics of two basic secondary structure modules. To understand the relationship between the two ensembles states, we prepared cross-α crystals at 4° C and measured their WAXS spectra at different temperatures over time. As shown in Figure 26a, the cross-α phases showed substantial stability at 37° C, but rapidly converted to cross-β-like structures and remained stable when heated to 50° C. The complete

conversion of cross-α crystal to cross-β fibrils confirmed that the former represents a metastable state, a generic feature of native polypeptide and protein assemblies. Further evidence for the metastable nature of a cross-α phase was obtained by measuring the equilibrium concentration of peptide monomers in solution, showing the cross-β-fibrils to be more stable than the native cross-α structures by 3.3 kJ mol^{-1} , as illustrated in the energy profile diagram (Figure 24 and Figure 26b).

Next, we analyzed the structural reorganization in real time by heating the SHR-FF helical ensembles, replicating the WAXS kinetic experimental conditions. At 37° C, all the crystals grew in size via addition of monomers to the crystal surfaces and maintained stability more than 12 h (Figure 26e). Upon increasing the temperature to 50° C, the crystals underwent dissolution by dissipating the monomers into the solution, whereas a subsection of the metastable structures transitioned into fibers in a spatially correlated region, as marked by a white circle in Figure 26e. This observation indicated that the nucleation of the cross-β oligomers occurred in the region with the highest peptide concentration and subsequently elongated, in accordance with a nucleated polymerization-like model. The kinetic profile delineated by real-time optical microscopy analysis correlated precisely with the WAXS kinetics (Figure 26a). The sharp transition in WAXS spectra during the heating process also supported the nucleated polymerization-like growth (inset, Figure 26a). In addition, we studied the kinetics of fibril formation starting from metastable cross-α crystals, and it afforded almost the same kinetic profile as if the aggregation was initiated from peptide monomers. Most importantly, the cross-α to cross-β transition did not require an increased temperature, but could proceed at constant conditions in a time-dependent manner, thus resembling the pathological amyloid aggregation. At

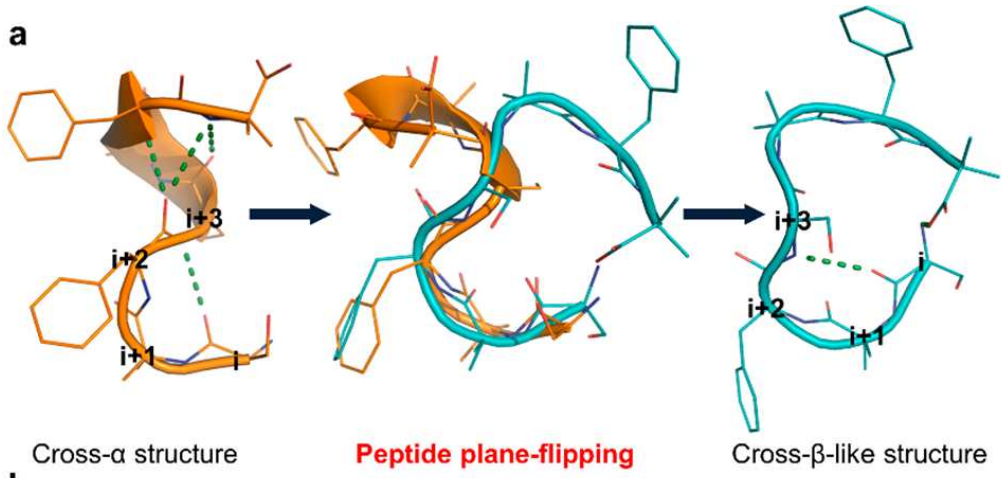

b

Residues	Cross-α crystals Type I turn		Cross-β-like fibrils Type II' turn	
	φ	ψ	φ	ψ
i	-	-	-	-
i+1	-51.3	-37.6	46.7	-130.7
i+2	-98.9	22.9	-96.1	5.2
i+3	-	-	-	-

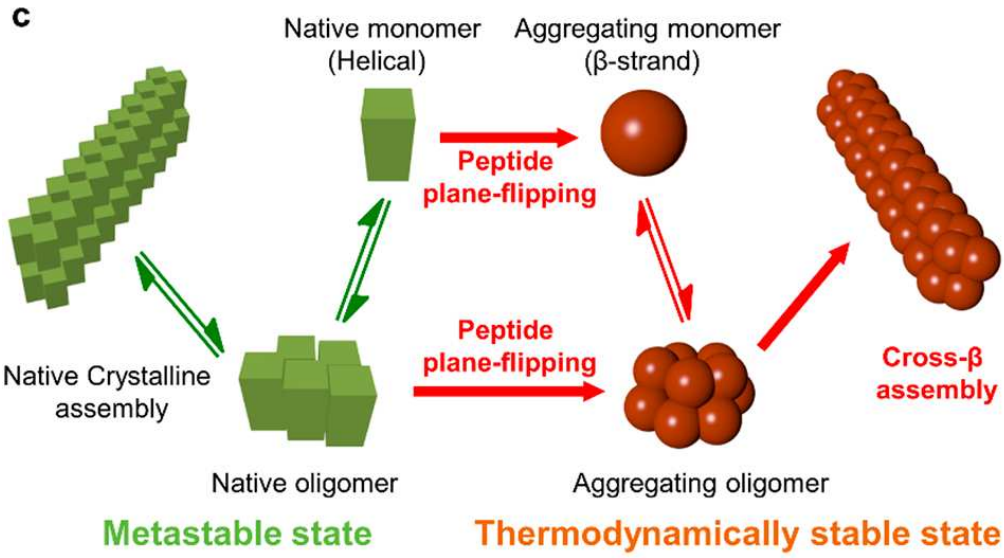

Figure 25: Atomistic details of cross-α to cross-β structural transition. (a) Active flipping of peptide planes from type I to type II$\prime$-β-turn. Residues associated with plane flip are labeled as i to $i+3$. (b) Changes in the dihedral angles of the key $i+1$ and $i+2$ residues during the transition from helical to β-sheet structure. (c) Schematic illustration of the possible transformation mechanism of native helical peptide conformation into cross-β fibrils by β-turn peptide plane-flipping.

a constant 30° C temperature, the conversion required $7-8$ days, as compared to several at 50° C. At 4° C, the time scale was further prolonged to $10-12$ months.

The transformation of native helical peptide structures to their cross-β assembly can be summarized as depicted in Figure 25c. In a solution, SHR-FF exists mainly in a helical conformation, as reported before [118] and validated by MD simulations. The facile conversion from a metastable crystalline to fibrils state was observed in the temperature ranges from 4 to 30° C and 50° C, reached with a decreasing time duration). The results indicate the formation of a metastable helical oligomer in the early stages of nucleation, which subsequently converts to the aggregation-prone oligomer by a peptide plane-flipping. In addition, the concentration-dependent kinetic assay provided further evidence for this process.

MD simulations: methods and results

MD simulations were performed with NAMD2.12 software [37]. The natural amino acids of the peptide and the solvent were described with the CHARMM36 protein force field [56,96,97]. The Aib amino acid was described with the generalized CHARMM force field [38,80], and the parameters were determined via the CGenFF ParamChem web interface [39, 40]. In all the simulations, the particle-mesh Ewald (PME) method [57] was used for evaluation of long-range Coulomb interactions. The time step was set to 1.0 fs, and long-range interactions were evaluated every 1 (van der Waals) and 2 (Coulombic) time steps. Then, the system was equilibrated by MD simulations without restraints on the single top layer of the peptides, while keeping the two bottom layers of peptides restrained as above. The simulations were performed in the NPT ensemble at a constant temperature of T = 277 K, constant pressure of P = 1 atm, and a Langevin constant of $\gamma_{Lang} = 1.00$ ps^{-1}. All simulations were performed in a 0.15 M NaCl aqueous solution to replicate the physiological conditions.

The solvated monomer system consisted of 10 peptides permanently separated from each other by harmonically constraining the alpha carbon on residue 4, so that the peptides would not translate and form clusters. The system was minimized for $5,000$steps and pre-equilibrated for 2 ns, before being further simulated. The alpha helical conformation is defined when RMSD of helical monomer is less than 3.10 Å and RMSD of single β-strand is greater than 2.50 Å. The non-alpha helical conformation is defined when RMSD of helical monomer is greater than 2.75 Å and RMSD of single β-strand is less than 2.50 Å. Both crystal systems were also initially minimized for $5,000$ steps. The crystalline systems were prepared in such a way that the water hydrogens were relaxed for 1 ns. Then, water molecules were relaxed for another 1 ns and the side groups $12 \times 12 \times 12$ peptides on desired facets were relaxed for an additional 1 ns, in separate runs for each facet, after which production runs were performed. The analyses of the simulated system were performed using VMD [59]. Images of simulated systems were also prepared with VMD.

In order to gain more insight into the relative stabilities of alpha helical and non-alpha helical peptide structures in free and crystalline forms, we modeled these systems by atomistic molecular dynamics (MD) simulations. First, we simulated 10 separated peptides solvated in a physiological solution at temperatures of 37, 50, and 70° C. Every 10 ps, we calculated RMSDs of all peptides best aligned with respect to the alpha helical and non-alpha helical forms, taken from their crystalline structures, and obtained a 2D histogram of their relative populations. Figure 26c shows the distribution of RMSDs for freely solvated peptides at 37° C; distributions for higher temperatures are shown in Figure 27. Each distribution has two main populations of peptide conformations for the helical (major) and non-helical (minor) conformations. As seen in Table VI and Figure 26c and Figure 27, as temperature increases, the population of helical conformation decreases and the non-helical increases. There is a dramatic change of 10% from 37 to 50° C, but only a slight change of 1% from 50

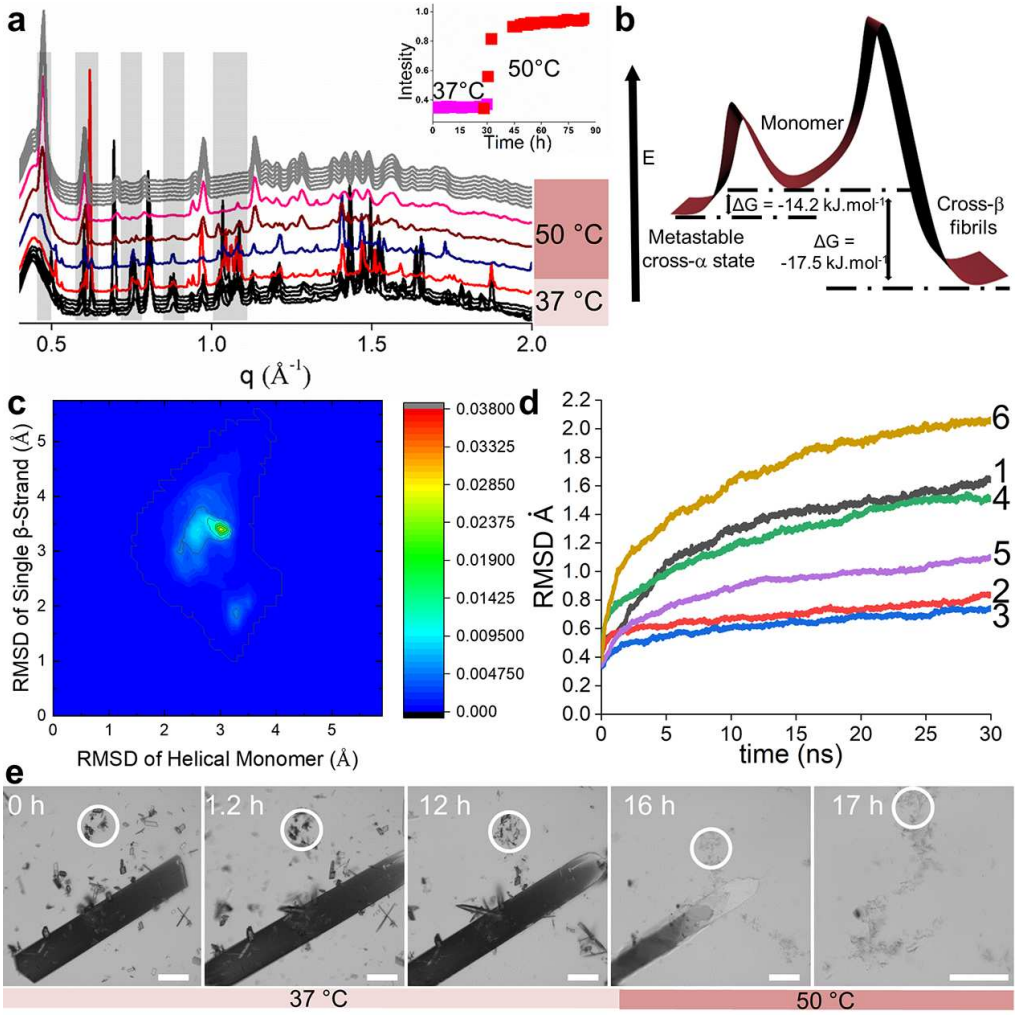

Figure 26: Kinetic studies of cross-α to cross-β-like structural conversion. (a) Real-time WAXS analysis of the conversion from the cross-α to cross-β fibrillar state. The cross-α crystals persisted at 37° C (black curves) and showed a sharp transition (colored curves) into the stable cross-β structure (gray curves) upon increasing the temperature to 50° C. Major differences in peaks are highlighted with a shaded bar. The data sets are vertically offset. Inset: Kinetic profile of fibrils assembly generated by plotting the peak intensity at 0.475 Å^{-1} versus time. The temperatures corresponding to different measurements are shaded with two different colors. (b) Schematic representation of the free energy profile of the metastable cross-α crystals and thermodynamically stable cross-β like fibrils. (c) A 2-D histogram of RMSDs for 10 solvated peptides (90 ns) evaluated with respect to their helical and β-strand-like conformations. The analysis was performed for $90,000$ snapshots of individual peptides. Density = (counts/$90,000$). (d) RMSDs of 100 peptides averaged for each crystal facet of two crystalline structures ($1-3$ represent cross-β facets and $4-6$ represent cross-helix facets, respectively). (e) Progressive images of the fibril formation (white circle) from the dissolution of metastable cross-α crystals on increasing the temperature from 37 to 50° C (scale bar, 100 μm).

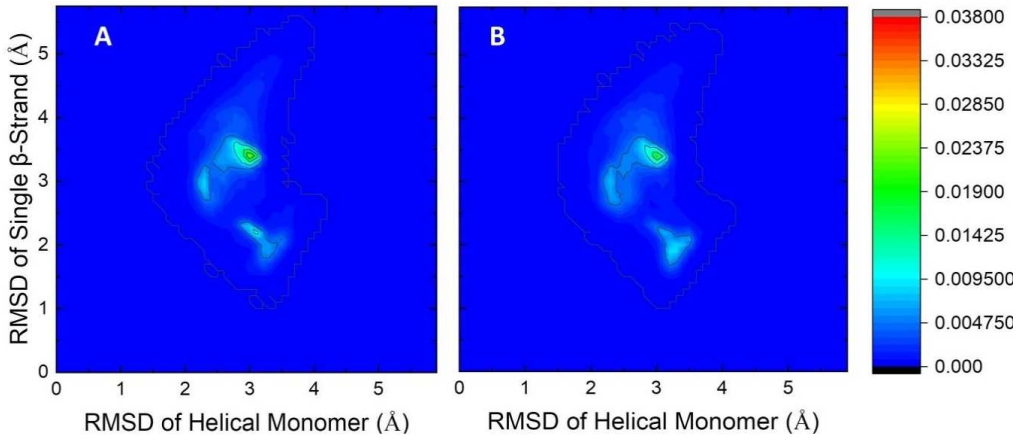

Figure 27: Atomistic molecular simulation of monomer. (A, B) Distribution of relative populations of RMSDs with respect to helical and non-helical conformations for 10 peptides (90 ns) at 50° C and 70° C, respectively. The analysis was performed on 90, 000 snapshots of individual peptides. Density = counts/90000.

to 70°C; $90 - 95\%$ of all peptides are always within these two regions. The obtained results reveal that freely solvated peptides are significantly more likely to assume conformations resembling the helical (crystal) form than the non-helical form. At higher temperatures there is a stronger presence of peptides in non-alpha helical form because it is entropically favored.

Finally, we simulated Cross-α and Cross-β crystallites with $12 \times 12 \times 12$ peptides. On each facet, we allowed the central 10×10 peptides to freely diffuse, while the remaining peptides in the crystal were frozen. We calculated RMSDs of each free peptide (best match) with respect to its initial conformation. Figure 26d shows the evolution of RMSDs averaged over the 100 respective peptides. Among the six observed RMSD dependencies, peptides on two non-helical and (partly) one helical facets largely preserve their initial conformations, revealing that in the crystalline form the Cross-β structure might be more stable than the Cross-α structure.

Figure 28 shows conformational changes of peptides in cross-α and cross-β crystals. In the cross-α crystal, only facet 2 has the RMSD below 1 Å, since its peptides undergo minimal conformational

changes in their backbones (Figure 28c). In facet 1 of the helical crystal, there is an arrangement of five bilayers (Figure 28a). The top, central, and bottom bilayers undergo little conformation backbone changes, whereas the remaining two bilayers undergo more significant changes. Facet 3 for the cross-α crystal has the highest RMSD values because most peptides undergo drastic backbone conformational changes (Figure 28e).

In the cross-β crystal, only facet 1 has RMSD values exceeding 1 Å. In this facet, slightly less than half of the peptides undergo significant conformational changes (Figure 28b). There are instances of groups peptides being completely displaced from their initial configuration, but these displacements are not reflected in RMSD calculations. Nevertheless, the displacements allow the peptides to undergo more conformational changes. In the remaining two facets (Figure 28d, f), the peptides translate significantly, perhaps due to a built in electric field in the crystal. However, this translation is relatively uniform and does not affect the backbone configurations, which remain relatively rigid throughout the simulation. Therefore, these facets have the lowest RMSD values.

Temperature (°C)	Relative Population of Alpha Helical Conformation (%)	Relative Population of Non-Alpha Helical Conformation (%)
37	78.5	11.7
50	69.2	21.3
70	68.2	22.3

TABLE VI. RELATIVE POPULATIONS IN ALPHA HELICAL AND NON-ALPHA HELICAL CONFORMATIONS AT DIFFERENT TEMPERATURES.

Conclusion

In summary, we have identified a minimal peptide module that, similar to many natural protein or peptide sequences, demonstrates dynamic transformation between native crystalline state and cross-β amyloidal state. This simple system recapitulated the complex amyloid aggregation pattern recognized in Alzheimer's, Parkinson's, and prion diseases.

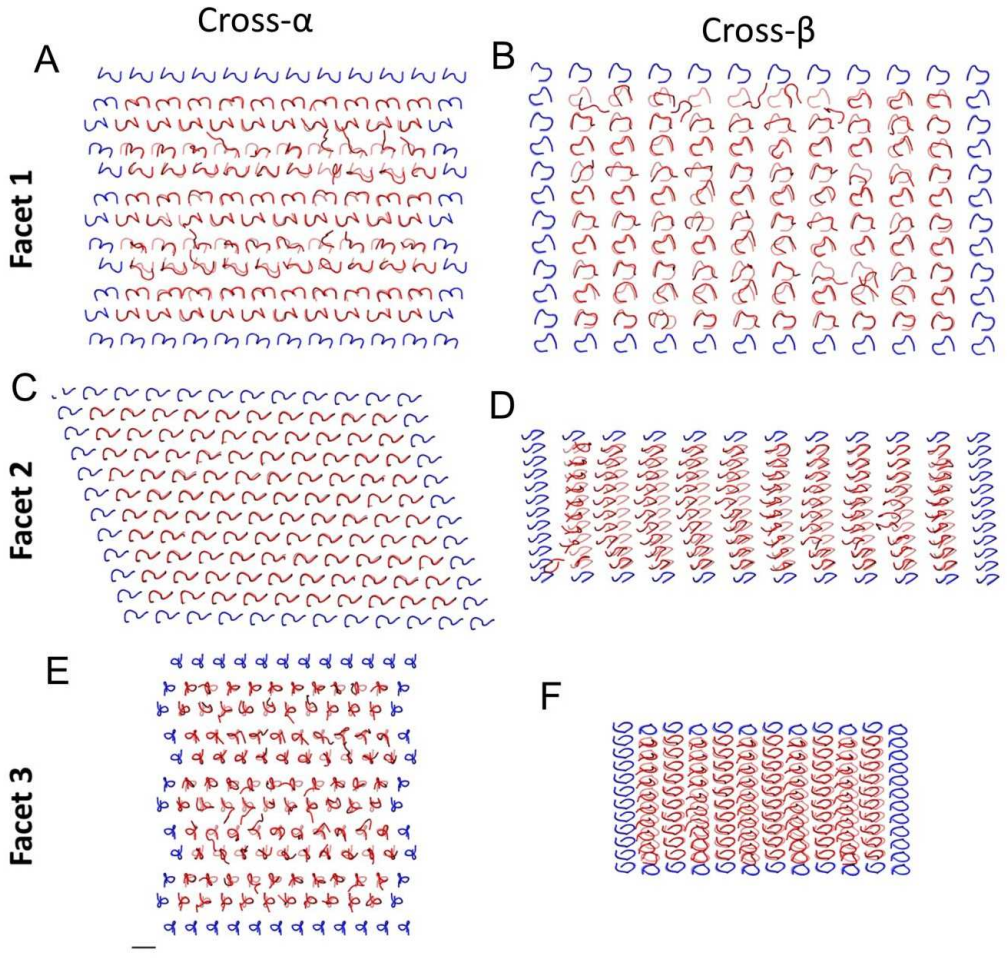

Figure 28: (a,c,e) Facets 1 after 18 ns of simulation, 2 after 17 ns of simulation, 3 after 17 ns of simulation of alpha helical peptide crystal respectively. (b,d,f) Facets 1 after 26 ns of simulation, 2 after 22 ns of simulation, 3 after 15 ns of simulation of non-alpha helical crystals respectively. Blue peptides are constrained during the simulation; transparent red represent initial configuration of peptide before diffusion; solid red represents peptides after equilibration. Separate MD runs were performed for each facet.

Furthermore, it allowed us to decipher, for the first time, the crucial role of the β-turn, the minimal regular secondary structural motif abundant in both native proteins and amyloid fibrils, as a transient intermediate in peptide aggregation. The energetically favorable transformation between β-turn conformations, permissible in the Ramachandran plot, can convert a native peptide backbone into an amyloidogenic sequence. The X-ray crystallographic coordinates for structures reported in

this study have been deposited in the Cambridge Crystallographic Data Centre (CCDC), under deposition number CCDC 1569244, and in the Protein Data Bank with PDB code 5VSG.

3.6 Anisotropic assembly of Metal Nanostructures onto an Asymmetric Peptide-Based Nanofibers

Introduction

Assemblies of one-dimensional (1D) architecture of metal nanoparticles have unique and collective properties [121–127]. 1D organization has many advanced applications ranging from the plasmonic waveguides to surface enhanced Raman spectroscopy to optical metamaterials to enhanced magnetic effect [128–134]. These applications originate from the unparalleled physical properties of the 1D chain-like arrangements and inspire the development of diverse fabrication strategies.

Peptide self-assembly depends on the interplay between peptide building blocks directed by various non-covalent interactions to afford dynamic ensembles such as nanofibers and nanotubes [121, 135–138]. Although the dynamic nature of assembled structures exhibit short and/or long range ordering, they have low crystallinity. Consequently, the final nanostructures have isotropic or symmetrical orientation of the building blocks [139,140]. Thus, the peptide nanofibers or nanotubes templated synthesis of 1D nanoparticle architecture results in the complete isotropic covering of the whole surface or the formation of quasi 1D array by collinear symmetric deposition of more than one 1D chain [121,141–145]. Crystalline peptide nanostructures with asymmetric surfaces along the long 1D axis originating either from the differences in the electrostatic charges or amino acid side-chain functionality have great potential to template the 1D nanoparticles arrangement. The supramolecular assembly of asymmetric amphiphiles leads to the formation of nanoribbons with asymmetric faces as evidence by the preferential but sparse attachment of gold nanoparticles (AuNPs) on only one face [146]. Crystalline peptide and amino acid based microstructures have been shown to possess facet-dependent asymmetric surfaces amenable for asymmetric decoration of AuNPs as clus-

ter [147, 148]. The bottom-up formation of asymmetric self-assembled peptide nanostructure having the capability of templating 1D chain-like organization of metal nanoparticles is yet to be realized.

We report the 1D chain-like assemblies of metal nanoparticles directed by asymmetric surface presented by crystalline amyloid-like peptide nanofibers. Microscopy studies confirm that the nanoparticles chains occupy only a fraction of the accessible nanofiber surface and this unique attribute also leads to the formation of 1D chain with single nanoparticle width, a value which is much smaller than the nanofibers diameters. These non-selective interactions allows us to align nanoparticles with diverse capping agents without any post-synthetic functionalization as well as incorporate different types nanoparticles (such as gold and magnetic) and shapes (such as spherical and rod), thus enabling one of the most versatile peptide nanofiber templates.

Experimental results

Recently, we demonstrated the self-assemble of short seven-residue sequence SHR-FF to nanofibers [5, 118]. Microcrystal X-ray diffraction of SHR-FF revealed the cross-β arrangement of the peptide in the nanofibers confirming its amyloid-like characteristic [5]. As reported before, contrary to the extended conformation of the peptides in amyloid fibers composed of coded amino acids, SHR-FF adopted loop-like structure in which the C-terminal carboxyl group and N-terminal amine formed intermolecular H-bonding. This pseudo cyclic conformation of SHR-FF can be attributed to the presence of the 2-aminoisobutyric acid, a natural non coded amino acids, that prefer non β-sheet dihedral angles. An interesting feature of SHR-FF conformation as observed in crystal structure is that although the peptide contains two polar serine residues, only the side chain of the residue located at the N-terminus (Ser1) was protruding outward of the cyclic-like conformation (Figure 29a). This phenomenon along with the outward exposure of only hydrophobic phenylalanine and Aib side chains along the periphery resulted in the asymmetric display of electrostatic charged surface in the

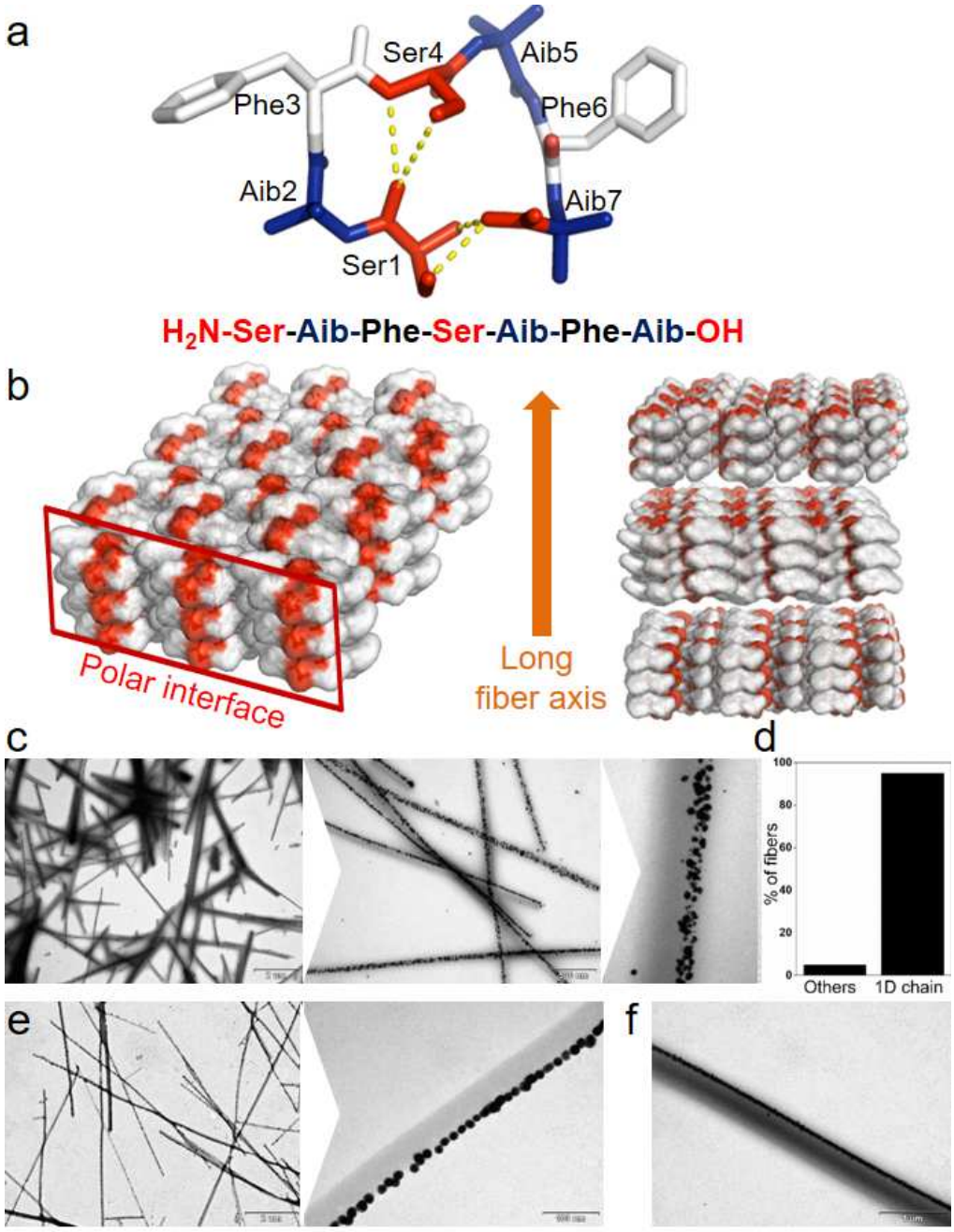

Figure 29: SHR-FF peptide assembly and asymmetric nanoparticles deposition. (a) Sequence and crystal structure of SHR-FF. The polar segments are depicted in red, whereas the Aib residues are displayed as blue. (b) Higher order packing of SHR-FF reveals asymmetric surface along the long axis of the fiber. (c) In situ synthesis of AuNPs leads to the asymmetric linear 1D chain formation. The nanoparticles forms nearly continuous array and maintained excellent linearity. (d) The 1D chains have very high yields ($\approx 95\%$) compared to other types fibers population (empty fibers or complete AuNPs coverage). (e) Decoration of preformed AuNPs (citrate stabilized) in SHR-FF fiber template. The representative zoomed image depict the formation of 1D chain having single nanoparticle width. (f) Decoration of preformed AuNPs (lipoic acid stabilized) in SHR-FF fiber template.

SHR-FF monomer. Most importantly, the asymmetry in the SHR-FF conformation at the monomer level was amplified in the higher-order packing and the fiber displayed charged interface along the long axis due to Ser1 and the free terminals (Figure 29b). To the best of our knowledge, except the peptide amphiphiles designed by Stupp and coworker, asymmetry along the long axis of the fibers was never realized. As shown in Figure 29b, the fibers presented hydrophobic interface along three different facets and polar interface in only one facet, confirming that the majority of the fiber circumference are hydrophobic in nature with a small stretch of charged domain run along the fibers length. The extreme ends of the fibers also harbor polar surface owing to the presence of the Ser3 side chain and amide bonds.

MD simulations: methods and results

MD simulations were performed with NAMD2.12 software [37]. The natural amino acids of the peptide and the solvent were described with the CHARMM36 protein force field [56,96,97]. The Aib amino acid was described with the generalized CHARMM force field [38,80], and the parameters were determined via the CGenFF ParamChem web interface [39, 40]. In all the simulations, the particle-mesh Ewald (PME) method [57] was used for evaluation of long-range Coulomb interactions. The time step was set to 1.0 fs, and long-range interactions were evaluated every 1 (van der Waals) and 2 (Coulombic) time steps. The simulations for completely solvated crystals were performed in the NPT ensemble and the broad crystal was performed at NAPT ensemble. The area for NAPT ensemble was taken from unit cell parameters of the crystal. The simulations had temperature T = 310 K, constant pressure of P = 1 atm, and a Langevin constant of $\gamma_{Lang} = 1.00$ ps^{-1}. All NP simulations were performed in with a gold NP diameter was 7 nm and had citrate ligands randomly distributed with surface density 1.69 ligands/nm^2. The NR had a diameter of 4 nm and length of 10 nm and was coated with the same surface density of citrate ions as the NP. Sodium counter ions were placed to

balance charge of the NP or NR. Systems were simulated in 0.1 M phosphate buffer solution of pH 7.4 determined by the ratio of $H_2PO_4^-$ and HPO_4^{2-} ions to screen image peptide crystals. Additional simulations were also performed in the absence of buffer.

The systems were first minimized for $5,000$ steps. Then, they were heated to the desired temperature, at 5 steps/K for $2,000$ steps, where they were equilibrated. In the first simulation production runs were taken even when the NP was attracted to the free counterions in the solution more strongly than the crystal. In all other simulations, we waited for enough counterions to be attracted to the NP and then we forced the NP to the crystal surface before we took production runs.

In order to understand better the experimentally observed coupling of charged NPs with SHR-FF fibers, we studied the systems by atomistic molecular dynamics (MD) simulations. Figure 30a shows a small isolated crystallite formed by SHR-FF with a gold nanoparticle (NP) hovering above it in aqueous solution. During the simulations, the neutral but highly polar $6,912$ peptides forming the crystal were partly stabilized from solvation by fixing the positions of heavy atoms. The AuNP (7 nm in diameter) coated with negatively charged citrate ligands (a surface density of 1.69 ligands/nm^2, NP net charge of -780 e) was placed above the crystallite. Sodium counterions balancing the negative NP charge and 0.1 M phosphate buffer at pH 7.4 were added to the aqueous solution.

The dynamics of the negatively charged NP was largely driven by an electric field exerted by the non-centrosymmetric peptide crystal. The electric field is generated by electric dipole moments of peptides arranged in a parallel manner in the crystal. Figure 30 b-d reveals the electric field obtained for selected cross-sections through the crystal by VMD [59]. The potential at the top (bottom) left crystal corner has a highly positive (negative) value, thus attracting the negatively charged NP. In 5 ns simulations, the NP and the negative regions of the crystal became covered by adsorbed positive counterions. The partly screened electric field of the crystallite eventually attracted NP toward one of

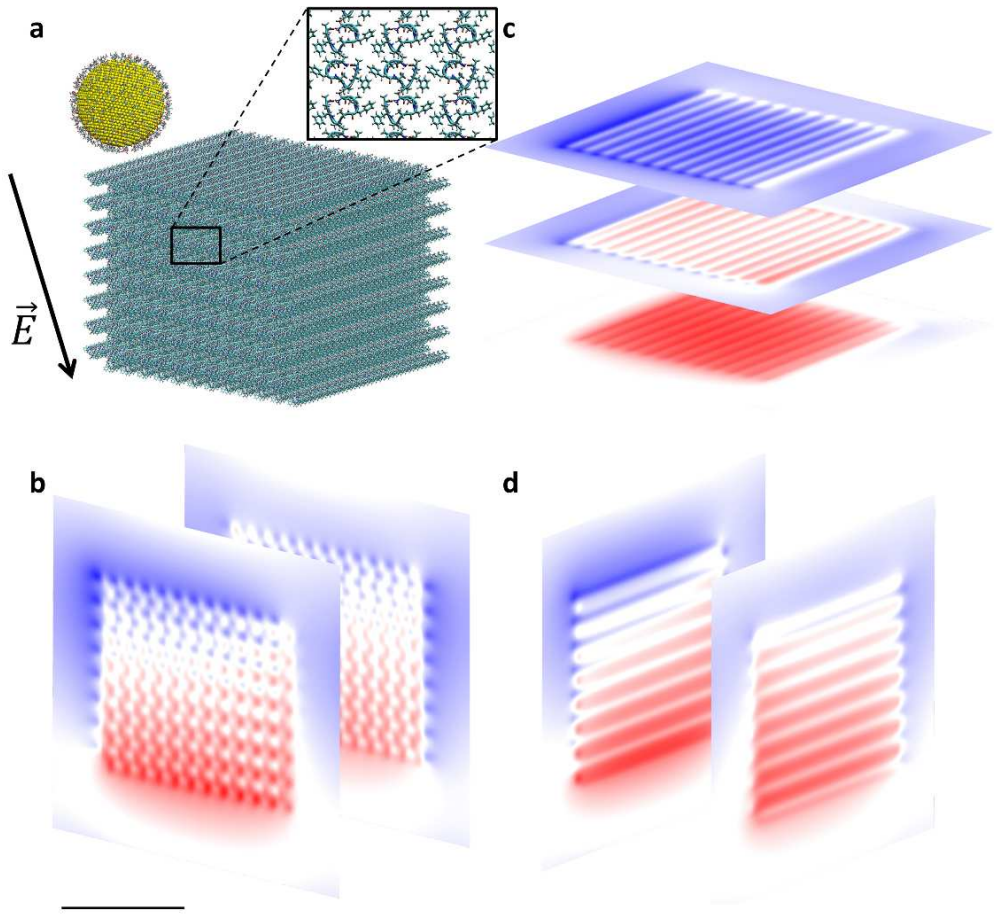

Figure 30: (a) SHR-FF crystal with a citrate ligands-covered AuNP stabilized above it after 26 ns (details of crystal shown); approximate direction of electric field exerted by the crystal. (b-d) Slices through the crystal revealing values of electrostatic potential. Scale bar is 10 nm.

its top corner with the most positive potential (indicated by the darkest shade of blue in Figure 30b-d), where the NP pivoted ≈ 7.4 Å above the surface (Figure 30a). Its average binding energy to the crystal normalized with respect to number of peptides was -2.2 kcal/mol. These results support the experimental observations, showing that the NPs coalesce along the crystal edges.

Next, we simulated the same crystal with periodic boundary conditions applied to model an infinite crystal surface. Since the electric field above the surface became uniform (Figure 31 b-d), the interaction energy between NP and the crystal only depends on their mutual separation. Therefore,

once NP got close to the crystal surface, it randomly hovered within $4-17$ Å above it (Figure 31a). Its average binding energy to the crystal normalized with respect to number of peptides was -5.9 kcal/mol. As shown in Figure 30e, NP was attracted only to one side of the infinite crystal.

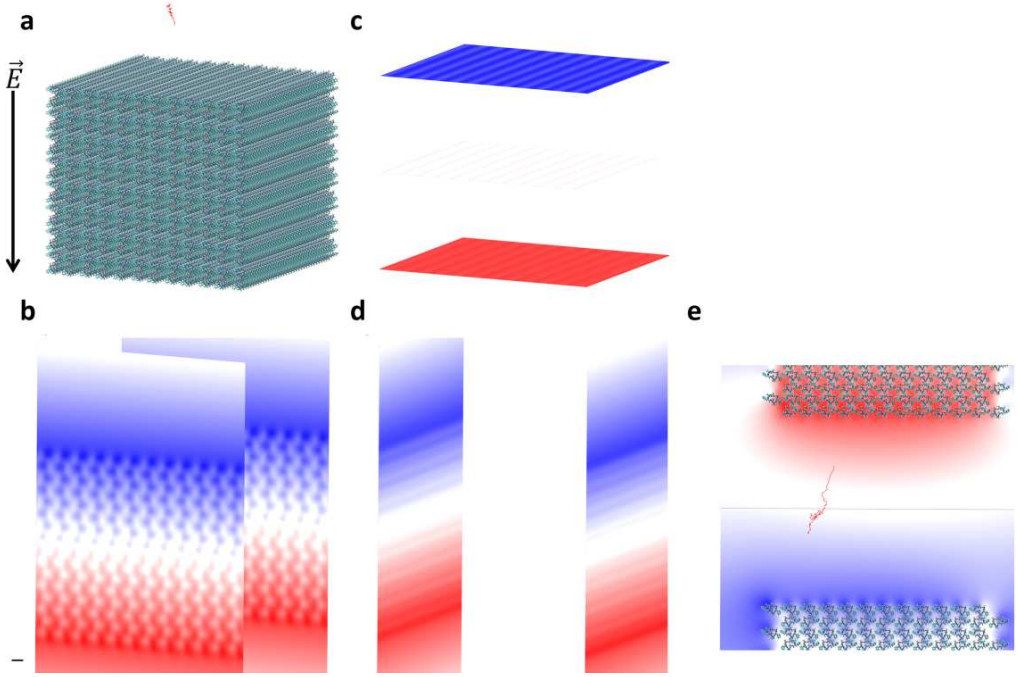

Figure 31: (a) 8 ns trajectory of center of mass of NP along crystal extended by PBC and electric field exerted by crystal; b) electric field slices along the aaxis c) electric field slices along the b axis; and d) electric field slices along the c axis. Scale bar represents 1nm. e) NP trajectory (12 ns), when NP is initially placed on the repulsive side and then diffuses to the attractive side of the crystal.

The detail insights about the nanoparticle-fiber interactions and its non-specific nature indicates that SHR-FF asymmetric template can be employed beyond AuNPs or spherical shapes. To explore this, we selected magnetic nanoparticles (MagNPs) owing to its multifaceted applications [131, 133]. Following similar protocol, bare preformed MagNPs having negative surface charge were mixed with SHR-FF nanofibers. The TEM images revealed the formation of 1D nanochain reminiscence of AuNPs chain probing the versatility of the template (Figure 32a). It also demonstrated partial alignment of SHR-FF nanofibers coated with 1D MagNPs implying enhance magnetic properties. The latter may arises from the alignment of magnetic dipoles along the chain as this ensure energy

minimize association of magnetic nanoparticles. The enhanced collective magnetic effect was also demonstrated by comparing the effects of external magnet towards the dispersed nanoparticles and 1D chain in solution separately. As shown in Figure 32b, 1D chains were strongly pulled towards the magnet whereas isolated nanoparticles remained completely dispersed despite the higher concentration of nanoparticles in the latter. This study clearly emphasize that the SHR-FF templated magnetic chain can be advantageous for magnetic separation in low magnetic field. We have also try to ascertain the shape dependence on the templating ability of SHR-FF fibers by utilizing gold nanorods (AuNRs). Initially, we simulated the orientation of the AuNRs onto SHR-FF crystals (Figure 32c). A gold nanorod (NR) with a diameter of 4 nm, a length of 10 nm and the same density of citrate ligands as the NP was placed above the attractive side of the small peptide crystal. As before, the nanoparticles diffused to the edge with the highest positive potential. The NR wobbled ≈ 18.4 Å above the attractive surface (Figure 32b). The interaction energy of NR to a crystal normalized with respect to number of peptides was about -2.9 kcal/mol. Upon adding AuNRs in solution containing fibers and subsequent TEM imaging demonstrated end-to-end arrangement of nanorods validating the theoretical prediction (Figure 32d).

Conclusion

We have developed a novel self-assembling peptide template that allows the formation of linear 1D nanoparticle chains with high fidelity. The linearity of the 1D chains was attributed to the crystallinity of the nanofibers and asymmetric display of polar surface along the long axis of fibers. This asymmetric nature further facilitated the assembly of single nanoparticle width 1D chains in which the in fibrillar template has much larger total surface area than the nanoparticle sizes, a feature not reported before. The rigid linear chain like organization of nanoparticles demonstrated

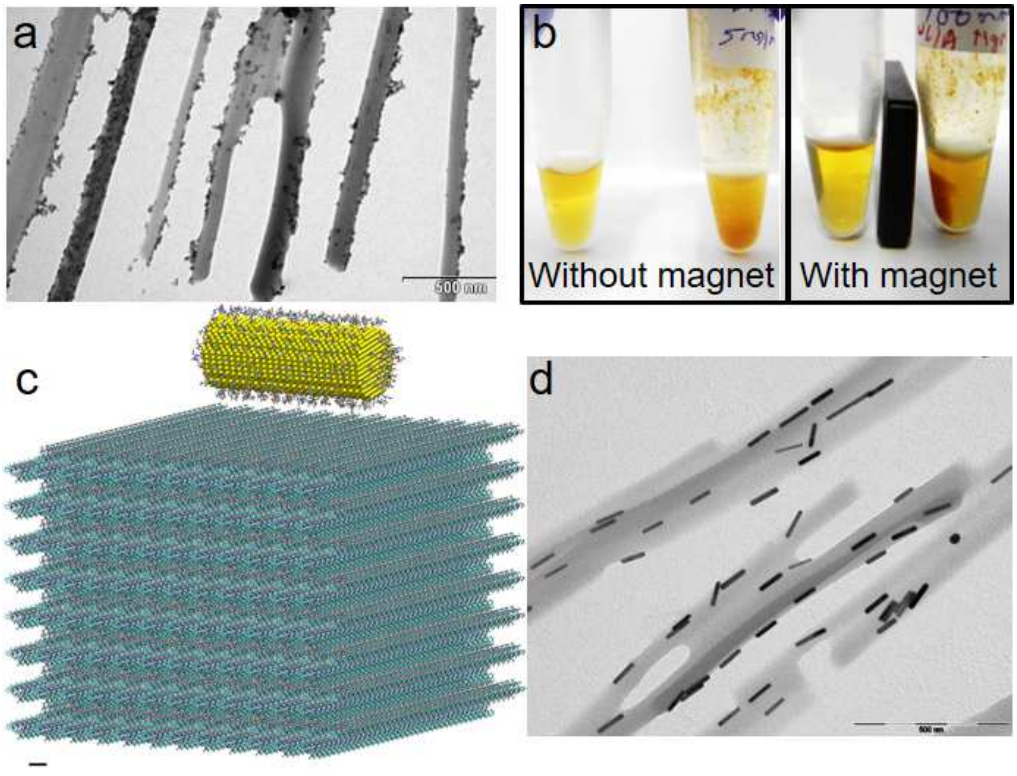

Figure 32: Vestality of SHR-FF fibrillar template. (a) Linear asymmetric 1D chain-like assembly of magnetic nanoparticles. (b) Comparison of cumulative magnetic moments of 1D chain and disperse nanoparticles in the absence or presence of magnetic field, respectively. (c) Gold nanorod (AuNR) on SHR-FF crystal after 11 ns of simulation; Scale bar present 1 nm. (d) Edge-to-edge assembly of AuNRs in peptide template.

in this study will be highly beneficial for the construction of ordered 2D array [149]. Moreover, detail molecular dynamic simulation confirm the non-specific electrostatic nature of interactions and paved the way for the 1D chain-like assembly of nanostructures with diverse features such as magnetic nanoparticles and gold nanorods. It can be envisioned that the control over the fiber diameters, an elusive concept in peptide self-assembly, can be harnessed to afford highly homogeneous 1D chains comparable to lithography and DNA nanotechnology based approaches but with tremendous cost effectiveness. The SHR-FF self-assembly mechanism, established at atomic resolution, may provide valuable impetus in controlling the fiber diameters [5]. Finally, the incorporation of Aib in

β-sheet based peptide design have the potential to afford a new paradigm in fibrillar assembly with asymmetric surface.

3.7 Electrical Conductivity, Selective Adhesion, and Biocompatibility in Bacteria-Inspired Peptide-Metal Self-Supporting Nanocomposites

Adapted from Ref. [6] (*Adv. Mater. 2019*, 31 DOI:10.1002/adma.201807285) with permissions from John Wiley and Sons Publishing Groups.

Introduction

Bacterial type IV pili (T4P) are an abundant class of supramolecular nanofibers composed mainly of pilin protein monomers [150]. *Geobacter sulfurreducens* (GS) are metal reducing bacteria, which participate T4P in anaerobic respiration. They facilitate physical contact with metallic ions and subsequent electron transfer to extracellular metal species, such as Fe(III)-oxide-containing minerals [151] and U ions [152]. The molecular under-pinnings of this interaction are unknown, as is the exact structure of the GS T4P [153]. Evidence suggests that the physical contact is mediated by the evolutionary variable polar C-terminal region of the GS pilin monomer [154]. The C-terminal region of homologous pilins is solvent-exposed to interact with the molecular environment, whereas the N-terminal region is associated with pilin in vivo assembly and constitutes the hydrophobic core of the assembled pilus [155, 156].

We envision their biosynthetic peptide mimetics as a useful class of bioinspired materials [157], deriving from the unique biological functionality of GS T4P. We reported the self-assembly of designed 20-mer peptide building blocks into T4P-like nanofibers [158]. The C-terminal segment of a 20-mer peptide adopts a native-like helical conformation and is nonessential for self-assembly. Its N-terminal segment presents a divergent β-type conformation and drives the self-assembly process [158]. The 20-mer T4P-like nanofibers have been studied from the structural aspect, their functionality has not been explored. We hypothesized that an analogous interaction would occur in the case of the T4P-like peptide nanofibers, due to the inherent propensity of native GS T4P to interact with metal oxide

particles and metal ions. A variety of self-assembled protein [159–172] or peptide [138, 173–178] filaments have been decorated by metals or metal oxides, and in some cases the decorated filaments were successfully utilized for specific applications [166–172]. Interactions between proteinaceous filaments and metallic species were not directly inspired by a native biological system. Moreover, substantial decoration at the single nanofilament level was typically achieved in previous studies following multistep processes or by using extrinsic additives. We show that the T4P-like peptide nanofibers efficiently bind metal and non-metal oxide particles by simple coincubation. The nanofibers also reduce ionic Au in a single-step, an additive-free process that leads to their exceptionally dense decoration by gold nanoparticles (AuNPs).

Experimental results

Inspired by the ability of GS to reduce U ions via its T4P, we explored the interaction of the 20-mer peptide nanofibers with metal ions. Native GS T4P are associated with a c-type cytochrome [179], implicated as the terminal reductase of a variety of metallic substrates owing to a low midpoint redox potential [180]. In the absence of cytochrome, we limited our investigation to the interaction with Au ions, which can be reduced by peptides [181], do not precipitate or become reduced in phosphate buffer [182] that is required for the 20-mer self-assembly, and yield application-relevant reduced species [183]. $HAuCl_4$ was chosen as the ionic Au source due to the expected attraction of the $AuCl_4^-$ ion to the positively charged nanofibers.

Mechanistic insights into the process of AuNP decoration, i.e., ionic Au reduction and binding of the formed AuNPs, were obtained by combining analytical and spectroscopic methods, and molecular dynamics (MD) simulations. Next, the binding of AuNPs to the nanofibers was studied by spectroscopic methods and MD simulations. Using D NMR spectroscopy, we determined the solution structure of the 20-mer peptide in water (Figure 33d), which was overall consistent with its previous

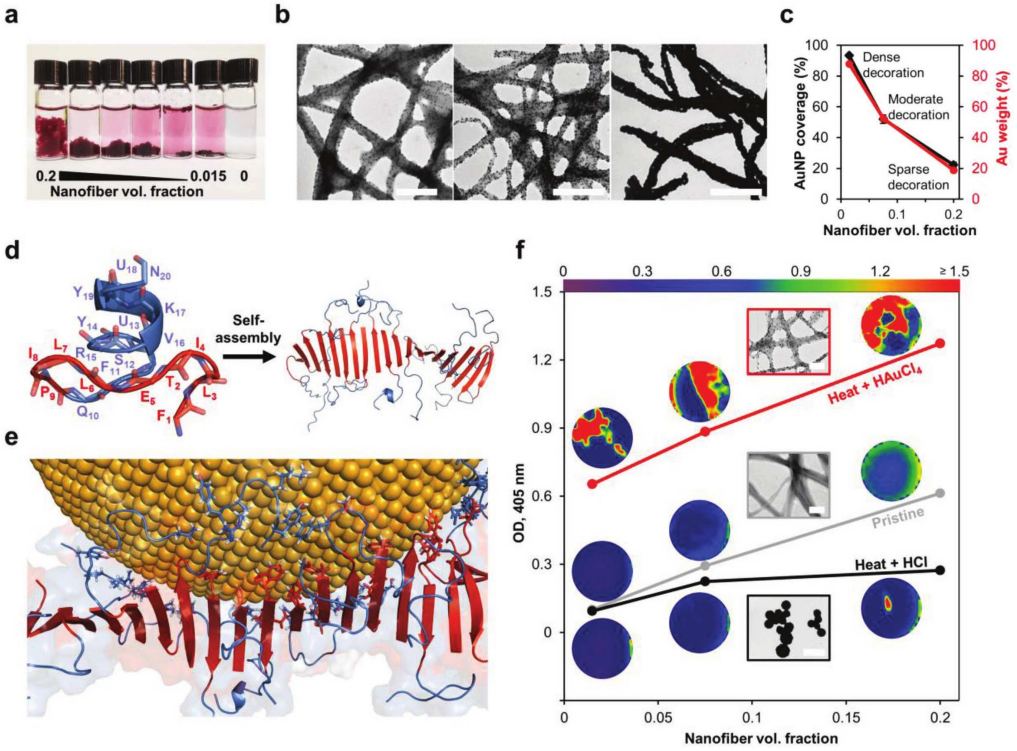

Figure 33: Formation of peptide-AuNPs nanocomposite. a) Photograph of peptide nanofibers and $HAuCl_4$ mixtures incubated at 90°C. Rightmost vial is a similarly prepared control without peptide nanofibers. b) TEM images of AuNP-decorated nanofibers from 0.2, 0.075, and 0.015 volume fraction conditions (from left to right). Scale bars, 500 nm. c) TEM image analysis of single decorated nanofibers for estimating their coverage by AuNPs. Data represent mean ± standard error of the mean (n = 30 nanofibers per condition), for some data points the error bars are smaller than the symbol size. Au weight fraction, as determined by TGA, is shown for comparison. d) Lowest target function NMR structure of the 20-mer peptide, and a simplistic nanofiber model by MD simulation after 80 ns. NMR structure shows the peptide backbone as cartoon and sticks. Simulated model includes 20 peptide monomers, the backbones of which are shown as cartoon. P9 and the residues N-terminal to it are shown in red, residues C-terminal to P9 are shown in light blue. U denotes α-aminoisobutyric acid. e) Binding of a AuNP (10 nm diameter) to the nanofiber as modeled by MD simulation after 9 ns. All backbones are shown as cartoon and surface. Side chains of residues that strongly interact with the AuNP surface ($d \leq 4.5$ Å) are shown as sticks. Color coding corresponds to the previous panel. f) Thermal stabilization of the peptide nanofibers by $HAuCl_4$ as evident by turbidometric area mapping. Plotted values are averages of turbidometric area maps at 405 nm. Color scale of the maps is defined in the top legend. Insets are corresponding TEM images from the 0.2 volume fraction condition. Frame colors of insets correspond to line colors. Scale bars: 200 nm for red and gray frames, 5μm for black frame.

reductionist investigation [158]. This structure was utilized for constructing a simplistic nanofiber model in buffer, where residues N-terminal to the central proline residue (P9) are organized as a single supramolecular antiparallel β-sheet (Figure 33d, red), whereas the residues C-terminal to P9 flank the sheet and present partial helicity and high conformational flexibility (Figure 33d, light blue). AuNP binding was then investigated by simulating a single AuNP, modeled by a polarizable force field, in the proximity of the nanofiber for 9 ns. As shown in Figure 33e, multiple C-terminal regions interact with the AuNP, where mainly amine- or hydroxyl-bearing and aromatic residues form close contact with its surface (d $\leq$ 4.5 Å), in line with their strong affinity to Au [178, 181]. Considerably fewer N-terminal residues interacted thus with the AuNP surface, and the β-sheet hydrogen bonding network remained intact. These observations were supported experimentally by Fourier transform infrared (FTIR) spectroscopy. C-terminal hook-like stretches provide multiple anchoring points for binding the AuNP strongly to the nanofiber, the structure of which remains essentially unchanged in this process. Congruent with the latter conclusion is the observation that the decoration process structurally stabilizes the nanofibers. Turbidometric area mapping (Figure 33f) showed that nanofiber dispersions subjected to the decoration procedure present increased OD at 405 nm compared to dispersions of pristine nanofibers. In contrast, when $HAuCl_4$ is substituted in this procedure with HCl at an equivalent pH, the measured OD is lower than that of pristine nanofibers. These measurements suggest that pristine nanofibers may be impaired following incubation at 90°C, unless supplemented by $HAuCl_4$. TEM imaging confirmed this assertion, showing that following incubation at 90°C, $HAuCl_4$ -treated nanofibers become decorated with AuNPs as described above, whereas HCl-treated nanofibers transform into coalescing spheres (Figure 33f). The interaction with $HAuCl_4$ enhances the thermal stability of the nanofibers and prevents phase transition of the peptide.

MD simulations: methods and results

MD simulations were performed to study the interaction between 20-mer peptide monomers, construct a simplistic naofiber model, and examine its interaction with AuNPs. All simulations were performed in 10 mM phosphate buffer solution with the ratio of $H_2PO_4^-$ and HPO_4^{2-} to maintain pH = 7.4. In the nanofiber model simulation, potassium ions were omitted so as maintain the system neutral. In all other simulations, additional $H_2PO_4^-$ and HPO_4^{2-} ions were added as counterions for the peptides, maintaining the pH of 7.4. Trajectories were calculated using NAMD2 [37] package and the CHARMM [38–40,80] force field. Langevin dynamics was used in NPT ensemble with a damping coefficient of 1 ps^{-1}, temperature of 310 K, and pressure of 1 atm. In the simulations without AuNP, time step was 2 fs; in the simulation of AuNP binding to the nanofiber, the time step was 0.25 fs. Particle Mesh Ewald [57] was used with grid spacing of 1.0. The non-bonded interactions used the SHAKE switching algorithm with the switch on/off distance at 10/12 Å. Non-bonded pairs lists were 13.5 Å, with the list updated every 20 steps; $1-4$ non-bonded interactions were not scaled. There were $5,000$ steps of minimization followed by $1,000,000$ steps of equilibration, after which the simulations were performed. The AuNP was modeled in the same manner as in Colangelo et al. [184], with parameters from Wright et al. [185] and Lori et al. [186]

Nanofiber model construction

A simplistic nanofiber model was constructed based on MD simulations and spectroscopic data. First, 40 copies of the intact NMR monomer structure, as given in Figure 33d, were allowed to freely interact in an MD simulation in potassium phosphate buffer (the assembly medium of the nanofibers) for 208 ns. The simulation showed that residues N-terminal to the central proline (P9) are capable of interacting to form a stable two-stranded supramolecular antiparallel β-sheet (Figure 34). This

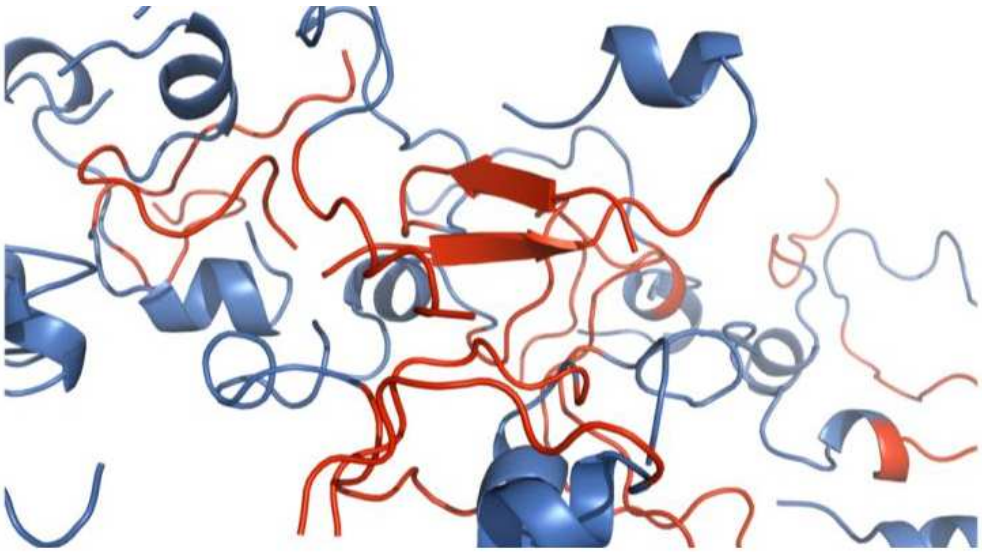

Figure 34: Formation of a two-stranded supramolecular antiparallel β-sheet by 20-mer peptide monomers in an MD simulation. Forty peptide monomers were allowed to freely interact for 208 ns in the simulation. Peptide backbones are shown as cartoon, P9 and the residues N-terminal to it are shown in red and residues C-terminal to P9 are shown in light blue.

result is consisted with the previous investigation of the 20-mer peptide and its shorter fragments, which showed that residues N-terminal to P9 drive the nanofiber self-assembly process by forming a supramolecular β-sheet [158]. Given the reported nanofiber self-assembly kinetics [158], this interaction is presumed to propagate well beyond the timeframe of the simulation, and thus further drive the nanofiber self-assembly process. The existence of a supramolecular β-sheet of antiparallel nature in the assembled state is supported by previous deconvolution of the amide I band in the FTIR spectrum of the nanofibers [158], as well as by current BestSel analysis [187] of their reported circular dichroism spectrum [158], which suggests a right-twisted antiparallel β-sheet conformation. Based on these data, we constructed a simplistic nanofiber model by MD simulation. In this model, the residues N-terminal to P9 were organized as a single supramolecular antiparallel β-sheet, whereas the residues C-terminal to P9 were embedded from the monomeric NMR structure to flank the sheet. We observed that the modeled nanofiber had remained stable throughout the simulation (80 ns) and

that the C-terminal residues were partially helical but overall conformationally flexible (Figure 33d). During the simulation the modeled nanofiber became right-twisted, in line with the above mentioned BestSel analysis. Yet, the magnitude of the twist appears to be considerable and such property of the nanofiber was not observed by high-resolution microscopy [158]. We propose that lamination of β-sheets in the nanofibers [188] could reduce the twisting and account for this discrepancy. Thus, we consider the constructed model as representing an exposed interfacial layer of the nanofiber, available for AuNPs decoration.

Conclusion

In summary, the current work presents for the first time the multifunctionality of the recently reported T4P-like peptide nanofibers. The bioinspired interaction of these designed self-assembled nanostructures with metal oxides or ions resulted in highly diverse nanocomposite materials. The interaction with Au ions is especially remarkable considering the exceptional degree of decoration by AuNPs, the simplicity of its formation, and the lack of need to employ external additives such as reducing agents. The preferential formation of isotropic AuNPs over large anisotropic Au crystals is worth noting, as the latter were reported to form in recent studies utilizing amyloid nanofibers for elemental Au synthesis [170–172, 189]. This dissimilarity may be explained by one or more crystallographic and redox chemistry mechanisms [190], which are likely instigated by differences in sequence and localization of amino acids along the nanofiber. Such differences could facilitate binding of the nanofibers to a specific crystallographic face of Au nuclei and lead to their anisotropic growth, or alternatively enable nonspecific binding that results in isotropic growth and nanoparticle formation. In this context, we note that strongly reducing and binding cysteine residues as well as strongly complexing or reducing histidine or tryptophan residues [181] are absent in the T4P-like nanofibers but were present in amyloid nanofibers in the aforementioned studies. Moreover,

the effect of amino acid identity and localization may be modulated by conformational flexibility of the nanofiber or regions thereof. Specifically, high conformational flexibility, as presented by the C-terminal stretches of the T4P-like nanofibers, is associated with increased binding affinity of peptides to the surface of AuNPs [181]. Further modulation could be exerted by higher-order organization of nanofibers into, e.g., a liquid crystalline nematic phase [189] or specific reaction conditions [190].

CHAPTER 4

MATERIAL ASSEMBLIES

(Previously published as Kim, H., Guo, X., Rehak, P., Král, P., Colvn V. **in Preparation**; Cohen, E., Weissman, H., Pinkas, I., Shimoni, E., Rehak, P., Král, Rybtchinski, B. Controlled Self-Assembly of Photofunctional Supramolecular Nanotubes. *ACS Nano* **12**, 317 (2018); Qian E., A., Wixtrom, A. I., Axtell, J. C., Saebi, A., Jung, D., Rehak, P., Han, Y., Moully, E. H., Mosallaei, D., Chow, S., Messina, M. S., JWang, J. Y., Royappa, A. T., Rheingold, A. L., Maynard, H. D., Král, P., Spokoyny, A. M. Atomically Precise Organomimetic Cluster Nanomolecules Assembled Via Perfluoroaryl-Thiol SNAr Chemistry. *Nature Chemistry* **9**, 333 (2017); Rehak, P., král, P. Hybridization of Biomolecular Crystals and Inorganic Nanomaterials. *ACS Nano* **submitted**, (2021); Yang, Y., Rehak, P., Xie, T., Feng, Y., Sun, X., Chen, J., Li, H., Král, P., Liu, T. Nanosheets and Hydrogels Formed by 2 nm Metal-Organic Cages with Electrostatic Interaction. *ACS Applied Materials and Interfaces* **12**, 56310 (2020). Banner, D. J., Firlar, E., Rehak, P., Foroozan, T., Osborn, J. K., Narayanan, S., Tahseen, T., Baggia, Y., Král, P., Shokuhfar, T., Shahbazian-Yassar, R. *In Situ* Liquid-Cell TEM Observation of Multiphase Classical and Nonclassical Nucleation of Calcium Oxalate. *Advanced Fnctional Materials* **submitted**.)

In this chapter, we study the self-assembly of supramolecular structures with applications to material science. We study the co-crystallization mechanism of naturally occurring proteins in the presence of AUNP in order to hasten protein crystallization without changing unit cell parameters. Next, we investigate the formation and stability of supramolecular nanotubes in different solvent environments. Then, we examine the sizes of atomically precise nanomedicines. Next, we explore

the properties of hybrid biomolecular crystals and low dimensional nanosurfaces. Next, we study the gelation process of single molecule thick suprastructures involving platinum cages. We conclude the chapter with the investigation of the crystallization of calcium oxalate in the absence and presence of citrate inhbitors.

4.1 Co-Crystallization of Proteins and NP-Polymer Conjugates

Introduction

Understanding protein structure is essential in obtaining information to treat and understand human diseases. XRD is the dominant tool in determining protein structure and crystal structure of of proteins. There are $150,000$ protein structures deposited in the Protein Data Bank, yet many more structures have yet to be determined. In order to obtain protein structures more efficiently, rapid crystallization is required. PEGylated AUNPs are promising nucelation sites that can hasten crystallization without changing the unit cell parameters of the corresponding protein crystal. Here we observe the crystallization of lysozyme, as a model system, whose crystal structure is well known. We investigate the co-crystallization of lyszyme in the presence of PEGylated AUNPs and AUNRs.

Experimental results

In the experiments, we observed a co-crystallization of lysozyme proteins and gold nanoparticles (NPs) covered with PEGylated chains. The co-crystallization occurred only for NPs covered with long PEGylated chains and not short PEGylated chains.

MD simulations: methods and results

In order to gain insight into these observations, we performed atomistic molecular dynamics (MD) simulations of lysozyme proteins coupled to NPs covered with PEGylated ligands of two different lengths: 1) short, whose molecular weight is 1 kDa/chain and surface density is 3.2 chains/nm^2 and 2) long, whose molecular weight is 10 kDa/chain and surface density is 0.8 chains/nm^2.

The molecular weight of long PEGylated chains was 10 kDa/chain, corresponding to 227 links per chain; the molecular weight of short PEGylated chains was 1 kDa/chain, corresponding to 23 links per chain. Two simulations were performed for each NP, labelled as systems 1 and 2. Chains

were placed on a sphere of gold atoms (100 crystal), with a diameter of 5nm. The long chain NP had a surface density of 0.8 chains/nm^2; the short chain had a surface density of 3.2 chains/nm^2.

MD simulations were performed with NAMD2.12 [37]. The amino acids of the protein modeled with the CHARMM36 protein force field [39, 40, 80] and all other species were modelled with generalized CHARMM force field [38, 56, 97]. The Particle-mesh Ewald (PME) method [57] was used for evaluation of long-range Coulomb interactions, in all the simulations. The time step was set to 1.0 fs for systems with short PEG chain and 2.0 fs for systems with long PEG chain, and long-range interactions were evaluated at every 1 (van der Waals) and 2 (Coulombic) time steps. The simulations were performed in the NPT ensemble at a constant temperature of 310 K, constant pressure of 1 atm, and a Langevin constant of $\gamma_{Lang} = 1.00$ ps^{-1}. All simulations were performed in a 1.0 M NaCl aqueous solution and 0.1 M acetate buffer with a ratio of acetate ion and acetic acid similar to an environment of pH 4.6 to replicate the experimental conditions. Additional acetate ions were added to balance the charge of the lysozyme protein, compensated by acetic acid to preserve the pH.

Simulations were first minimized for 5,000 steps and pre-equilibrated for at least 2 ns, keeping gold atoms and backbone atoms on proteins constrained. Then backbone atoms were released and only a few gold atoms were constrained to prevent NP from diffusing. The systems were deemed equilibrated when the contact area between proteins and NP stabilized, at which time we started data analysis.

Contact area was determined by examining the surface accessible areas (SASAs) of 1) the lysozyme proteins, 2) the AUNP, and 3) the union of lysozyme proteins and AUNP. Contact area is determined by Equation 4.1, where A is the contact area, SASA$_{prot}$ is the SASA of the lysozyme proteins, SASA$_{AUNP}$ is the SASA of the AUNP, and SASA$_{prot,AUNP}$ is the SASA of the union of the lysozyme proteins and AUNP.

$$A = \frac{SASA_{prot} + SASA_{AUNP} - SASA_{prot,AUNP}}{2} \tag{4.1}$$

The analysis of the protein's orientation on the NP surface was determined by the vector that spans from the center of mass of the NP to the center of mass of the protein and obtaining the azimuthal and polar angles with respect to the protein's internal coordinate system, shown in Figure 37. The dipolar potential was determined by modifying the protein atoms' charges to obtain neutral systems as in Equation 4.2. The dipolar potential was visualized, using GUI PME electrostatics in VMD [59]. In the simulations, 10 lysozyme proteins were placed close to the surfaces of the 2 different NPs solvated in NaCl (1.0 M) and acetate buffer (0.1M) at pH 4.6. Moreover, 2 different initial configurations were considered in the simulations in each of these 2 systems. In the first configurations (shown in Figure 35 a, c and labeled as system 1) all 10 proteins were placed in the vicinity of the NP, such that the principal moments of inertia for all proteins were parallel (see Figure 36 for definition of axes). In the second configurations (shown in Figure 35 b, d and labeled as system 2), the orientations of the 10 lysozyme proteins were random. After $40-60$ ns of simulations, proteins were considered to be relatively well adsorbed and equilibrated on the NP surfaces.

Figure 35 shows the 2 systems, each in 2 different configurations. The final configurations of these systems reveal that NPs with longer PEG chains can better accommodate lysozyme proteins. Further analysis summarized in Table VII shows that NPs with longer PEG chains have a larger contact area (energy) per protein than NPs with shorter PEG chains (approximately 15.8 nm^2 versus 11.4 nm^2). There are also more proteins bound to NPs with longer PEG chains.

We have also evaluated the protein-NPs interaction energies normalized with respect to either 1) the number of proteins that are located within 5 Å of NP ligands or 2) the contact area of the

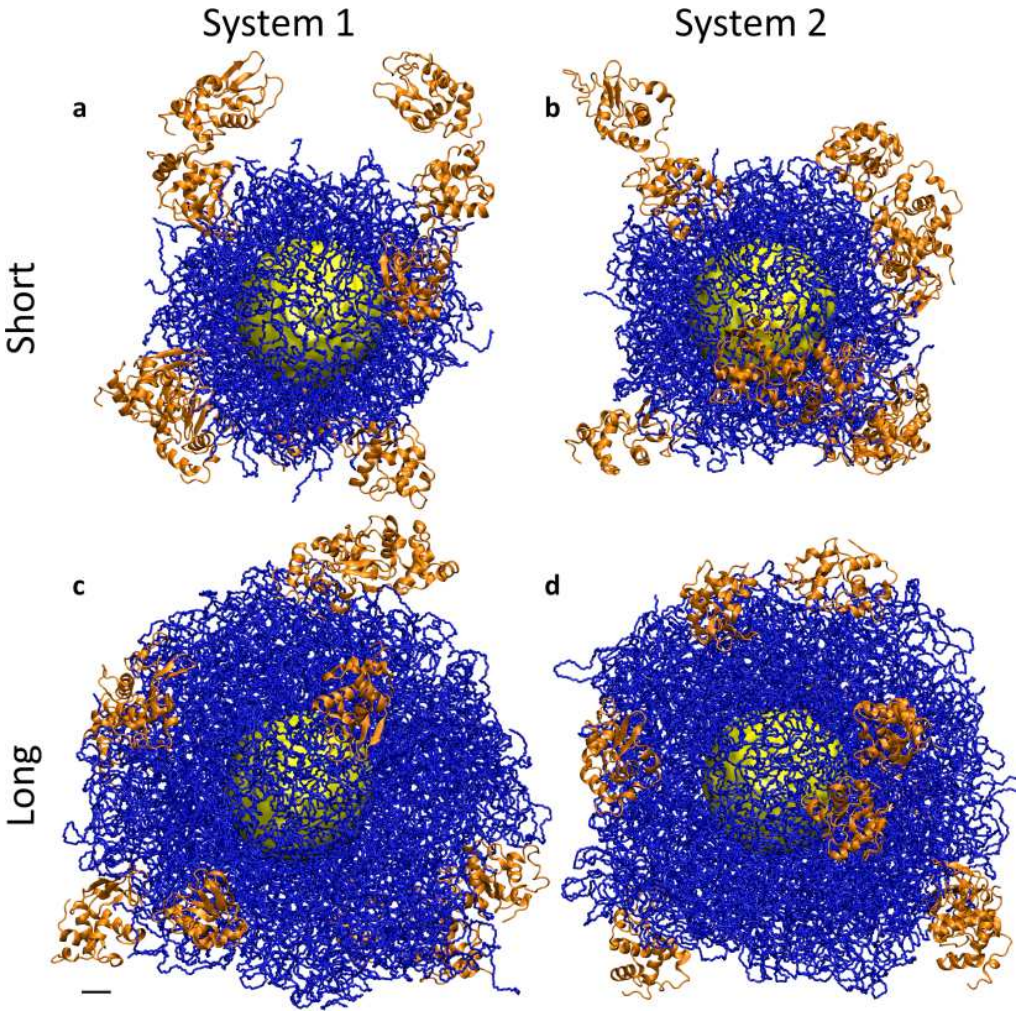

Figure 35: Simulated systems with NPs of a-b) short PEG simulated for 100 ns and c-d) long PEG simulated for 126 and 166 ns. Gold atoms are in yellow; heavy atoms of PEGylated chains are in blue; backbone structure of lysozyme protein is in orange. Scale bar represents 1 nm.

interacting components. As shown in Table VIII, NPs with long PEG chains have larger energies of binding to individual proteins than do NPs with short PEG chains (−254 kcal/mol versus −158 kcal/mol). In contrast, the coupling energies per unit area are similar in both types of NPs (−16 kcal/mol nm^2 versus −14 kcal/mol nm^2). These results can be explained by the fact that proteins can't equally submerge in the corona of NPs with a different PEG coverage, but their coupling energy surface density is about the same in the submerged area of the proteins. Therefore, the free energy

System	Net Contact Area (nm^2)	Interacting Proteins	Contact Area per Protein (nm^2)
Short 1	83.85 (8.90)	7.71 (0.74)	10.90 (0.79)
Short 2	116.11 (13.45)	9.67 (0.58)	12.01 (1.19)
Long 1	154.51 (15.13)	9.74 (0.44)	15.87 (1.36)
Long 2	158.24 (10.54)	10 (0)†	15.82 (1.05)

TABLE VII. CONTACT AREA, NUMBER OF PROTEINS BOUNDED TO NP SURFACE, AND CONTACT AREA PER PROTEIN. NUMBERS IN PARENTHESIS ARE STANDARD DEVIATIONS. †NUMBERS ARE EXACT.

of binding of the long PEG NPs to lysozyme protein crystals might also be larger than that of the short PEG NPs. This implies that the long PEG NPs might more likely solvate (co-crystallize) in the lysozyme protein crystals.

System	Electrostatic per protein (kcal/mol)	Dispersion per protein (kcal/mol)	Net Interaction per protein (kcal/mol)	Electrostatic per Area (kcal/mol nm^2)	Dispersion per area (kcal/mol nm^2)	Net Interaction per area (kcal/mol nm^2)
Short 1	- 58.92 (11.21)	-85.33 (6.87)	-144.25 (15.34)	-5.41 (0.95)	-7.83 (0.20)	-13.24 (1.00)
Short 2	-77.18 (11.11)	-95.19 (9.96)	-172.37 (19.19)	-6.43 (0.71)	-7.92 (0.16)	-14.36 (0.76)
Long 1	-131.55 (20.33)	-127.56 (11.46)	-259.11 (29.81)	-8.27 (0.97)	-8.04 (0.15)	-16.31 (1.05)
Long 2	-119.72 (14.49)	-128.86 (9.68)	-248.58 (22.47)	-7.56 (0.66)	-8.14 (0.15)	-15.70 (0.71)

TABLE VIII. AVERAGE ELECTROSTATIC, DISPERSION, AND NET INTERACTION ENERGIES NORMALIZED WITH RESPECT TO THE NUMBER OF PROTEINS INTERACTING WITH NPS AND CONTACT AREA BETWEEN PROTEINS AND NP. NUMBERS IN PARENTHESIS REPRESENT STANDARD DEVIATIONS.

Next, we have analyzed the orientations of lysozyme proteins on NP-surfaces, in order to better understand their coupling to NPs. Figure 36a shows the internal coordinate system of the lysozyme protein aligned with the principal axes of the moment of inertia. The protein orientation on the AuNP surface is defined by the azimuthal θ and polar ϕ angles. The protein orientation on the NP surface is defined by the two angles of a vector that is spanning from the NP center of mass to the protein center of mass. For example, for $\theta = 90^{\circ}$ and $\phi = 0^{\circ}$, a (unit) vector going along the x axis is parallel with the norm vector at the NP surface.

To better understand the protein orientations, we need to analyze the interactions of proteins with different NPs. Inside the lysozyme crystal, the overall charge of each protein (+8e) is neutralized by Cl^- counterions; crystallization takes part in a highly concentrated ionic solution with a screening length of 3 Å. In order to approximate this screening effect, in the lack of knowledge of the precise counterions positions, we neutralized the proteins using (uniform modification all protein charges),

$$q_i^{mod} = q_i^0 - \frac{Q_{tot}}{N_{tot}} \tag{4.2}$$

Here, q^i_{mod} is the modified charge of the i^{th} protein atom, q^0_i is the charge of the i^{th} protein atom used in the simulations, Q_{tot} is the net charge of protein atoms and N_{tot} is the total number of protein atoms. Figure 36 b, c shows regions of highly positive (blue) and negative (red) equipotentials in the lysozyme protein with original and modified charges (Equation 4.2), respectively.

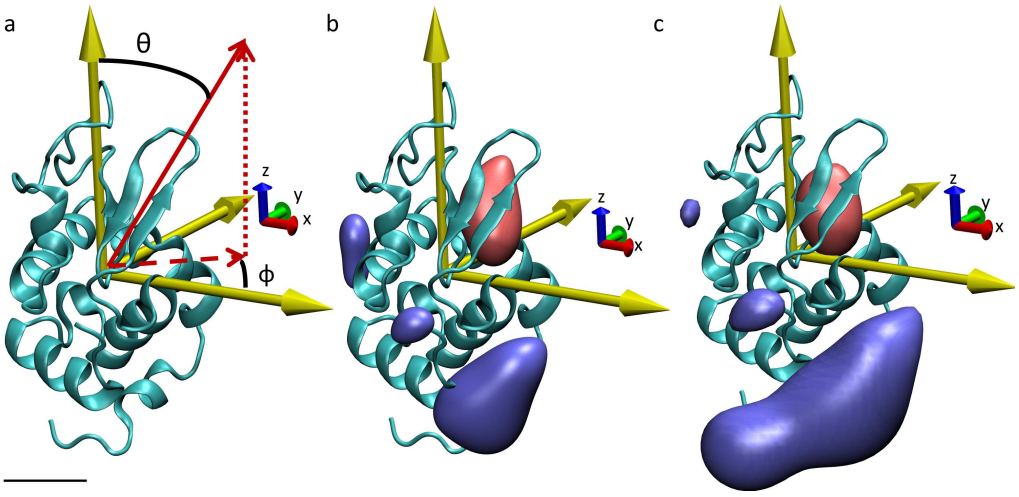

Figure 36: a) Internal coordinates of the lysozyme protein. The origin is at the center of mass of the protein and the (x,y,z) internal coordinate system are given by the moment of inertia's principal axes. b) Potential isosurfaces of single lysozyme protein. c) Potential isosurfaces (based on neutralized lysozyme protein using charge modification shown in Equation 4.2). Blue regions: positive potential, red regions: negative potential. Scale bar represents 1 nm.

Figure 37 shows the preferred distributions of orientations of lysozyme proteins on NP surfaces, covered with short and long-PEG ligands, averaged over two separate systems for each PEG length. In Figure 37, ϕ defined in Figure 36a is shifted by 180° (the coordinate system is rotated about the z axis by 180°). We can see that NPs with short PEG chains have sharper protein distributions (higher peaks), whereas NPs with long PEG chains have broader protein distributions (lower peaks). In particular, $-60°<\phi<60°(+180°)$ in both systems, but $90°<\theta<180°$ and $0°<\theta < 180°$ in systems with short and long PEG chains, respectively. The highest peak (Figure 37a) corresponds to the protein orientation in which the potential isosurface with the most positive value (blue in Figure 36b) is in direct contact with the short PEGylated chains of the NP. This is a highly stable configuration of the protein on the short-PEG NP. Coulombic interactions can largely contribute to the binding enthalpy between lysozyme protein and NP (Table VIII). In particular, the positive region (with arginines) of the lysozyme protein has a strong affinity to the oxygen atoms on the PEG chains. These observations reveal that lysozyme proteins can be better nested and have more orientations on NP-surfaces with long PEG chains. This means that it should be easier to co-crystallize these long-PEG-chain NPs together with the protein crystal, since they could be accommodated on any surfaces of potential cavities formed in the protein crystal.

We also use MD simulations to better understand why Au nanorods (NR) co-crystallize in certain orientations within the lysozyme proteins crystals. As in the case of NPs, the charged and highly polar nature of the lysozyme proteins might be responsible for the highly oriented NR co-crystallization. In Figure 38, we have calculated the isosurfaces (equipotentials) in different (neutralized) lysozyme crystals, constructed from a tetragonal unit cell ($a = b = 78.540$ Å; $c = 37.770$ Å) with $P4_32_12$ symmetry that consists of 8 protein molecules [191]. We consider two different cuts: 1) 10×1 (10 unit cells extended in the (110) and (001) directions) and 2) 5×2 (2 unit cells extended in the

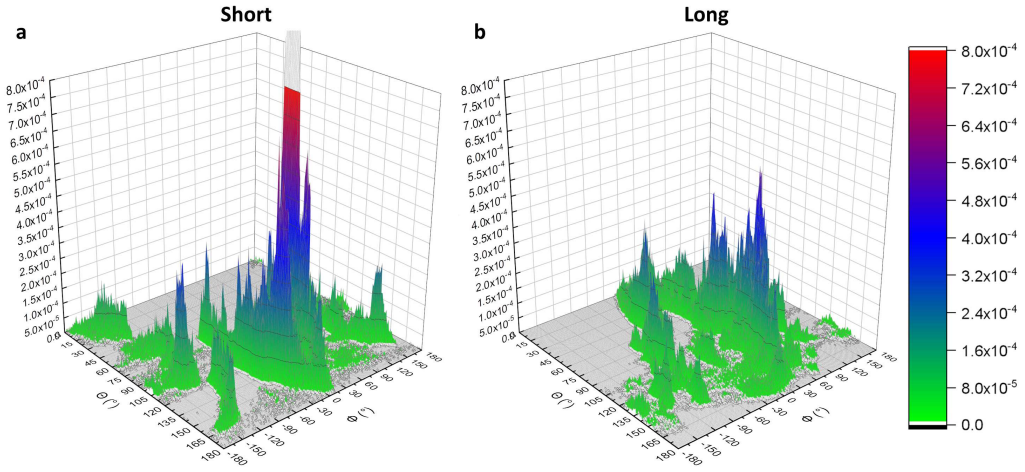

Figure 37: Average 2D angular distributions of lysozyme proteins on NPs surfaces with a) short PEG ligands and b) long PEG ligands. Angle definitions are given in Figure 36a. Note: ϕ in the graph is defined by the rotation of 180° about the z axis given in Figure 36a.

(100), (010), and (001) directions 5 times). In the first cut, the boundaries correspond to the unit cell's (integral numbers 0 to 1). In the second cut, the boundaries are in the middle of the unit cell (half integers -0.5 to 1.5). When the crystals are cut along the boundary of the unit cell (as in the 10×1 cut) they have symmetric fields that cancel each other because the proteins are oriented with rotational symmetry within the unit cell. When the crystals are cut in in the middle of the cells (as in the 5×2 cut), there is an equipotential that builds along the (001) axis. During the co-crystallization, highly polarizable AuNRs might be submerged in the crystal in such a way that they are parallel to the c-axis (001) of the crystal in Figure 38e. In this way, the NR might be largely transversally polarized by the electrostatic field of the crystal.

Conclusion

Our results showed that the mechanism of co-crystallization of lysozyme proteins with AUNPs and AUNRs is driven equally between electrostatic and dispersion interactions, which have approximately equal binding enthalpies. However the orientations of lysozyme proteins results primarily through

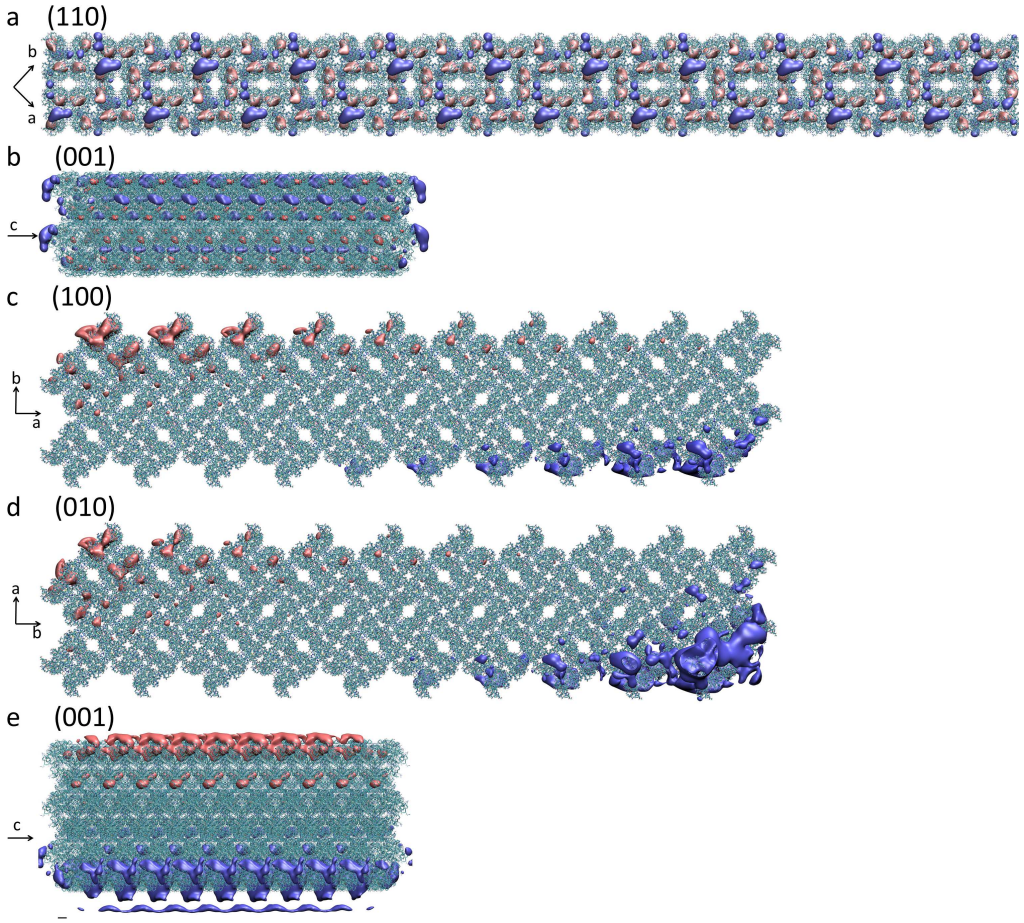

Figure 38: Positive and negative potential isosurfaces of lysozyme crystals based on modified charges (neutralized proteins): a) 10×1 unit cells in the (110) direction; b) 10×1 unit cells in the (001) direction; c) 5×2 unit cells in the (100) direction; d) 5×2 unit cells in the (010) direction; e) 5×2 unit cells in the (001) direction. Scale bar represents 1 nm.

electrostatic interactions due to the higher anisotropy of the charge distribution on the protein. The electrostatic buildup within a crystal of lysozyme also causes AUNRs to have orientations parallel to the c axis.

4.2 Controlled Self-Assembly of Photofunctional Supramolecular Nanotubes

Adapted from Ref. [7] (*ACS Nano 2018*, 12 DOI:10.1021/acsnano.7b06376) with permissions from ACS Publishing Groups.

Introduction

Supramolecular nanotubes (SNTs) represent an important class of noncovalent arrays [192–198], whose nanoporosity enables the capture, storage, transport, and release of different molecular and macromolecular cargos [197, 198]. SNTs having diameters of several nm are rare [196, 199, 200] and most supramolecular tubes have diameters ranging from tens of nm to several micrometers. Usually SNTs are assembled in aqueous media from monopolar amphiphiles, asymmetric bolaamphiphiles, or macrocycles [196–198, 201, 202]. Simpler symmetric bolaamphiphiles are rarely employed [203, 204]. Tuning their diameter at the nanoscale is a key challenge [195,196]. Size control is essential to enable accommodation of various molecular cargos. Synthetic schemes to control SNT structures are lacking due to complex assembly mechanisms that are only partially understood [196, 205, 206].

We report a SNT self-assembly from symmetric bolaamphiphiles based on the same hydrophobic core. A combination of specific molecular interactions and solvation enable precise structural control. This enables a precise tuning of tubular structures, including their diameters. Conversion of one type of nanotube into another was also demonstrated. Molecular dynamics (MD) simulations provide an insight into the stability of the tubular superstructures and their initial stages of self-assembly that involves pairwise, side-by-side stacking interactions between several molecular units. This represents a distinctive general mode of molecular interactions leading to tubular assembly based on a bis-aromatic motif.

Experimental results

We have shown that PP2b derivatives with medium-sized PEGs self-assemble into supramolecular polymers in water/THF mixtures [207]. In these systems, aromatic cores stack one on top of the other in register, which is typical for many aromatic amphiphiles [194]. Recently, it has been shown that aromatic amphiphiles can exhibit complex interaction modes, leading to unique assembly structures [208, 209]. Our previous work suggested that perylenediimide (PDI) stacking can be controlled in aqueous medium under conditions of kinetic control, leading to nonstacked or stacked systems as a result of organic cosolvent addition/evaporation [210]. We envisioned that in bisaromatic systems connected by a linker, such as PP2b (Figure 39a), interactions between aromatic cores can be attenuated to result in side-by-side stacking (Figure 39b), leading to new supramolecular polymerization modes. For this purpose, we investigated self-assembly of PEG-PP2b (PEG13 and PEG44, see Figure 39a) at a wide range of conditions. Bulky PEG44 was expected to partially suppress in-register stacking, while for shorter PEGs, organic cosolvent content was tuned in a broad range in order to control stacking/hydrophobic interactions. Using this methodology, tunable tubular assemblies could be prepared that are based on side-by-side stacking interactions (Figure 39b). Assembly of diverse tubular motifs from symmetric building blocks (see below) contradicts the common SNT design concept, implying that nonsymmetric amphiphiles should be employed for SNT self-assembly [198].

First, we investigated self-assembly of PP2b PEG44 bearing relatively large PEG substituents. Cryogenic transmission electron microscopy (cryo-TEM) imaging of PP2b PEG44 in neat water revealed the formation of nanotubes with an average width of 4.6 ± 0.3 nm, which were hundreds of nm long at 10^{-3} M concentration and mostly tens of nm long at 10^{-4} M. The hexagonal tube assemblies convert into molecular fibers within 7 days, apparently in order to optimize hydrophobic interactions, indicating that the nanotube assembly occurs under kinetic control. The hexagonal

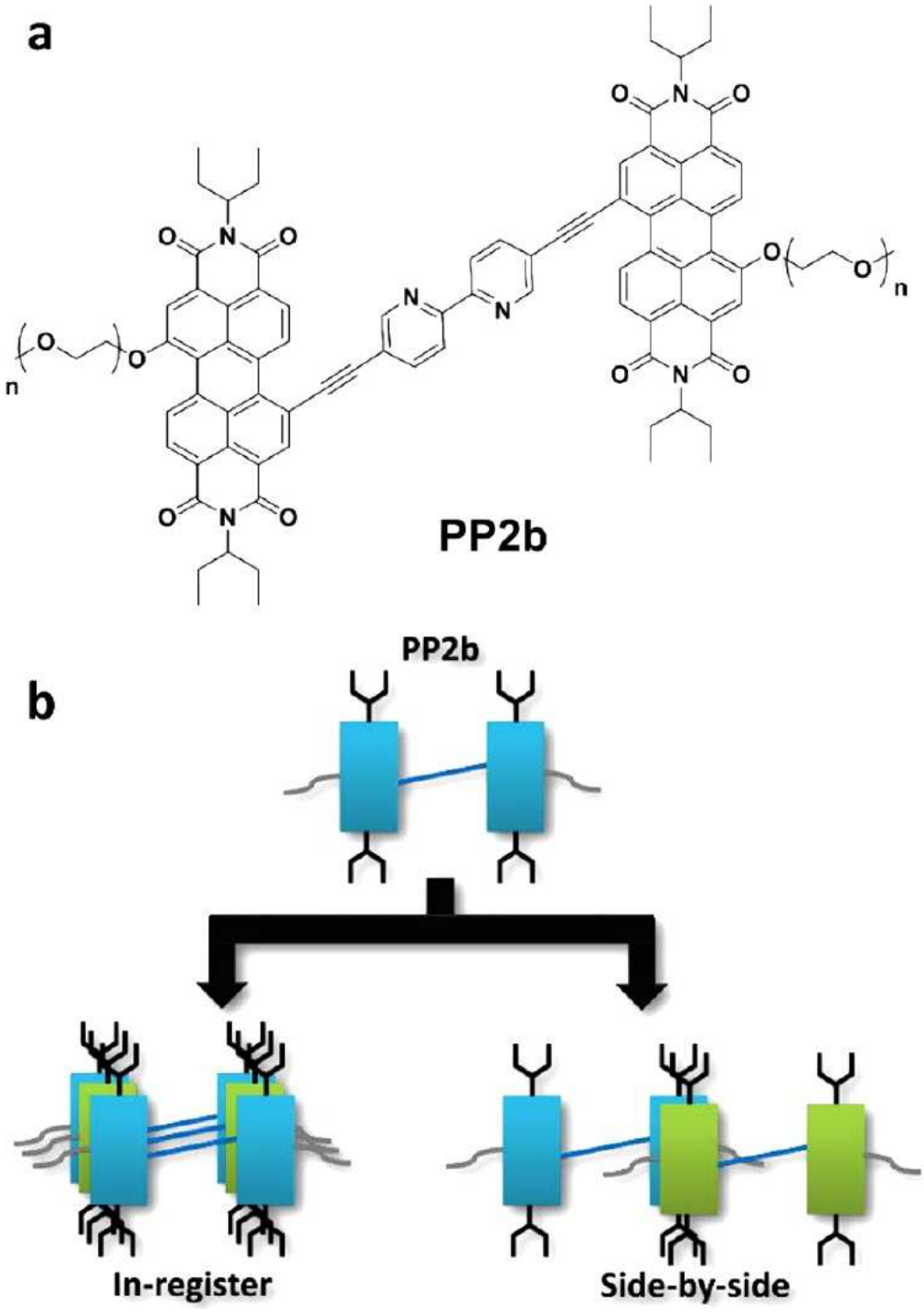

Figure 39: (a) PP2b amphiphile building blocks, PEG lengths: n = 13 or n = 44. (b) Schematic illustration of PP2b stacking interactions: In-register (left) and side-by-side (right).

SNTs are relatively stable due to high kinetic barriers in aqueous media [194, 211]. The addition of THF to the aqueous solution of nanotubes led to vesicles (40% THF) or large fibrous aggregates (5% THF), underscoring a critical role of a solvent in aqueous self-assembly [212]. Formation of lower curvature vesicular structures upon addition of an organic cosolvent further confirms that SNTs are formed under kinetic control [194,211]. Importantly, diverse structures can be obtained from a single molecular building block.

In the case of shorter PEG13, PP2b PEG13 in water:THF = 8 : 2 (v/v, 10^{-4} M) assembles into molecular fibers. In contrast, PP2b PEG13 in water:THF = 6 : 4 (v/v, 10^{-4} M) forms nanotubes with rectangular cross sections that have an average width of 3.5 ± 0.4 nm and are hundreds of nm in length. The dimensions of the rectangular cross-section (3.7×3.2 nm) correspond well to those in the model (3.9×3.3 nm). Cryo-TEM imaging and molecular modeling suggest that two parallel PP2b molecules are stacked on top of another perpendicularly oriented pair of PP2b molecules, eventually forming a nanotube with a rectangular cross-section. The width of the inner cavity in the model is 0.8 nm (the dimensions of the inner cavity observed in high-resolution cryo-TEM images are difficult to estimate due to contrast limitations; it appears to be < 1.5 nm). Interestingly, a transformation of the rectangular tubes (4 nm in diameter) into larger (4.8 ± 0.4 nm diameter) and more rigid ones (almost no bending observed) was achieved by heating the assembly at 55°C for 30 min. The resultant tubes are stable and do not change upon further heating. These nanotubes were also observed by SEM imaging, revealing diameters of 6.5 ± 0.8 nm, where the larger diameter is consistent with the presence of PEG chains (wrapping the SNTs) that become visible in SEM images. The nanotubes may have hexagonal cross-section (not seen in cryo-TEM images), as they are rigid and exhibit diameters close to the ones of the rigid hexagonal tubes based on PP2b PEG44.

The observed cross-section and molecular modeling suggest a structure in which three PP2b molecules are stacked in a helical arrangement with a triangle-like geometry and a twisting angle of 120° relative to each other. This structure results in a helical tube with an outer diameter of 3.1 nm and an inner one of roughly 0.3 nm, in agreement with the cryo-TEM imaging. The observed fine structure of the nanotubes appears to be compatible with helical packing. We note that resolution of cryo-TEM images precluded further unequivocal confirmation of helicity and precise determination of SNTs' inner diameters. The absence of self-sorting in this system (formation of two distinct aggregate types) is probably due to strong driving forces that result in efficient irreversible interactions between all moieties [213].

Unlike the rectangular ones, these nanotubes are stable at 55°C (see summary of SNTs properties in Table IX). Our attempts to further control the structure by altering the PP2b PEG44/PP2b PEG13 ratio resulted in diverse assemblies. For instance, increasing the PP2b PEG44 content to 10% leads to molecular fibers (1% THF) or a dense 3D network of fibers (40% THF). Likewise, the ratio of 95% PP2b PEG44/ 5% PP2b PEG13 resulted in molecular fibers (1% THF) or vesicles (40% THF).

tube composition	solvent	cross section geometry	diameter (nm)	stability
PP2b PEG13	6:4 water /THF (v/v)	rectangular	3.5 ± 0.4	stable at rt
PP2b PEG13 (heated to 55° C for 30 min)	6:4 water /THF (v/v)	probably hexagonal	4.8 ± 0.4	stable
5% PP2b PEG44/ 95% PP2b PEG13	6:4 water /THF (v/v)	triangle-like	3.2 ± 0.2	stable
PP2b PEG44	water	hexagonal	4.6 ± 0.3	kinetically stable, transform gradually to molecular

TABLE IX. SUMMARY OF SNTS PROPERTIES

MD simulations: methods and results

Trajectory calculations

MD simulations were performed with NAMD [37] package, using the CHARMM force field [38–40, 56, 80]. Internal molecular and dispersion parameters were taken from the CHARMM36 general force field [80]. Due to difficulties of ab initio frequency calculations of alkyne and extended aromatic groups in the PP2b core, missing parameters were approximated using the parachem software [214]. Ab initio calculations using Gaussian 09 [74] package were performed on the linker group between the two extended aromatic groups, the extended aromatic groups themselves, and the terminal noncyclical aromatic ring, using $MP2/6-31g(d)//MP2/6-31g(d)$ level of theory to determine partial charges of PP2b core using the ChelpG algorithm [76]. CHARMM TIP3P water model was employed for explicit water simulations.

Two types of simulations were performed: (i) self-assembly and (ii) superstructure simulations. In the self-assembly system, each of the PP2b molecules were placed and rotated randomly in their respective environment. PEGylated chains with 44 oxygen atoms were simulated in pure water, whereas PEGylated chains with 13 oxygen atoms were placed in water/THF mixtures. There were two different mixtures of water and THF: (i) 60% water: 40% THF (v:v) and (ii) 80% water: 20% THF (v:v). Experimental density [215] of pure THF was used to determine the number of THF molecules per system. The volume of each system was determined by placing the PP2b molecules and then adding 3 nm to the maximum and minimum coordinate values of the PP2b molecules.

A total of three self-assembly systems were constructed (i) with pure water and 12 PP2b molecules with PEGylated chains, having 44 oxygen atoms, (ii) in 60% water and 40% THF with 8 PP2b with PEGylated chains, having 13 oxygen atoms, and (iii) in 80% water and 20% THF with 6 PP2b molecules, with PEGylated chains, having 13 oxygen atoms. A total of three superstructure

simulations were constructed (i) hexagonal structure with PEGylated chains 44 oxygen atoms long in pure water, (ii) square structure in 60% water: 40% THF (v:v), (iii) square structure (actually giving rise to molecular fibers) in 80% water: 20% THF (v:v). Because those superstructures had the PEGylated chains of $-O(CH_2 - CH_2)OCH_3$ groups, additional PEGylated links were added until desired length was achieved.

Water and THF were initially placed immiscibly ,and during minimization and pre-equilibration they were allowed to diffuse without any constrains until the solvent was homogeneous. During minimization ($50,000$ steps) and pre-equilibration (at least 3 ns), only atoms in the PP2b core were subjected to constraints, whereas the solvent molecules and PEGylated chains were allowed to move without any constraints. During the production runs, the self-assembly molecules had no constraints; in the superstructure simulations, only the linking bipyridine carbons and the nitrogen atoms on the bipyridine group, on one molecule per superstructure, were constrained, with 20% of value of the constraints employed during minimization.

Simulations were done with NPT ensemble at a temperature of 310 K and a pressure of 1 atm and periodic boundary conditions. Langevin dynamics were used to maintain pressure and temperature, with a damping constant of 1 ps^{-1} , temperature bath was 310 K, hydrogen atoms were excluded from the thermal bath, piston period was 100 fs, piston decay was 50 fs. Excluding minimization, particle mesh Ewald [57] was used with a grid spacing of 1.0. Velocity Verlet integrator was used to solve equations of motion, with a time step of 2 fs. The SHAKE algorithm was used for the hydrogen atoms. Nonbonded interaction used the switching algorithm, with the switch-on distance at 10 Å and the switch-off at 12 Å. Nonbonded pair lists were used for atoms within 13.5 Å of each other, with the list updated every 20 steps. $1 - 4$ nonbonded interactions were not scaled. Data and snapshots were recorded every 10 ps or every 5000 steps. The pure water simulation system

lasted 200 ns, due its computational expense, whereas all other systems were 300 ns or longer. In order to improve efficiency of the simulations, the size of the 60% water self-assembly system was first decreased by excluding only solvent molecules, but the number of PP2b molecules was kept constant. Subsequently the size was further decreased from eight molecules to only five PP2b molecules. When constructing the superstructure for the aqueous system, the original length of the PEGylated chains was lengthened to 44 oxygen atoms, in an extended conformation. Then the superstructure was allowed to minimize and equilibrate in vacuum, so that the PEGylated chains would fold onto the superstructure, thus requiring a smaller volume for the simulation.

Self-assembly simulations

In order to gain mechanistic molecular-scale insight into the self-assembly of different PP2b molecules and the stability of molecular superstructures formed, we used all-atom molecular dynamics (MD) simulations in explicit solvent to model: (i) the process of PP2b molecular self-assembly and (ii) the spatial organization of molecular/solvent components in the self-assembled superstructures. For PP2b PEG44 (Figure 40a,b, neat water), the simulations show the outcome for 12 monomers self-assembling for 150 ns in a water box of $5,400$ nm^3. The simulations revealed that within 10 ns PP2b PEG44 formed a large cluster, resembling a micelle [216, 217], where the hydrophobic PP2b moieties closely interacted, while the long PEG chains surrounded the core of the cluster. Within 22 ns, a first PP2b dimer featuring two stacked PDIs (side-by-side arrangement) formed within the core, which was followed by the formation of a trimeric chain at 25 ns. Around 70 ns, another monomer joined the trimer to form a jiggling linear tetramer. At 88 and 115 ns, additional dimers formed outside and within the cluster core, respectively. The rigid and flat bipyridine (bipy) linker was found to promote initial stacking interactions, eventually leading to side-by-side stacking of PDI

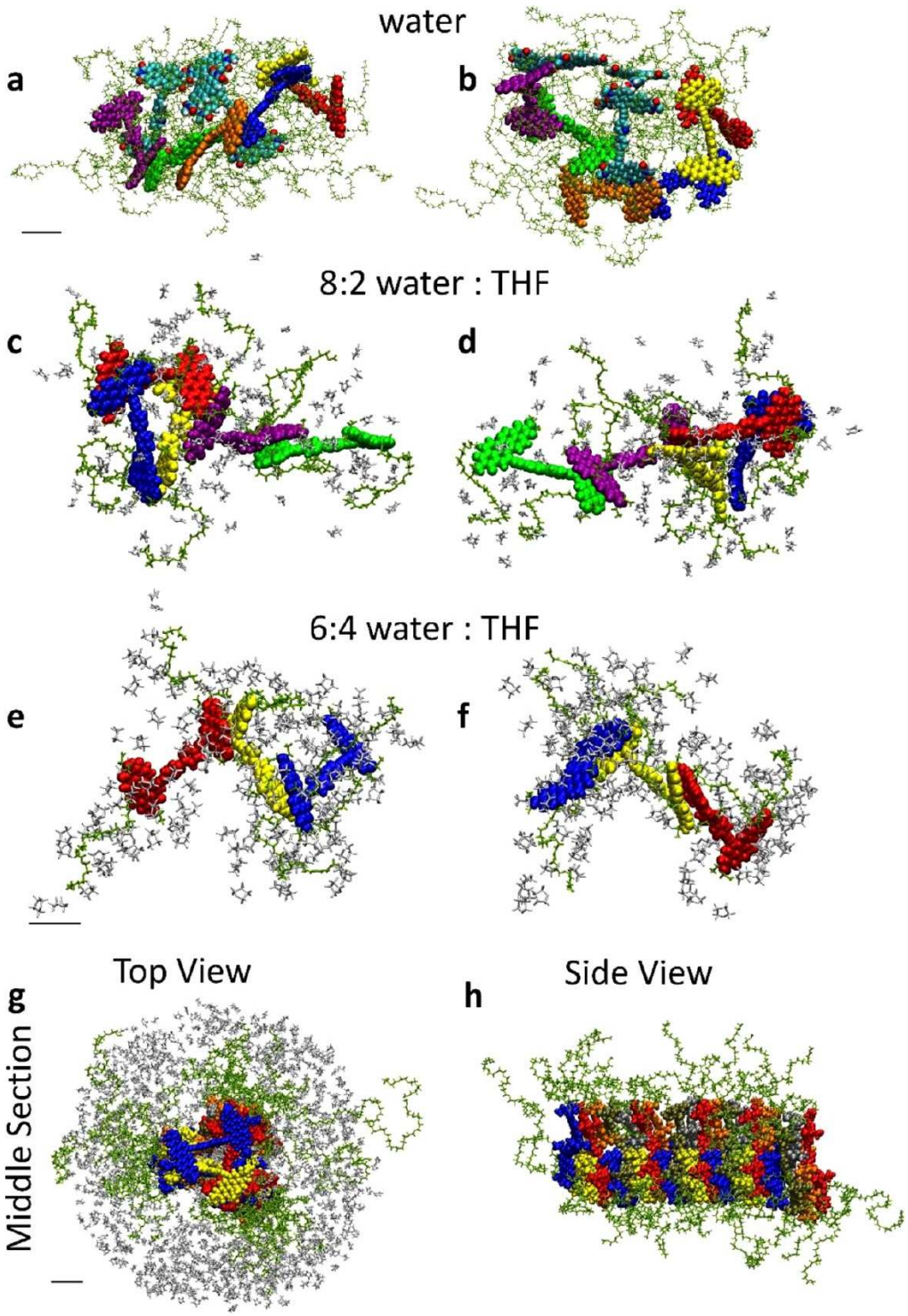

Figure 40: MD simulations of the self-assembly of PEG-ylated PP2b monomers. PP2b molecules are vividly colored, PEG chains are shown in a finer representation, and gray structures represent THF molecules. Scale bars are 1 nm. (a, b) Two views of the main cluster core formed from PP2b PEG44 monomers in pure water at 150 ns. (c, d) Two views of the main cluster core formed from PP2b PEG13 monomers in water:THF solvent at 266 ns. (e, f) Two views of the main cluster core formed from PP2b PEG13 monomers in water:THF = 6 : 4 (v/v) at 674 ns. (g, h) MD simulations of a fragment (middle section) of a SNT pre-assembled from PEG-ylated PP2b monomers. Top and side views of helical superstructures of 29 PP2b PEG13 and 1 PP2b PEG44 in water:THF = 6 : 4 (v/v) at 20 ns. For clarity, in a side view, the solvent molecules are not shown.

moieties resulting in stable oligomers. The rigid nature of the linker most probably restricts a range of possible geometries, promoting oligomer cyclization that eventually leads to nanotubes.

In the case of PP2b PEG13 (Figure 40c,d), the simulations show the results for 6 PP2b PEG13 monomers after self- assembling for 266 ns in a water:THF = 8 : 2 (v/v) solvent in a box of 2200 nm^3. These monomers with shorter PEG chains quickly formed pairs, before forming larger clusters, surrounded by THF molecules (better solvent for hydrophobic cores). The first dimer formed at 12 ns, a second dimer formed at 27 ns, and a trimer formed from the second dimer at 66 ns. Later on, at 185 ns, this trimer formed a closed triangle. The structures formed were also relatively rigid. Simulations of PP2b PEG13 (Figure 40e,f) show the outcome for 5 PP2b PEG13 monomers which self-assembled at 674 ns in the water:THF = 6 : 4 (v/v) solvent in a box of 560 nm^3. Here, the first dimer appeared only at 40 ns, a trimer at 150 ns (shown), and a second dimer only at 544 ns. Figure 40c,f also reveals a close distribution of THF molecules around the PDI cores. These results indicate that with the increasing concentration of a stabilizing THF solvent, the PDI dimerization via stacking is a much slower process in comparison with water:THF = 8 : 2 system, indicating importance of specific solvation. Simulations of the fully assembled tubes (Figure 40g,h, Figure 41 and Figure 42) support our experimental results. They show that the 3 nm (triangular-like, Figure 40g,h) and 5 nm (hexagonal) SNTs are more stable compared with a more flexible 4 nm (rectangular) tube. The latter is in accordance with the experimentally observed transformation of rectangular to the hexagonal tubes upon heating. The high stability of the hexagonal SNTs may be due to highly ordered (crystalline- like) structures, while the triangular-like SNTs (Figure 40g,h) may be stabilized by helical arrangement.

Two mechanisms of noncovalent bonds formation have been observed in the simulations: i) two PDI groups establish direct contact with each other (direct process) and ii) a PDI group comes

in contact with a bipyridine linker group and then slides down the alkyne group to make contact with another PDI group (indirect process). The direct process is slower because the extended rings need to come close to each other in a desirable orientation to form stable noncovalent interactions. Aggregation of PEG13 PP2b in the 8 : 2 solvent tends to follow the faster indirect process, whereas in the 6 : 4 solvent, aggregation follows slowly the direct process. Both mechanisms were observed in PEG44 systems, where the aggregation is much faster due to the close proximity of the PP2b molecules in the PEG-entrapped cluster. In general, as THF concentration decreases, PEG chains play a more important role in protecting the hydrophobic core from the aqueous surroundings. Specific solvation effects in water/THF mixtures revealed by our MD simulations lead to diverse and unique assembly outcomes. In general, it has been recognized that self-assembly in water-organic co-solvent mixtures depends on multiple effects and is difficult to predict [192, 218–220]. Notably, our experimental and theoretical studies indicate that an interplay of hydrophobic interactions and specific solvation by water and an organic co-solvent can be utilized to achieve structural control.

Superstructures simulations

PEG44**.** Figure 41a-b show the results of 100 ns simulations of 12 PP2b PEG44 monomers pre-assembled in water into a hexagonal nanotube, which is based on the experimental ONT superstructure presented in of the main text. In these simulations, some PEG chains tend to spread far away from the nanotube, while others tend to fold around the apolar carbon-rich areas of PP2b moieties forming the nanotube core. These carbon-rich areas of PP2b are sufficiently strongly coupled to stabilize the superstructure in the original hexagonal shape during the simulations time of 100 ns. However, a steric repulsion together with the entropy of long PEG chains might prevent the forma-

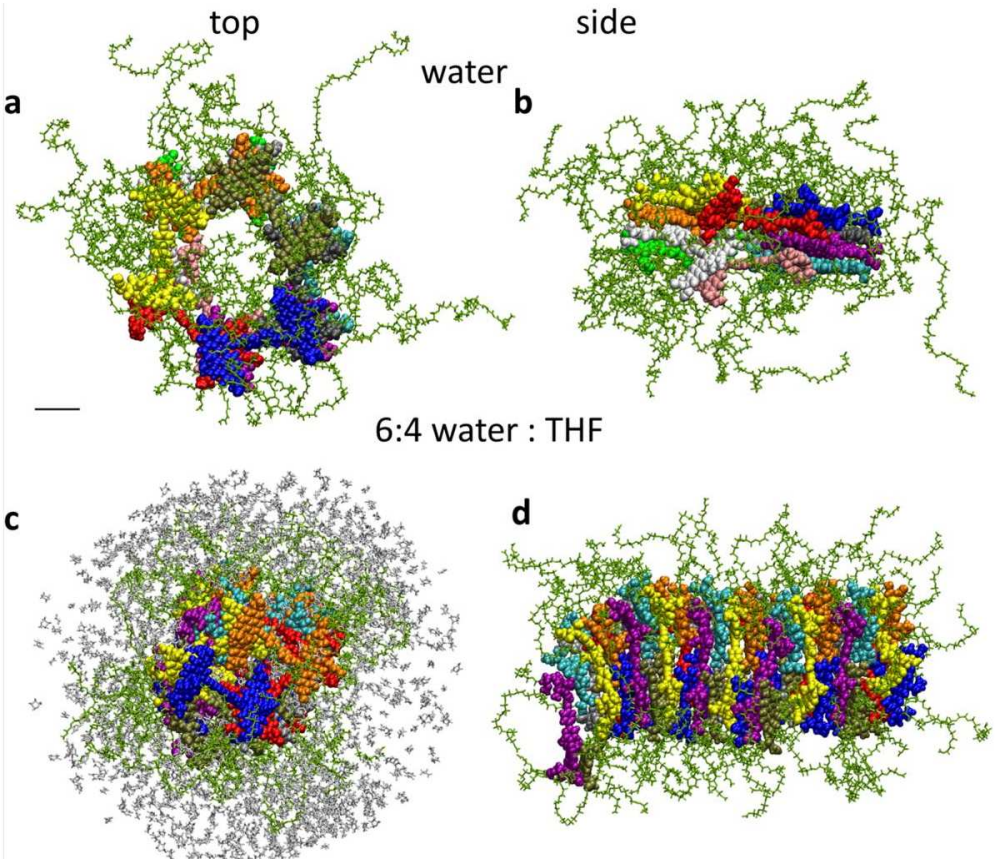

Figure 41: MD simulations of preassembled ONT superstructures from PEG-ylated PP2b monomers. (a-b) Top and side views of hexagonal superstructures of PP2b PEG44 in water at 100 ns. (c-d) Top and side views of square superstructures of PP2b PEG13 in water:THF (6:4) at 33 ns. Top view shows THF molecules (in gray) in the vicinity of a molecular nanotube.

tion of more closed nanotubes. A relative exposure of apolar PP2b regions to water might trigger a further transformation of the nanotubes into more compact fibers (as observed experimentally).

PEG13. Figure 41c-d show 40 PP2b PEG13 monomers preassembled into a rectangular superstructure in a water:THF (6 : 4) solvent simulated for 33 ns. In the square superstructure two opposite sides are placed in one layer and the two complementary sides on another layer. Over the simulation time, the square nanotube profile becomes deformed into a rhombus shape. Other deformations also appear within the nanotube, where the noncovalent interactions between the PDI groups become broken. Perhaps, the nanotube requires a partial clamping during its relaxation,

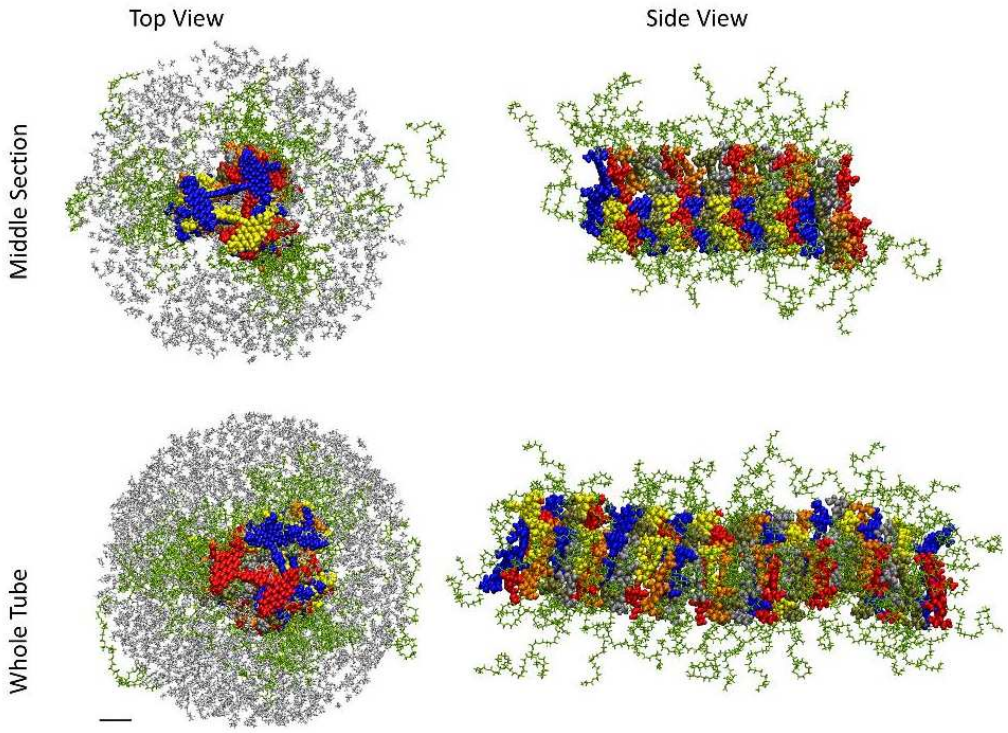

Figure 42: MD simulations of preassembled ONT superstructures from PEG-ylated PP2b monomers. Top and side views of helical ("triangle") superstructures of 29 PP2b PEG13 and 1 PP2b PEG44 in water:THF (6:4) at 20 ns. Top view shows THF molecules (in gray) in the vicinity of a nanotube. Scale bars are 1 nm.

when the solvent and PEG chains redistribute. For example, THF molecules might be needed in the hydrophobic core to prevent its dissolution. Figure 41c reveals that THF molecules largely assemble outside the nanotube. Flexibility of this superstructure may explain the experimentally observed rectangular-to-hexagonal tube conversion upon heating.

Figure 42 shows 29 PP2b PEG13 and one PP2b PEG44, present close to the nanotube center, preassembled into a helical nanotube in a water:THF (6 : 4) solvent, after 20 ns of simulations. The nanotube forms a helical structure (spiraling staircase), and its "triangular" shape is not much deformed during the simulations, consistent with the stability observed experimentally. The highly interconnected staircase structure appears to be responsible for the array's stability.

Overall, our simulations confirm that the formation of PP2b PEG assemblies is driven by side-by-side $\pi - \pi$ stacking/ hydrophobic interactions between the PDI groups leading to supramolecular oligomerization, which is a common process in all systems. Once the interaction has been established, it cannot be easily reversed. Importantly, *pairwise noncovalent interactions leading to side-by-side stacking appear to be a general initial step in oligomerization of bis-aromatic systems*, reminiscent of supramolecular polymerization of molecules bearing bifunctional noncovalent binding motif [221]. The insight into aromatic oligomerization in aqueous media and its relevance to tubular self-assembly has not been observed so far. Complete ring closure was not observed at the explored time scales as such nucleation events are slow and in general are difficult to observe in MD simulations [222]. Further MD studies aimed at elucidating the mechanism of tubular assembly are necessary in order to understand the entire assembly progression.

Conclusion

In conclusion, we have shown that symmetric bolaamphiphiles are capable of assembling into a variety of nanometer-scale nanotubes. Our experimental and theoretical studies reveal that an interplay of molecular structure and solvation specifics have a profound effect on self-assembly. This enabled tuning of molecular nanotube structures based on identical hydrophobic cores. Additionally, photoinduced symmetry-breaking charge transfer was observed in SNTs, demonstrating that SNTs enable photoactive wire function. Simplification of molecular design, control *via* self-assembly conditions, and photofunction provide tools to create complex functional supramolecular systems.

4.3 Atomically precise organomimetic cluster nanomolecules assembled via perfluoroaryl-thiol S_NAr chemistry

Adapted from Ref. [8] (*Nature Chemistry 2017*, 9 DOI:10.1038/NCHEM.2686) with permissions from Nature Publishing Groups.

Introduction

Natural systems have complex three-dimensional (3D) molecular architectures that interact at a high degree of specificity and fidelity. One example of such an interaction is multivalency that enables a variety of biological events by strengthening individually weak interactions between biomolecules that are either native or foreign to the organism [223]. These types of interactions are found a variety of processes, such as infection (viral/bacterial proteins-cell receptors), immune recognition (antibodies-cell receptors/antigens, cytokines-cell receptors) and gene-expression regulation (transcription factors-DNA). They occur due to the higher avidity and better recognition compared with the corresponding monovalent bindings [223, 224]. Chemists have taken an interest in developing synthetic multivalent ligands with the ability to bind specific target receptors with a high affinity in order to (1) elucidate the mechanistic details of multivalent interactions and to (2) promote or inhibit biological interactions of interest [225].

We develop a new strategy to build robust atomically precise hybrid nanomolecules using air-stable inorganic clusters [226–232], densely decorated with perfluoroaromatic functional groups. Using this organomimetic strategy [231], one can mimic the rigid surface of a Au-based nanoparticle core and simultaneously produce assemblies that are fully covalent and thus stable under relatively harsh conditions. We study dodecaborate clusters [231, 233–238] that have a dense layer of rigid pentafluoroaryl functional groups that can serve as excellent scaffolds for constructing atomically precise multivalent organomimetic cluster nanomolecules (OCNs). The perfluoroaryls can undergo nucle-

ophilic aromatic substitution (S_NAr) with a wide range of thiols at room temperature within hours, creating robust carbon-sulfur bonds ($80 - 90$ kcal mol^{-1}) [239] and thereby produce nanomolecules decorated with well-defined functional surfaces. This enables the functional advantages of using dendrimers at the same time mimicking the synthetic ease with which thiol-capped AuNPs are normally constructed. The resulting assemblies are highly rigid and can be synthesized and purified within hours, unlike the majority of dendritic scaffolds [240, 241]. In addition, these OCNs are purely covalent and feature improved stability in serum and various pH environments.

Experimental results

Next, to test whether more-complex molecular architectures could also be introduced onto the clusters, we turned our attention to poly(ethylene glycol) (PEG) 4,22,45,46. Complete 12-fold conjugation between 2 and commercially available mPEG-thiol (M_w = 356 Da) occurred within 24 hours at room temperature to yield OCN 2i (Figure 43, entry 1). Subsequently, larger mPEG-thiols (M_w = 766 Da and 2,000 Da) were tested and similarly afforded 2j and 2k, respectively, in quantitative conversions based on ^{19}F NMR spectroscopy (Figure 43, entries 2 and 3). As expected, PEGylation conferred considerable hydrophilicity to these clusters: 2i-2k are readily soluble in water. Owing to the full covalency of PEGylated OCNs, we hypothesized that these species should be structurally stable under biological conditions. Using 2i as a model, we conducted stability studies in biologically relevant media. A purified sample of 2i was exposed to cell-culture media that contained fetal bovine serum for five days at room temperature, and no changes or degradation products were observed by monitoring this sample by ^{19}F and ^{11}B NMR spectroscopy. Similarly, no degradation occurred when this sample was incubated for an additional five days at 37°C. Importantly, samples of 2i were dissolved in buffers of various pH (5, 7 and 9) for five days, and these were found to remain structurally intact as well. These results suggest that OCNs retain their structural integrity under

the wide range of biologically relevant conditions. We then decided to investigate the stability of the conjugation linkage between the cluster core and the thiol. Given the full covalency of 2i, we expected that it should not undergo ligand-exchange, a process that commonly occurs with many ligand-capped AuNPs [242]. Significantly, no thiol-exchange occurred when 2i (0.8 mM) was exposed to 2−mercaptoethanol (20 mM) over a period of 11 days. Similar results were obtained with 2 mM glutathione. Overall, these experiments clearly demonstrate that the OCNs constructed via the S_NAr approach feature superior robustness compared with many AuNP-based assemblies [243,244].

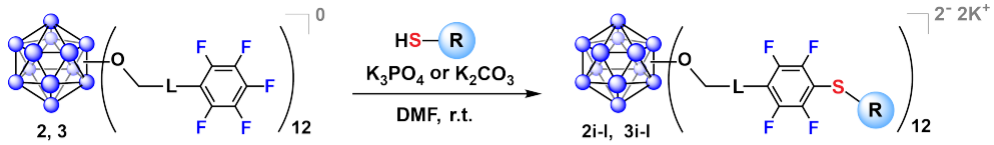

Symbol	L	R	Time (h)	*in situ* yield[a] (%)	Isolated yield[b] (%)
2i	none	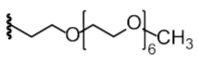	24	99	81
2j	none	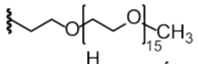	24	99	19
2k	none	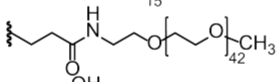	24	99	41
2l[c]	none	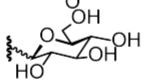	24	99	17
3i	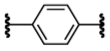	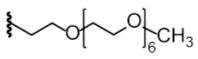	5	99	78
3j	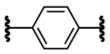	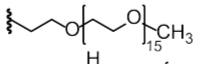	4	99	21
3k	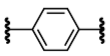	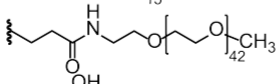	20[d]	99	54
3l[c]	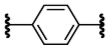	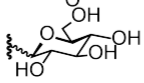	5	99	32

Figure 43: **PEGylation and glycosylation of 2 and 3.** *Yield determined by ^{19}F NMR spectroscopy; †Isolated yields after purification; ‡2l and 3l underwent partial K^+/Na^+ counterion exchange during the deprotection rection with NaOMe; §Small-scale reaction shows full conversion within 5 h.

PEGylated OCNs were characterized by a number of techniques to ensure their proposed nearly monodisperse composition (whereas the OCN cores are monodisperse, the PEG chains used in this

study feature some compositional variability because of the inherent limitations of PEG oligomer synthesis) 47 . First, we con- ducted 2D diffusion ordered spectroscopy (2D DOSY) ^1H NMR experiments with purified samples of 2i-2k and the more-extended OCNs 3i-3k (Figure 43, entries $5-7$) in D_2O. Based on the diffusion constants obtained from these 2D DOSY experiments, the respective hydrodynamic diameters were estimated (Figure 44a). As expected, the results reveal a gradual increase in the sizes of the PEGylated clusters, both as a function of the cluster core size (from 2 to 3) and the length of the PEG chain used. The size of 3i measured by 2D DOSY was larger than expected, most probably because of aggregation under the conditions the measurement was performed, which suggests the small number of PEG units in 3i could not fully stabilize the hydrophobic core against self-aggregation. To determine the size of a single non-aggregated OCN 3i, we performed additional transmission electron microscopy (TEM) experiments on 3i (Figure 44b). The TEM images reveal the presence of nearly monodisperse particles with an average size of 1.9 nm, which is in agreement with the expected value for a non-aggregated single particle. Consistent with these results, gel-permeation chromatography (GPC) traces of 2k and 3k in water (Figure 44c) also reveal nearly monodisperse samples ($D = 1.003 \pm 0.02$ and 1.081 ± 0.007, respectively). Furthermore, we performed molecular dynamics (MD) simulations of species 2i-2k and 3i-3k in water and calculated their hydrodynamic radii and radii of gyration (snapshots after 21 ns are shown in Figure 44d). The results are in good agreement with the non-aggregated OCN sizes measured by TEM, and moreover exhibit a trend similar to that observed by 2D DOSY. A small discrepancy arises between the sizes estimated based on computational studies/TEM and 2D DOSY and is probably due to some aggregation of the particles under the conditions employed in the 2D DOSY experiments. Overall, our measurements clearly show that using the developed S_NAr assembly strategy, one can rationally prepare robust and nearly monodisperse samples of size-tunable PEGylated OCNs.

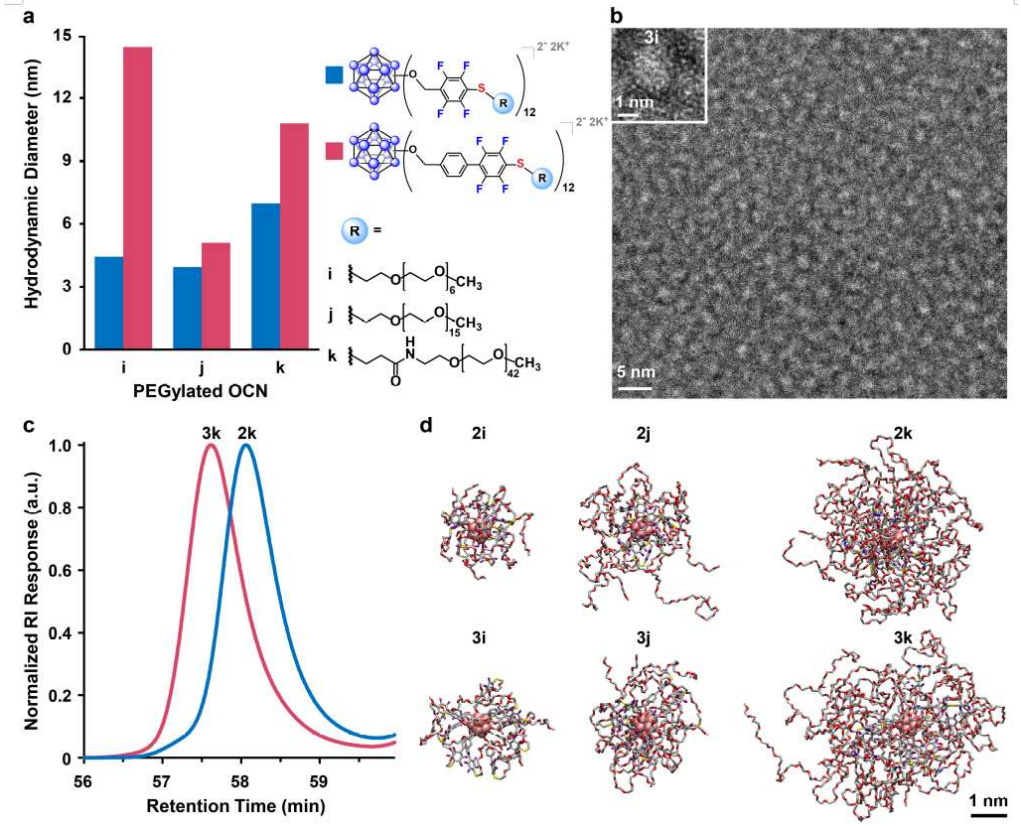

Figure 44: **Characterization of the PEGylated OCNs 2i-2k and 3i-3k.** a, Plot of the particle sizes of the PEGylated OCNs 2i-2k and 2i-2k obtained via 2D DOSY ^{1}H NMR experiments. The plot reveals a trend of a gradual increase in the sizes of the OCNs, both as a function of the cluster precursor dimension and of the chain length of the PEG reagent. The size of 3i is larger than expected, probably because of aggregation. b, TEM images of a negatively stained sample of 3i reveal the presence of nearly monodisperse particles with an average size of 1.9 nm, consistent with the expected size of 3i. c, GPC traces of 2k and 3k measured in water further confirm the monodispersity of the samples ($D = 1.003 \pm 0.02$ and 1.081 ± 0.007, respectively). d, MD-calculated structures of the PEGylated nanomolecules in pure water after 21 ns of simulation indicate a trend in the sizes of the OCNs consistent with that observed through the 2D DOSY experiments. RI, refractive index; a.u., arbitrary units.

MD simulations: methods and results

PEGylated nanoparticles (NPs) 2i-k and 3i-k (see Figure 43) were modeled using molecular dynamics (MD) simulations in: i) water with counter ions and ii) a buffer solution of HPO_4^{2-} and $H_2PO_4^-$ at a total 0.08 M concentration, where the ratio of the two ions was used matched pH 7.4. The MD simulations were performed with NAMD [37] , using the CHARMM force field [38–40, 56, 79, 80]. Ab initio calculations were done with Gaussian09 [74] to determine unknown parameters for the dodecaborate cluster center and the non-PEGylated (2 or 3 type ligand) section of the ligand. The boron center was optimized using a $HF/6-31$g level of theory, with partial charges derived with a ChelpG algorithm [76]. Bonds, angles, and dihedrals force constants containing boron atoms were chosen to have relatively large values, approximately equal to those of double bonded or aromatic carbons, so that the boron center would be rigid. The type 2 and 3 ligands had their bond and angle parameters determined at the $MP2/6-31g(d)//HF/6-31g$ level of theory with VMD Force Field Toolkit plugin [75]. Unknown dihedral parameters were chosen based on similar atom types in the CHARMM force field [38–40, 56, 79, 80]. Partial charges were determined through the ChelpG aglorithm [76]. Amide and PEGylated geometries, parameters, and charges were taken from the CHARMM force field [38–40, 56, 79, 80].

Each of the 6 NPs was separately simulated in water and ionic solutions. Each system is first minimized for 10,000 steps. Afterwards it is heated to 310 K, with 1 K increments per 20 steps until the system reaches a temperature of 310 K, when a pre-equilibration is done. Simulations are performed in an NPT ensemble, at 310 K and a pressure of 1 atm, with Langevin dynamics and a damping constant of 0.01 ps^{-1}. Langevin piston is used with a period of 200 fs and decay of 100 fs. Particle Mesh Ewald [57] is used for long range electrostatic interactions with a grid spacing of 1.0. Short range interactions are performed with the $12-6$ Lennard-Jones potential, using a

switching function. Velocity Verlet integration is used with the SHAKE algorithm and a time step of 2 fs. Data and snapshots are recorded every 10 ps or $5,000$ steps. Simulation times of 25 ns for the water solution and 30 ns for the salt system were used, respectively. Figure 45 and Figure 46 show snapshots of PEGylated NPs in water (21 ns) and in the ionic solution (31 ns), respectively. Notice that as the chain length increases, the chains are fluctuating significantly to the extent that the chain distributions become asymmetric. In the following, we describe some characteristics of these systems.

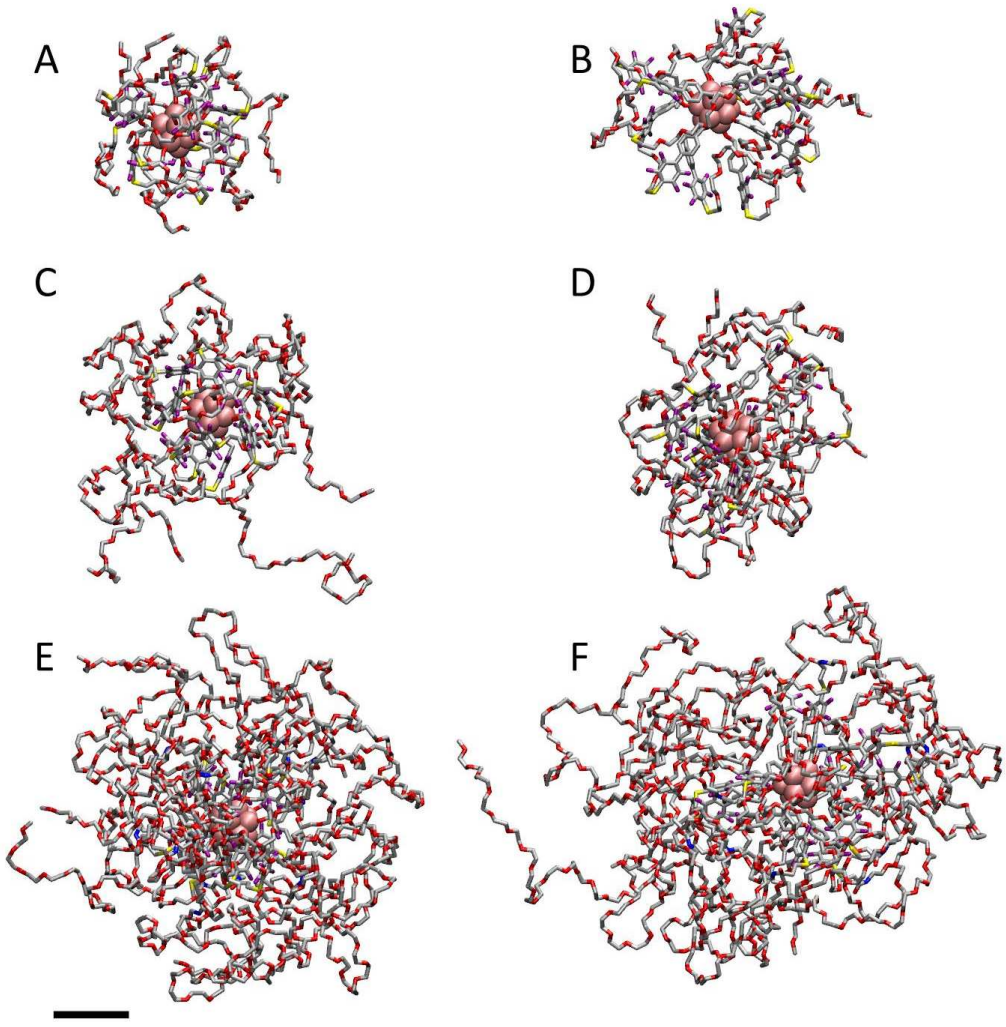

Figure 45: Nanoparticles snapshots in water after 21 ns of simulations. Scale bar is 1 nm. A) 2i B) 3i C) 2j D) 3j E) 2k F) 3k.

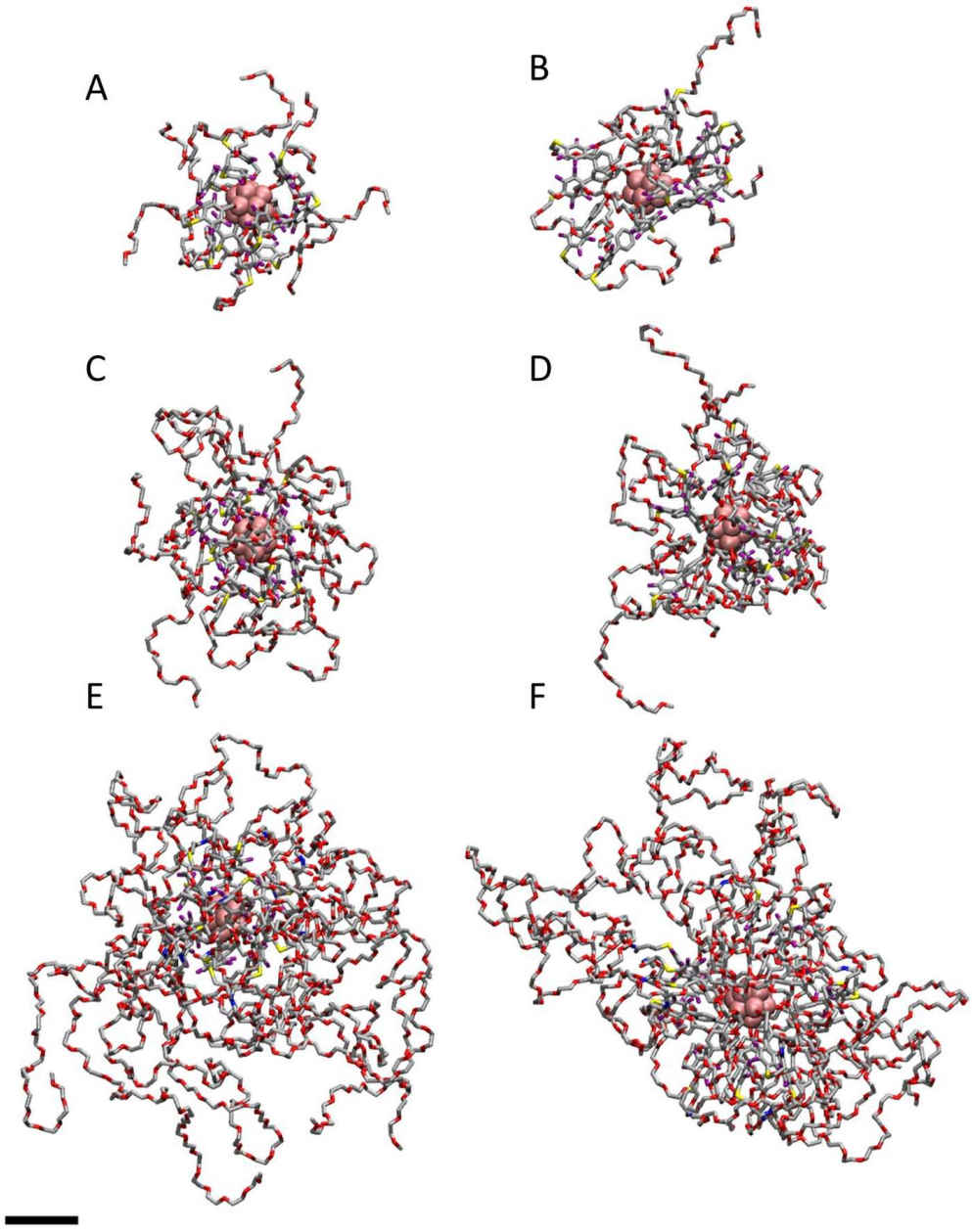

Figure 46: Nanoparticles snapshots in 0.08 M buffer solution at pH=7.4 (salt) after 31 ns of simulations. Scale bar is 1 nm. A) 2i B) 3i C) 2j D) 3j E) 2k F) 3k.

We use the simulated trajectories of the NPs to calculate the radial distribution functions (RDF), g(r), from Equation 4.3. It gives the relative probability of finding the j^{th} atom at a distance r from the i^{th} atom with respect to the bulk density:

$$g(r) = \frac{1}{V\rho_N} \sum \delta(r - r_{ij}). \tag{4.3}$$

In Equation 4.3, δ is a delta function, r_{ij} is the distance of i^{th} and j^{th} atoms, and V is a volume, $\int 4\pi r^2 dr$, used in a normalization, and ρ_N is the number density of the used species (the number of atoms N_O used in Equation 4.3 divided by the volume of the simulation box). We use Equation 4.3 when we analyze the distribution of C terminal atoms, which are fixed for a given number of ligands (12). When, we consider the distribution of all PEG-chain oxygens (varying number), we remove N_O (equal the total number of PEG chain oxygens) from ρ_N , by multiplying Eqn.1 by N_O , to get $g'(r)$, where we account for the growing distributions for longer PEG chains (more oxygens; system volume is fixed).

In Figure 47, we have calculated $g'(r)$ for (A, B) all the oxygens in PEGylated chains and g(r) for (C, D) terminal carbon atoms of the PEGylated chains. All the cases were calculated with respect to all the boron atoms. We can clearly see that as the chain becomes longer, the oxygen (A, B) distributions become wider and their peaks, r_{max} , become slightly shifted to higher values. Steric effects prevent longer PEGylated chains from folding and wrapping close to the B core, preventing them from significantly affecting r_{max}. The systems present in water and ionic solutions have almost the same PEG-oxygens distributions. On the contrary, in the terminal carbon (CD) distributions, the peaks maxima, r_{max} , are significantly shifted to higher values with the chain lengths, since the terminal C atoms are further away from the NPs cores, which they cannot reach. In these

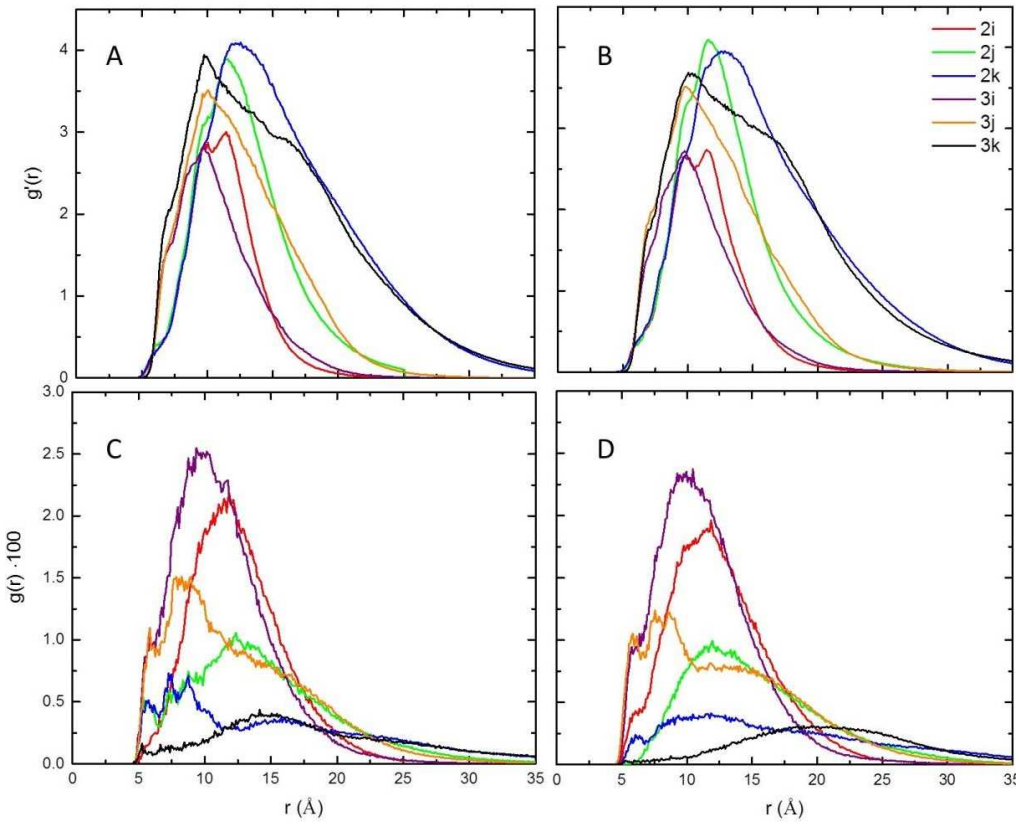

Figure 47: RDFs of 2i-k and 3i-k NPs. $g'(r)$calculated for A) boron-PEG oxygen atoms in water and B) boron-PEG oxygen atoms in ionic solution. $g(r)$ calculated for C) boron- terminal C atoms in water and D) boron-terminal C atoms in ionic solutions.

distributions, we can also see some differences between water and ionic solution cases, revealing that the terminal atoms in long PEGylated chains are slightly more outstretched in ionic solutions.

The $g'(r)$ distributions (Figure 47 A, B) are similar for the 2 and 3 types of ligands, except of some deformations present in the 3 types. These deformations slightly shift the 3 type peaks (r_{max}) to smaller values. For all but 2k and 3k terminal carbon RDFs, 3 type ligands have consistently smaller r_{max} values than their 2 type counterparts (Figure 47), even though 3 has an extra aromatic group, slightly increasing the maximum possible ligand length. The extra aromatic group in 3 ligands enhances $\pi - \pi$ stacking interactions between the ligands, thus causing the net length to decrease.

The split peak in 2i could be related to the fact that the B shell front and back sides can contribute by separate peaks.

The hydrodynamic radii of the studied NPs were estimated from the regions of decaying $g'(r)$ (half value compared to r_{max}) for the cases (A-B) (all oxygens). In water, the hydrodynamic radii of 2i and 3i are 12 Å; 2j and 3j are 15 Å; 2k and 3k are 20 Å. In the ionic solution, 2i, 3i, 2j, and 3j have very similar sizes as in water. At certain times, there are some chains on 2k or 3k that extend outwards, but most of the other chains are folded (Figure 45 E, F and Figure 46E, F). Interestingly, the maxima of distributions for the terminal C atoms in Figure 47C, D match relatively well to the hydrodynamic radii. One can assume that the terminal C atoms are distributed at the surface of the NPs, revealing thus their radii.

To confirm the previous results, next, the radii of gyration, $\langle r_{gyr} \rangle$, are also calculated for NPs using Equation 4.4:

$$r_{gyr} \equiv \sqrt{\frac{I}{m}} = \sqrt{\frac{\sum_{i=atoms} m_i (\vec{r}_i - \vec{r}_{com})^2}{\sum_{i=atoms} m_i}}. \tag{4.4}$$

Here, I is the moment of inertia of the molecule, m is the total mass of the molecule formed by individual contributions, m_i , of atoms shifted with respect to a molecular center of mass, $r_i - r_{com}$. Time averaged $\langle r_{gyr} \rangle$ was calculated by using Equation 4.4 every 10 ps over 26 ns trajectory (water) or 34 ns trajectory (salt solution) and then averaged. Standard deviations and confidence intervals were also computed.

Table X shows the radii of gyration, $\langle r_{gyr} \rangle$ and their $> 99.5\%$ confidence intervals for PEGylated species in water and salt solutions. As expected, 2i and 3i molecules have the smallest diameters, whereas 2k and 3k have the largest diameters in both environments. 2i and 3i molecules, with 7

Molecule	Solvent	$\langle r_{gyr} \rangle$ (Å)
2i	water	11.5 ± 0.9
2j	water	15.0 ± 1.7
2k	water	20.7 ± 2.2
3i	water	12.1 ± 1.2
3j	water	14.7 ± 1.3
3k	water	21.1 ± 2.0
2i	ionic solution	11.7 ± 1.0
2j	ionic solution	14.7 ± 2.0
2k	ionic solution	21.0 ± 2.5
3i	ionic solution	12.2 ± 1.5
3j	ionic solution	14.8 ± 1.6
3k	ionic solution	22.1 ± 4.5

TABLE X. RADII OF GYRATION, $\langle R_{GYR} \rangle$, AND THEIR CONFIDENCE INTERVALS FOR PEGYLATED SPECIES IN WATER AND SALT SOLUTIONS.

PEGylated oxygens per ligand have diameters of more than 2 nm; 2j and 3j, with 16 PEGylated oxygens per ligand, less than 3 nm; 2k and 3k, with 43 oxygens per ligand, more than 4 nm. NPs with the type 3 ligands tend to have a slightly larger diameter than those with the type 2 ligands. This size increase could be due to the extra aromatic group in type 3 ligands, which is absent in the 2 type ligands. $\langle r_{gyr} \rangle$ does not change appreciably between the two environments. However, 2k and 3k ligands are slightly more outstretched in the ionic solutions.

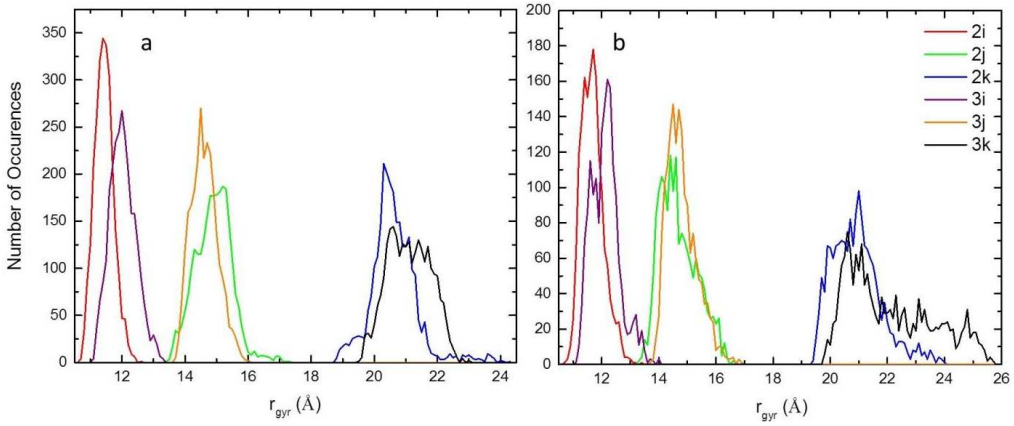

Figure 48: Distributions of r_{gyr} in a) water and b) ionic solutions.

Figure 48a and b show the distributions of r_{gyr} in water and salt solutions, respectively. The distributions are asymmetrically broadened at higher values for all molecules, especially for long chains. This reflects that a few chains could extend and then fold back. Comparing the radii of gyration, $\langle r_{gyr} \rangle$, from Table X and Figure 48 with the above hydrodynamic radii and the most likely positions of terminal C atoms, we can see that all these parameters are in good agreement.

Conclusion

We have developed a new strategy that allows a rapid assembly of fully covalent nanoparticles with atomic precision. Specifically, we demonstrated that the rigid clusters densely decorated with perfluoroaryl-containing functional groups undergo efficient conjugation with a variety of thiols via $S_N Ar$ chemistry under very mild conditions at room temperature. Importantly, this chemistry is operationally reminiscent of the chemoselective assembly conditions associated with thiol-capped AuNPs. Furthermore, similarly to thiol-capped AuNPs, these OCNs can be easily tuned in size and surface chemistry by choosing a specific thiol reagent. OCNs exhibit dramatically improved structural stability under a wide range of biologically relevant conditions because of the full covalency of all the bonding interactions that comprise these nanomolecules. Finally, using this assembly strategy we show how one can design and synthesize nanomolecules that feature a 3D densely packed layer of saccharides that can participate in multivalent binding with a natural lectin and lead to a dramatic increase in binding affinity. This work ultimately opens a new avenue to create highly tailored synthetic mimics of ligand-capped AuNPs that feature rigid and fully covalent atomically precise assemblies.

4.4 Hybridization of Biomolecular Crystals and Low Dimensional Nanomaterials

Introduction

In recent years, planar and fibrillar crystals of metabolites, peptides, and other biomolecules were observed to form in cellular biosystems, where they are often toxic [245–247]. When these low-dimensional biomolecular crystals are adsorbed on inorganic nanomaterials or intercalated between them, they could form novel hybrid materials [248, 249]. Individual solvated biomolecules can easily be adsorbed on material surfaces [250–261]. Amino acids, peptides and nucleobases tend to couple to nanocarbons by a $\pi - \pi$ stacking of their aromatic groups. On the other hand, graphene and hydrophobic nanoparticles can be intercalated in biological membranes [262, 263]. When molecular crystals are hybridized with inorganic nanomaterials, each of the sub-component could provide complementary properties to the hybrid materials and affect each other.

Here, we apply atomistic molecular dynamics (MD) simulations to study complexation of biomolecular crystals and inorganic nanomaterials that can couple by a van der Waals (vdW) coupling [264]. As typical examples, we consider enantiopure and racemic crystals of tryptophan (TRP) and phenylalanine (PHE) [36, 44, 265] that have indole and phenyl side groups, respectively. We study hybrid nanostructures formed by biomolecular crystals adsorbed on planar and cylindrical nanosurfaces of graphene, phosphorene, and carbon nanotubes or intercalated in graphene cells.

Methods

Graphene and CNTs were constructed with Nanotube Builder in VMD [59]. Phosphorene was based on a single unit cell of 4 phosphorus atoms [266], which was propagated in two orthogonal directions. For simplicity, atoms on the nanosurfaces were not charged and not terminated by hydrogens. The polarizability of nanomaterials was neglected, even though armchair CNTs have a

metallic character. L-TRP-C, A-TRP-C, and L-PHE-C were constructed using known crystallographic data [36, 44, 265].

The MD simulations were performed with NAMD2.12 [37], using a CHARMM force field for metabolites and carbon atoms [56], whereas phosphorus atoms used another force field [266]. The TIP3P water model was employed for explicit water simulations. Non-bonded interactions used the switching algorithm, with the switch-on distance at 10 Å and the switch-off at 12 Å. Non-bonded pair lists were used for atoms within 13.5 Å of each other, with the list updated every 20 steps. $1-4$ non-bonded interactions were not scaled.

The Langevin dynamics was used with a damping constant of $\gamma_{Lang} = 1$ ps^{-1}, a piston period of 100 fs, a piston decay of 50 fs and a piston temperature of 310 K. The Velocity Verlet integrator was used to solve the equations of motion, with a time step of 2 fs. The SHAKE algorithm was used for hydrogens. Solvated simulations were done in the NPT ensemble with periodic boundary conditions applied, pressure of 1 atm, and under physiological conditions, [NaCl] = 0.15 M, with amino acids in zwitterionic forms and hydrogens excluded from the thermal bath. Simulations involving crystals sandwiched between graphene layers (without water) were done in the NVT ensemble, and periodic boxes 50% larger than the crystal-graphene systems. Except minimization, Particle Mesh Ewald summation [57] was used with a grid spacing of 1.0. Graphene sheets with L-TRP-C were minimized for 50,000 steps, whereas all other systems were minimized for 5,000 steps. During minimization and pre-equilibration, heavy atoms of amino acids and nanosurface atoms were constrained, but they well all released during the simulations. Data and snapshots were recorded every 10 ps.

The binding energies, with electrostatic and dispersion contributions, were calculated every 10 ps. Amino acids were classified as: 1) molecules that were in the layer of the crystal in direct contact with the nanosurfaces and stayed intact (labeled as *bottom*), colored orange in Figure 49, Figure 51

and Figure 54; 2) molecules that were in the layer away from the nanosurfaces and stayed intact (labeled as *top*), colored red in Figure 49, Figure 51, and Figure 54; and 3) molecules that dissolved from the crystal (labeled as *free*), colored gray in Figure 49, Figure 51, and Figure 54. Intra-crystal interaction energies were calculated between molecules within the same layer and between different layers, and normalized with respect to the number of molecules in each layer. The interaction energies between bottom amino acids and CNTs were normalized with respect to the number of amino acids that were within 4.5 Å of CNT at each time step. The coupling energies of free metabolites were normalized with respect to the number of amino acids that were within 4.5 Å of the nanosurfaces.

Results

Biomolecular crystals on planar nanosurfaces

Initially, we prepared a small bilayer L-TRP crystal (L-TRP-C) [36], placed it on a graphene sheet, shown in Figure 49a-c, and L-TRP-C, placed on a phosphorene sheet, as shown in Figure 49d-f. These systems were simulated in a physiological solution ($T = 310$ K) for 335 ns and 100 ns, respectively. The biomolecular crystals translated by diffusion on both nanosurfaces, but their motion was more constrained on phosphorene, due to its unidirectional grooves (Figure 49f). Nevertheless, the crystals remained largely intact on both nanosurfaces, with only a few molecules being dissolved.

When L-TRP-C, elongated along its aromatic zipper, was simulated in a physiological solution, it twisted (Figure 51a), signaling that it might form fibrils [1, 2]. Therefore, we simulated this L-TRP-C adsorbed on graphene and phosphorene nanoribbons in a physiological solution, shown in Figure 51b,c, respectively. However, within 100 ns simulations, L-TRP-C twisted much less on these nanosurfaces, most likely due to their relative rigidity. To promote a crystal twisting, we simulated L-TRP-C on deformed surfaces (below), in analogy to graphene adsorbed on CNTs [249].

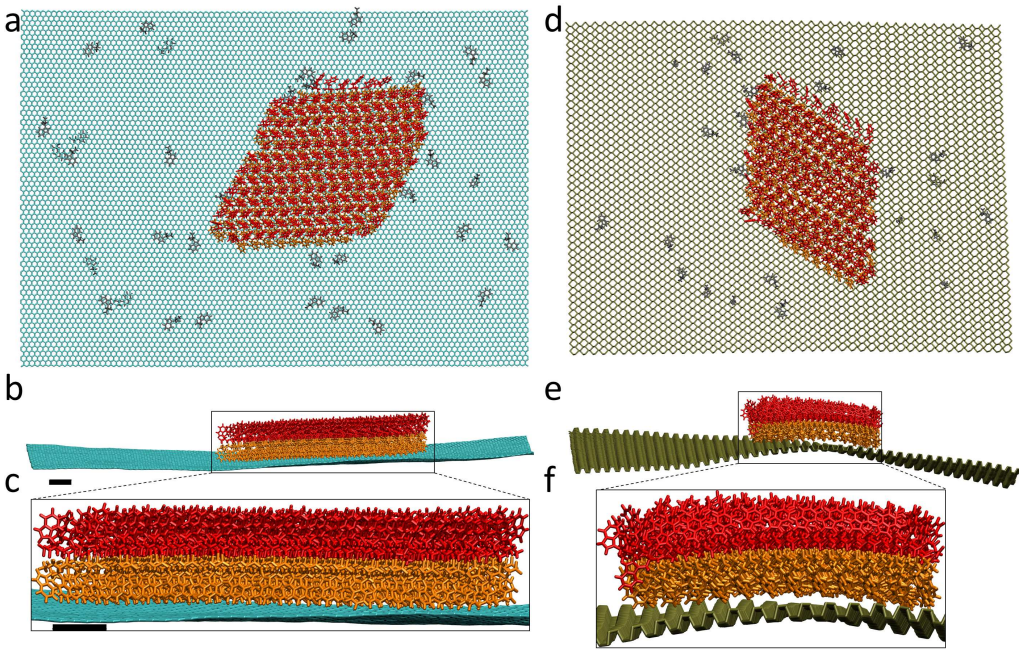

Figure 49: (a-c) L-TRP-C ($14 \times 14 \times 2$ amino acids) adsorbed on a graphene sheet (16.0×22.8 nm^2) after 335 ns of simulations in a physiological solution (top and side views). Isolated dissolved TRPs are omitted in side views. (d-f) L-TRP-C ($12 \times 12 \times 2$ amino acids) adsorbed on a phosphorene sheet (14.8×19.7 nm^2) at 100 ns. Scale bars are 1 nm.

L-TRP-Cs were simulated on graphene strips shown in Figure 49, Figure 51 and Figure 50. In all three systems, the molecular crystals diffused, without dissociating from the graphene. The crystals remained largely intact after 335 ns, 100 ns, and 560 ns, respectively.

L-TRP-Cs were also simulated on phosphorene strips shown in Figure 49, Figure 51 and Figure 52. In Figure 49 and Figure 52, the aromatic zipper of L-TRP-Cs were randomly oriented with respect to phosphorene grooves. All systems were simulated for 100 ns. The molecular crystals remained relatively static with respect to phosphorene, which largely inhibited their diffusion, in contrast to graphene.

When a racemic (achiral) bilayer TRP crystal (A-TRP-C) was simulated in a physiological solution, it manifested small bending fluctuations, as shown in Figure 51d, but on average it remained

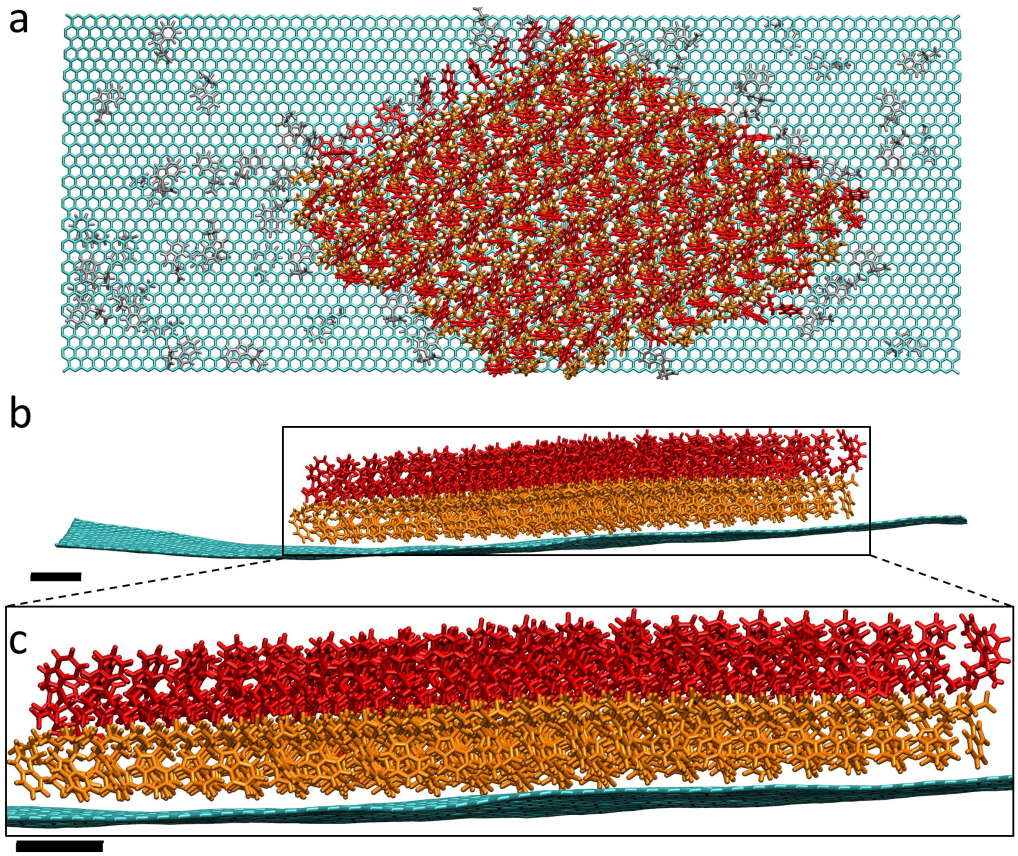

Figure 50: L-TRP-C ($14 \times 14 \times 2$ amino acids, with 6 amino acids omitted at the corner) and placed on graphene ribbon (7.1×17.9 nm^2) after 560 ns of simulation. (a) Top view, alongside solvated amino acids. (b,c) Side views, c is enlarged version, solvated amino acids are not shown. Scale bars represent 1 nm.

flat, regardless on the long axis orientation of the crystal (parallel or orthogonal to the aromatic zipper) [2]. When A-TRP-C was simulated (100 ns) with the long axis parallel to the aromatic zipper on the same graphene nanoribbon, it diffused along the nanoribbon, but it remained largely planar without significant bending fluctuations (Figure 51e).

In contrast, a freely solvated L-PHE-C cut orthogonal to the zipper was significantly twisting [2] (Figure 51f). When simulated on graphene nanoribbons, L-PHE-C was cut with their long axis orthogonal with respect to the aromatic zipper, Figure 51g, and parallel to it, as discussed in SI. After 100 ns, L-PHE-C with the orthogonal cut became significantly twisted on the graphene nanoribbon

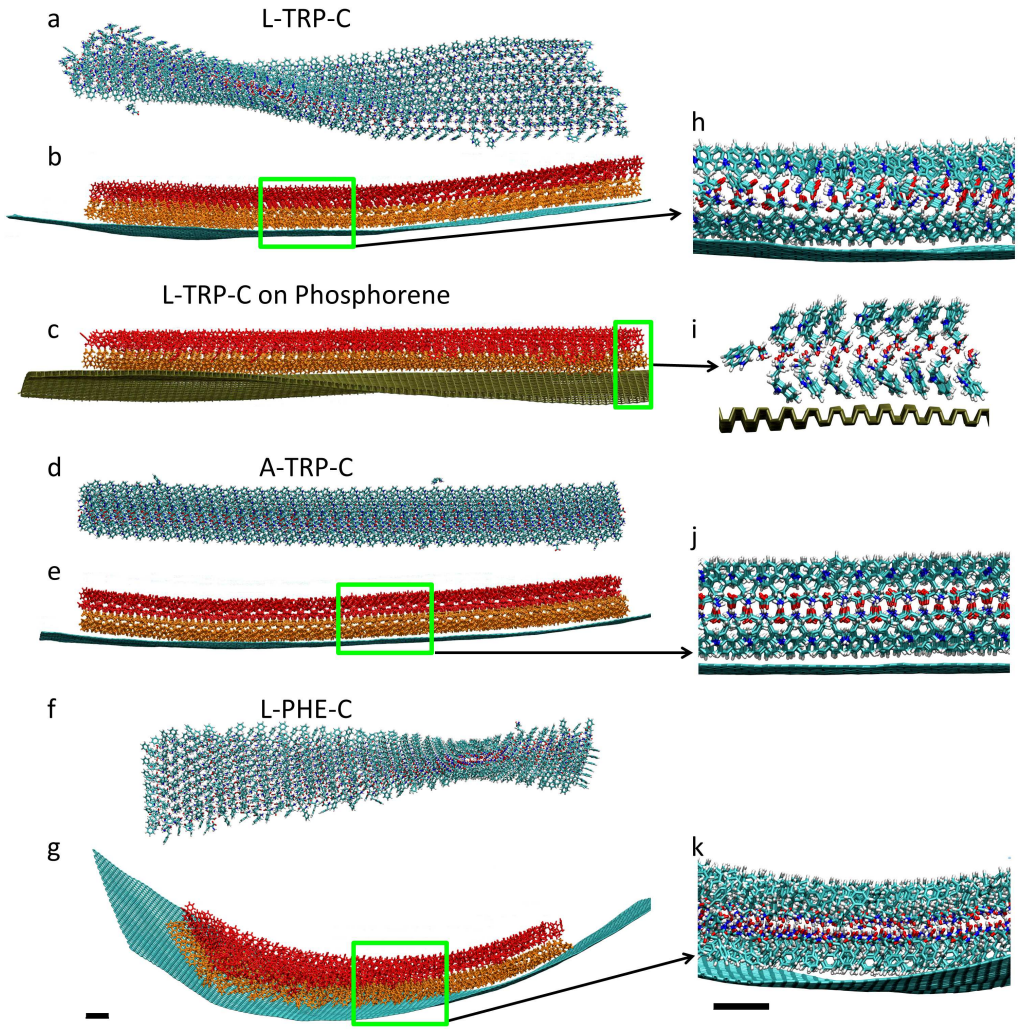

Figure 51: L-TRP-C ($40 \times 8 \times 2$ amino acids): (a) freely solvated in a physiological solution at 20 ns and (b) adsorbed on a graphene nanoribbon (7.9×28.9 nm^2) at 100 ns. (c) L-TRP-C from (a) on a phosphorene nanoribbon (33.0×12.3 nm^2) at 100 ns. (d) A-TRP-C ($40 \times 8 \times 2$ amino acids) freely solvated at 20 ns and (e) adsorbed on a graphene nanoribbon from (b) at 100 ns. (f) L-PHE-C ($8 \times 40 \times 2$ amino acids) freely solvated and (g) adsorbed on a graphene nanoribbon from (b) at 100 ns. (h-k) Magnified views of L-TRP-C, L-TRP-C on graphene and phosphorene nanoribbons, A-TRP-C, and L-PHE-C on graphene nanoribbons. Scale bars are 1 nm.

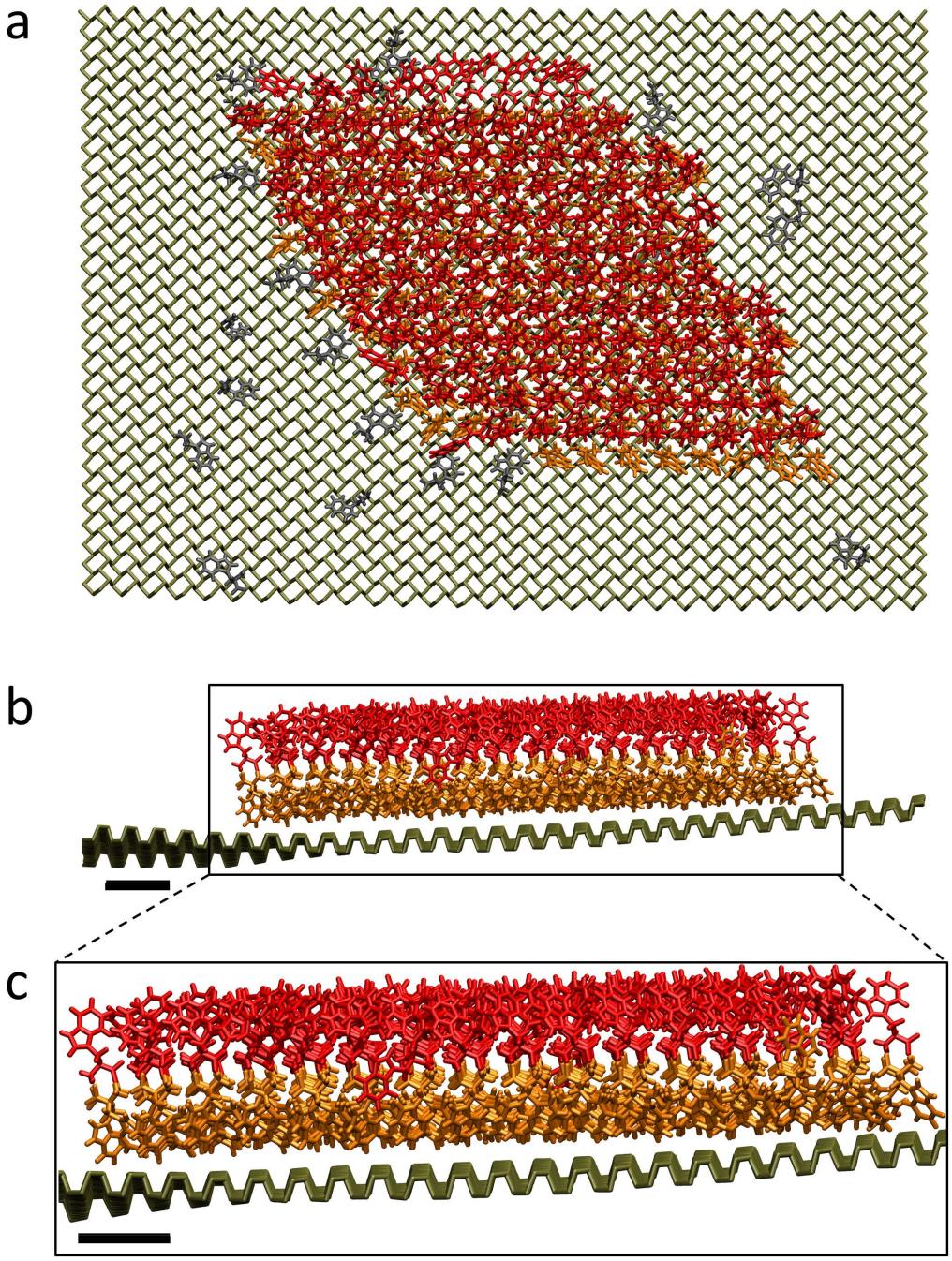

Figure 52: L-TRP-C ($12\times12\times2$ amino acids) and placed on the phosphorene ribbon (9.8×13.1 nm^2) at 100 ns. (a) Top view, alongside solvated amino acids. (b,c) Side views, (c) is enlarged version, solvated amino acids are not shown. Scale bars represent 1 nm.

(Figure 51g). The overall nanostructure became helical, which could provide the twisted (helical) graphene an optical activity in CD spectra. However, L-PHE-C with the parallel cut remained relatively flat and only slightly cracked on the graphene nanoribbon (Figure 53).

L-PHE-C was also differently cut and simulated on the graphene nanoribbons as in Figure 51b,e,g. L-PHE-C cut orthogonally to aromatic zipper is discussed in Figure 51g. L-PHE-C cut parallel to the aromatic zipper (Figure 53) bent orthogonally to the long axis of the crystal. After $\approx$ 30 ns, it formed a crack, which remained there through the rest of 100 ns simulations. Moreover, the graphene surface slightly bent like in the L-TRP-C or A-TRP-C systems, but not like in L-PHE-C oriented orthogonally.

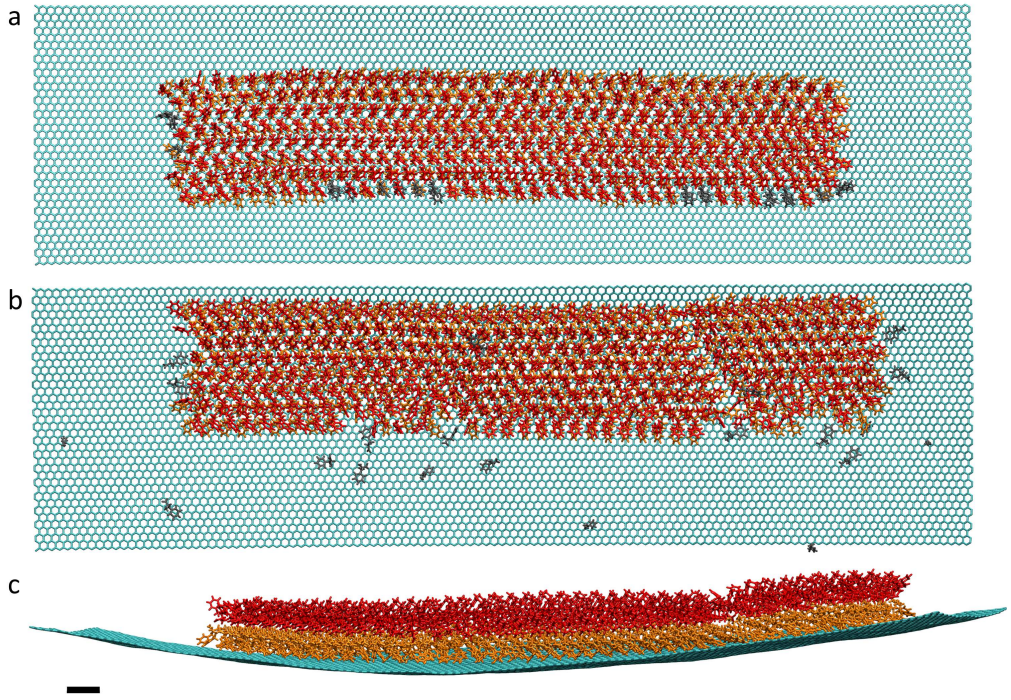

Figure 53: L-PHE-C oriented parallel ($40 \times 8 \times 2$ amino acids) to the aromatic zipper and placed on the graphene ribbon (7.9×28.9 nm^2). (a) Initial setup; (b,c) at 100 ns top and side views, respectively. Scale bar represents 1 nm.

In order to check the stability of molecular crystals adsorbed on nanomaterial surfaces, we have calculated intra-crystal (within molecular crystal) and inter-crystal (between crystal and nanoma-

terial) coupling energies of individual amino acids to their neighborhoods (SI). The intra-crystal coupling energies have been separately calculated for freely solvated crystals. In both PHE and TRP systems, the intra-crystal coupling energies were relatively large ($20 - 100$ kcal/mol) and practically unaffected by the presence of nanomaterials. The inter-crystal coupling energies were much weaker ($4 - 8$ kcal/mol), but they were slightly larger for amino acids freely adsorbed on nanomaterials ($15 - 20$ kcal/mol). Since the intra-crystal energies dominated, the molecular crystals had the tendency to stay relatively intact when adsorbed on nanomaterials.

Biomolecular crystals on carbon nanotubes

Next, we studied the adsorption of biomolecular crystals on CNTs submerged in a physiological solution. First, a $(35, 35)$ CNT was placed $2 - 4$ Å above the center of L-TRP-C and parallel to its aromatic zipper, as shown in Figure 54a. The adsorption of L-TRP-C on CNT occurred in steps (100 ns, 120 ns), determined by the initial configurations. Figure 54b,c show that L-TRP-C wrapped smoothly around CNT within 417 ns, without being significantly damaged. All enantiopure L-TRP-Cs twisted on CNTs in the same helical fashion (see Figure 55), due to their chiral structure. Even freely solvated L-TRP-Cs twisted in a similar manner, as shown in Figure 51a. Larger crystals might form multilayer systems or other superstructures [248, 249]. However, molecular crystals adsorbed on CNTs of very small diameters could break down, depending on their internal stability.

Biomolecular crystals were also modeled on carbon nanotubes (CNTs), as shown for L-TRP-Cs in Figure 54a,b,c and Figure 55. L-TRP-Cs were cut with their long axis parallel to the aromatic zipper and parallel to the axis of their CNTs, with initial setup of each system shown in Figure 54a and Figure 55a,d,g,j,m. All these enantiopure crystals twisted and wrapped around CNT in the same helical direction, as seen in Figure 54b,c and Figure 55. Smaller crystals, such as L-TRP-C

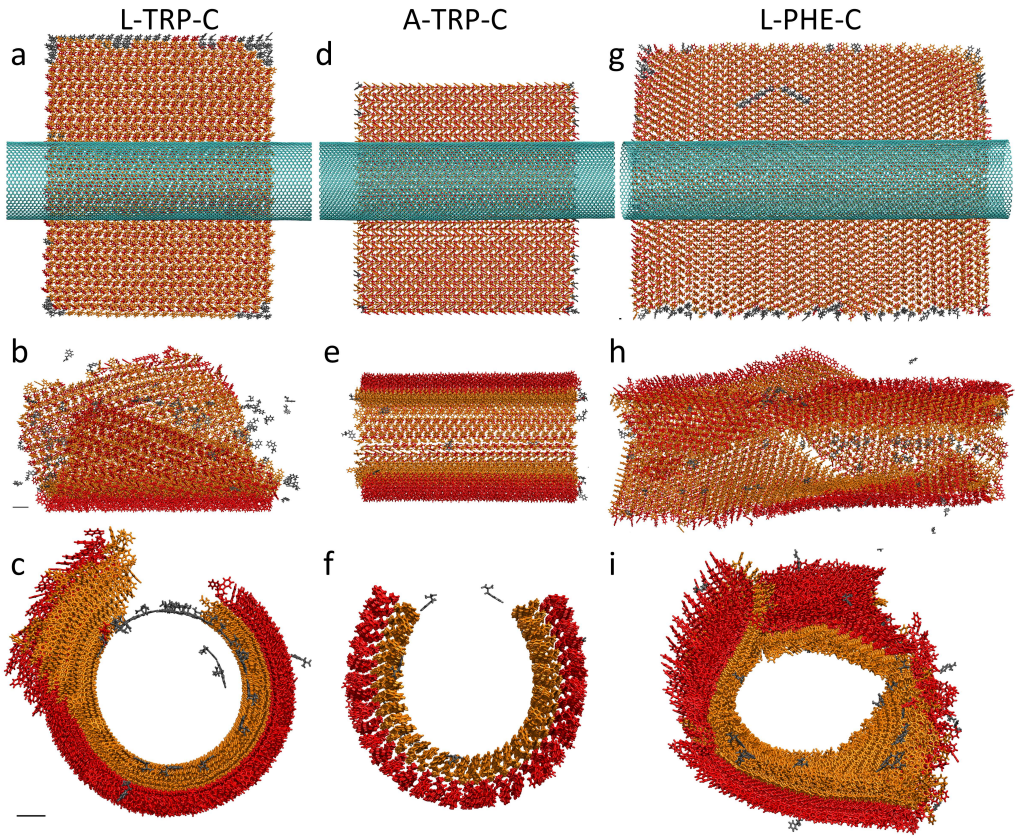

Figure 54: (a-c) (35, 35) CNT (18.8 nm long) was placed at the center of L-TRP-C (48 × 34 × 2 amino acids) and simulated for 417 ns (top - start, middle and bottom - CNT not shown). (d-f) This CNT was placed above the center of A-TRP-C (48 × 34 × 2 amino acids) and simulated for just 15 ns. (g-i) (35, 35) CNT (21 nm long) was placed above the center of L-PHE-C (34 × 48 × 2 amino acids) and simulated for 94 ns. Scale bar represents 1 nm.

(73 × 8 × 2 amino acids) in the presence of (18, 18) CNT (21.5 nm long) or L-TRP-C (60 × 20 × 2 amino acids) in the presence of (35, 35) CNT (21.5 nm long), wrapped around their respective CNTs relatively easily (Figure 55a,g). Larger crystals, such as L-TRP-C (60 × 20 × 2 amino acids) in the presence of (18, 18) CNT (21.5 nm long) or L-TRP-C (48 × 34 × 2 amino acids) in the presence of (35, 35) CNT (18.8 nm long) wrapped CNTs more slowly (Figure 55d,j). When a (35, 35) CNT (18.8

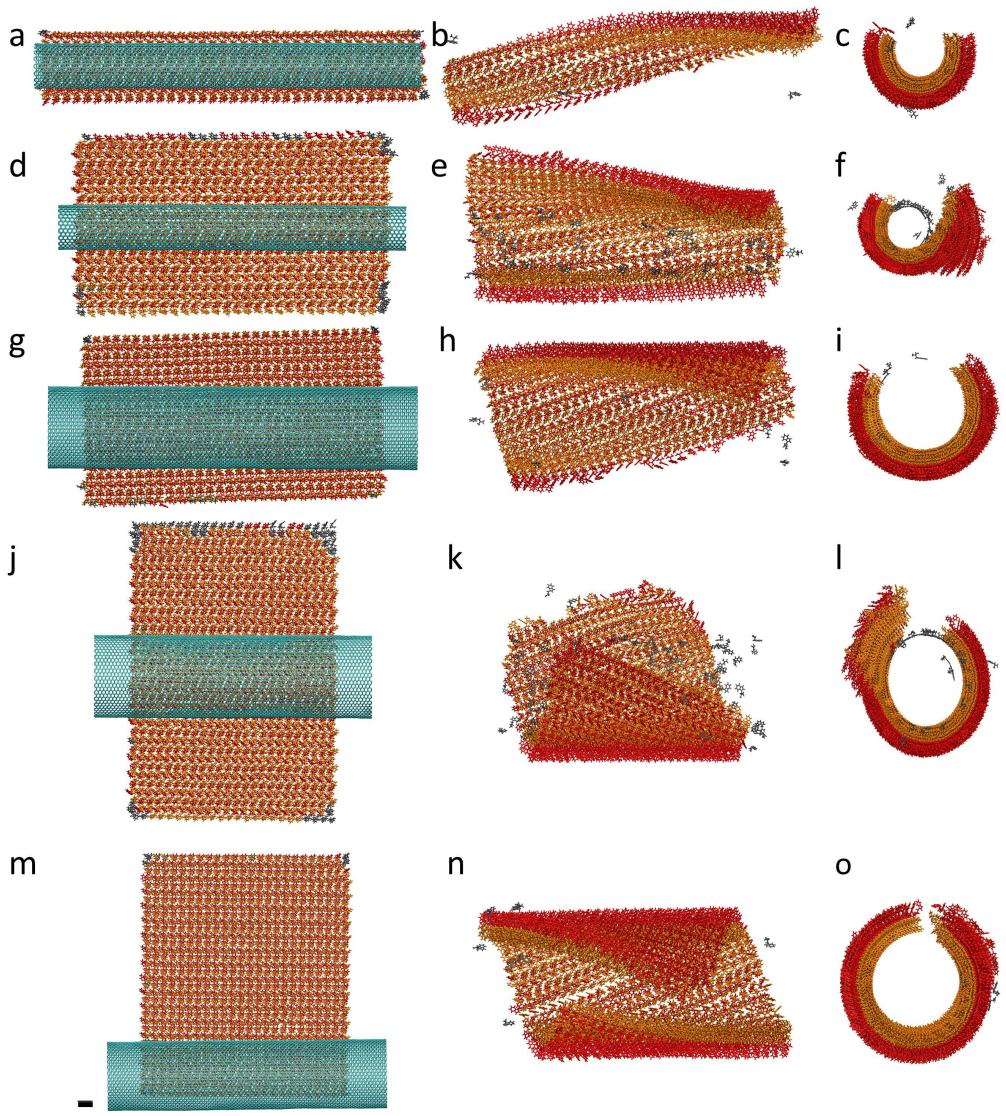

Figure 55: Different L-TRP-C CNT systems. (a) Initial setup of L-TRP-C ($73 \times 8 \times 2$ amino acids) in the presence of $(18, 18)$ CNT (21.5 nm long). (b,c) Top and side views of system in (a) at 33 ns. (d) Initial setup of L-TRP-C ($60 \times 20 \times 2$ amino acids) in the presence of the $(18, 18)$ CNT (19.3 nm long). (e,f) Top and side views of system in (d) at 248 ns. (g) Initial setup of the same crystal as in (d) in the presence of $(35, 35)$ CNT (21.5 nm long). (h,i) Top and side views of system in (g) at 54 ns. (j) Initial setup of L-TRP-C ($48 \times 34 \times 2$ amino acids) and $(35, 35)$ CNT (18.8 nm long). (k,l) Top and side views of system in (j) at 417 ns. (m) The same L-TRP-C and CNT as in (j), but CNT is placed on the edge of the crystal. (n,o) Top and side views of system in (m) at 70 ns. The CNTs are shown only at initial setup (a,d,g,j,m). Scale bar represents 1 nm.

nm long) was placed on the side of L-TRP-C ($48 \times 34 \times 2$ amino acids), it wrapped around it faster (Figure 55m).

We have also simulated the adsorption of A-TRP-C on this CNT aligned along the aromatic zipper. When CNT was placed above the center of A-TRP-C, the crystal wrapped within 15 ns around CNT, as shown in Figure 54d,e,f. The racemic crystal neatly folded around CNT without twisting (see also Figure 56). Different wrapping styles and speeds originated in different crystal structures [2]. Since, A-TRP-C has a plane of symmetry at the center of its unit cell, which is absent in L-TRP-C, it can be bent more easily than L-TRP-C, despite A-TRP-C being flat and L-TRP-C being twisted in solution. However, the intra-crystal or inter-crystal coupling energies are alike in both crystals.

Racemic TRP crystals (A-TRP-C) with a $1:1$ ratio of left and right-handed enantiomers were also modeled in Figure 54d,e,f and Figure 56. The A-TRP-C systems were set up analogously to the L-TRP-C systems in Figure 55j,m. A-TRP-C immediately wrapped around CNT, in contrast to enantiopure crystals. The intra-crystal and inter-crystal coupling energies between individual molecular components for both L-TRP-C and A-TRP-C were within ≈ 5 kcal/mol. Therefore, these coupling energies probably cannot explain a different wrapping dynamics of these crystals, which most likely originated from their different crystal structures: in A-TRP-C, one unit cell has a plane of symmetry, unlike in L-TRP-C [2].

Figure 54g,h,i also show (94 ns) wrapping of L-PHE-C around this CNT, oriented orthogonal to the aromatic zipper of the crystal. L-PHE-C became twisted and developed cracks, revealing that it is more fragile than L-TRP-C. Similar cracking happens when the L-PHE-C zipper is aligned along CNT (see SI). However, L-PHE-C is pretty stable on less deformed surfaces (Figure 51g,k).

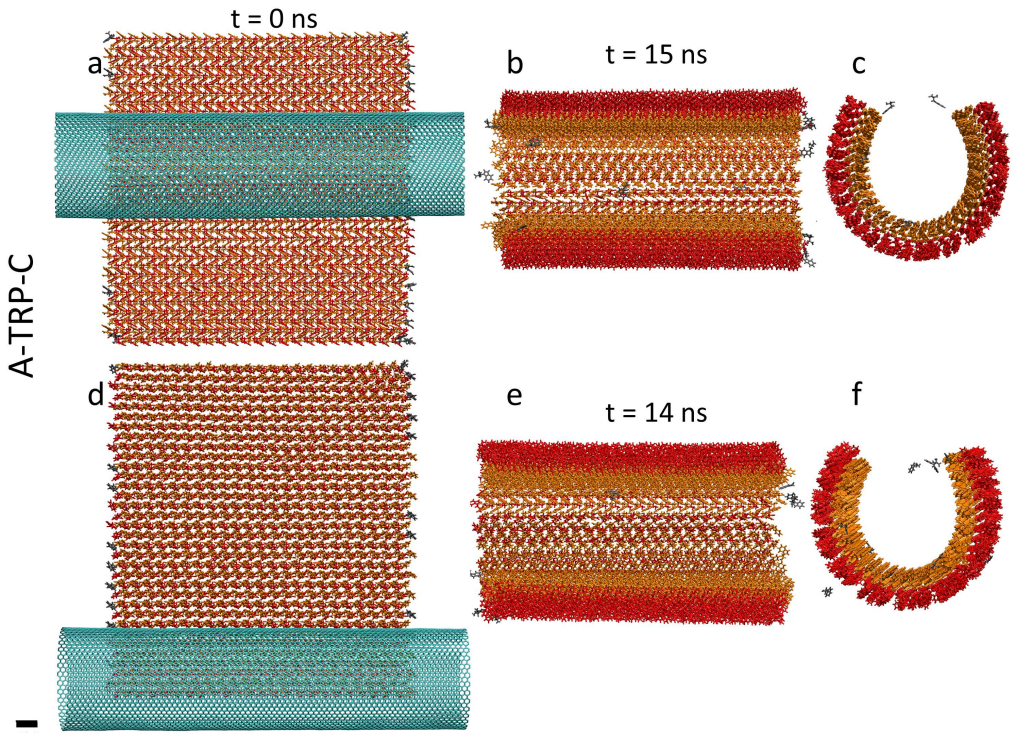

Figure 56: (a-c) A-TRP-C ($48 \times 34 \times 2$ amino acids) and $(35, 35)$ CNT (21.5 nm long) placed above the crystal center. (a) Initial setup; (b,c) top and side views at 15 ns, respectively. (d-f) A-TRP-C with the same CNT placed on the side of the crystal. (d) Initial setup; (e,f) top and side views at 14 ns, respectively. Scale bar represents 1 nm.

In Figure 54g,h,i, L-PHE-C was cut orthogonally to the aromatic zipper and its center was placed below the $(35, 35)$ CNT. Figure 57a,d,g,j show the initial configurations of four more systems. In one pair of the systems, the long axis of the crystal was cut parallel to the aromatic zipper ($48 \times 34 \times 2$ amino acids) and the CNT was placed above the center or edge of the crystal. In the other pair, the crystal was just cut orthogonally to the aromatic zipper ($34 \times 48 \times 2$ amino acids). In all these L-PHE-C systems, the crystal-nanomaterial coupling was relatively strong (by $\approx 10-15$ kcal/mol more than L-TRP-C or A-TRP-C), so that cracks appeared in L-PHE-C mostly oriented orthogonally to the aromatic zipper (slight energetic favorability ≈ 10 kcal/mol). From the same reason CNT was also slightly deformed from its circular cross-section. When L-PHE-C was cut orthogonally to the

aromatic zipper, it wrapped around CNT placed below the center of the crystal (Figure 57g), due to the combination of the long axis of the crystal being favorable and the relative position of CNT. The L-PHE-Cs dynamics was similar to that of L-TRP-Cs, due to helical unit cells, which caused the crystals to twist in a helical way. Moreover, the enantiopure crystals wrapped in leaps, unlike the racemic crystals, A-TRP-Cs, wrapping continuously.

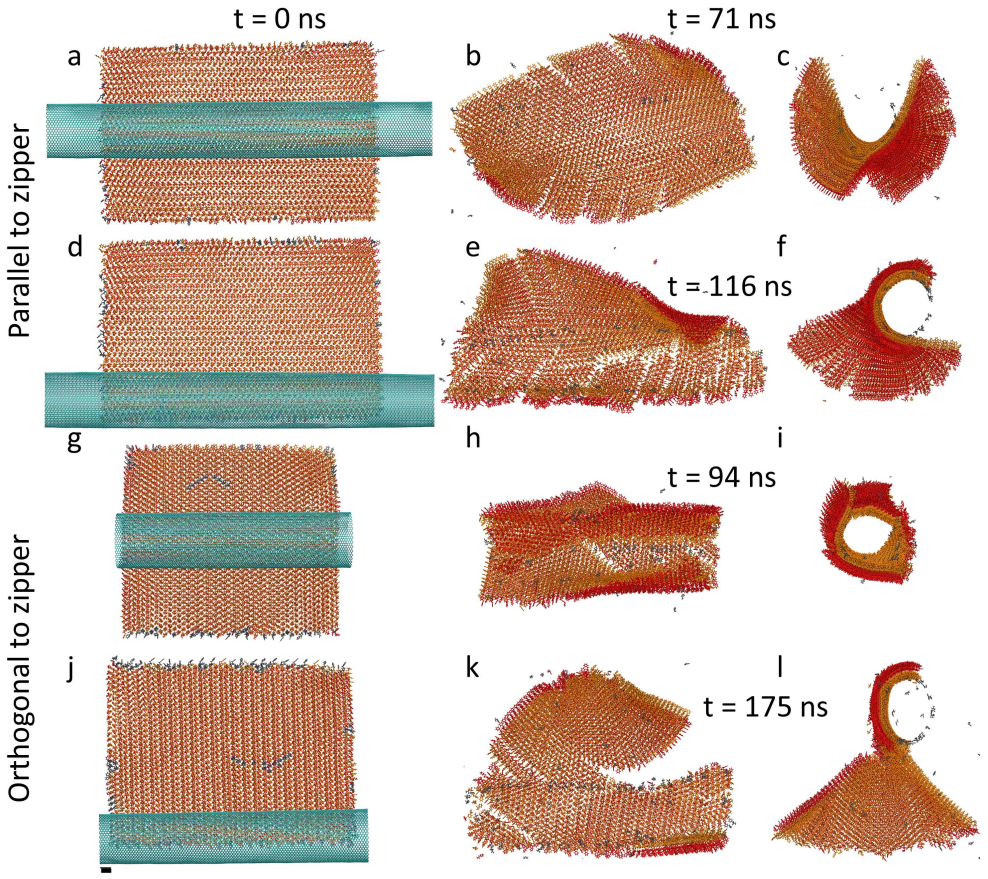

Figure 57: (a-c) L-PHE-C ($48 \times 34 \times 2$ amino acids) with $(35, 35)$ CNT (25.0 nm long) above the center of the crystal. (a) Initial setup; (b,c) top and side views at 71 ns, respectively. (d-f) The same L-PHE-C with CNT above the edge. (d) Initial setup; (e,f) top and side views at 116 ns, respectively. (g-i) L-PHE-C ($34 \times 48 \times 2$ amino acids) with CNT above the crystal center. (g) Initial setup; (h,i) top and side views at 94 ns, respectively. (j-l) The same crystal as in (g-i) with CNT above the edge. (j) Initial setup; (k,l) top and side views at 175 ns, respectively. In all systems, we used $(35, 35)$ CNT (21.5 nm long). Scale bar represents 1 nm.

Biomolecular crystals intercalated in graphene cells

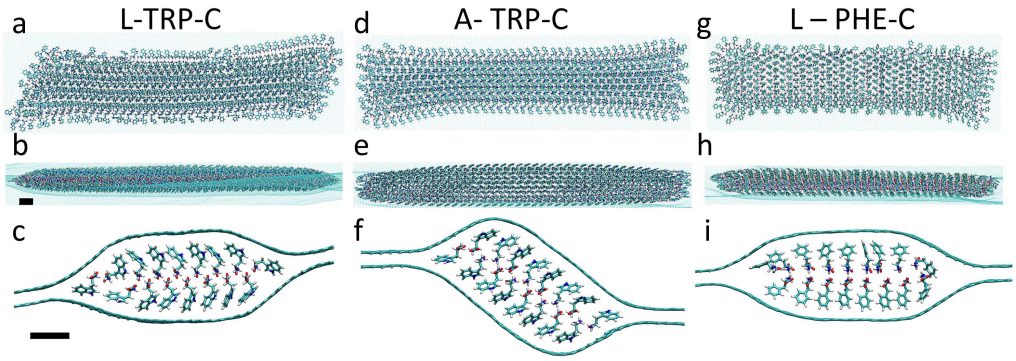

Figure 58: (a-c) Top, side, and single layer cross sectional views of same L-TRP-C as in Figure 51a sandwiched between two circular graphene sheets ($r = 30$ nm) at 11 ns. (d-f) Top, side, and single layer cross sectional views of same A-TRP-C crystal as in Figure 51d sandwiched between two graphene sheets at 12 ns. (g-i) Top, side, and single layer cross sectional views of same L-PHE-C in Figure 51f sandwiched between two graphene sheets at 11 ns. Scale bars represent 1 nm.

Finally, we have simulated L-TRP-C, A-TRP-C, and L-PHE-C (shown in Figure 51) intercalated between two circular graphene sheets (radius of $r = 30$ nm) without solvent. During the simulations, the biomolecular crystals diffused between the graphene sheets, but remained otherwise stable. Figure 58 shows that after ≈ 10 ns of simulations the crystals remained intact except at their edges, which became slightly deformed due to the pressure buildup from vdW-interaction coupled graphenes [10]. The intra-crystal coupling energies were practically also not affected by the intercalation. Interestingly, the chirality of metabolite crystals somewhat affected their wrapping by graphene sheets. The enantiopure L-TRP-C and L-PHE-C crystals were wrapped by the two graphene sheets more symmetrically, where the midline between the sheets bisected the crystal through the zwitterion layer (Figure 58c,i). The racemic A-TRP-C crystal was wrapped in a tilted way, where the midline went through the crystal diagonally.

Summary of binding intra-crystal enthalpies

In order to further examine the stability of these heterostructures, we calculated non-bonded (electrostatic and dispersion) interactions of amino acids: 1) within the same layer of the crystal, 2) between two different layers of the crystal, 3) between the bottom layer of the crystal and the substrate, and 4) between individual solvated amino acids and the substrate. The obtained binding energies are: 1) $80-90$ kcal/mol for L-TRP-C and A-TRP-C, 2) $50-60$ kcal/mol for L-TRP-C and A-TRP-C, 3) ≈ 6 kcal/mol between L-TRP-C/L-TRP-A and graphene, and ≈ 7 kcal/mol for phosphorene (L-TRP-C only), and 4) ≈ 17 kcal/mol for individual solvated TRP amino acids and graphene, and ≈ 19 kcal/mol for phosphorene (L-TRP-C only). The binding energies are: 1) $90-100$ kcal/mol for L-PHE-C, 2) $20-30$ kcal/mol for L-PHE-C, 3) ≈ 6 kcal/mol between L-PHE-C and graphene, and 4) ≈ 13 kcal/mol for solvated L-PHE-C amino acids and graphene. Variations in the intra-crystal interactions in the L-PHE-C are due to different orientations of the crystal (parallel versus orthogonal to the aromatic zipper). Since the intra-crystal coupling energies within L-TRP-C, A-TRP-C, or L-PHE-C are much larger than between the crystals and the substrates, those crystals should remain stable when adsorbed on the nanosurfaces.

Solvated (free) metabolites

Partial dissolution of amino acids from the molecular crystals was observed in all systems, as in the absence of substrates [1, 2]. Molecules that dissolved were usually on the edges or corners of the crystals, where the interactions with other metabolites in the crystal were $10-60$ kcal/mol weaker than in the bulk crystal. Solvated PHE amino acids exhibited slightly weaker binding to the nanosurfaces because they have less dispersion sites in the phenyl group than in the broader indole group found in TRP amino acids. The interactions of solvated amino acids with nanosurfaces were stronger

than interactions of crystalline amino acids with nanosurfaces ($^{TRP/PHE}$CH-carbon nanosurfaces or ^{TRP}CH-P nanosurfaces), although not strong enough to overcome intra-crystal interactions. Solvated metabolites on the cylindrical surfaces of CNTs exhibited the weakest coupling. As the diameter of the CNT increased, the metabolite-CNT interactions became stronger and approached values closer to graphene interactions.

Conclusion

We have shown that hybrid superstructures can be formed when biomolecular crystals are adsorbed on planar and cylindrical inorganic nanomaterials or when the crystals are intercalated between them. Due to large intra-crystal and relatively small inter-crystal coupling energies, the crystals remain stable. Racemic crystals tend to adsorb in a flat manner on planar nanosurfaces and wrap in a straight manner around CNTs. However, enantiopure crystals can naturally twist on the nanosurfaces, deform them in a helical way, and form helices on CNTs. These induced deformations of inorganic nanomaterials can induce their optical activity, unusual electronic and magnetic properties.

4.5 Nanosheets and Metallo-Hydrogel Formed by 2-nm Metal-Organic Cages based on electrostatic interaction

Adapted from Ref. [9] (*ACS Appl. Mater. Interfaces 2020*, 12 DOI:10.1021/acsami.0c16366) with permissions from ACS Publishing Groups.

Introduction

Nanosheets with large surface area but only atomic or molecular thickness have many promising applications [267]. These molecular-based bottom-up nanosheets have structural diversity, but their growth mechanism is still actively debated [268–271]. It is critical to identify the driving forces of the supramolecular structure formation with the goal to manipulate the sol-gel transitions to understand such gelation processes. Supramolecular gel from MOCs has been reported based on dynamic coordination bonds, [272] charge assisted H-bonds [273] or host-guest interactions [274] with organic [272, 274–276] or mixed solvents [276–280]. Nanoscale charged molecules (macroions, including MOCs) can attract each other via counterion-mediated attraction. Simulation results also confirm that the formation of 2D nanosheets is a common option. These MOCs spontaneously bend and form hollow, spherical, single layered blackberry type structures [281]. Gelation usually does not occur because these supramolecular structures do not possess large excluded volumes. Therefore, to seek for electrostatic interaction-based hydrogels, a viable approach is to choose macroions which can attract each other but restrain their assembly to open structures with the help of additional forces [282].

Metal-ligand coordination-driven self-assembly can construct supramolecular structures with control over designing 2D and 3D architectures [283–294], such as metal-organic cycles (metallacycles) and metal-organic cages (metallacages, MOCs). Supramolecular gels based on MOCs have diverse building structures, such as rod-like structures [279], fibrous structures [274, 275, 278, 280], and

nanoparticles [277] at critical gelation concentration (CGC). CGCs can range from 5 mg/mL [272] to >100 mg/mL [275]. Here, we investigate their structure.

Experimental results

Through the self-assembly of TPE-based ligands **1a** or **1b**, the dicarboxylate ligand **2a** or **2b**, and cis-Pt(PEt_3)$_2$ **3**, THE MOCs **4a**, **4b** and **4c**, respectively, were prepared according to previously reported methods.[23]

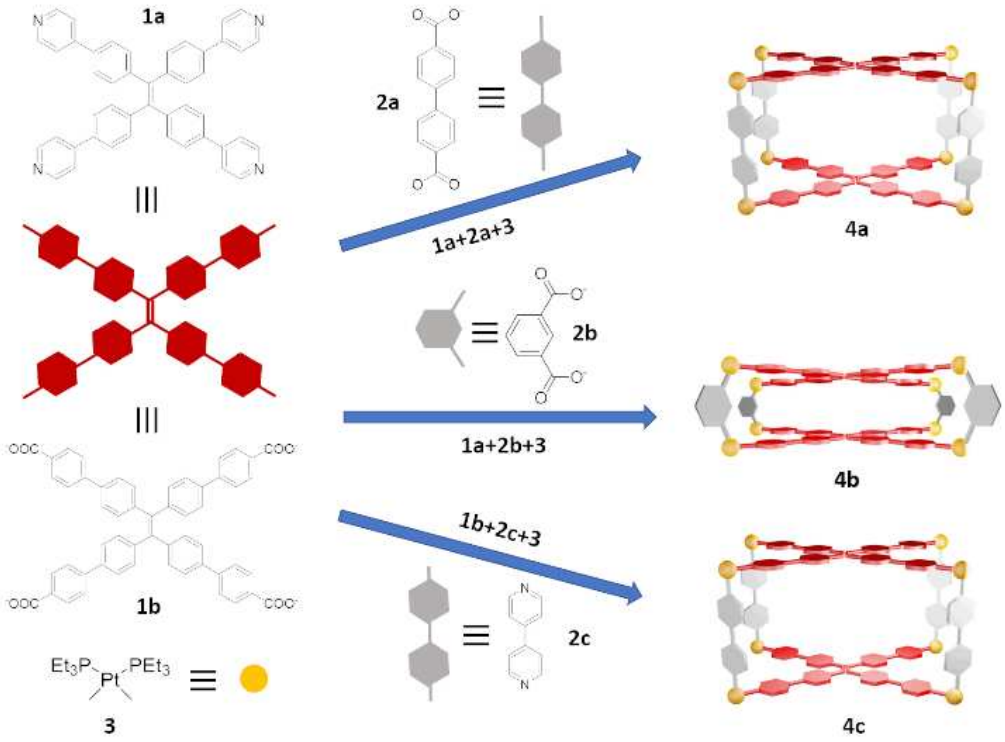

Figure 59: Self-assembly of the MOCs with NO_3^- as counterions.

Interestingly, the addition of $NaNO_3$ into concentrated aqueous solutions of **4a** ($\geq$ 15.0 mg/mL) leads to hydrogel formation. When 8 molar equivalents of $NaNO_3$ were added into 20.0 mg/mL **4a** solution, the solution turned into gel within seconds. This transparent gel has the same yellow color as the solution. Heating the gel at 90°C leads to a transparent and viscous solution and gel phase can be recovered after bringing the solution back to room temperature. This reversible sol-gel transition

suggests that the gel formed from **4a** in water is a physical gel based on non-covalent interactions. Because no strong NMR signal can be obtained from the cages in D_2O [295], the gel was dried and redissolved in CD_3CN, which leads to very similar ^{1}H-NMR spectra, further confirming that the cages are stable during the process and the gelation is not based on a chemical reaction. With 8 equivalents of $NaNO_3$, CGC was $\approx$ 15 mg/mL: below the CGC, further adding sufficient $NaNO_3$ did not lead to gelation, but only make **4a** aggregate and eventually precipitate; above the CGC, **4a** solution turned into hydrogel quickly.

In this hydrogel system, there are only **4a**, $NaNO_3$ and water but no high molecular weight gelators such as polymers. Small molecules have been reported to construct polymeric structures and form gels through non-covalent interactions, such as metal-ligand coordination, hydrogen bonding or hydrophobic interaction.[16] However, none of them seems to be the primary driving force in this study because: (1) there is no chemical reaction and thus no dynamic coordination sites are available; (2) **4a** are neither ordinary hydrogen bonding donors nor acceptors; (3) 1D fiber structures are not observed, which should be the primary structures if hydrophobic interactions are the major driving forces for gelation because **4a** contains two hydrophobic **1a** on the opposite faces. In addition, electrostatic interaction often does not favor gelation because the electrostatic repulsion stabilizes the single molecules and the electrostatic attraction will promote aggregation.

MD simulations: methods and results

We used NAMD2.12 [37] package to perform MD simulations and Particle-mesh Ewald (PME) method [57] to evaluate the long-range Coulomb interactions. We used time steps ranging 0.8 fs - 2.0 fs, evaluated long-range interaction lists every 1 (van der Waals) and 2 (Coulombic) time steps. We used a switching function with on/off distances 10/12 Å for non-bonded interactions, the NPT

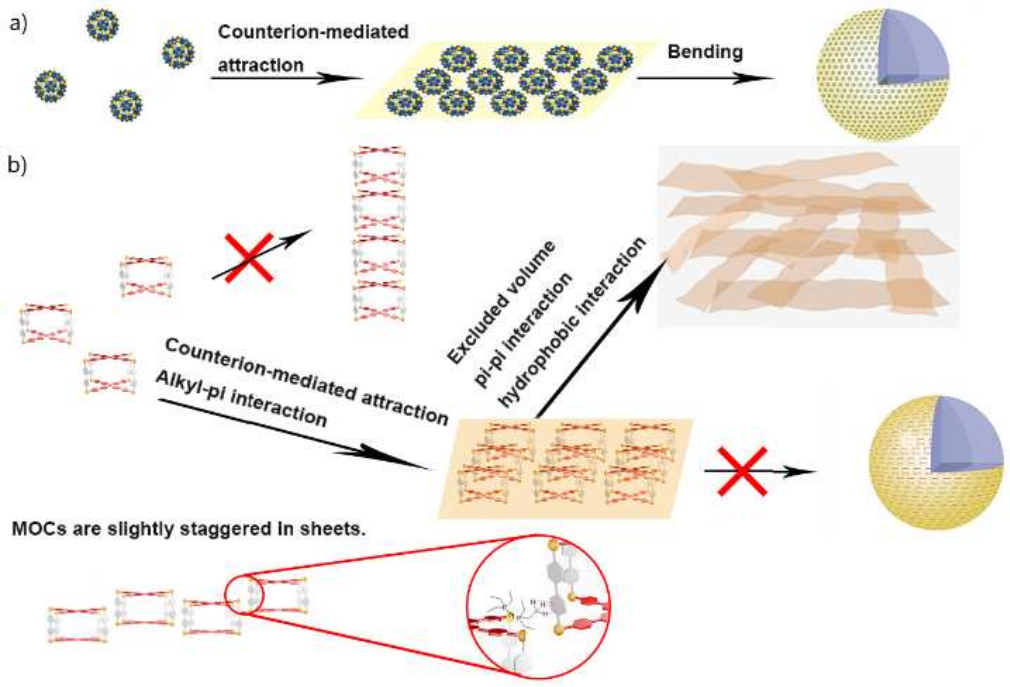

Figure 60: (a) Nanosheets and blackberry structure formed by polyoxometalate macroions. (b) Proposed self-assemble process from **4a** in aqueous solution with the addition of $NaNO_3$. Counterion-mediated attraction promotes the formation of nanosheet from **4a** and stabilized by unique cage conformation, charge distribution and $\sigma - \pi$ interaction. (Counterions are omitted for clear.)

ensemble at a constant temperature of 310 K, constant pressure of 1 atm, and a Langevin constant of $\gamma_{Lang} = 1.00$ ps^{-1}.

All systems had 6 cages in a box of $14.2 \times 14.2 \times 14.2$ nm^3 = 2863 nm^3 with 48 NO_3^- counter ions to balance the charges of these cages plus 60 $NaNO_3$ ion pairs so that there would be 10 times equivalence of those ion pairs in the solution. We modelled water molecules as TIP3P[6]. We imposed an improper angle of 180° and a force constant of 90 kcal/mol rad^2 on NO_3^- ions. We obtained all other parameters for the NO_3^- ions from literature[7].

We determined all bonds, angles, and non-aromatic dihedrals parameters for corner ligands, edges and faces through $MP2/6-31G*//MP2/6-31G*$ level of theory, using Gaussian [74]. We used VMD force field toolkit [59, 75] for parameter fitting from quantum mechanical calculations. We

obtained aromatic dihedral parameters from CHARMM36 generalized force field [39, 40]. During the quantum calculations, we modelled corner ligands, edges and faces as isolated molecules. Due to the large size of the faces, we broke the face molecules down to the smaller molecules: 1) a double aromatic system that would bond to a platinum atom and 2) the derivative of ethene, with four aromatic groups bonded directly to it. We obtained dispersion parameters from analogous atoms in CHARM36 force field [39, 40, 296]. We determined partial charges through the CHELPG algorithm [76] in implicit water solvent.

After we determined the force field parameters, we assembled the cages from the 16 (monodentate ligands) or eight (bidentate) corner ligands, four edges and two faces. We modelled the platinum - nitrogen bonds as 2.10 Å long with a force constant of 300 kcal/mol Å^2; platinum - oxygen bonds as 2.10 Å apart with a force constant of 300 kcal/mol Å^2; platinum - phosphorous bonds as 2.45 Å apart with a force constant of 300 kcal/mol Å^2.

First we minimized the systems for 5000 steps; then we heated the system for 2000 steps with an increment of 1 K every 5 steps, while keeping platinum atoms and atoms bonded to the platinum atoms constrained for both processes. During minimization and heating we had angles, which involved the platinum atom as the central atom constrained to enforce the square planar symmetry. After heating, we released all atoms and angles involving platinum atoms (i.e. we set those force constants equal to 0). We restrained any atom separated by at most two bonds from the platinum atom, as well as an aromatic carbon (on the one of the edges) on the opposite diagonal, analogous to keeping a table stable, in order to prevent the cages from collapsing. We enforced this restraint by setting the root-mean-square deviation to be less than 0.1 Å and the force constant 4000 kcal/mol, using the collective variables (colvar) module in NAMD. During the production runs, we recorded

snapshots of the trajectory every 10 ps, where the number of steps between each snapshot is inversely proportional to the timestep.

Atomic density isosurfaces were calculated in VMD volmap [59] function. We constructed volumeteric maps of atomic densities with a resolution of 0.5 Å, with all atoms having equal weight at each snapshot. We averaged the all maps for the entire trajectory. We selected one specific cage, recalculated the trajectory with the cage held at constant position through the RMSD align function [59], and calculated two volumeteric maps: 1) of all other cages and 2) NO_3^- ions. Isosurface values were chosen such that they could give a visible proximity of atomic density around the central cage.

To better understand the self-assembly of the above molecular cages, we have performed atomistic molecular (MD) dynamics simulations of separate **4a**, **4b** and **4c** cages (six in each system) in solutions with 10 equivalents of $NaNO_3$ and neutralized by additional NO_3^- counterions. Figure 61 shows the top and side views of the final supramolecular configurations for **4a**, **4b** and **4c** as well as atomic density isosurface of neighboring cages and NO_3^- ions around a specific cage. **4a** (Figure 61 a-c) forms a 2D unimolecular network, through $\sigma - \pi$ noncovalent bonds from its corner to the edge of neighboring cages. Since **4a** has two aromatic groups on the edges, it can easily form a "double $\sigma - \pi$ noncovalent bond", which strengthens this interaction. The atomic density isosurface of neighboring cages shows that the neighboring cages bind primarily through the edge aromatic groups and corner ligands, but not the face aromatic groups. This steric arrangement facilitates a "lock and key" binding that propagates into a 2D network because propagation through the faces does not occur.

There is only one aromatic group on each edge in **4b**, so the "double $\sigma - \pi$ noncovalent bond" is not structurally very likely. Therefore, the alkyl groups of the ligands at the corners interact weaker

with the edges and some of those ligands interact with the faces of a neighboring cage (Figure 61 g). As a result, the supramolecular cluster of **4b** is less ordered than the supramolecular cluster of **4a** (Figure 61 e and f). After the supramolecular structure forms, it undergoes internal conformational changes. A 3D disordered supramolecular structure of **4b** forms because the cages can bind through the faces as well as the ligands, unlike the cages of **4a**.

The formation of "double $\sigma - \pi$ noncovalent bonds" is structurally possible in **4c**, giving different supramolecular structures than **4a** or **4b** (Figure 61 i and j). Rather than forming a 2D network or a highly disordered 3D cluster, **4c** cages form 1D chains. This is because the $\sigma - \pi$ interaction occurs through the faces rather than through the edges (Figure 61 i). In **4c**, the functional groups on faces and edges, which bind to the Pt center, are reversed from those of **4a**, i.e. the carboxyl groups are on the faces and the pyridine groups are on the edges. The **4c** cages bind through the faces rather than through the edges. This causes a 1D chain growth rather than the formation of a broader 2D network observed in **4a**. It seems that the corner ligands in **3** have a preference to form $\sigma - \pi$ interactions with aromatic groups adjacent to carboxyl acids rather than pyridine groups.

The carboxyl groups in **1b**, **2a**, and **2b** tend to withdraw electrons from the neighboring aromatic groups, whereas the pyridine groups in **1a** and **2c** add electrons within the adjacent aromatic groups. The $\sigma - \pi$ interactions would more likely occur with aromatic groups that have lower electron densities, i.e. those adjacent to carboxyl groups. Therefore, **4a** has an electronic and steric structure that fits the formation of a 2D network, which is not possible in **4b**, due to steric effects. **4c** has a different electronic structure in the faces and sides, leading to different supramolecular structures. More cages with different corners, yet the same edges and faces as **4a** and **4b**, have been simulated and discussed in SI.

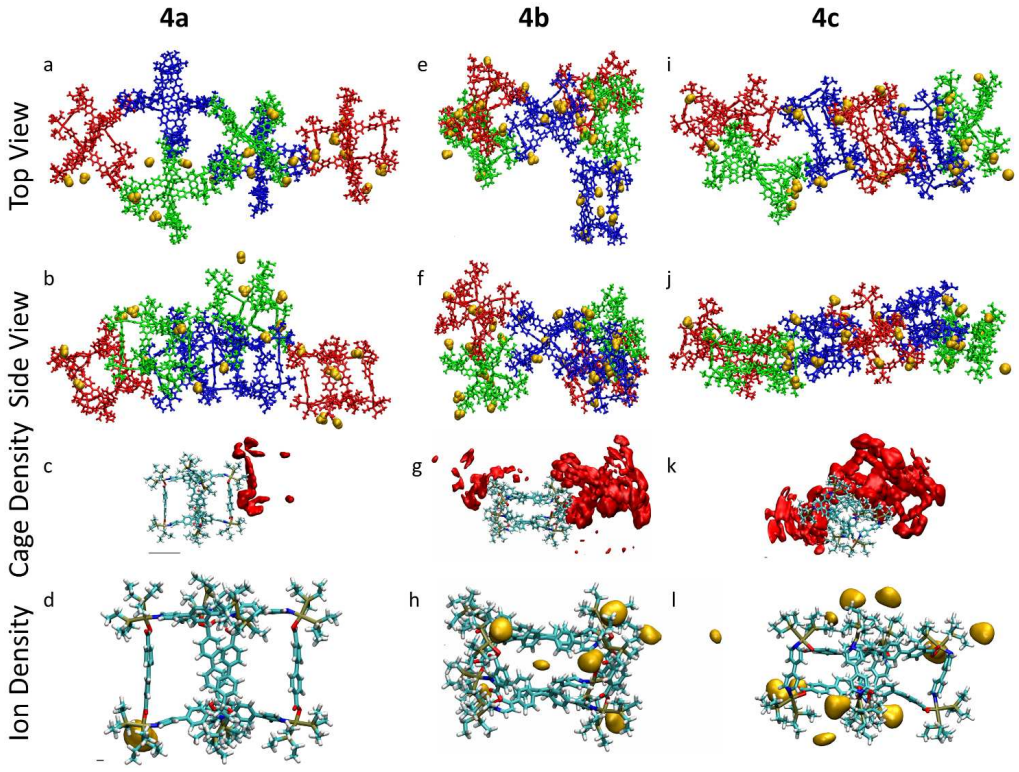

Figure 61: (a,b) Top and side views of supramolecular structure of **4a** and neighboring NO_3^- ions after 205 ns long simulations. c) Atomic density isosurface of neighboring cages around one cage with **4a** structure. d) Atomic density isosurface of NO_3^- ions around one cage with **4a** structure. (e,f) Top and side views of a supramolecular structure of **4b** and neighboring NO_3^- ions after 259 ns. g) Atomic density isosurface of neighboring cages around one cage with **4b** structure. h) Atomic density isosurface of NO_3^- ions around one cage with **4b** structure. (i,j) Top and side views of supramolecular structure of **4c** and neighboring NO_3^- ions after 340 ns. k) Atomic density isosurface of neighboring cages around one cage with **4c** structure. l) Atomic density isosurface of NO_3^- ions around one cage with **4c** structure. Scale bar in inset c represents 1 nm for insets a-c, e-g, and i-k. Scale bar in inset l represents 1 Å for insets d, h, and l.

Counterion-mediate attraction among the cages is important for the self-assembly processes, since each cage has a net charge of +8e. In all radial distribution functions of the N atom in the NO_3^- with respect to the Pt atom, the most intense peaks occurred at r $\approx$ 3.5Å. Integration of the peak yields 1, which means that there is a high probability an NO_3^- ion located close to the charged Pt atom, which screens the charge of the Pt atom. NO_3^- ions were all outside the cages and close to the Pt atoms, according to our atomic density isosurfaces (Figure 61 d, h and l). This enables bridging between the

highly charged cages. In addition, the NO_3^- ions had a tendency to be closer to the faces, rather than the sides regardless of the electronic structure of the faces. This indicates that steric factors influence the position of counterions more than electronic structure of the cages. The counterion-mediated attraction among cages was indicated by the Pt-Pt distance, determined to be 7.8 Å by XRD, and Pt-NO_3^- distance, 3.5 Å obtained by simulation. During the self-assembly process, cages come close to each other due to counterion-mediated attraction, forming 2D nanosheets, stabilized by $\sigma - \pi$ interaction and the large excluded volume leads to gelation with assistance of hydrophobic/partially $\pi - \pi$ interactions.

We modelled the same cages as **4a** and **4b** with different corner ligands, whose definitions and nomenclature are shown in Figure 62. We modelled the same face and two edges, yet there are three types of new corner ligands: 1) with a phosphorus atom bonded to three phenyl groups (named PPh3), 2) a bidentate dipyridine group (named diNPh), and 3) a bidentate ethylenediamine group, thus giving a total of 6 new types of cages.

When the corner ligands are PPh3, there is a strong assembly of cages through the aromatic stacking of the ligands, as shown in Figure 63 a,b,d,e. The composition of edges are unimportant because binding occurs mainly through the ligands. The corner ligands are multivalent with each ligand having three phenyl groups. The multivalency between the two binding ligands can increase the binding strengths between two cages. We observed the effects enhanced binding of multivalent nanoparticles to protein in a previous study [8]. The cages coalesce mostly along the edges as shown in Figure 63 c,g, thus they have a supramolecular structure similar to that of **4a** in main text. The two PPh3 cages are the only systems where the NO_3^- ions are further away the 3.75 Å from the Pt center due to the highly bulky nature of the ligands (Figure 63 d,h). In PPh3 **4a**, the NO_3^- coalesce in a plane that bisects the cages through the faces (Figure 63d). This is possible because

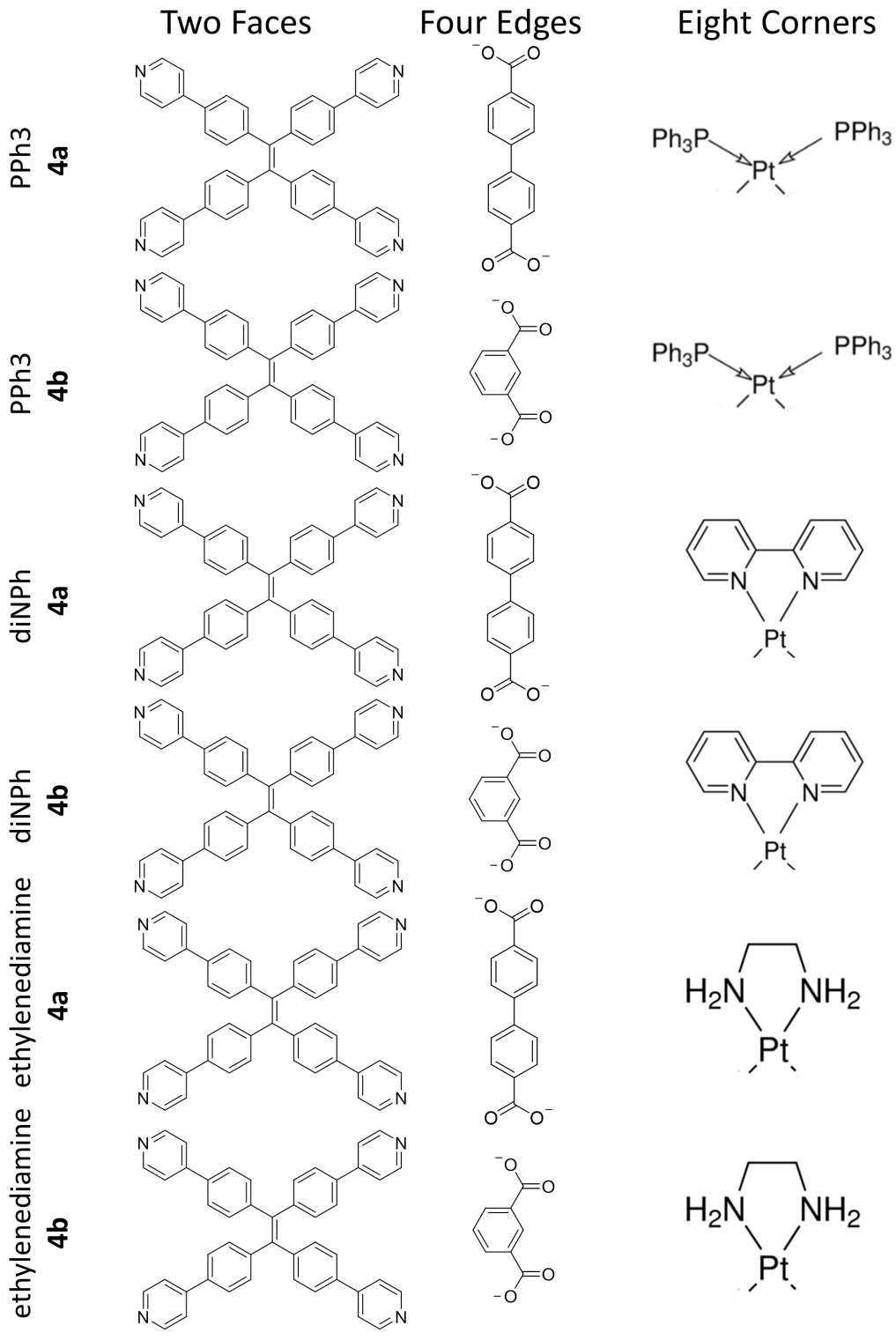

Figure 62: Faces, edges and corners for **4a** and **4b** with different corner ligands.

the edges are longer, with two aromatic groups, thus enabling the NO_3^- ions to diffuse between the bulky ligands. In PPh3 **4b**, the edges only have one aromatic group. Therefore, the NO_3^- ions are found only in the center of the cage, due to steric hindrance from the bulky ligands.

When corner ligands are diNPh, there is an extremely weak noncovalent bond between the cages. The ligands are more constrained because they are bidentate. In addition there are fewer aromatic groups in the diNPh corner ligands than in the PPh3 corner ligands. This can cause a drop in multivalency. We see both assembly and disassembly in the both networks throughout the simulations, though diNPh **4b**, which had only one aromatic group on the edge, is more prone to disassembly. Binding occurs between the pyridine-like ligand and the pyridine group on the faces, as shown in Figure 63 k,o. Coalescence between aromatic groups with similar electronic structure. Therefore, there is the cages bind between the pydrine groups. Disordered 3D structures form as the supramolecular structures of both cages with diNPh corner ligands, rather than 2D networks, as shown in Figure 63 i,j,m,n.

Finally when the ligands are ethylenediamine, the weakest binding between cages occurs from all other cages with different corner ligands. Assembly and disassembly of supramolecular clusters occurs in both systems throughout the simulations, though disassembly was more prevalent in **4b**, which had one aromatic group on the edges, rather than **4a**, which had two aromatic groups on the edges. Binding occurs mainly through $\sigma - \pi$ interactions from alkyl hydrogen, bonded to carbon atoms on the ligands, with pyridine aromatic groups on the faces (Figure 63 q-s, u-w). Binding is weaker with ethylenediamine corner ligands than the corner ligands in **3** (refer to main text) because ethylenediamine is a single bidentate ligand, which has more constrained motion and a lack of multivalency. In addition, the ethylenediamine corner ligand fewer alkyl atoms to bind.

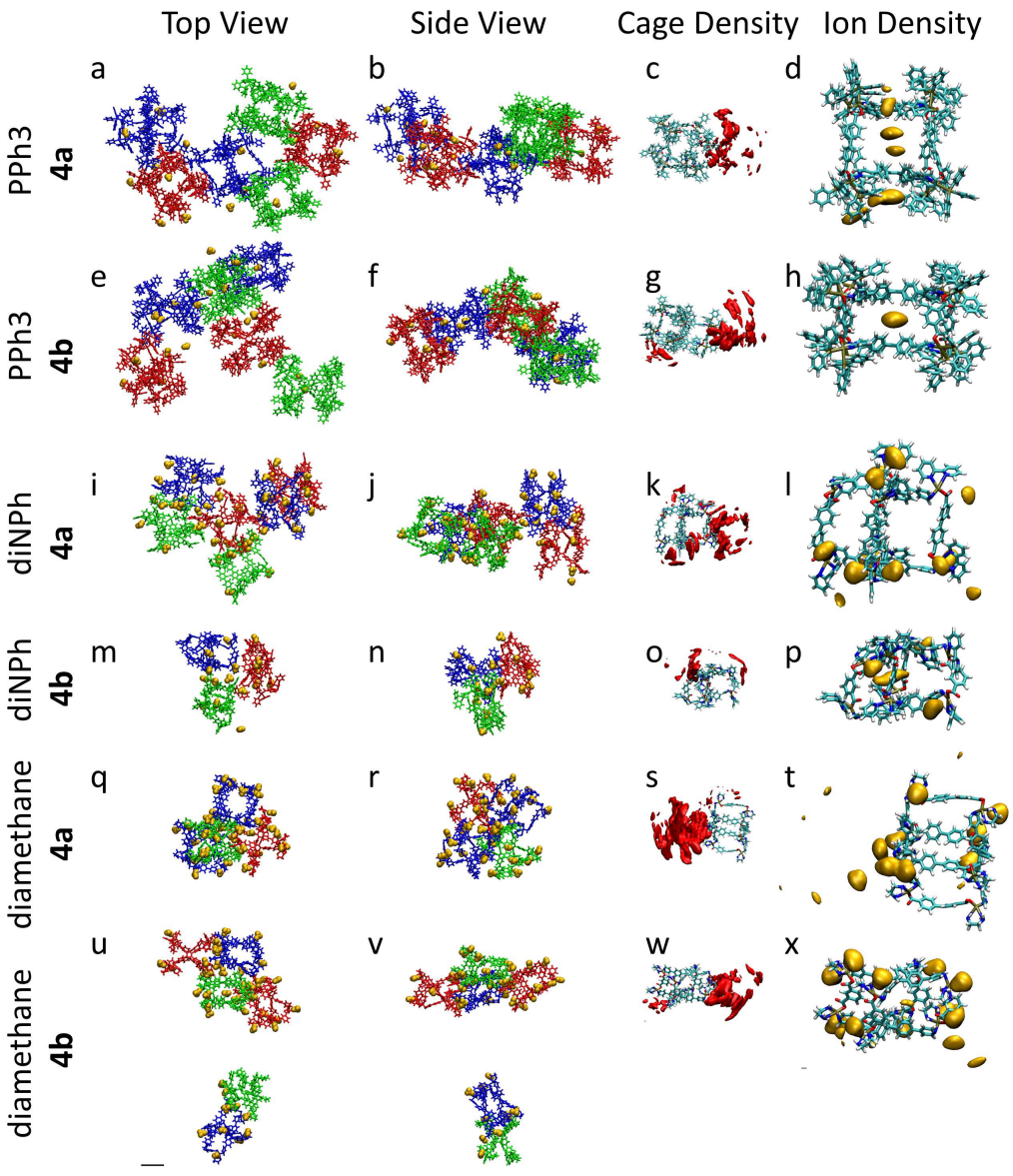

Figure 63: (a,b) Top and side views of supramolecular structure of PPh3 **4a** and neighboring NO_3^- ions after 202 ns. c) Atomic density isosurface of neighboring cages around one PPh3 **4a**. d) Atomic density isosurface of NO_3^- ions around one PPh3 **4a**. (e,f) Top and side views of supramolecular structure of PPh3 **4b** and neighboring NO_3^- ions after 194 ns. g) Atomic density isosurface of neighboring cages around one PPh3 **4b**. h) Atomic density isosurface of NO_3^- cages around one PPh3 **4b**. (i,j) Top and side views of supramolecular structure of diNPh **4a** and neighboring NO_3^- ions after 257 ns. k) Atomic density isosurface of neighboring cages around one diNPh **4a**. l) Atomic density isosurface of NO_3^- ions around one diNPh **4a**. (m,n) Top and side views of supramolecular structure of diNPh **4b** and neighboring NO_3^- ions after 257 ns. o) Atomic density isosurface of neighboring cages around one diNPh **4b**. p) Atomic density isosurface of NO_3^- ions around one cage diNPh **4b**. (q,r) Top and side views of supramolecular structure of ethylenediamine **4a** and neighboring NO_3^- ions after 204 ns. s) Atomic density isosurface of neighboring cages around one ethylenediamine **4a**. t) Atomic density isosurface of NO_3^- ions around one ethylenediamine **4a**. (u,v) Top and side views of supramolecular structure of ethylenediamine **4b** and neighboring NO_3^- ions after 408 ns. (Two separate clusters are shown). (w) Atomic density isosurface of neighboring cages around one ethylenediamine **4b**. x) Atomic density isosurface of NO_3^- ions around one ethylenediamine **4a**. Scale bar in inset u represents 1 nm for insets a-c, e-g, i-k, m-o, q-s, and u-w. Scale bar in inset x represents 1 Å for insets d, h, l, p, t, and x.

Next we evaluated the radial distribution functions (RDFs) of cages, normalized with respect to the number of atoms in each cage as shown in Figure 64. Peaks of g(r) are the most intense for values of r <5 Å, due to the higher internal structure of the cages. In addition there are also neighboring cages binding, which have atoms in the same vicinity. Weakly bonded cages, such as those with bidentate ligands have higher intensities of g(r), than those of strongly bonded cages for values r >5 Å. Since weakly bonded cages can diffuse away from each other more easily, they have higher intensities at higher values of r. When cages have one aromatic group on the edges, their bonding is weaker. Therefore at higher values of r the values of g(r) is higher for the **4b** than their **4a** counter parts. The only exception are the PPh3 systems, where the binding occurs primarily between ligands of different cages and the g(r) of these systems practically overlap.

We calculated RDFs of neighboring cages around a specific cage, normalized with respect to the number of atoms in each cage, in order to understand interactions between different cages better, as shown in Figure 65. All RDFs, except for **4a** and the PPh3 systems, show similar patterns of being bimodal, having either two distinct peaks or one distinct peak and a shoulder with a distinct minimum at r >40 Å. This is due to the disordered arrangement in the clusters as shown in Figure 63. **4a** and the PPh3 systems show strikingly different patterns, where they have broad two plateaus in the RDF at values r = 5 to 15 Å and r = 20 Å to 35 Å, yet no distinct peaks or valleys. The unimolecular layer of 2-D network, formed by **4a** or PPh3 systems, causes smaller values at lower values of r, yet consistent values of RDF at higher values of r, unlike a 3-D disordered structure. **4c** is also somewhat broad due to its ability to make a 1-D chain.

Finally in order to understand screening effects of cages we calculated RDFs of the nitrogen atom in the NO_3^- ion (named as NNO_3) with respect to the platinum atom (named as Pt) as shown in Figure 66. In all cages, with the exception of PPh3 **4b**, there is an intense peak at r $\approx 3.50 - 3.75$

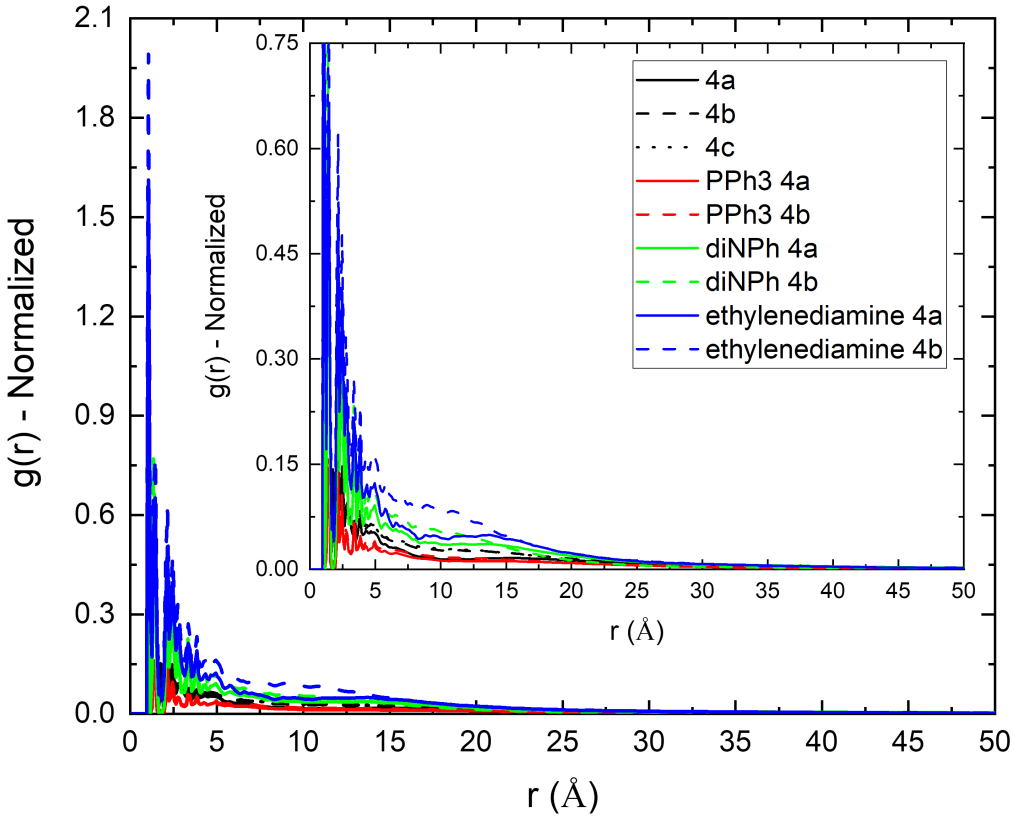

Figure 64: Radial distribution functions of cage atoms with other cage atoms, with intensities normalized with respect to number of atoms in each cage. Inset shows the same functions, whose normalized values are below 0.75.

Å. The Pt atom is modelled as having a charge of +2e, yet each edge has a charge of −2 e. Each cage has a net charge of +8 e, yet when examining one Pt center the net charge should be +1 e. The presence of the NO_3^- ion screens the Pt atom. In the region of 5 Å < r <27.5 Å, there are distinct peaks and valleys. This is a reflection of the highly ordered cages, where other NO_3^- ions are bonded strongly. There are higher intensities for the weakly bonded cages, which have bidentate ligands. Ions can bind more strongly to a Pt site when solvated. In addition, the weakly bonded cages (**4b**) have higher intensity g(r) than their more strongly bonded counter parts (**4a**). In a supramolecular cluster, these ions could be coupled to other cages or NO_3^- ions. PPh3 **4b** has a different ion distribution as shown in Figure 63 h and was discussed earlier.

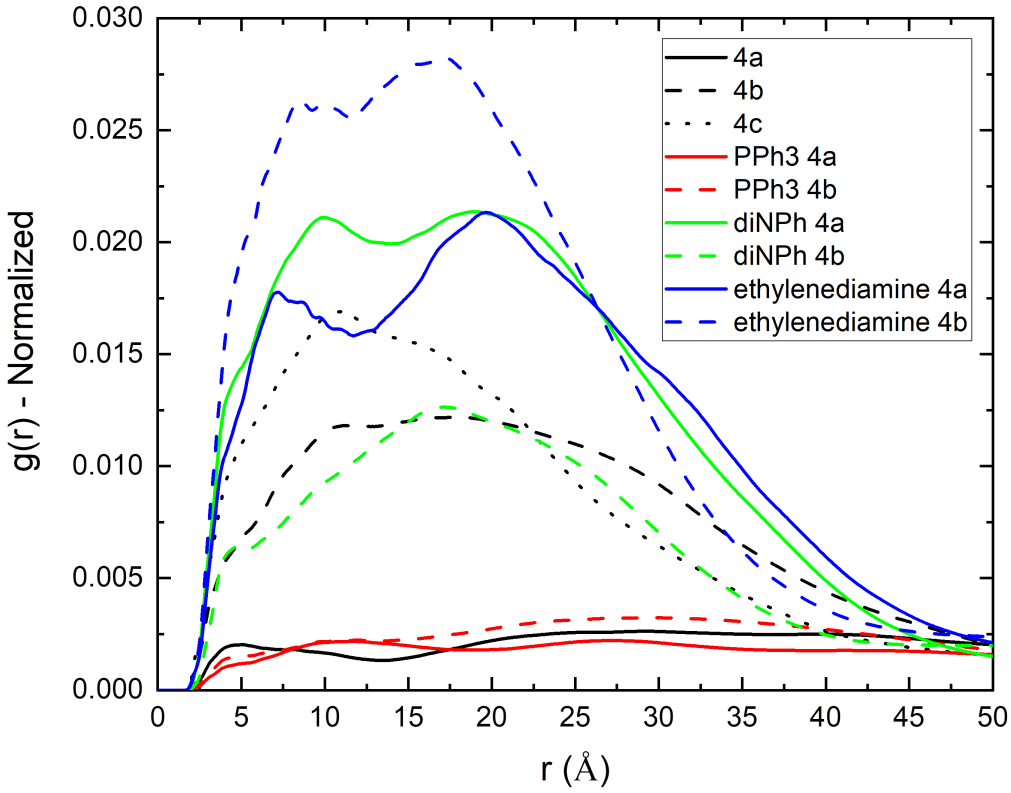

Figure 65: Radial distribution functions neighboring cage atoms around a central cage, with intensities normalized with respect to number of atoms in each cage.

Conclusion

In summary, we report a physical hydrogel formation process from a 2-nm sized cuboid-like metal-organic cage at low cage concentrations based on counterion-mediated attraction. With the addition of extra salts, the cages will first form large 2-D nanosheets in aqueous solution based on counterion-mediated attraction and stabilized by unique cage conformation, charge density as well as sigma-pi interaction, which is confirmed by the simulation results; the resulting hydrophobic sheets behave similarly to graphene oxide and form porous network, where the hydrophobic sheets were stacked due to hydrophobic/$\pi - \pi$ interactions. The hydrogel present typical weak physical gel properties and can undergo temperature-controlled sol-gel transitions. This work elaborates the

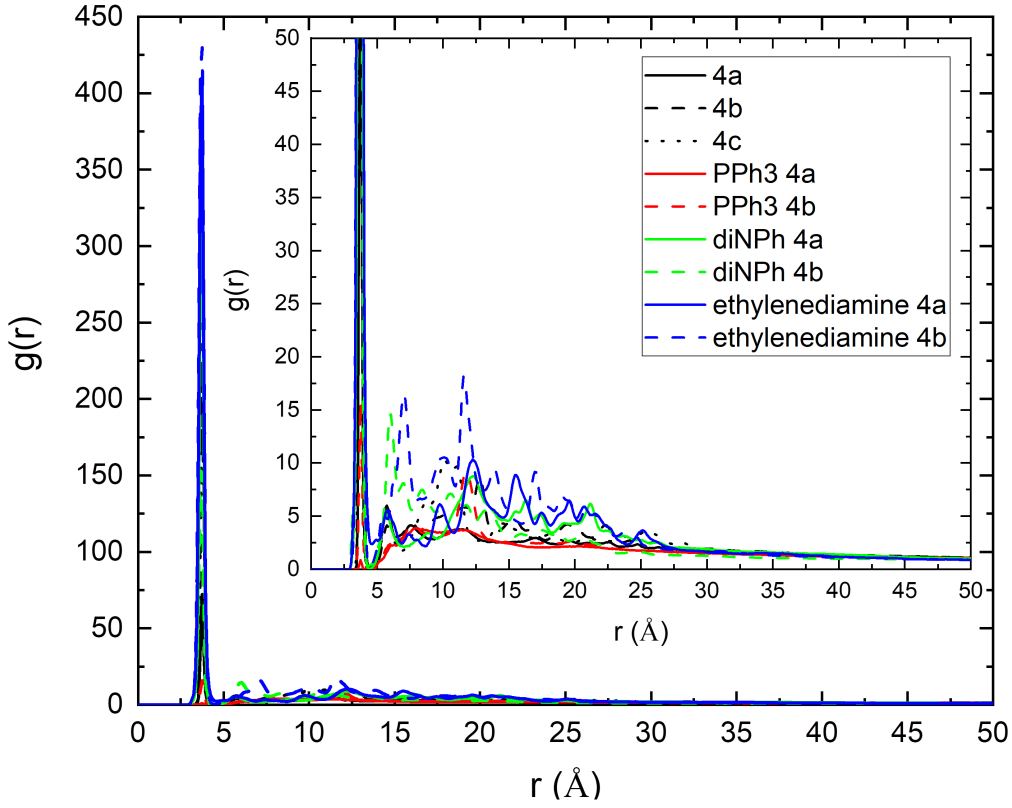

Figure 66: Radial distribution functions of NNO_3 atoms with respect to Pt atoms. Inset shows the same functions, whose values are below 50.

gelation process from low molecular weight gelators with electrostatic interaction dominated, which distinguishes itself from traditional gel systems, for instance, fiber entanglements.

4.6 In Situ Liquid-Cell TEM Observation of Multiphase Classical and Nonclassical Nucleation of Calcium Oxalate

Adapted from Ref. [297] (submitted)

Introduction

Calcium oxalate ($CaC_2O_4 \cdot H_2O$, or CaOx) is an important crystal for plants and fungi that may be involved in environmental CO_2 capture [298–300]. Oxalate is a downstream metabolite of CO_2. Oxalate sequesters calcium within sub-cellular vacuoles to regulate calcium and stores excess CO_2 in plants [298–300]. In nature, CaOx the most common mineral form of CaOx is monohydrate (COM). The other mineral forms of CaOx, in decreasing abundance and thermodynamic stability, are dihydrate (COD), trihydrate (COT), or amorphous (ACO) (extremely rare), [301]. COM is the most common CaOx phase in kidney stones, while COD is less common, and COT is exceedingly rare [302, 303]. Plants primarily contain COM and COD [304]. ACO is highly unstable and quickly crystallizes environmentally, but it has been prepared in the laboratory setting [305–307]. Previous studies have characterized the structure, morphology, and chemical content of CaOx minerals in plants [304], humans [308], and in vitro chemical studies [309–311]. Transmission electron microscopy (TEM) studies of CaOx have primarily focused on ex situ interactions of CaOx with biologicall systems [312–314], or as a characterization technique for benchtop experiments [315,316]. No studies have documented real-time CaOx nucleation.

Previously, in situ atomic force microscopy (AFM) was used to study the real-time growth of CaOx from seed crystals [317–322]. AFM is limited to the analysis of material surfaces, and cannot determine the crystal structure and local chemical changes during nucleation and growth. Graphene liquid cell (GLC) encapsulation of a liquid sample has been used for in situ imaging of colloid nanocrystals, ferritin, or bacteria [323–326]. We use GLC within a TEM to observe real-time CaOx

nucleation and mineral growth. In these experiments, a supersaturated liquid solution of calcium and oxalate ($C_2O_4H_2O^{2-}$) ions was encapsulated in GLC, allowing observation of nucleation and growth of CaOx [324, 326–330]. In a similar way, the effect of citrate on the mineralization of CaOx was also studied in GLC. Select-area electron diffraction (SAED) was used to characterize the crystal structure of particles formed in the GLC.

Experimental results

GLCs containing both CaOx and citrate (Figure 67) display markedly different CaOx crystal nucleation for most of the particles observed to nucleate. In Figure 67A a particle first appears at approximately 20 nm in diameter with very low contrast throughout 0 to 1.3 seconds. From 1.3 through 3 seconds the particle contrast increases while remaining the same diameter (Figure 67A-H). The particle then dissolves from 3 seconds to 17.3 seconds (Figure 67H-J). Several underlying phenomena may explain these observations. First, the particle may grow in the z direction only, without apparent growth in the image plane in Figure 67. This changes the contrast due to increased thickness. Second, the particle may be rotating. This rotation may cause changes in the diffraction contrast of the particle if the particle is crystalline. Thirdly, the particle may be dissolving and reforming at the same location. This may occur due to high local concentrations of ions. The contour plot of the growth phase (0 to 3 seconds) resembles previous observations of CaCO3 growth from dense liquid droplets [331]. Here, high ionic concentrations may not be visible in Figure 67. Regardless of the underlying mechanism of particle appearance and disappearance, here citrate lim-

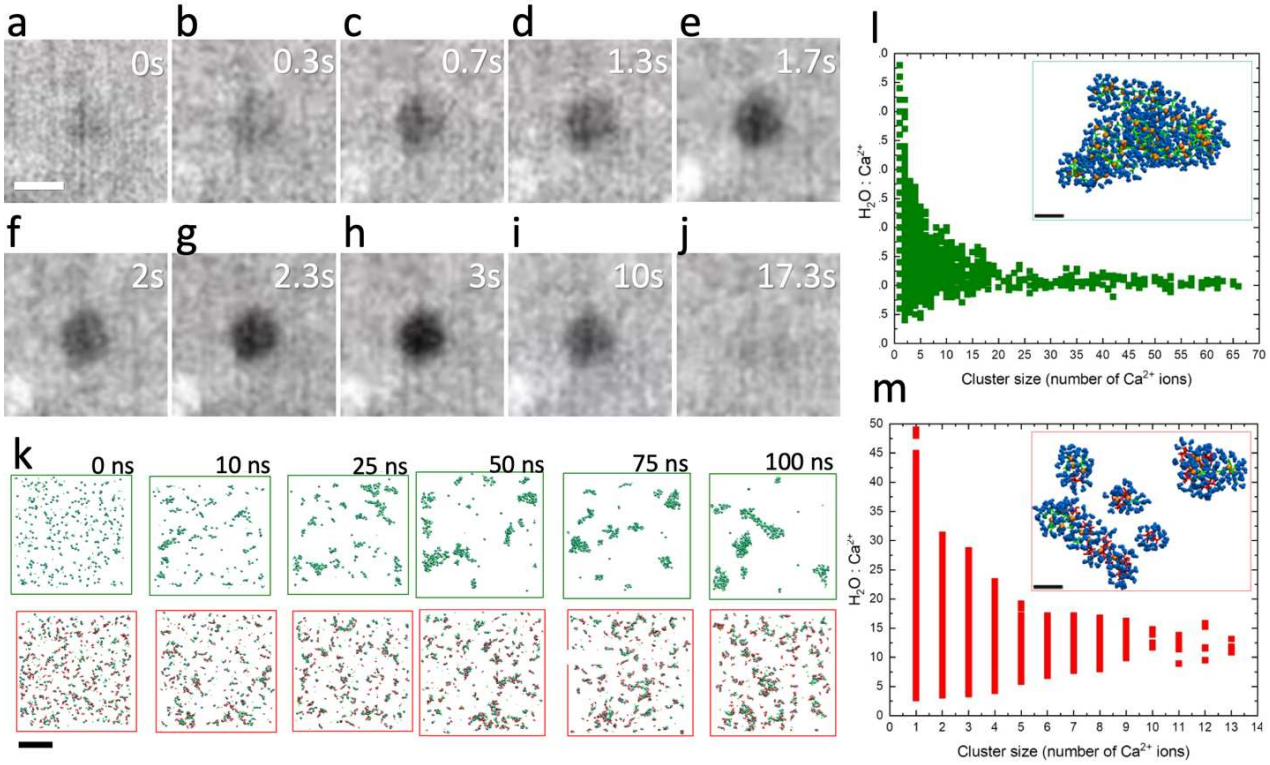

Figure 67: **Repeated CaOx formation and dissolution in the presence of citrate.** The particle forms with a diameter of approximately 20 nm, and increases in contrast throughout A. At 3 seconds, the particle develops 90° corners. This particle fluctuates in diameter, contrast, and corner sharpness before dissolving. In the upper row of B, MD simulations shows aggregation of calcium and oxalate ions during nucleation. In contrast, the lower row of B MD simulations show that calcium:citrate interactions prevent nucleation of CaOx. The upper panel of C displays the local water molecule concentration in the MD simulations in the absence of citrate. The lower panel of C, displays the local water molecule concentration in the presence of citrate. A representative aggregation of CaOx formed without citrate illustrates the presence of water molecules (blue) around a CaOx particle in the upper inset of C. Oxalate anions are indicated in green, and calcium cations in orange. In the lower panel of C, in the presence of citrate CaOx has a much higher water molecule to calcium ratio along the Y axis, suggesting an increase in the hydration state. Further, there is reduced aggregation along the X axis in the presence of citrate (lower panel) as compared to the upper panel without citrate C. In the inset in the lower panel of C, smaller CaOx clusters formed in the presence of citrate illustrate a higher local water molecule to calcium ratio as compared to the upper panel. Citrate anions are indicated in red. The scale bar in A is 20 nm, 5 nm in B, and 1 nm in C. All TEM images were collected at the same magnification in the same area.

its the formation of CaOx to approximately 20 nm in diameter. It is unclear if the particles are crystalline, semi-crystalline or amorphous due to the limited resolution of the figure.

Formation of CaOx dihydrate in the presence of citrate

Citrate may increase the solubility of CaOx. Previous works have reported this possibility at different concentrations of CaOx and citrate. The increase in the solubility of CaOx was only reported to be $\approx$ 0.4 mM of CaOx in previous works [332]. Here, much higher concentrations of CaOx were used, which may alter the effect of citrate [332]. The GLC confinement may alter the local ion concentrations, which permits the particle dynamics observed in Figure 67A-J [332–334]. The nucleation of CaOx or calcium citrate at higher ionic concentrations must also be considered. At sufficiently high ion concentrations the chelating effect of citrate may be overcome and precipitation of CaOx observed as previously documented [332].

In addition to the inhibitory effect of citrate, discussed above, MD simulations also determined the correlation between the ratio of water molecules and calcium ions present in each cluster and the size of that cluster (determined by the number of calcium ions in the respective cluster) (Figure 67L-M). In both the absence and presence of citrate the above ratio reached a limiting value with increasing cluster sizes (Figure 67L-M). Without citrate, this limiting value is around 5, whereas with citrate it increases to 12.5 (Figure 67L-M). In the presence of citrate, we can expect that the finger-like clusters eventually collapse and capture more waters than do the round compact clusters formed in the absence of citrate. This suggests that the presence of citrate may increase the hydration state of the CaOx formed (Figure 67M), in agreement with experimental observations (COD formation observed in the presence of citrate).

In addition to the dissolution of CaOx previously observed at equilibrium in Figure 67, other GLCs containing CaOx and citrate showed formation of irregular nanoparticles. However, SAED of CaOx particles formed in the presence of citrate shows the presence of polycrystalline COD overlapped with graphene peaks [335–337]. The individual, distinct spots identify the (100) and (210) planes of graphene [335,336]. The side by side dots in the SAED pattern indicate the presence of two layers of graphene [336]. This shows that the GLC consists of a lower single layer of graphene under the sample, while another single layer of graphene covers the sample to encapsulate it. Circles rather than individual diffraction spots indicate the presence of many crystals which make up the overall polycrystalline structure and identify the formation of COD rather than COM [335–337]. The presence of COD shows an increase in the hydration state from COM, consistent with MD simulations (Figure 67L-M).

The formation of COD in the presence of citrate observed in GLC was also supported by ex situ experiments. SEM imaging showed CaOx morphologies representative of COD, while XRD confirmed the crystal structure of COD [337]. EDS chemical analysis identified the oxygen signal increase from the expected 5 : 1 O:Ca in COM synthesized in the absence of citrate. In the presence of citrate, there was a 6 : 1 O:Ca ratio indicative of the formation of COD. EELS showed slightly lower values as compared to EDS, which is likely due to electron beam sample damage. EELS did however confirm the increased oxygen signal. EDS mapping showed no significant background oxygen signal in the ex situ samples.

MD simulations: methods and results

MD simulations were performed with NAMD2.12 [37]. Water molecules were described using TIP3P model [338]. Monoatomic ions were modeled by their Lennard-Jones parameters and integral charges [339]). Parameters for citrate and oxalate ions were determined using $MP2/6-31G*$

$//MP2/6-31G*$ level of theory, in implicit water solvent through Gaussian program [74], using VMD force field toolkit [75]. In all simulations, the particle-mesh Ewald (PME) method [57] was used for evaluation of long-range Coulomb interactions. Long-range interactions were evaluated every 1 (van der Waals) and 2 (Coulombic) time steps. The simulations were performed in the NPT ensemble at a constant temperature of 310 K, constant pressure (varied for different simulations) and a Langevin constant of $\gamma_{Lang} = 1.00$ ps^{-1}. The pure CaOx simulations had the same number of water, calcium, oxalate ions, such that $[CaOx] = 0.125$ M at 1 atm. There were a total of 254 oxalate ions in all simulations. Simulations with citrate ions had the same number of citrate and oxalate ions. Spectator ions were also added into the system in order to replicate experimental conditions. The systems (citrate present or absent) differed by applied pressures of 1 and 100 atm. MD simulations at 100 atm were included to control for the possible increase in pressure due to GLC encapsulation (SI note S3). The 100 atm pressure was selected since it is an order of magnitude greater than pressure predicted by previous studies [340]. The systems were minimized for $5,000$ steps and then pre-equilibrated for 2 ns, with a time step set to 2.0 fs. During minimization and pre-equilibration, one carbon atom on each oxalate and citrate (if applicable) molecule was harmonically constrained in order to allow these molecules to rotate, but not diffuse. There were no constraints during the simulations, which ran for 100 ns and with a time step of 1.0 fs.

During the evaluation of number of water molecules within clusters, we assume that a cluster has at least 1 calcium ion and one oxalate or citrate molecule, which have at least one their atoms within 2.5 Å of that calcium ion. Clusters were determined by selecting a calcium or oxalate ion and finding the neighboring calcium, oxalate, or citrate ions within 2.5 Å. This process is repeated until the whole cluster is determined. Iterations ended when no new neighbors were found. After the cluster size was determined, we determined the number of water molecules that were within 2.5 Å

of any calcium, oxalate, or citrate molecule in the final cluster. In order to eliminate effects related to a finite simulation box, we determined whether any molecule in the final cluster was within 4.5 Å of the boundary of simulation box. If there was a cluster close to the boundary of the box, we displaced the entire cluster and neighboring water molecules and repeated the calculations. The sizes of clusters were determined by the number of calcium ions in those clusters. Evaluations of cluster sizes were determined for every 1.00 ns, due to memory limitations. The computational power of modern computers limited the volume of the MD simulations to several nanometers.

Nucleation of CaOx from a supersaturated solution without and with 0.1M citrate were modelled by MD simulations (Figure 67K). While the magnification of figure exceeds many previous works on low-contrast carbon-based particles, liquid TEM is limited in its resolution due to the thickness of the sample. MD simulations are however limited to small volumes due to the current limitations of modern computers. Thus, the MD approach provides insight beyond what can be observed in liquid TEM rather than direction comparisons. In the MD simulations, in the absence of citrate, CaOx aggregated to form amorphous clusters. These clusters then continued increasing in size and combining with other clusters. (Figure 67K). However, when citrate was present, the calcium ions interacted with the citrate and formed small and unstable complexes (Figure 67K). The alternative calcium:citrate interactions prevented stable precipitation of CaOx, similar to the CaOx and citrate solution in Figure 67. This effect occurs because the tridentate citrate anion, with three carboxylic acids groups capable of accepting calcium cations, exhibits stronger Ca:O bonds than the bidentate oxalate [332,341] The MD simulations were also performed at higher pressure to control for possible changes in pressure due to GLC encapsulation.

The alternative calcium:citrate interactions thus reduce the free calcium present which prevents stable formation of CaOx (Figure 67K). However, calcium citrate does not precipitate since the

overall structure of calcium citrate is less stable than CaOx [332]. Thus, throughout Figure 67, an equilibrium between the calcium:citrate and calcium:oxalate exists, which prevents stable precipitation of CaOx. Excess calcium ions in the solution temporarily overcome the formation of soluble calcium:citrate complexes, which form CaOx nanoparticles (Figure 67A-H. However, the interactions of calcium with citrate dissolves the CaOx particles, which leads to the cyclic formation and dissolution of unstable CaOx experimentally observed in Figure 67H-J and modelled in Figure 67K. This supports the third possible explanation for the phenomena observed in Figure 67A-J, wherein a high ionic concentration forms, condenses into a 20 nm in diameter particle, before dissolving due to the presence citrate.

Conclusion

The presence of citrate alters the solubility, hydration state, crystal structure, and morphology of the CaOx crystals during the nucleation process. Citrate-induced changes in the formation of CaOx were previously predicted to occur by interaction with amorphous precursors [315], polynuclear complexes [315], or by step-pinning of crystal facets as in the C-V model [342]. Ruiz-Agudo et al. [315] showed that CaOx was inhibited by citrate due to citrate coating growing amorphous particles to prevent further aggregation. Here, it is difficult to find evidence for such coating. Instead, it was observed that the dihydrate form of CaOx can become more stable due to integration of water molecules in the CaOx aggregates. These differences may arise due to variations in the reagent concentrations, background electrolytes, or addition of additives reported in many studies.

CHAPTER 5

NANOFLUIDICS

(Previously published as Ghodsi, S. M., Sharifi-Asl, S. S., Rehak, P., Král, P., Megaridis, C. M., Shahbazian-Yassar, R., Shokuhfar T. Assessment of Pressure and Density of Confined Water in Graphene Liquid Cells. *Advanced Material Interfaces* 1901727 (2020); Pendse, A., Cetindag, S., Rehak, P., Gao, H., Behura, S., Wang, T., Berry, V., Král, P, Shan, J., Kim, S. High Efficiency Osmotic Energy Harvesting in Charged Membranes Formed Aligned Boron-Nitride Nanopores. *Advanced Fnctonal Matrials* 2009586 (2021).)

In this chapter, we investigate at two different studies of nanofluidics. In the first study we examine the pressure of water droplets encased between in a graphene liquid cell. In the second study we look at power generation through osmotic energy harvesting by allowing the reverse dialysis flow of KCl through a charge boron-nitride nanotube.

5.1 Assessment of Pressure and Density of Confined Water in Graphene Liquid Cells

Adapted from Ref. [10] (*Adv. Mater. Interfaces 2020*, 7 DOI:10.1002/admi.201901727) with permissions from John Wiley and Sons Publishing groups.

Introduction

Nanometer-thick films of liquids encased in Van der Waals (vdW) materials may deviate from the behavior of bulk confined matter [325, 343–347]. This deviation of behavior can provide a novel platform to study fundamental thermodynamic studies on liquid solutions in confined environments [348]. In closely-confined systems, vdW forces are inversely proportional to the size of confinement. Thus, they act more strongly with decreasing thickness of the encased liquid film [346]. The energy cost of bending a 2D membrane over the confined sample should be studied, because the vdW forces and bending strain energies impose substantial pressure on the entrapped liquid. For example, water trapped between hydrophobic graphene membranes appears as ice at room temperature [349] and was confirmed by molecular simulations [350–354]. Atomic force microscopy (AFM) has been used to directly measure the pressure of confined water, where pressures as high as 1 GPa were reported [340]. The advent of graphene liquid cell (GLC) transmission electron microscopy (TEM) has enabled the study of water and liquid solutions with unprecedented spatial and analytical resolutions [355–357].

While previous studies confirmed the existence of high pressure in liquid solutions under graphene confinement [348], the magnitude of the pressure of these confined films is still under investigation. Previous studies have utilized nontransmission probes, including AFM, Raman, and Fourier-transform infrared (FT-IR) spectroscopy, to examine the liquid samples confined between vdW materials and atomically-smooth substrates like hBN and MoS_2 [340, 348], but have not reported on the thermodynamic state of liquids confined solely between vdW material interlayers. The relatively

small size of graphene liquid pockets in GLC compared to the spatial resolution and probe size of conventional analytical methods constrains the application of common nontransmission spectroscopy tools in studying such confined samples. Our experimental results indicate a 12% elevation in the density of graphene-entrapped water where pressures as high as 400 MPa are reached at room temperatures. Furthermore, our energy conservation analysis and simulations of GLCs considering the effect of vdW forces, Laplace pressure, and strain energy is in agreement with the experimental results.

Experimental results

Rise of water density with pressure escalation inside GLCs

While the pressure of water in either liquid-flow holder or GLC cannot be derived directly from low-loss EELS, electron spectroscopy can estimate the relative density of water in GLC as discussed earlier. Using the equation of state (EOS) for water at room temperature, we derived the pressure exerted on water due to graphene encapsulation by taking into account the change of water density. Assuming that the density of water in the liquid-flow holder is close to that of water at ambient conditions (0.99 g cm^{-3} at 25° C and 1 bar), [358, 359], the density of water in this particular GLC is 1.12 ± 0.10 g cm^{-3}.

The possibility of such high pressures under graphene encapsulation agrees with some previously reported studies [340, 350, 360]. For instance, the AFM measurements and ab initio calculations on argon enclosures formed between layers of graphene and atomically-smooth Ir (100) wafer revealed internal pressure of Ar of the order of 5 GPa [361]. However, not all previous reports agree with the existence of such high pressure inside graphene enclosures. Khestanova et al. [340] reported pressures of the order of 10 MPa using the AFM-exerted force measurements on enclosures formed

between graphene and Si-SiOx wafers. There have also been attempts to explain the pressure inside graphene-confined water using the Laplace pressure correlation, $\Delta P = \frac{2\gamma}{R}$ where ΔP is the pressure gradient across the graphene membrane, γ the interfacial energy of graphene-water and R is the radius of the graphene blisters [362]. Replacing $\gamma = 90$ mJ m^{-2} [363] and R = 10 nm, the internal pressure of GLCs could reach 18 MPa. The disagreement between our results and some other reports on the pressure of graphene enclosures is due to the fundamental differences between these systems [340, 362]. In the GLC system, the hard supporting substrate is replaced by graphene layers to encase the sample. Moreover, the entrapped phase in a GLC is a liquid (mostly water), while in reported AFM measurements the specimen is a dilute inert gas. The GLC samples are also a few orders of magnitude thicker than gas cells, which signifies the role of graphene elasticity in the total pressure. Thus, the Laplace correlation underestimates the actual pressure of GLC samples as it does not take elasticity effects into account.

Energy analysis of graphene-encapsulated water

Although extreme pressures inside enclosures of nanometer-thick graphene layers appear to be eccentric, such values have been physically and mathematically justified. Khetonesa et al. [340] have analyzed the energy components playing a role in the pressure buildup in graphene enclosures on a solid substrate. The shape and the pressure of graphene bubbles on a solid substrate were stabilized in equilibrium conditions formed between graphene layers, the solid substrate, and the enclosure content. Thus, the energy inside each graphene enclosure was modeled by three main components: 1) graphene-graphene and graphene-liquid interactions, 2) graphene elasticity, and 3) internal energy of the content. Herein, applying the same approach, we have modeled each GLC with respect to its geometry and energy components. Assuming isothermal conditions, the pressure buildup inside each GLC was modeled as the product of energy spent in the GLC fabrication procedure. In our model,

GLCs are formed upon squeezing nanodroplets of water between graphene sheets. The magnitude of GLCs' internal pressure is a function of its size and stems from four main energy components: 1) the adhesion energy between graphene layers (E_{vdW}), 2) the adhesion energy between graphene and water ($E_{Laplace}$), 3) the elasticity energy of graphene substrate (E_{el}), and 4) the internal energy of water (E_l). E_{vdW} is the energy spent to peel adjacent graphene layers and keep them apart. Second comes the interfacial energy between graphene sheet and water ($E_{Laplace}$), which contributes to the final pressure of the sample. Our calculations show that the contribution of vdW interactions between water and graphene substrate (disjoining pressure) is negligible in final pressure buildup inside GLCs with thicknesses above 1 nm [364, 365]. The E_{el} component is the energy spent to bend graphene sheets around water nanodroplets and keep them askew. Lastly, E_l is the elevation of water nanodroplet internal energy upon encapsulation between graphene sheets. Assuming the initial energy state of water and graphene sheets at zero, the final energy of the system could be written as Equation 5.1:

$$E_{tot} = E_{vdW} + E_{Laplace} + E_{el} + E_l(V) \tag{5.1}$$

The vdW energy stems from close contact of graphene sheets and only acts on the footprint of the GLC, which could be estimated as $\gamma_{GG} S_{foot}$, where γ_{GG} is the graphene adhesion energy (120 mJ m^{-2}) and S_{foot} is the GLC footprint. The Laplace energy component is the result of nanoscale interaction of water and graphene which applies on the surface of the graphene exposed to water $\gamma_{GW} S_t$, where γ_{GW} is the adhesion energy of water-graphene and S_t is the total area of graphene exposed to water inside the GLC. The elasticity component of energy is derived based on first order Hooke's law $\frac{1}{2l} Y S_{foot} \Delta l^2$ where Y is graphene's young modulus ($50 - 100$ MPa) [366–368] and Δl

is graphene's strain upon GLC fabrication. The internal energy of water rises as it gets squeezed between graphene sheets.

MD simulations: methods and results

The MD simulations were performed with the NAMD2.13 package [37], using a CHARMM27 force field [56] for graphene. The TIP3P model [338] was used for water molecules. The simulations were described by a Langevin dynamics in a NVT ensemble for systems with GLC and T = 310 K, where V varied according to number of water molecules, and NPT ensemble for bulk water system, with P = 1, 100, 300 atm and T = 310 K. A Particle Mesh Ewald [57] summation was used to calculate long-range Coulombic interactions, with a grid spacing of 1.0. Short-range dispersion interactions used a switching algorithm, with an on-off distance of 10/12 Å. Pairlists were recorded for atoms 13.5 Å apart, updated every 20 steps; $1-4$ interactions were not scaled.

Bulk water simulations had $133,050$ water molecules. GLC systems have only two graphene sheets, modeled as structure of neutral carbon atoms, with no terminal hydrogen atoms. Constraints for preparation, minimization, pre-equilibration, and production runs of the system were only applied to atoms within 5 Å from the edges, restrained harmonically in the z direction only. GLC systems were prepared by selecting carbon atoms which were within 10 nm from the center and pulling them apart in the z direction. Each GLC had different-sized cavities. Ellipsoid shaped solvation boxes were placed in the cavities between the graphene sheets. The periodic boundary condition was set up such that, in the xy directions, the graphene surfaces in the principal box were 1 nm away from the box. In the z-direction, the graphene surfaces were separated by 50% above the dimensions of the ellipsoidal water droplet, to minimize interactions. Both types of systems were minimized for 5000 steps and pre-equilibrated for 0.100 ns. Bulk water systems had 2 ns of production runs, whereas GLC systems had 10 ns of production runs. Coordinates were recorded every 10 ps.

The water densities in different systems were determined from a calculation of the radial dependence of the number of water molecules within concentric spheres. We took concentric spheres of a different diameter, r (starting at r = 5Å), and increments of $1 - 5$ Å, until the maximum height of graphene was reached for the entire simulation. We calculated the mass of all water atoms within the sphere. At each value of r, we determined the average density and its standard deviation, integrated with respect to time. From the standard deviations, we determined the uncertainty at the 99.5% confidence level. We estimated the value of the density, using the density values at intermediate values of r, which were consistent with each other and had low uncertainty. When r was too small, the uncertainty was large; when r was too large, the density could be underestimated, because the volume could include regions outside the GLC, which was vacuum.

In order to describe microscopic conditions in GLCs of different sizes, we modeled these systems by atomistic molecular dynamics simulations. In earlier studies, we have shown that water nanodroplets can fold graphene into different superstructures to form GLCs [248]. Here, we ran molecular dynamic simulations on two type of GLCs with: 1) square graphene sheets (60×60 nm^2) and 2) circular graphene sheets with a radius of 30 nm. Each type of GLC was simulated with different numbers of water molecules, ranging from 2.5×10^4 to 3.2×10^5 molecules. We calculated the densities of each system in order to determine its pressure. In all GLC systems shown in Figure 69 and Figure 70, we determined the radial profile of water density. In order to assess the density vs. pressure in bulk water and benchmark these densities with our GLC calculations, we did the same type of calculations in bulk water (without the GLC) at pressures of 0.101325, 10.325, and 30.3975 MPa, shown in Figure 71. From these dependencies on the known applied pressures, we have determined density vs pressure for water in an arbitrary environment, ($\frac{\partial \rho}{\partial p}_T \approx 5.9 \times 10^{-4}$ g MPa^{-1} cm^{-3} , as

shown in Figure 68c (inset). This benchmarking allows us to determine the pressures inside GLCs from the water densities within them.

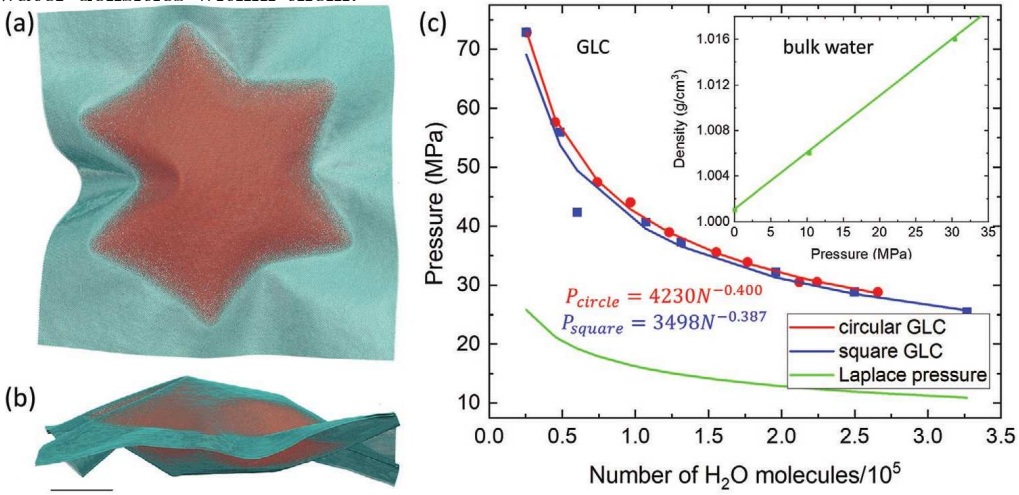

Figure 68: a) Top, and b) side views of a GLC with square graphene containing 3.2×10^5 water molecules. Scale bar denotes 10 nm. c) Water pressure in GLCs with square and circular graphene sheets vs. number of entrapped water molecules. The red and blue lines are fitted pressure curves for the number of water molecules enclosed in each circular and square GLC. The green line represents the Laplace pressure inside free water droplets containing the same number of water molecules as the GLCs. The inset is a scatter graph of densities of bulk water with respect to pressure.

Figure 68c shows the calculated pressures based on the densities of water in GLCs as a function of the number of entrapped water molecules. The deviation of density ($\Delta\rho$) from the ambient density (1 g cm^{-3}) and the pressure of water droplet in the GLCs are inversely proportional to the number of water molecules confined inside each GLC. The densities and shapes of the cavities of GLCs formed with either square or circular graphene with the same number of entrapped water molecules are very similar (Figure 69 and Figure 70). The significantly lower pressure of water in Figure 68c for the square GLC with 0.6×10^5 water molecules is an outlier and could be the result of high simulation uncertainty when calculating the radial profile of water density in that GLC (Figure 69c). In order to determine the contribution of Laplace pressure in the pressure build-up in the GLC-encapsulated water, the Laplace pressures of free water droplets containing the same number of water molecules in

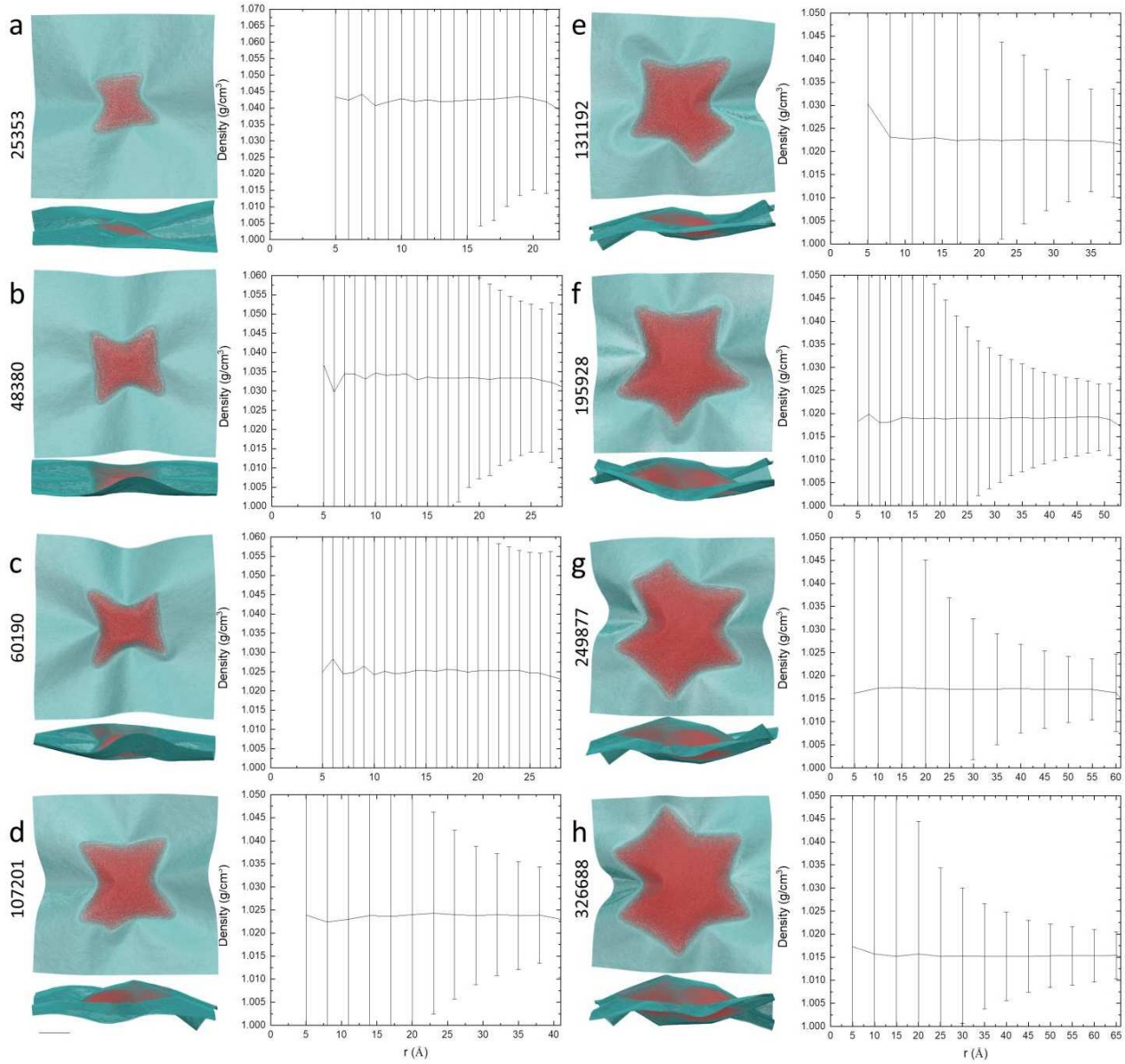

Figure 69: *Images and radial profiles of GLC systems with square graphene.* Number of molecules (indicated at left) increase down the column and left to right. Error bars represent a 99.5% confidence interval. Scale bar in d represents 10 nm.

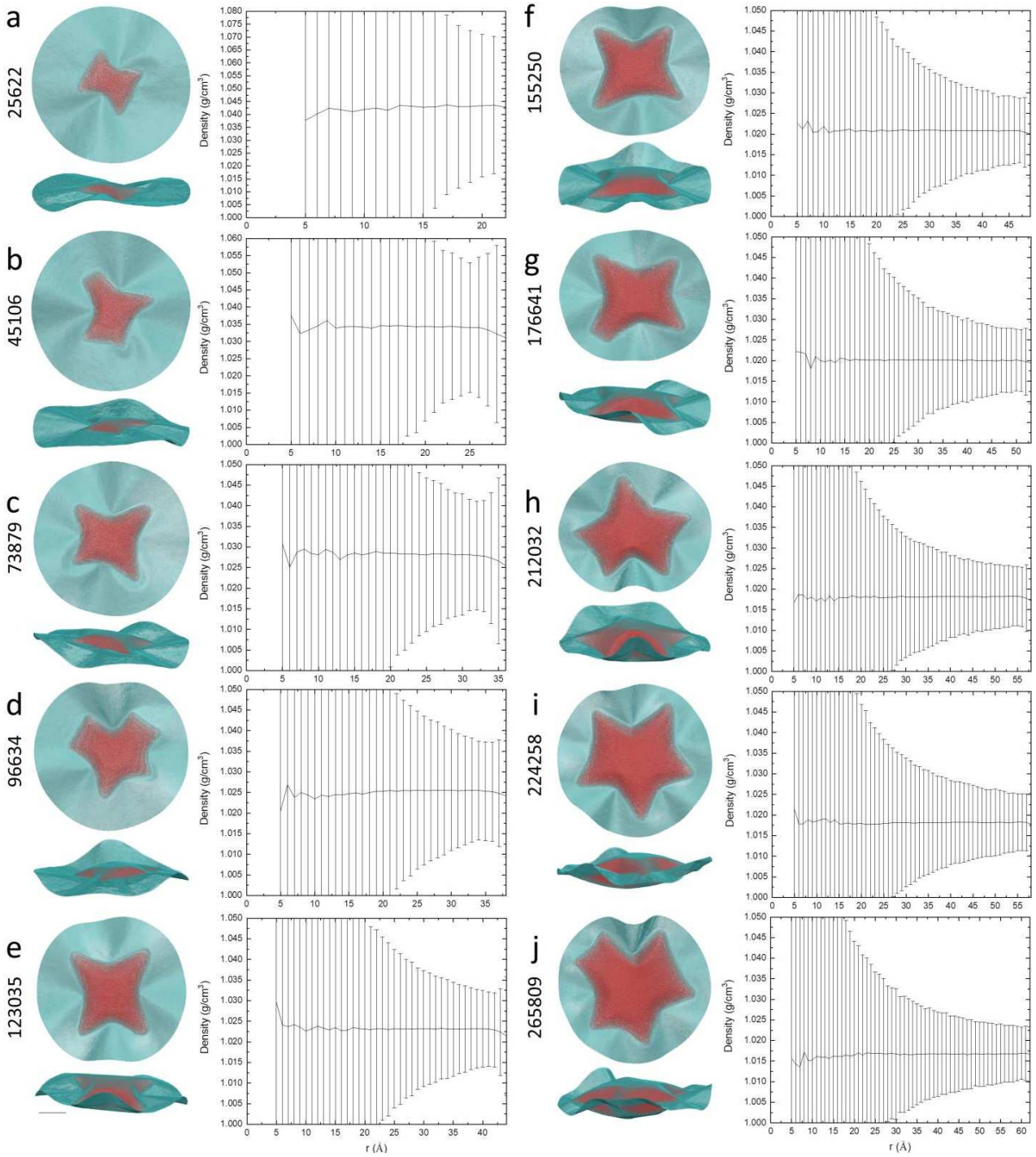

Figure 70: *Images and radial profiles of GLC systems with circular graphene.* Number of molecules (indicated at left) increase down the column and left to right. Error bars represent a 99.5% confidence interval. Scale bar in e represents 10 nm.

each GLC were calculated (Figure 68c). The calculated Laplace pressure in the free water droplets constitute $\approx 25 - 33\%$ of the final pressure in each GLC, while graphene-graphene vdW interactions and the graphene elasticity component make up the rest.

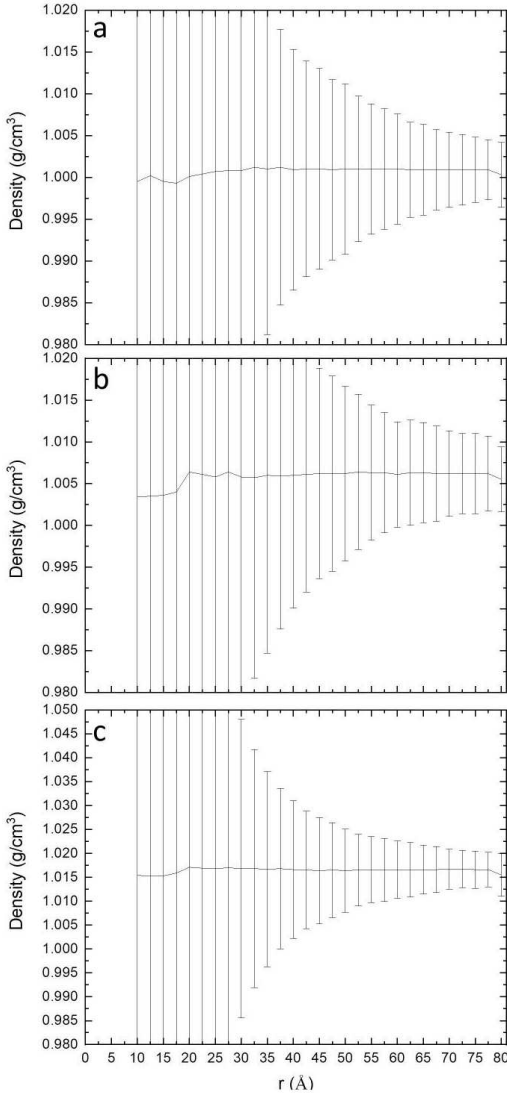

Figure 71: *Radial profile of density for bulk water:* a) p = 0.101325 MPa; b) p = 10.1325 MPa; and c) p = 30.3975 MPa. Error bars represent 99.5% confidence interval.

Conclusions

In summary, the density and pressure of water entrapped between sheets of graphene were measured using low-loss EELS, and validated by energy conservation models and molecular dynamics simulations. The density of water in the GLC was derived using the free electron model and was correlated to the pressure of water in the GLC system. The density of water in the GLC sample with basal length of 200 nm reached 1.12 ± 0.10 g cm^{-3} indicating that the internal pressure of GLC was up to 400 ± 50 MPa. To evaluate our experimental results, an energy conservation method was applied on water within GLCs. The total pressure buildup in water upon GLC fabrication was determined from three main components of pressure: Laplace, vdW, and elasticity effects. It was concluded that graphene elasticity and interlayer vdW interactions have the most significant contribution on the pressure buildup inside relatively large graphene enclosures. Finally, our atomistic molecular dynamic simulations revealed the density and pressure of graphene-enclosed water with respect to the number of encased water molecules in GLCs featuring square or circular geometries. The present work offers new insight on the thermodynamic state of water under graphene encasement, and opens new opportunities for examination of liquid specimens under confinement using advanced TEM and EELS techniques.

5.2 High Efficiency Osmotic Energy Harvesting from Vertically Aligned Boron-Nitride-Nanopore Membrane

Adapted from Ref. [369] (submitted)

Introduction

Two membrane-based approaches, namely pressure-retarded osmosis [370] and reverse electrodialysis (RED) [371] have been employed to recover the Gibbs free energy from salinity gradients. Their low power density (approximately $1 - 3$ W/m^2 from seawater), low efficiencies, and high membrane cost [372] have caused interest to shift towards the use of nano-fluidic RED (NF-RED) systems for efficient power generation using novel electrokinetic phenomena [373, 374]. A recent study on the electric current generation induced in highly charged boron nitride nanotube (BNNT) has highlighted the great potential for the NF-RED due to its enormous surface charge density, as high as 1C/m^2 [375]. This highly charged BN surface is expected to cause a locally high salt ion concentration that in turn generates an osmotic pressure gradient at the channel wall in the same direction as the salinity gradient [376]. A single BNNT used in an NF-RED device showed giant electrokinetic energy conversion, as high as 1.2 nA that is two orders of magnitude greater than the pressure-driven streaming current in the same BNNT pore, 15 pA [375]. Extrapolating this result to a macroscopic BNNT membrane with a nanotube density of $\approx 10^{10}$ nanotubes/cm^2 would result in a power density of ≈ 4 kW/m^2 that is three orders of magnitude higher than the performance of prototype pressure-retarded-osmosis power plants. Despite these merits, no such macroscopic vertically aligned BNNT membranes have ever been fabricated and their fundamental ion transport properties through the charged nanopores are unknown.

We discuss the fabrication of a macroscopic boron-nitride-nanopore (VA-BNNP) membrane comprising of high-density vertically aligned pores with a density of 10^8 nanopores/cm^2 and demonstrate

its high-efficiency electrokinetic energy conversion. We investigate the effect of the solution pH (surface-charge) on the osmotic current and the power density in the VA-BNNP membranes. A device maximum power density of ≈ 100 W/m^2 and energy conversion efficiency of 12% has been obtained with the BNNP membrane in this study that is higher than the other reverse electrodialysis systems based on ion exchange membranes or the nanofluidic channel devices [372, 377–379].

Experimental results

Electric current through the BNNP membrane was measured at different KCl concentration gradients ranging from $0.001 - 1$ M to $0.001 - 0.01$ M at pH = 7.5, 9.5, and 11, as illustrated in Figure 72a. It is important to note that no electric double layer (EDL) overlap occurs inside the membrane pores with ≈ 30 nm inner diameter for the electrolyte concentrations of high concentration side (1M and 0.3 nm of Debye length) and low concentration side (1 mM and ≈ 9.6 nm of Debye length). The current corresponding to the zero-applied external bias was extracted by measuring the I-V response of the membrane in the concentration gradient system. The pure osmotic current (I_{os}), was then obtained by subtracting the redox potential at the electrode-solution interface determined by the Nernst equation. We validated the measurement of redox potential by using track-etched polycarbonate (TEPC) membranes of 100 nm diameter size. Figure 72b shows that the osmotic current values of three BNNP membranes with different areas all increase as the solution pH increases, which clearly supports the osmotic current generation mechanism in other charged nanopore systems (e.g. BNNT, MoS_2). As pH increases, I_{osm} values increase sharply because OH- ions can be chemisorbed on the BN surface due to water dissociation on a h-BN surface ($BN_3 + H_2O \rightleftharpoons BN_3 - OH^- + H^+$) [375]. As mentioned above, the increased surface charge consequently leads to stronger electrostatic interactions between the membrane fixed charges and the mobile ions. In order to investigate further the effect of pH on surface charges of the BNNP membrane, zeta potential of the

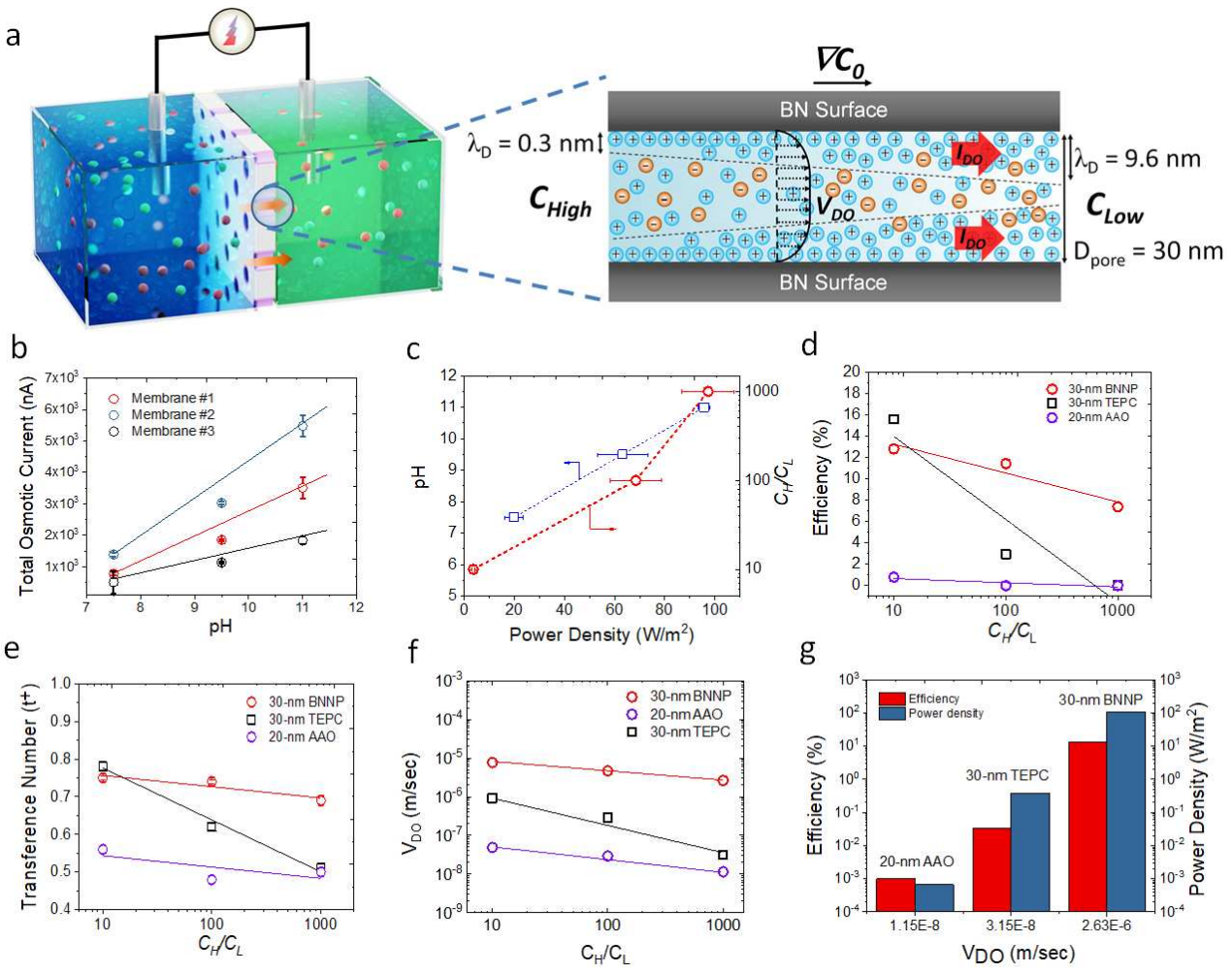

Figure 72: **Osmotic current and power generation.**a, Schematic of RED experimental set up and diffusio-osmosis flux (V_{DO}) and osmotic current (I_{DO}). b, Osmotic current generation for three different BNNP membranes at pH= 7.5, 9.5, and 11 with $C_H/C_L = 1,000$. Error bars represent standard deviation of four different measurements. c, Maximum power generation of the BNNP membrane at different pH and KCl concentration gradient. d, Efficiency of BNNP membrane at different KCl concentration gradient and its comparison with similar channel size of ion-selective track-etched polycarbonate (TEPC) membrane (30−nm pore diameter) and bare AAO membrane (20−nm pore diameter). e, Comparison of transference number with 30−nm TEPC and 20−nm AAO membrane at pH= 11. f, Calculated diffusio-osmosis velocity. C_{infty} values were calculated using COMSOL Multiphysics software at pH = 11. g, Linear scaling of the diffusio-osmosis velocity for efficiency and power density of membranes at pH = 11 and $C_H/C_L = 1,000$ at pH = 11.

surface of BNNP was measured using the streaming potential technique under varying pH conditions. The zeta potential, ζ, increases with increases in pH, suggesting the accumulation of more negative charges on the BN surface. It has been reported that the surface charge density estimated from pressure-driven flow (e.g. streaming zeta potential method) is much smaller than the estimated charge density calculated from diffusion-based conductance measurements [375]. Thus, to obtain an accurate value for the surface charge density in BNNP, we measured the ion current, I, generated through the BNNP membrane under an electric potential drop, ΔV, and deduced the electric conductance, $G = \frac{I}{\Delta V}$, as a function of salt concentration. For the given membrane, these curves show saturation of the conductance at low salt concentration, which is a signature of a surface conductance and charge. An increase in the surface charge is seen as the solution pH is increased, with a high value of $\approx$ 110 mC/m^2 at pH 11. This value is higher than other materials (e.g. silica [380], AAO [381], TiO_2 [382]).

MD simulations: methods and results

The ionic solution flow is simulated by a boron nitride nanotube (BNNT) functionalized on its inner walls by charged hydroxyl groups at 108 mC/m^2, 76.7 mC/m^2 , and 32.3 mC/m^2 concentrations (Figure 74). The diameter and length of BNNT are about 5.8 nm and 15 nm, respectively. The BNNT is connected to two chambers with potassium chloride (KCL) solution at 1 mol/L (left) and 0.001 mol/L (right) KCl concentrations, respectively. A fixed graphene slabs is located at the end of each solution chamber with a vacuum layer in order to cut off the connection between the two chambers, meantime the vacuum layer can keep ions and water freely exchange between the two chambers.

The MD simulations were performed with NAMD [37] , using a modified CHARMM force field. Water molecules (TIP3P model [338], ions, hydrogen group and graphene sheet were described by

the CHARMM general force field [39, 40]. The Lennard-Jones (LJ) parameters for B and N atoms were evaluated form literature [383, 384], using $MP2/6-31G*$ level of theory to determine partial charges of functionalized BNNTs. The systems were simulated at a temperature of 300 K with a Langevin dynamics, a damping constant of 0.1 ps^{-1} and a time step of 2 fs in an NVT ensemble, with periodic boundary conditions imposed in all three directions. The partial mesh Ewald summation (PME) [57] was used to describe a long-rang Columbic coupling. The switching distance for non-bonded interactions was set to 8 Å, and the cut-off was set to 10 Å. Figure 74-Figure 76 shows the average radial ion concentration profiles calculated at different positions along the functionalized BNNT after $\approx$ 30 ns of simulations. The ions distributions were averaged over 3 nm long regions selected at the BNNT entrance (high concentrated solution), center and exit (low concentrated solution).

In order to gain better insights on how the interfacially driven salt-concentration difference builds an osmotic pressure gradient inside the tube to drive diffusio-osmosis, we have performed molecular dynamics (MD) simulations. In our MD studies, we built BNNPs of 5.8 nm diameter and 15 nm length whose inner walls were functionalized with charged hydroxyl groups at one of three surface charge densities: 0.0323 C/m^2 (pH= 7.5), 0.0767 C/m^2 (pH= 9.5), and 0.108 C/m^2 (pH= 11). We computed ionic solution concentration profiles through a BNNP connecting two chambers with potassium chloride (KCL) solution at 1 M and 0.27 M KCl concentrations, as shown in Figure 73a. Here, we use 0.27 M for the low concentration side of the BNNP instead of the 0.001 M of the experimental case because the diameter in the MD simulations is only 5.8 nm rather than the 30 nm of the experiment. This increased molarity ensures that the EDL does not overlap, as consistent with the experiment. Figure 73b and c reveal the radial ion concentrations of K^+ and Cl^- at pH= 7 and pH= 11, respectively. The radial water and ion concentrations at all considered pH conditions are also

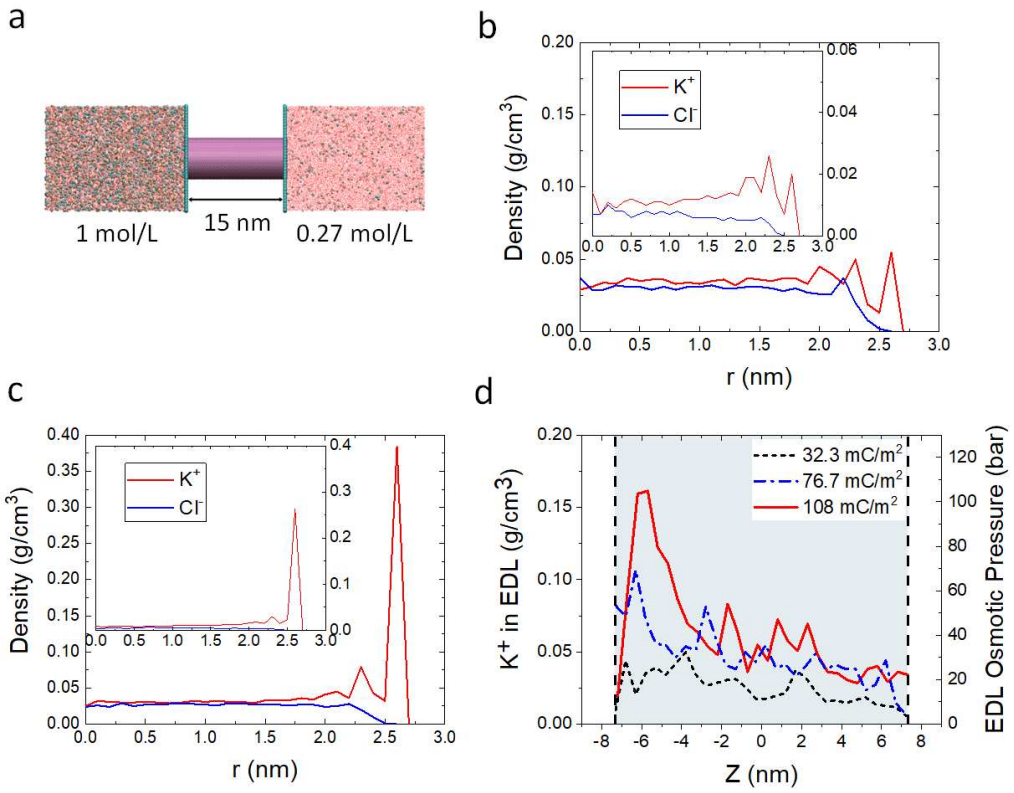

Figure 73: **Ion transport studies.** a, Molecular dynamics simulation model system. K^+ and Cl^- ion radial concentration profile near pore entrance at charge densities of b, 32.3 mC/m^2 and c, 108 mC/m^2 . Insets indicate ion concentration profile near exit (low concentration side). d, K^+ ion concentration gradient (left axis) along z direction and osmotic pressure gradient (right axis) along the z direction at charge densities of 108 mC/m^2 . Blue-colored regions indicate inside BNNP.

shown in Figure 74, Figure 75, and Figure 76. At the lower surface charge density of 0.0323 C/m^2 at pH= 7, K^+ and Cl^- concentrations are similar in entire BNNP and the salt concentration difference in EDL between the pore entrance and exit is approximately only 0.03 g/cm^3 (the longitudinal K^+ concentration profile in Figure 73b). As the surface charge increases (Figure 75 and Figure 76), the K^+ cations highly adsorb on the BNNP walls and the ion concentration in the EDL become larger than the lower surface charge density (Figure 74). In particular, as shown in Figure 73c and d (right axis of K^+ ion concentration), at the highest surface charge concentration (0.108 C/m^2), K^+ ions are highly concentrated on the BN surface and the axial ion concentration difference in the EDL reaches

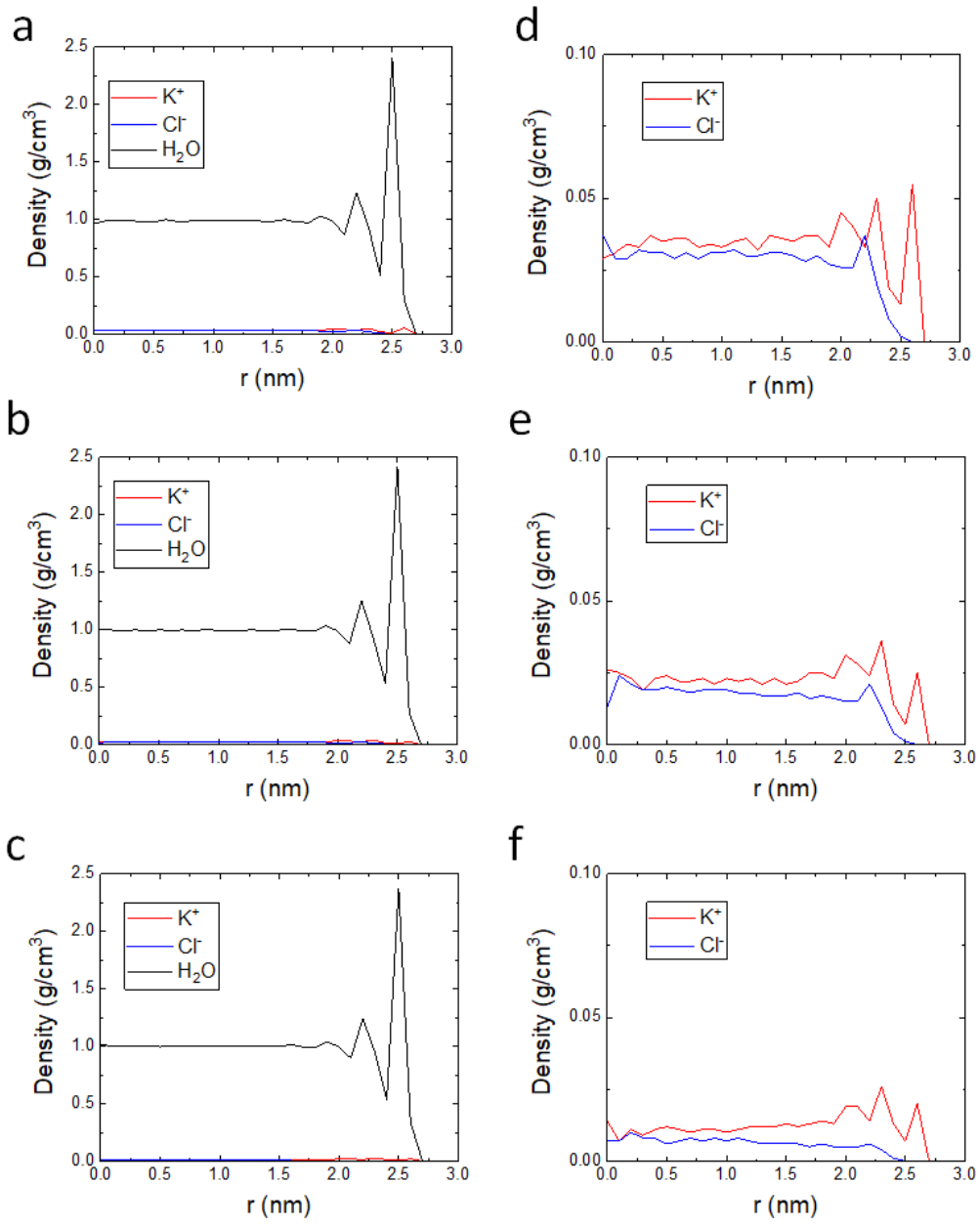

Figure 74: **Radial distributions of ions at different longitudinal positions of a functionalized BNNP at 32.3 mC/m^2.** Average K^+ , Cl^- and water concentration profiles along the radial direction at the nanotube a, entrance, b, center, and c, exit, calculated for inner surface charge densities of 32.3 mC/m^2 . K^+ and Cl^- concentration in high resolution are shown in d, entrance, e, center, and f, exit.

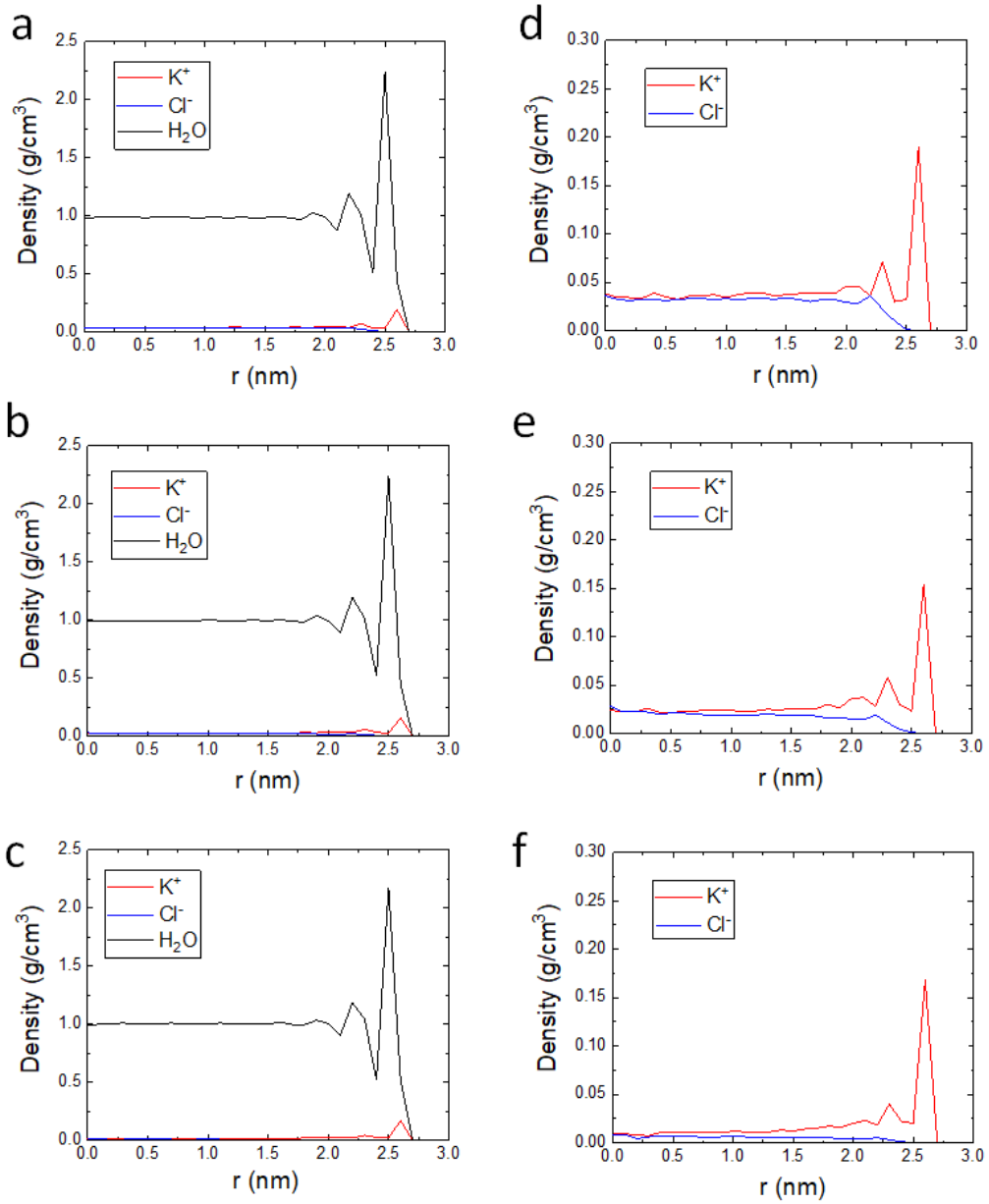

Figure 75: **Radial distributions of ions at different longitudinal positions of a functionalized BNNP at 76.7 mC/m^2.** Average K^+ , Cl^- and water concentration profiles along the radial direction at the nanotube a, entrance, b, center, and c, exit, calculated for inner surface charge densities of 76.7 mC/m^2 . K^+ and Cl^- concentration in high resolution are shown in d, entrance, e, center, and f, exit.

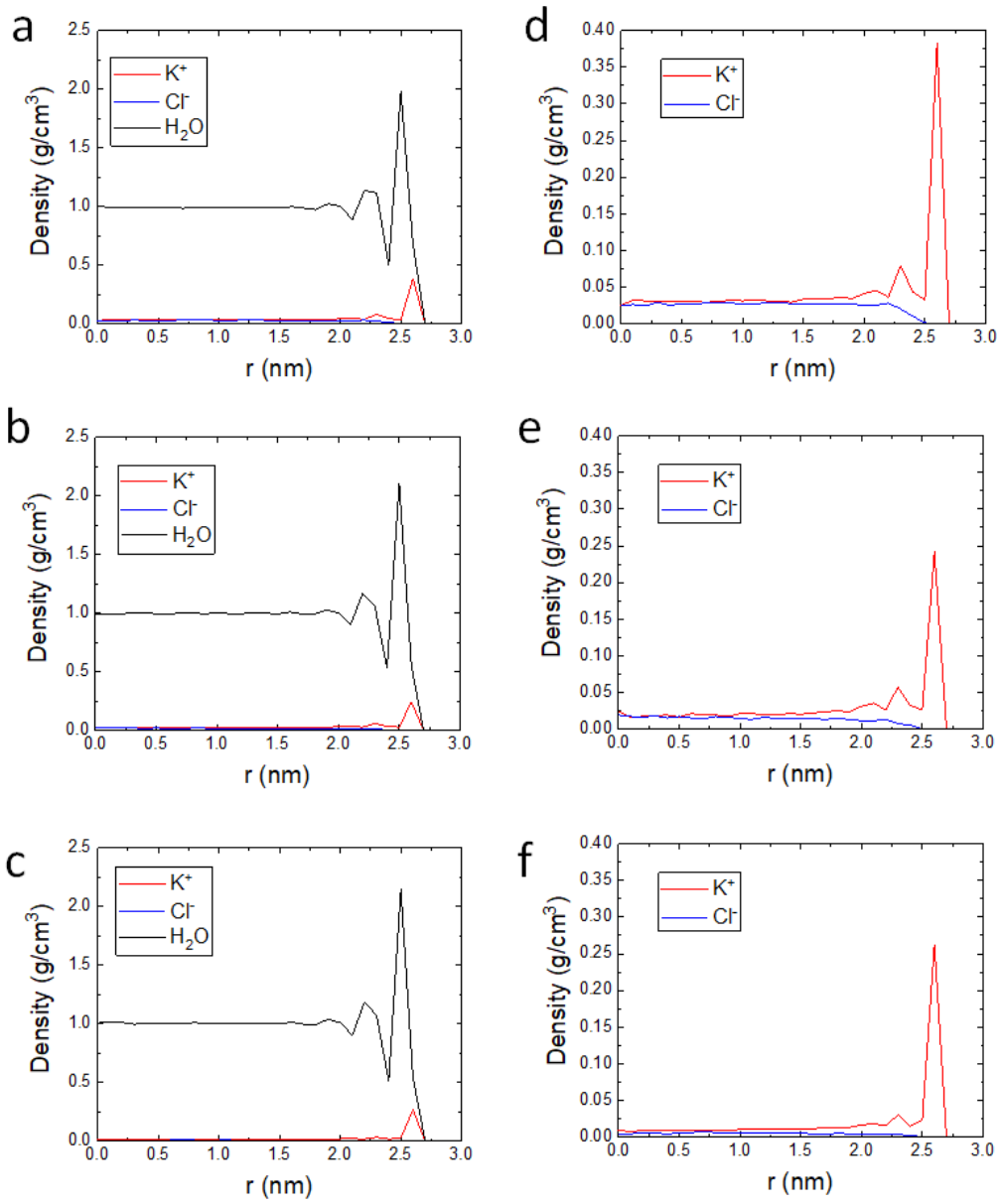

Figure 76: **Radial distributions of ions at different longitudinal positions of a functionalized BNNP at** 108 **mC/m^2.** Average K^+ , Cl^- and water concentration profiles along the radial direction at the nanotube a, entrance, b, center, and c, exit, calculated for inner surface charge densities of 108 mC/m^2. K^+ and Cl^- concentration in high resolution are shown in d, entrance, e, center, and f, exit.

0.12 g/cm^3 , compared to the small (0.03 g/cm^3) concentration difference present at pH= 7 (0.0323 C/m^2). It has been reported that monovalent and divalent ions can be condensed on the surface of electrode [385], and such high ion-concentration differences across the ends of BNNPs can result in large osmotic pressure gradient within the diffuse layer, resulting in significant diffusio-osmotic flux and osmotic current [375, 386]. Indeed, as shown in Figure 73d (right axis), the osmotic pressure difference in the EDL of 15-nm length BNNP at pH= 11 (108 mC/m^2) is approximately 75 bars (based on Van't Hoff equation). Thus, the high ion concentration and osmotic pressure gradient in the BNNP causes cationic charges within the diffuse layer to be dragged by diffusio-osmotic flow, thus resulting in high transference number and osmotic currents. The radial ion distribution results also reveal that at the high surface density of OH^- groups, K^+ is highly concentrated at the nanotube wall, while both K^+ and Cl^- ions are present in a similar amount in the tube core (Figure 74, Figure 75, and Figure 76).

Conclusion

We compare the performance of the BNNP membrane with other single stage NF-RED systems. The maximum power density of the BNNP membrane, $\approx$ 105 W/m^2 , is much higher than that of silica nanochannel and nanofluidic crystal RED devices. Compared to single BNNT pore and single MoS_2 pore RED devices, the BNNP membrane shows lower power density, however, it is important to note that their power densities in the table are calculated based on power density per unit pore surface and extrapolate its nm-scale area to meter-scale. Thus, actual generated power from the single pore system ranges only few pW per unit, while BNNP membrane with high pore density have powers five orders of magnitude higher than single-pore-based RED system. Moreover, the BNNP fabrication method is scalable to large areas, and the areal power density of the single stage BNNP device is already 165 mW/m^2 which is an order of magnitude higher than the 27 mW/m^2

of the electric-eel-inspired hydrogel system [387]. The areal power density of the BNNP membrane could be further enhanced by increasing BN pore density from the current $\approx 10^8$ pores/cm^2 to $\approx 10^{11}$ pores/cm^2 , which can be accomplished by optimizing the thickness of the BN layer, as well as electrolyte solution condition and electrochemical process for AAO membrane fabrication [388]. However, it is very challenging to increase pore density of other single pore systems up to certain level to achieve practical power per device. Among all other RED systems, only the BNNP membranes can surpass the tradeoff curve with its macroscopic size, high efficiency, and power density. Thus, our high-efficiency BNNP membranes show a strong prospect for the application for large-scale energy harvesting as well as for powering small-scale devices.

In summary, we demonstrate rationally designed nanostructured vertically aligned boron-nitride-nanopore membranes (VA-BNNP) which can efficiently harness osmotic power from salinity gradients. A thin h-BN layer was uniformly deposited within the pores of anodized alumina substrates by low-pressure chemical vapor deposition to produce the first-ever macroscopic VA-BNNP membrane with high nanopore density, up to $\approx 10^8$ pores/cm^2. The results of scanning confocal Raman spectroscopy and X-ray photoelectron spectroscopy (XPS) showed the high quality of the h-BN layers in the AAO pores. We investigated the power generation of the macroscopic VA-BNNP membranes at different pH and salinity concentrations. The power generation per unit pore area increased as the salt concentration and pH increased. The highest power density of the membrane was up to ≈ 100 W/m^2 which is two orders of magnitude higher than that of other macro-scale, salinity-gradient-driven, power-generation systems reported so far. In addition, we also elucidate the fundamental ion transport mechanism in BN nanopore using analyses and molecular dynamic simulations to show the impact of surface-charge-associated diffusion-osmotic transport in the pores. These findings in-

dicate the great potential of large-area VA-BNNP membranes as next-generation nanostructured membranes for renewable energy harvesting.

CHAPTER 6

CONCLUSIONS

This thesis includes research on projects describing processes occurring on the nanoscale. First we looked as at supramolecular self-assembly processes. We started with single amino acids and nucleobases forming nanoscale. Then we graduated to polypeptides. In these systems with applications to biology we saw structure stability and interactions with other molecules. Then we transferred our applications to material science, where we saw self-assembly mechanisms and stability of non-biological supramolecular assemblies. We even observed interactions of supramolecular structures with biomolecules. We then looked at nanofluidics, where we tested well-known macro size phenomenon to see if they occur at the nanoscale.

Section 3.1 - Formation of Apoptosis-Inducing Amyloid Fibrils by Tryptophan: The crystal of pure left handed enantiomer TRP bent along the aromatic zipper. This bending could be the precursor of the nucleation site of the crystal, thus we observe preferential fibrillar growth of this crystal.

Section 3.2 - Chirality-induced self-assembly of aromatic amino acids into supramolecular materials: The racemic mixture of TRP molecules in the crystal did not bend in any preferential direction, thus the precursor of the nucleation crystal does not have any directional growth and the crystal is then 2D. The pure PHE enantiomer grows in 1D because it is energetically favorable for the PHE amino acids to coalesce such that the crystal grows elongating the aromatic zipper.

Section 3.3 - Differential inhibition of metabolite amyloid formation by generic fibrillation-modifying polyphenols: We saw inhibition of formation of metabolite fibril suprastructure with

polyphenols TA and EGCG. TA and EGCG can binding equally strongly to the same metabolite in the same phase (solvated or crystalline). TA is a bigger molecule with more functional groups. Therefore, it can bind to more solvated metabolites, thus is a more effective inhibitor of fibril formation before crystallization has occurred. TA and EGCG can bind to the same number of crystalline metabolites, yet the collaborators used 10-fold higher concentration of EGCG, thus saw more inhibition with EGCG.

Section 3.4 - Metabolite amyloid-like fibrils interact with model membranes: The polar head groups of phospholipids interact with the metabolite crystal such that electrostatic interactions are optimized. TRP has an apolar head group. Therefore, the zwitterions in TRP crystal interact directly with the lipid bilayer membrane. TYR has a polar head group that interacts directly with the lipid bilayer. ADN is quadrupolar. Therefore, it needs the highest dispersion interactions to compensate for weak electrostatic interactions. The plane of ADN molecules in the crystal are parallel to the plane of the lipid bilayer. Our enthalpies of binding per contact area match closely with experimental results when comparing the same metabolite to different phospholipid membranes.

Section 3.5 - Transition of Metastable Cross-α Crystals into Cross-β Fibrils by β-Turn Flipping: The α helical structure (healthy state) represents a metastable state, whereas the cross-β linker (disease state) is the true global minimum. As temperature increases the peptide folds into the cross-*beta* linker due to entropic effects, when peptides are solvated or dimerized. Trimers and higher order oligomers are not so temperature dependent. Trimers and higher oligomers as well as crystalline peptides have a tendency to have the cross$-\beta$ linker conformation. Cross-β linker is more presence at higher temperatures or in the presence of other peptides.

Section 3.6 - Anisotropic assembly of Metal Nanostructures onto an Asymmetric Peptide-Based Nanofibers: The unit cell of the crystal of SHR-FF in the cross-β conformation has a strong

net dipole moment. Therefore, propagation of this crystal causes the crystal to have a strong dipole moment. The AUNP has a strong charge due to the coating of citrate ligands. The attraction of AUNP and SHR-FF crystal is a monopole-dipole interaction. The AUNP, which is negatively charged will diffuse to the highest positive end of the SHR-FF crystal.

Section 3.7 - Electrical Conductivity, Selective Adhesion, and Biocompatibility in Bacteria-Inspired Peptide-Metal Self-Supporting Nanocomposites: In another polypeptide, there is an antiparallel beta sheet formation upon its self-assembly. This configuration remains intact even in the presence of a AUNP. There are at least two layers of antiparallel beta sheet to prevent twisting.

Section 4.1 - Co-Crystallization of Proteins and NP-Polymer Conjugates: Both the PEG and the AUNP can bind to the lysozyme proteins. Each PEG link has the same enthalpy of binding, yet the longer chains can have more links bind to the proteins, thus increasing the net enthalpy of binding. In addition there is less entropy loss of co-crystallization with the longer PEG. The oxygen atoms bind to the positively charged groups of the lysozyme proteins. The AUNR also aligns itself in the center of the unit cell for maximum exposure to the positive dipole region of the crystal, i.e. parallel to the c axis.

Section 4.2 - Controlled Self-Assembly of Photofunctional Supramolecular Nanotubes: PEG links on the PP2b molecules can form localized apolar environments, which protect the apolar core from a polar environment when necessary. When we have 100% water a solvent, we need long PEG chains (44 link long). The PP2b molecules form a huge cluster, where the PEG chains protect the inner core of the molecules from the aqueous environment. This cluster is the precursor to the hexagonal nanotube. When there is 80 : 20 v:v of water:THF, the solvent is relatively polar. Therefore, the PEG chains still are need to protect the apolar cores. This causes fast oligomerization, where the oligomers are rigid, thus fibrils form rather than nanotubes. Finally when 60 : 40 v:v of

water:THF, the solvent is relatively apolar. Therefore the PEG chains are not needed to protect the PP2b cores. We have slow oligomerization, yet they are flexible, thus nanotubes form.

Section 4.3 - Atomically precise organomimetic cluster nanomolecules assembled via perfluoroaryl-thiol S N Ar chemistry: As the number of PEG links increase the average size of the atomically precise NP increases with a relation $r_{gyr} \propto \sqrt{n_{links}}$ as expected with Fick's law of diffusion. Longer links have a higher skew to larger values of r_{gyr} because these larger chains are flexible and can extend and then fold back. We see higher skews when the NPs are in PBS solution because the motion of PEG chains can couple with the motion of ions.

Section 4.4 - Hybridization of Biomolecular Crystals and Inorganic Nanomaterials: Biomolecular crystal and planar nanosurfaces become more rigid when they came into contact with each other. There is a strong coupling between biomolecular crystals and nanosurfaces that keep them attracted. The crystal does not dissolve because the intra-crystal interactions are significantly stronger than inter-crystal interactions with the nanosurfaces. When we have enantiopure crystals, the crystal can wrap around a CNT in leaps after some delay. This is due to the predisposition for enantiopure crystals to have helical bending in solvated environments. Relative sizes and position of the CNT and crystal determines how much this crystal will wrap around the CNT. When we have racemic mixture of metabolites in the biomolecular crystal, then the crystal wraps around the CNT continuously and immediately, due to their predisposition not to bend in solvated environments.

Section 4.5 - Nanosheets and Metallo-Hydrogel Formed by 2-nm Metal-Organic Cages based on electrostatic interaction: Electronic structure and steric effects determine how the cages bind with each other, which ultimately determine whether gelation occurs or precipitation. We need $\sigma - \pi$ bonds from the alkyl group in the ligand with the aromatic group in the neighboring cages. There seems to be preferential binding when the aromatic group is covalently bonded to an electron

withdrawing group (such as the carboxyl group) rather than an electron donating group (such as a pyridine group). We need two such aromatic groups next to each other to form a unimolecular network, which then leads to gelation.

Section 4.6 - In Situ Liquid-Cell TEM Observation of Multiphase Classical and Non-classical Nucleation of Calcium Oxalate: When there are no citrate inhibitors present, Calcium oxalate clusters form and grow without limit. Once they reach a certain size, consisting of ≈ 10 Ca^{2+} ions in the cluster the ratio of water:Ca^{2+} reaches a limiting value ≈ 5. When we have the citrate inhibitors present, the clusters are limited in size and are more are more finger-like. Once these cluster reach a certain size ratio of water:Ca^{2+} reaches a limiting value ≈ 12.5. The cluster we see in the absence of citrate inhibitors is the precursor of the COM crystals, whereas the finger-like clusters formed in the presence of citrate inhibitor is the precursor of COD crystals.

Section 5.1 - Assessment of Pressure and Density of Confined Water in Graphene Liquid Cells: Pressure builds up mostly due to attraction of the graphene slabs through dispersion interactions between the graphene layer. The Laplace pressure accounts only $\approx 33\%$ of the pressure in the water droplet. As the number of water molecules in the droplet increases the pressure decays faster than $N_{water}^{-\frac{1}{3}}$.

Section 5.2 - High Efficiency Osmotic Energy Harvesting from Vertically Aligned Boron-Nitride-Nanopore Membrane: The charged BNNP has enhanced power generation through filtration of osmotic diffusion. The positively charge cations builds up on the walls. When we increase the pH of the solution there is a larger flow of positive ions flowing into the tube.

We used all atomistic simulations to model self-assembly processes (with applications to biology and material science) and explored nanofluidics. We confirmed macroscale phenomenon originating

at the molecular level through these simulations. We enhanced our understanding of these processes by elucidating the mechanisms at the molecular level and in many cases even helped the experimental understand the results of their experiments. Sometimes we suggested experiments for our collaborators to do based on our observations at the molecular level.

CITED LITERATURE

1. Shaham-Niv, S., Rehak, P., Vuković, L., Adler-Abramovich, L., Král, P., and Gazit, E.: Formation of apoptosis-inducing amyloid fibrils by tryptophan. *Isr. J. Chem.* , 57(7-8):729–737, July 2017.

2. Bera, S., Xue, B., Rehak, P., Jacoby, G., Ji, W., Shimon, L. J. W., Beck, R., Král, P., Cao, Y., and Gazit, E.: Self-assembly of aromatic amino acid enantiomers into supramolecular materials of high rigidity. *ACS Nano* , 14(2):1694–1706, February 2020.

3. Shaham-Niv, S., Rehak, P., Zaguri, D., Levin, A. a., Adler-Abramovich, L., Vukovic, L., Kral, P., and Gazit, E.: Differential inhibition of metabolite amyloid formation by generi c fibrillation-modifying polyphenols. *Communications Chemistry* , 1(1):1–11, 2018.

4. Shaham-Niv, S., Rehak, P., Zaguri, D., Kolusheva, S., Král, P., and Gazit, E.: Metabolite amyloid-like fibrils interact with model membranes. *Chem. Commun.* , 54(36):4561–4564, 2018.

5. Mondal, S., Jacoby, G., Sawaya, M. R., Arnon, Z. A., Adler-Abramovich, L., Rehak, P., Vuković, L., Shimon, L. J. W., Král, P., Beck, R., and Gazit, E.: Transition of metastable cross-α crystals into cross-β fibrils by β-turn flipping. *J. Am. Chem. Soc.* , 141(1):363–369, January 2019.

6. Guterman, T., Ing, N. L., Fleischer, S., Rehak, P., Basavalingappa, V., Hunashal, Y., Dongre, R., Raghothama, S., Král, P., Dvir, T., Hochbaum, A. I., and Gazit, E.: Electrical conductivity, selective adhesion, and biocompatibility in bacteria-inspired peptide-metal self-supporting nanocomposites. *Adv. Mater.* , 31(10):1807285, March 2019.

7. Cohen, E., Weissman, H., Pinkas, I., Shimoni, E., Rehak, P., Král, P., and Rybtchinski, B.: Controlled self-assembly of photofunctional supramolecular nanotubes. *ACS Nano* , 12(1):317–326, January 2018.

8. Qian, E. A., Wixtrom, A. I., Axtell, J. C., S aebi, A., Jung, D., Rehak, P., Han, Y., Moully, E. H., Mosallaei, D., Chow, S., Messina, M. S., Wang, J. g. Y., Royappa, A. T., Rheingold, A. L., Maynard, H. D., Král, P., and Spokoyny, A. M.: Atomically precise organomimetic cluster nanomolecules assembled via perfluoroaryl-thiol snar chemistry. *Nature Chemistry* , 9(4):333–340, 2017.

9. Yang, Y., Rehak, P., Xie, T.-Z., Feng, Y., Sun, X., Chen, J., Li, H., Král, P., and Liu, T.: Nanosheets and hydrogels formed by 2 nm metal–organic cages with electrostatic interaction. *ACS Applied Materials & Interfaces* , 12(50):56310–56318, dec 2020.

10. Ghodsi, S. M., Sharifi-Asl, S., Rehak, P., Král, P., Megaridis, C. M., Shahbazian-Yassar, R., and Shokuhfar, T.: Assessment of pressure and density of confined water in graphene liquid cells. *Adv. Mater. Interfaces* , 7(12):1901727, June 2020.

11. Karamanos, T., Kalverda, A., Thompson, G., and Radford, S.: Visualization of transient protein-protein interactions that promote or inhibit amyloid assembly. *Molecular Cell* , 55(2):214–226, 2014.

12. Krishnan, R., Goodman, J. L., Mukhopadhyay, S., Pacheco, C. D., Lemke, E. A., Deniz, A. A., and Lindquist, S.: Conserved features of intermediates in amyloid assembly determine their benign or toxic states. *Proc Natl Acad Sci USA* , 109(28):11172, July 2012.

13. Sawaya, M. R., Sambashivan, S., Nelson, R., Ivanova, M. I., Sievers, S. A., Apostol, M. I., Thompson, M. J., Balbirnie, M., Wiltzius, J. J. W., McFarlane, H. T., Madsen, A. Ø., Riekel, C., and Eisenberg, D.: Atomic structures of amyloid cross-β spines reveal varied steric zippers. *Nature* , 447(7143):453–457, 2007.

14. Knowles, T. P. J., Vendruscolo, M., and Dobson, C. M.: The amyloid state and its association with protein misfolding diseases. *Nature Reviews Molecular Cell Biology* , 15(6):384–396, 2014.

15. Eisenberg, D. and Jucker, M.: The amyloid state of proteins in human diseases. *Cell* , 148(6):1188–1203, 2012.

16. Kapurniotu, A.: Shedding light on alzheimer's β-amyloid aggregation with chemical tools. *ChemBioChem* , 13(1):27–29, January 2012.

17. Buell, A. K., Galvagnion, C., Gaspar, R., Sparr, E., Vendruscolo, M., Knowles, T. P. J., Linse, S., and Dobson, C. M.: Solution conditions determine the relative importance of nucleation and growth processes in α-synuclein aggregation. *Proc Natl Acad Sci USA* , 111(21):7671, May 2014.

18. Porat, Y., Kolusheva, S., Jelinek, R., and Gazit, E.: The human islet amyloid polypeptide forms transient membrane-active prefibrillar assemblies. *Biochemistry* , 42(37):10971–10977, September 2003.

19. Buell, A. K., Dhulesia, A., White, D. A., Knowles, T. P. J., Dobson, C. M., and Welland, M. E.: Detailed analysis of the energy barriers for amyloid fibril growth. *Angew. Chem. Int. Ed.* , 51(21):5247–5251, May 2012.

20. Rambaran, R. N. and Serpell, L. C.: Amyloid fibrils: abnormal protein assembly. *Prion* , 2(19158505):112–117, 2008.

21. Do, T. D., de Almeida, N. E. C., LaPointe, N. E., Chamas, A., Feinstein, S. C., and Bowers, M. T.: Amino acid metaclusters: Implications of growth trends on peptide self-assembly and structure. *Anal. Chem.* , 88(1):868–876, January 2016.

22. Buell, A. K., Esbjörner, E. K., Riss, P. J., White, D. A., Aigbirhio, F. I., Toth, G., Welland, M. E., Dobson, C. M., and Knowles, T. P. J.: Probing small molecule binding to amyloid fibrils. *Phys. Chem. Chem. Phys.* , 13(45):20044–20052, 2011.

23. Gazit, E.: A possible role for π-stacking in the self-assembly of amyloid fibrils. *The FASEB Journal* , 16(1):77–83, January 2002.

24. Inouye, H., Sharma, D., Goux, W. J., and Kirschner, D. A.: Structure of core domain of fibril-forming phf/tau fragments. *Biophysical Journal* , 90(5):1774–1789, 2006.

25. Shlomo, Z., Vinod, T. P., Jelinek, R., and Rapaport, H.: Stacking interactions by two phe side chains stabilize and orient assemblies of even the minimal amphiphilic β-sheet motif. *Chem. Commun.* , 51(15):3154–3157, 2015.

26. Makin, O. S. and Serpell, L. C.: Structures for amyloid fibrils. *The FEBS Journal* , 272(23):5950–5961, December 2005.

27. Gazit, E.: Global analysis of tandem aromatic octapeptide repeats: The significance of the aromatic-glycine motif. *Bioinformatics* , 18(6):880–883, June 2002.

28. Pawar, A. P., DuBay, K. F., Zurdo, J., Chiti, F. b., Vendruscolo, M., and Dobson, C. M.: Prediction of "aggregation-prone" and "aggregation-susceptible" re gions in proteins associated with neurodegenerative diseases. *Journal of Molecular Biology* , 350(2):379–392, 2005.

29. Frederix, P. W. J. M., Scott, G. G., Abul-Haija, Y. M., Kalafatovic, D., Pappas, C. G., Javid, N., Hunt, N. T., Ulijn, R. V., and Tuttle, T.: Exploring the sequence space for (tri-)peptide self-assembly to design and discover new hydrogels. *Nature Chemistry* , 7(1):30–37, 2015.

30. Santiveri, C. M., Jiménez, M. a., Rico, M., van Gunsteren, W. F., and Daura, X.: β-hairpin folding and stability: molecular dynamics simulations of designed peptides in aqueous solution. *J. Peptide Sci.* , 10(9):546–565, September 2004.

31. Richard, D. M., Dawes, M. A., Mathias, C. W., Acheson, A., Hill-Kapturczak, N., and Dougherty, D. M.: L-tryptophan: Basic metabolic functions, behavioral research and therapeutic indications. *International journal of tryptophan research : IJTR* , 2(20651948):45–60, March 2009.

32. Martin, J. R., Mellor, C. S., and Fraser, F. C.: Familial hypertryptophanemia in two siblings. *Clinical Genetics* , 47(4):180–183, April 1995.

33. Hypertryptophanemia. http://www.orpha.net/consor/cgi-bin/OC_Exp.php?Lng = GB&Expert = 2224Orphanet, June2006, as accessed on the website:.

34. Hypertryptophanemia, familial. September 2014, as accessed on the website: http://www.omim.org/entry/600627.

35. Hartnup Disorder. HND (OMIM: 234500), July 2014, asaccessed on the website: https://omim.org/entry/234500.

36. Görbitz, C. H., Törnroos, K. W., and Day, G. M.: Single-crystal investigation of L-tryptophan with Z' = 16. *Acta Crystallographica Section B* , 68(5):549–557, Oct 2012.

37. Phillips, J. C., Braun, R., Wang, W., Gumbart, J., Tajkhorshid, E., Villa, E., Chipot, C., Ske el, R. D., Kalé, L., and Schulten, K.: Scalable molecular dynamics with namd. *J. Comput. Chem.* , 26(16):1781–1802, December 2005.

38. Vanommeslaeghe, K., Hatcher, E., Acharya, C., Kundu, S., Zhong, S., Shim, J., Darian, E., Guvench, O., Lopes, P., Vorobyov, I., and Mackerell Jr., A. D.: Charmm general force field: A force field for drug-like molecules compatible with the charmm all-atom additive biological force fields. *J. Comput. Chem.* , 31(4):671–690, March 2010.

39. Vanommeslaeghe, K. and MacKerell, A. D.: Automation of the charmm general force field (cgenff) i: Bond perception and atom typing. *J. Chem. Inf. Model.* , 52(12):3144–3154, December 2012.

40. Vanommeslaeghe, K., Raman, E. P., and MacKerell, A. D.: Automation of the charmm general force field (cgenff) ii: Assignment of bonded parameters and partial atomic charges. *J. Chem. Inf. Model.* , 52(12):3155–3168, December 2012.

41. Foloppe, N. and MacKerell, A. D.: Conformational properties of the deoxyribose and ribose moieties of nucleic acids: a quantum mechanical study. *J. Phys. Chem. B* , 102(34):6669–6678, August 1998.

42. Mackerell Jr., A. D.: Empirical force fields for biological macromolecules: Overview and issues. *J. Comput. Chem.* , 25(13):1584–1604, October 2004.

43. York, D. M., Darden, T. A., and Pedersen, L. G.: The effect of long-range electrostatic interactions in simulations of macromolecular crystals: A comparison of the ewald and truncated list methods. *J. Chem. Phys.* , 99(10):8345–8348, November 1993.

44. Mossou, E., Teixeira, S. C. M., Mitchell, E. P., Mason, S. A., Adler-Abramovich, L., Gazit, E., and Forsyth, V. T.: The self-assembling zwitterionic form of L-phenylalanine at neutral pH. *Acta Crystallographica Section C* , 70(3):326–331, Mar 2014.

45. Görbitz, C. H.: The structure of nanotubes formed by diphenylalanine, the core recognition motif of alzheimer's β-amyloid polypeptide. *Chem. Commun.* , (22):2332–2334, 2006.

46. Aizen, R., Tao, K., Rencus-Lazar, S., and Gazit, E.: Functional metabolite assemblies–a review. *Journal of Nanoparticle Research* , 20(5):125, 2018.

47. Tadepalli, S., Slocik, J. M., Gupta, M. K., Naik, R. R., and Singamaneni, S.: Bio-optics and bio-inspired optical materials. *Chem. Rev.* , 117(20):12705–12763, October 2017.

48. Knowles, T. P. J. and Buehler, M. J.: Nanomechanics of functional and pathological amyloid materials. *Nature Nanotechnology* , 6(8):469–479, 2011.

49. Ménard-Moyon, C., Venkatesh, V., Krishna, K. V., Bonachera, F., Verma, S., and Bianco, A.: Self-assembly of tyrosine into controlled supramolecular nanostructures. *Chem. Eur. J.* , 21(33):11681–11686, August 2015.

50. Babar, D. G. and Sarkar, S.: Self-assembled nanotubes from single fluorescent amino acid. *Applied Nanoscience* , 7(3-4):101–107, 2017.

51. Singh, P., Brar, S. K., Bajaj, M., Narang, N., Mithu, V. S., Katare, O. P., Wangoo, N., and Sharma, R. K.: Self-assembly of aromatic α-amino acids into amyloid inspired nano/micro scaled architects. *Materials Science and Engineering: C* , 72:590–600, 2017.

52. Jiang, S., Chekini, M., Qu, Z.-B., Wang, Y., Yeltik, A., Liu, Y., Kotlyar, A., Zhang, T., Li, B., Demir, H. V., and Kotov, N. A.: Chiral ceramic nanoparticles and peptide catalysis. *J. Am. Chem. Soc.* , 139(39):13701–13712, October 2017.

53. Yeom, J., Yeom, B., Chan, H., Smith, K. W., Dominguez-Medina, S., Bahng, J., Zhao, G., Chang, W.-S., Chang, S.-J., Chuvilin, A., Melnikau, D., Rogach, A. L., Zhang, P., Link, S., Král, P., and Kotov, N. A.: Chiral templating of self-assembling nanostructures by circularly polarized light. *Nature Materials* , 14(1):66–72, 2015.

54. Yang, G., Zhang, S., Hu, J., Fujiki, M., and Zou, G.: The chirality induction and modulation of polymers by circularly polarized light. *Symmetry (20738994)* , 11(4):474, 2019.

55. Shaham-Niv, S., Adler-Abramovich, L., Schnaider, L., and Gazit, E.: Extension of the generic amyloid hypothesis to nonproteinaceous metabolite assemblies. *Science advances* , 1(26601224):e1500137–e1500137, August 2015.

56. MacKerell, A. D., Bashford, D., Bellott, M., Dunbrack, R. L., Evanseck, J. D., Field, M. J., Fischer, S., Gao, J., Guo, H., Ha, S., Joseph-McCarthy, D., Kuchnir, L., Kuczera, K., Lau, F. T. K., Mattos, C., Michnick, S., Ngo, T., Nguyen, D. T., Prodhom, B., Reiher, W. E., Roux, B., Schlenkrich, M., Smith, J. C., Stote, R., Straub, J., Watanabe, M., Wiórkiewicz-Kuczera, J., Yin, D., and Karplus, M.: All-atom empirical potential for

molecular modeling and dynamics studies of proteins. *J. Phys. Chem. B* , 102(18):3586–3616, April 1998.

57. Darden, T., York, D., and Pedersen, L.: Particle mesh ewald: An n·log(n) method for ewald sums in large systems. *J. Chem. Phys.* , 98(12):10089–10092, June 1993.

58. Ihlefeldt, F. S., Pettersen, F. B., von Bonin, A., Zawadzka, M., and Görbitz, C. H.: The polymorphs of l-phenylalanine. *Angew. Chem. Int. Ed.* , 53(49):13600–13604, December 2014.

59. Humphrey, W., Dalke, A., and Schulten, K.: Vmd: Visual molecular dynamics. *Journal of Molecular Graphics* , 14(1):33–38, 1996.

60. Yeates, T. O. and Kent, S. B. H.: Racemic protein crystallography. *Annu. Rev. Biophys.* , 41(1):41–61, May 2012.

61. DaSilva, K. A., Shaw, J. E., and McLaurin, J.: Amyloid-β fibrillogenesis: Structural insight and therapeutic intervention. *Experimental Neurology* , 223(2):311–321, 2010.

62. Young, L. M., Saunders, J. C., Mahood, R. A., Revill, C. H., Foster, R. J., Tu, L.-H., Raleigh, D. P., Radford, S. E., and Ashcroft, A. E.: Screening and classifying small-molecule inhibitors of amyloid formation using ion mobility spectrometry-mass spectrometry. *Nature Chemistry* , 7(1):73–81, 2015.

63. Feng, B. Y., Toyama, B. H., Wille, H., Colby, D. W., Collins, S. R., May, B. C. H., Prusiner, S. B., Weissman, J., and Shoichet, B. K.: Small-molecule aggregates inhibit amyloid polymerization. *Nature Chemical Biology* , 4(3):197–199, 2008.

64. Doig, A. J. and Derreumaux, P.: Inhibition of protein aggregation and amyloid formation by small molecules. *Current Opinion in Structural Biology* , 30:50–56, 2015.

65. Bhullar, K. S. and Rupasinghe, H. P. V.: Polyphenols: multipotent therapeutic agents in neurodegenerative diseases. *Oxidative medicine and cellular longevity* , 2013(23840922):891748–891748, 2013.

66. Ebrahimi, A. and Schluesener, H.: Natural polyphenols against neurodegenerative disorders: Potentials and pitfalls. *Ageing Research Reviews* , 11(2):329–345, 2012.

67. Porat, Y., Abramowitz, A., and Gazit, E.: Inhibition of amyloid fibril formation by polyphenols: Structural similarity and aromatic interactions as a common inhibition mechanism. *Chemical Biology & Drug Design* , 67(1):27–37, January 2006.

68. Kocisko, D. A., Baron, G. S., Rubenstein, Richard an d Chen, J., Kuizon, S., and Caughey, B.: New inhibitors of scrapie-associated prion protein formation in a library of 2,000 drugs and natural products. *J. Virol.* , 77(19):10288, October 2003.

69. Ehrnhoefer, D. E., Bieschke, J., Boeddrich, A., Herbst, M., Masino, L., Lurz, R., Engemann, S., Pastore, A., and Wanker, E. E.: Egcg redirects amyloidogenic polypeptides into unstructured, off-pathway oligomers. *Nature Structural & Molecular Biology* , 15(6):558–566, 2008.

70. Bieschke, J., Russ, J., Friedrich, R. P., Ehrnhoefer, D. E., Wobst, H., Neugebauer, K., and Wanker, E. E.: Egcg remodels mature α-synuclein and amyloid-β fibrils and reduces cellular toxicity. *Proc Natl Acad Sci USA* , 107(17):7710, April 2010.

71. Rezai-Zadeh, K., Shytle, D., Sun, N., Mori, T., Hou, H., Jeanniton, D., Ehrhart, J., Townsend, K., Zeng, J., Morgan, D., Hardy, J., Town, T., and Tan, J.: Green tea epigallocatechin-3-gallate (egcg) modulates amyloid precursor protein cleavage and reduces cerebral amyloidosis in alzheimer transgenic mice. *J. Neurosci.* , 25(38):8807, September 2005.

72. Ono, K., Hasegawa, K., Naiki, H., and Yamada, M.: Anti-amyloidogenic activity of tannic acid and its activity to destabilize alzheimer's β-amyloid fibrils in vitro. *Biochimica et Biophysica Acta (BBA) - Molecular Basis of Disease* , 1690(3):193–202, 2004.

73. D'Amico, M., Di Carlo, M. G., Groenning, M., Militello, V., Vetri, V., and Leone, M.: Thioflavin t promotes aβ(1-40) amyloid fibrils formation. *J. Phys. Chem. Lett.* , 3(12):1596–1601, June 2012.

74. Frisch, M. J.: *Gaussian09* . Wallingford CTWallingford CT, 2016. Gaussian Inc.

75. Mayne, C. G., Saam, J., Schulten, K., Tajk horshid, E., and Gumbart, J. C.: Rapid parameterization of small molecules using the force field toolkit. *J. Comput. Chem.* , 34(32):2757–2770, December 2013.

76. Breneman, C. M. and Wiberg, K. B.: Determining atom-centered monopoles from molecular electrostatic potentials. the need for high sampling density in formamide conformational analysis. *Journal of Computational Chemistry* , 11(3):361–73, 1990.

77. Mahapatra, S., Nayak, S. K., Prathapa, S. J., and Guru Row, T. N.: Anhydrous adenine: Crystallization, structure, and correlation with other nucleobases. *Crystal Growth & Design* , 8(4):1223–1225, April 2008.

78. Mostad, A., Nissen, H. M., and Roemming, C.: Crystal structure of l-tyrosine. *Acta Chemica Scandinavica (1947-1973)* , 26(10):3819–33, 1972.

79. Mackerell Jr., A. D., Feig, M., and Brooks III, C. r. L.: Extending the treatment of backbone energetics in protein force f ields: Limitations of gas-phase quantum mechanics in reproducing protein conform ational distributions in molecular dynamics simulations. *J. Comput. Chem.* , 25(11):1400–1415, August 2004.

80. Yu, W., He, X., Vanommeslaeghe, K., and MacKerell Jr., A. D.: Extension of the charmm general force field to sulfonyl-containing compounds and its utility in biomolecular simulations. *J. Comput. Chem.* , 33(31):2451–2468, December 2012.

81. Tartaglia, G. G., Pechmann, S., Dobson, C. M., and Vendruscolo, M.: Life on the edge: a link between gene expression levels and aggregation rates of human proteins. *Trends in Biochemical Sciences* , 32(5):204–206, 2007.

82. Dobson, C. M.: Protein misfolding, evolution and disease. *Trends in Biochemical Sciences* , 24(9):329–332, 1999.

83. Tsemekhman, K., Goldschmidt, L., Eisenberg, D., and Baker, D.: Cooperative hydrogen bonding in amyloid formation. *Protein science : a publication of the Protein Society* , 16(17327394):761–764, April 2007.

84. Banik, D., Kundu, S., Banerjee, P., Dutta, R., and Sarkar, N.: Investigation of fibril forming mechanisms of l-phenylalanine and l-tyrosine: Microscopic insight toward phenylketonuria and tyrosinemia type ii. *J. Phys. Chem. B* , 121(7):1533–1543, February 2017.

85. Grudzielanek, S., Velkova, A., Shukla, A., Smirnovas, V., Tatarek-Nossol, M., Rehage, H., Kapurniotu, A., and Winter, R.: Cytotoxicity of insulin within its self-assembly and amyloidogenic pathways. *Journal of Molecular Biology* , 370(2):372–384, 2007.

86. Loo, D. T., Copani, A., Pike, C. J., Whittemore, E. R., Walencewicz, A. J., and Cotman, C. W.: Apoptosis is induced by beta-amyloid in cultured central nervous system neurons. *Proc Natl Acad Sci USA* , 90(17):7951, September 1993.

87. Jelinek, R. and Sheynis, T.: Amyloid - membrane interactions: experimental approaches and techniques. *Current Protein and Peptide Science* , 11(5):372–384, 2010.

88. Jelinek, R. and Kolusheva, S.: Polymerized lipid vesicles as colorimetric biosensors for biotechnological applications. *Biotechnology Advances* , 19(2):109–118, 2001.

89. Oren, Z., Ramesh, J., Avrahami, D., Suryapr akash, N., Shai, Y., and Jelinek, R.: Structures and mode of membrane interaction of a short αhelicallytic peptide and its diastereomer determined by nmr, ftir, and fluorescence spectroscopy. *European Journal of Biochemistry* , 269(16):3869–3880, August 2002.

90. Lee, S.-H., Meng, X. W., Flatten, K. S., Loegering, D. A., and Kaufmann, S. H.: Phosphatidylserine exposure during apoptosis reflects bidirectional trafficking between plasma membrane and cytoplasm. *Cell Death & Differentiation* , 20(1):64–76, 2013.

91. Ferrier, D. R. and Harvey, R. A.: *Lippincott's illustrated reviews: biochemistry* . Philadelphia, Wolters Kluwer Health : Lippincott Williams & Wilkins, 2014.

92. ed. B. V. K. W. K. S. E. A. A. B. K. M. G. G. D. Valle, A. L. Beudet *The Online Metabolic and Molecular Bases of Inherited Disease* . McGraw-Hill, 2014.

93. Woolf, T. B. and Roux, B.: Structure, energetics, and dynamics of lipid-protein interactions : A molecular dynamics study of the gramicidin a channel in a dmpc bilayer. *Proteins* , 24(1):92–114, January 1996.

94. Lasch, J.: Interaction of detergents with lipid vesicles. *Biochimica et Biophysica Acta (BBA) - Reviews on Biomembranes* , 1241(2):269–292, 1995.

95. Jo, S., Lim, J. B., Klauda, J. B., and Im, W.: Charmm-gui membrane builder for mixed bilayers and its application to yeast membranes. *Biophysical Journal* , 97(1):50–58, 2009.

96. Best, R. B., Zhu, X., Shim, J., Lopes, P. E. M., Mittal, J., Feig, M., and MacKerell, A. D.: Optimization of the additive charmm all-atom protein force field targeting improved sampling of the backbone ϕ, ψ and side-chain $\chi 1$ and $\chi 2$ dihedral angles. *J. Chem. Theory Comput.* , 8(9):3257–3273, September 2012.

97. MacKerell, A. D., Feig, M., and Brooks, C. L.: Improved treatment of the protein backbone in empirical force fields. *J. Am. Chem. Soc.* , 126(3):698–699, January 2004.

98. Gorbenko, G., Trusova, V., Girych, M., Adachi, E., Mizuguchi, C., Akaji, K., and Saito, H.: Fret evidence for untwisting of amyloid fibrils on the surface of model membranes. *Soft Matter* , 11(31):6223–6234, 2015.

99. Han, S., Kollmer, M., Markx, D., Claus, S., Walther, P., and Fändrich, M.: Amyloid plaque structure and cell surface interactions of β-amyloid fibrils revealed by electron tomography. *Scientific reports* , 7(28240273):43577–43577, February 2017.

100. Ma, X., Sha, Y., Lin, K., and Nie, S.: The effect of fibrillar a β 1-40 on membrane fluidity and permeability. *Protein and Peptide Letters* , 9(2):173–178, 2002.

101. Milanesi, L., Sheynis, T., Xue, W.-F., Orlova, E. V., Hellewell, A. L., Jelinek, R., Hewitt, E. W., Radford, S. E., and Saibil, H. R.: Direct three-dimensional visualization of membrane disruption by amyloid fibrils. *Proc Natl Acad Sci USA* , 109(50):20455, December 2012.

102. Chiti, F. and Dobson, C. M.: Protein misfolding, amyloid formation, and human disease: A summary of progress over the last decade. *Annu. Rev. Biochem.* , 86(1):27–68, June 2017.

103. Eisele, Y. S., Monteiro, C., Fearns, C., Encalada, S. E., Wiseman, R. L., Powers, E. T., and Kelly, J. W.: Targeting protein aggregation for the treatment of degenerative diseases. *Nature Reviews Drug Discovery* , 14(11):759–780, 2015.

104. Wong, Y. C. and Krainc, D.: α-synuclein toxicity in neurodegeneration: mechanism and therapeut ic strategies. *Nature Medicine* , 23(2):1–13, 2017.

105. Perutz, M. F., Pope, B. J., Owen, D., Wanker, E. E., and Scherzinger, E.: Aggregation of proteins with expanded glutamine and alanine repeats of the glutamine-rich and asparagine-rich domains of sup35 and of the amyloid β of amyloid plaques. *Proc Natl Acad Sci USA* , 99(8):5596, April 2002.

106. Fiumara, F., Fioriti, L., Kandel, E. R., and Hendrickson, W. A.: Essential role of coiled coils for aggregation and activity of q/n-rich prions and polyq proteins. *Cell* , 143(7):1121–1135, 2010.

107. Abedini, A. and Raleigh, D. P.: A critical assessment of the role of helical intermediates in amyloid formation by natively unfolded proteins and polypeptides. *Protein Eng Des Sel* , 22(8):453–459, August 2009.

108. Jahn, T. R., Parker, M. J., Homans, S. W., and Radford, S. E.: Amyloid formation under physiological conditions proceeds via a native-like folding intermediate. *Nature Structural & Molecular Biology* , 13(3):195–201, 2006.

109. Chiti, F. and Dobson, C. M.: Amyloid formation by globular proteins under native conditions. *Nature Chemical Biology* , 5(1):15–22, 2009.

110. Fändrich, M., Fletcher, M. A., and Dobson, C. M.: Amyloid fibrils from muscle myoglobin. *Nature* , 410(6825):165–166, 2001.

111. Gazit, E.: The "correctly folded" state of proteins: Is it a metastable state? *Angew. Chem. Int. Ed.* , 41(2):257–259, January 2002.

112. Baldwin, A. J., Knowles, T. P. J., Tartaglia, G. G., Fitzpatrick, A. W., Devlin, G. L., Shammas, S. L., Waudby, C. A., Mossuto, M. F., Meehan, S., Gras, S. L., Christodoulou, J., Anthony-Cahill, S. J., Barker, P. D., Vendruscolo, M., and Dobson, C. M.: Metastability of native proteins and the phenomenon of amyloid formation. *J. Am. Chem. Soc.* , 133(36):14160–14163, September 2011.

113. Adamcik, J. and Mezzenga, R.: Amyloid polymorphism in the protein folding and aggregation energy landscape. *Angew. Chem. Int. Ed.* , 57(28):8370–8382, July 2018.

114. Schlichting, I., Berendzen, J., Phillips, G. N., and Sweet, R. M.: Crystal structure of photolysed carbonmonoxy-myoglobin. *Nature* , 371(6500):808–812, 1994.

115. Trinh, C. H., Smith, D. P., Kalverda, A. P., Phillips, S. E. V., and Radford, S. E.: Crystal structure of monomeric human β-2-microglobulin reveals clues to its amyloidogenic properties. *Proc Natl Acad Sci USA* , 99(15):9771, July 2002.

116. Fusco, G., Chen, S. W., Williamson, P. T. F., Cascella, R., Perni, M., Jarvis, J. A., Cecchi, C., Vendruscolo, M., Chiti, F., Cremades, N., Ying, L., Dobson, C. M., and De Simone, A.: Structural basis of membrane disruption and cellular toxicity by α-synuclein oligomers. *Science* , 358(6369):1440, December 2017.

117. Neudecker, P., Robustelli, P., Cavalli, A., Walsh, P., Lundström, P., Zarrine-Afsar, A., Sharpe, S., Vendruscolo, M., and Kay, L. E.: Structure of an intermediate state in protein folding and aggregation. *Science* , 336(6079):362, April 2012.

118. Mondal, S., Adler-Abramovich, L., Lampel, A., Bram, Y., Lipstman, S., and Gazit, E.: Formation of functional super-helical assemblies by constrained single heptad repeat. *Nature Communications* , 6(1):8615, 2015.

119. Tayeb-Fligelman, E., Tabachnikov, O., Moshe, A., Goldshmidt-Tran, O., Sawaya, M. R., Coquelle, N., Colletier, J.-P., and Landau, M.: The cytotoxic staphylococcus aureus psmα3 reveals a cross-α amyloid-like fibril. *Science* , 355(6327):831, February 2017.

120. Zhang, S.-Q., Huang, H., Yang, J., Kratochvil, H. T., Lolicato, M., Liu, Y., Shu, X., Liu, L., and DeGrado, W. F.: Designed peptides that assemble into cross-α amyloid-like structures. *Nature Chemical Biology* , 14(9):870–875, 2018.

121. Tang, Z. and Kotov, N. A.: One-dimensional assemblies of nanoparticles: Preparation, properties, and promise. *Adv. Mater.* , 17(8):951–962, April 2005.

122. Kitching, H., Shiers, M. J., Kenyon, A. J., and Parkin, I. P.: Self-assembly of metallic nanoparticles into one dimensional arrays. *J. Mater. Chem. A* , 1(24):6985–6999, 2013.

123. Wang, W., Ramezani, M., Väkeväinen, A. I., Törmä, P., Rivas, J. G., and Odom, T. W.: The rich photonic world of plasmonic nanoparticle arrays. *Materials Today* , 21(3):303–314, 2018.

124. Nie, Z., Petukhova, A., and Kumacheva, E.: Properties and emerging applications of self-assembled structures made from inorganic nanoparticles. *Nature Nanotechnology* , 5(1):15–25, 2010.

125. Wang, L., Xu, L., Kuang, H., Xu, C., and Kotov, N. A.: Dynamic nanoparticle assemblies. *Acc. Chem. Res.* , 45(11):1916–1926, November 2012.

126. Dong, Z., Asbahi, M., Lin, J., Zhu, D., Wang, Y. M., Hippalgaonkar, K., Chu, H.-S., Goh, W. P., Wang, F., Huang, Z., and Yang, J. K. W.: Second-harmonic generation from sub-5 nm gaps by directed self-assembly of nanoparticles onto template-stripped gold substrates. *Nano Lett.* , 15(9):5976–5981, September 2015.

127. Srivastava, S. and Kotov, N. A.: Nanoparticle assembly for 1d and 2d ordered structures. *Soft Matter* , 5(6):1146–1156, 2009.

128. Halas, N. J., Lal, S., Chang, W.-S., Link, S., and Nordlander, P.: Plasmons in strongly coupled metallic nanostructures. *Chem. Rev.* , 111(6):3913–3961, June 2011.

129. Février, M., Gogol, P., Aassime, A., Mégy, R., Delacour, C., Chelnokov, A., Apuzzo, A., Blaize, S., Lourtioz, J.-M., and Dagens, B.: Giant coupling effect between metal nanoparticle chain and optical waveguide. *Nano Lett.* , 12(2):1032–1037, February 2012.

130. Kravets, V. V., Ocola, L. E., Khalavka, Y., and Pinchuk, A. O.: Polarization and distance dependent coupling in linear chains of gold nanoparticles. *Appl. Phys. Lett.* , 106(5):053104, February 2015.

131. Kim, J., Chung, S. E., Choi, S.-E., Lee, H., Kim, J., and Kwon, S.: Programming magnetic anisotropy in polymeric microactuators. *Nature Materials* , 10(10):747–752, 2011.

132. Vogele, K., List, J., Pardatscher, G., Holland, N. B., Simmel, F. C., and Pirzer, T.: Self-assembled active plasmonic waveguide with a peptide-based thermomechanical switch. *ACS Nano* , 10(12):11377–11384, December 2016.

133. Mehdizadeh Taheri, S., Michaelis, M., Friedrich, T., Förster, B., Drechsler, M., Römer, F. M., Bösecke, P., Narayanan, T., Weber, B., Rehberg, I., Rosenfeldt, S., and Förster, S.: Self-assembly of smallest magnetic particles. *Proc Natl Acad Sci USA* , 112(47):14484, November 2015.

134. Maier, S. A., Kik, P. G., Atwater, H. A., Meltzer, S., Harel, E., Koel, B. E., and Requicha, A. A. G.: Local detection of electromagnetic energy transport below the diffraction limit in metal nanoparticle plasmon waveguides. *Nature Materials* , 2(4):229–232, 2003.

135. Mondal, S. and Gazit, E.: The self-assembly of helical peptide building blocks. *ChemNanoMat* , 2(5):323–332, May 2016.

136. Bera, S., Mondal, S., Xue, B., Shimon, L. J. W., Cao, Y., and Gazit, E.: Rigid helical-like assemblies from a self-aggregating tripeptide. *Nature Materials* , 18(5):503–509, 2019.

137. Mondal, S., Varenik, M., Bloch, D. N., Atsmon-Raz, Y., Jacoby, G., Adler-Abramovich, L., Shimon, L. J. W., Beck, R., Miller, Y., Regev, O., and Gazit, E.: A minimal length rigid helical peptide motif allows rational design of modular surfactants. *Nature Communications* , 8(1):14018, 2017.

138. Reches, M. and Gazit, E.: Casting metal nanowires within discrete self-assembled peptide nanotubes. *Science* , 300(5619):625, April 2003.

139. Mondal, S., Basavalingappa, V., Jacoby, G., Shimon, L. J. W., Beck, R., and Gazit, E.: Functional coiled-coil-like assembly by knob-into-hole packing of single heptad repeat. *ACS Nano* , 13(11):12630–12637, November 2019.

140. Yuan, C., Ji, W., Xing, R., Li, J., Gazit, E., and Yan, X.: Hierarchically oriented organization in supramolecular peptide crystals. *Nature Reviews Chemistry* , 3(10):567–588, 2019.

141. Tian, Y., Zhang, H. V., Kiick, K. L., Saven, J. G., and Pochan, D. J.: Fabrication of one- and two-dimensional gold nanoparticle arrays on computationally designed self-assembled peptide templates. *Chem. Mater.* , 30(23):8510–8520, December 2018.

142. Kang, E. S., Kim, Y.-T., Ko, Y.-S., Kim, N. H., Cho, G., Huh, Y. H., Kim, J.-H., Nam, J., Thach, T. T., Youn, D., Kim, Y. D., Yun, W. S., DeGrado, W. F., Kim, S. Y., Hammond, P. T., Lee, J., Kwon, Y.-U., Ha, D.-H., and Kim, Y. H.: Peptide-programmable nanoparticle superstructures with tailored electrocatalytic activity. *ACS Nano* , 12(7):6554–6562, July 2018.

143. Pazos, E., Sleep, E., Rubert Pérez, C. M., Lee, S. S., Tantakitti, F., and Stupp, S. I.: Nucleation and growth of ordered arrays of silver nanoparticles on peptide nanofibers: Hybrid nanostructures with antimicrobial properties. *J. Am. Chem. Soc.* , 138(17):5507–5510, May 2016.

144. Song, C., Wang, Y., and Rosi, N. L.: Peptide-directed synthesis and assembly of hollow spherical copt nanoparticle superstructures. *Angew. Chem. Int. Ed.* , 52(14):3993–3995, April 2013.

145. Merg, A. D., Slocik, J., Blaber, M. G., Schatz, G. C., Naik, R., and Rosi, N. L.: Adjusting the metrics of 1-d helical gold nanoparticle superstructures using multivalent peptide conjugates. *Langmuir* , 31(34):9492–9501, September 2015.

146. Yu, Z., Tantakitti, F., Palmer, L. C., and Stupp, S. I.: Asymmetric peptide nanoribbons. *Nano Lett.* , 16(11):6967–6974, November 2016.

147. Yoo, S. H., Eom, T., Kwon, S., Gong, J., Kim, J., Cho, S. J., Driver, R. W., Lee, Y., Kim, H., and Lee, H.-S.: Foldecture as a core material with anisotropic surface characteristics. *J. Am. Chem. Soc.* , 137(6):2159–2162, February 2015.

148. Fujiki, Y., Tokunaga, N., Shinkai, S., and Sada, K.: Anisotropic decoration of gold nanoparticles onto specific crystal faces of organic single crystals. *Angewandte Chemie International Edition* , 45(29):4764–4767, July 2006.

149. Lee, S.-W., Mao, C., Flynn, C. E., and Belcher, A. M.: Ordering of quantum dots using genetically engineered viruses. *Science* , 296(5569):892, May 2002.

150. Georgiadou, M.; Pelicic, V.: *Bacterial Pili: Structure, Synthesis and Role in Disease* . CAB International, 2014.

151. Reguera, G., McCarthy, K. D., Mehta, T., Nicoll, J. S., Tuominen, M. T., and Lovley, D. R.: Extracellular electron transfer via microbial nanowires. *Nature* , 435(7045):1098–1101, 2005.

152. Cologgi, D. L., Lampa-Pastirk, S., Speers, A. M., Kelly, S. D., and Reguera, G.: Extracellular reduction of uranium via geobacter conductive pili as a protective cellular mechanism. *Proc Natl Acad Sci USA* , 108(37):15248, September 2011.

153. Lovley, D. R.: Electrically conductive pili: Biological function and potential applications in electronics. *Current Opinion in Electrochemistry* , 4(1):190–198, 2017.

154. Lundgren, B. R., Bailey, F. J., Moley, Gabriella an d Nomura, C. T., and O'Toole, G.: Ddar (pa1196) regulates expression of dimethylarginine dimethylaminohydrolase for the metabolism of methylarginines in pseudomonas aeruginosa pao1. *J. Bacteriol.* , 199(8):e00001–17, April 2017.

155. Craig, L., Volkmann, N., Arvai, A. S., Pique, M. E., Yeager, M., Egelman, E., and Tainer, J. A.: Type iv pilus structure by cryo-electron microscopy and crystallography: Implications for pilus assembly and functions. *Molecular Cell* , 23(5):651–662, 2006.

156. Kolappan, S., Coureuil, M., Yu, X., Nassif, X., Egelman, E. H., and Craig, L.: Structure of the neisseria meningitidis type iv pilus. *Nature Communications* , 7(1):13015, 2016.

157. Guterman, T., Gazit, E., and Gazit, E.: Toward peptide-based bioelectronics: reductionist design of conduc tive pili mimetics. *Bioelectronics in medicine* , 1(2):131–137, 2018.

158. Guterman, T., Kornreich, M., Stern, A., Adler-Abramovich, L., Porath, D., Beck, R., Shimon, L. J. W., and Gazit, E.: Formation of bacterial pilus-like nanofibres by designed minimalistic self-assembling peptides. *Nature Communications* , 7(1):13482, 2016.

159. Kirsch, R., Mertig, M., Pompe, W., Wahl, R., Sadowski, G., Böhm, K. J., and Unger, E.: Three-dimensional metallization of microtubules. *Thin Solid Films* , 305(1):248–253, 1997.

160. Scheibel, T., Parthasarathy, R., Sawicki, G., Lin, X.-M., Jaeger, H., and Lindquist, S. L.: Conducting nanowires built by controlled self-assembly of amyloid fibers and selective metal deposition. *Proc Natl Acad Sci USA* , 100(8):4527, April 2003.

161. Patolsky, F., Weizmann, Y., and Willner, I.: Actin-based metallic nanowires as bio-nanotransporters. *Nature Materials* , 3(10):692–695, 2004.

162. Wei, G., Reichert, J., and Jandt, K. D.: Controlled self-assembly and templated metallization of fibrinogen nanofibrils. *Chem. Commun.* , (33):3903–3905, 2008.

163. Plascencia-Villa, G., Saniger, J. M., Ascencio, J. A., Palomares, L. A., and Ramírez, O. T.: Use of recombinant rotavirus vp6 nanotubes as a multifunctional t emplate for the synthesis of nanobiomaterials functionalized with metals. *Biotechnol. Bioeng.* , 104(5):871–881, December 2009.

164. Yang, T., Zhang, Y., and Li, Z.: Formation of gold nanoparticle decorated lysozyme microtubes. *Biomacromolecules* , 12(6):2027–2031, June 2011.

165. Fang, G., Yang, Y., Yao, J., Shao, Z., and Chen, X.: Formation of different gold nanostructures by silk nanofibrils. *Materials Science and Engineering: C* , 64:376–382, 2016.

166. Orza, A., Soritau, O., Olenic, L., Diudea, M., Florea, A., Rus Ciuca, D., Mihu, C., Casciano, D. e., and Biris, A. S.: Electrically conductive gold-coated collagen nanofibers for place ntal-derived mesenchymal stem cells enhanced differentiation and proliferation. *ACS Nano* , 5(6):4490–4503, June 2011.

167. Bolisetty, S., Adamcik, J., Heier, J., and Mezze nga, R.: Amyloid directed synthesis of titanium dioxide nanowires and thei r applications in hybrid photovoltaic devices. *Adv. Funct. Mater.* , 22(16):3424–3428, August 2012.

168. Bolisetty, S. and Mezzenga, R.: Amyloid-carbon hybrid membranes for universal water purification. *Nature Nanotechnology* , 11(4):365–371, 2016.

169. Shen, Y., Posavec, L., Bolisetty, S., Hilty, F. M., Nyström, G., Kohlbrecher, J., Hilbe, M., Rossi, A., Baumgartner, J., Zimmermann, M. B., and Mezzenga, R.: Amyloid fibril systems reduce, stabilize and deliver bioavailable nanosized iron. *Nature Nanotechnology* , 12(7):642–647, 2017.

170. Li, C., Bolisetty, S., and Mezzenga, R.: Hybrid nanocomposites of gold single-crystal platelets and amyloi d fibrils with tunable fluorescence, conductivity, and sensing properties. *Adv. Mater.* , 25(27):3694–3700, July 2013.

171. Zhou, J., Saha, A., Adamcik, J., Hu, H., Kong, Q., Li, C., and Mezzenga, R.: Macroscopic single-crystal gold microflakes and their devices. *Adv. Mater.* , 27(11):1945–1950, March 2015.

172. Nyström, G., Fernández-Ronco, M. P., Bolisetty, S., Mazzotti, M., and Mezzenga, R.: Amyloid templated gold aerogels. *Adv. Mater.* , 28(3):472–478, January 2016.

173. Banerjee, I. A., Yu, L., and Matsui, H.: Cu nanocrystal growth on peptide nanotubes by biomineralization: S ize control of cu nanocrystals by tuning peptide conformation. *Proc Natl Acad Sci USA* , 100(25):14678, December 2003.

174. Gottlieb, D., Morin, S. A., Jin, S., and Raines, R. T.: Self-assembled collagen-like peptide fibers as templates for metallic nanowires. *J. Mater. Chem.* , 18(32):3865–3870, 2008.

175. Lamm, M. S., Sharma, N., Rajagopal, K., Beyer, F. L., Schneider, J. P., and Pochan, D. J.: Laterally spaced linear nanoparticle arrays templated by laminated β-sheet fibrils. *Adv. Mater.* , 20(3):447–451, February 2008.

176. Sone, E. D. and Stupp, S. I.: Bioinspired magnetite mineralization of peptide-amphiphile nanofibers. *Chem. Mater.* , 23(8):2005–2007, April 2011.

177. Ceylan, H., Ozgit-Akgun, C., Erkal, T. S., Donm ez, I., Garifullin, R., Tekinay, A. B., Usta, H., Biyikli, N., and Guler, M. O.: Size-controlled conformal nanofabrication of biotemplated three-d imensional tio_2 and zno nanonetworks. *Scientific reports* , 3(23892593):2306–2306, 2013.

178. Kasotakis, E., Mossou, E., Adler-Abramovich, L., Mitchell, E. P., Forsyth, V. T., Gazit, E., and Mitraki, A.: Design of metal-binding sites onto self-assembled peptide fibrils. *Biopolymers* , 92(3):164–172, January 2009.

179. Leang, C., Qian, X., Mester, T., and Lovley, D. R.: Alignment of the c-type cytochrome omcs along pili of geobacter sulfurreducens. *Appl. Environ. Microbiol.* , 76(12):4080, June 2010.

180. Qian, X., Mester, T., Morgado, L., Arakawa, T., Sharma, M. L., Inoue, K., Joseph, C., Salgueiro, C. A., Maroney, M. J., and Lovley, D. R.: Biochemical characterization of purified omcs, a c-type cytochrome required for insoluble fe(iii) reduction in geobacter sulfurreducens. *Biochimica et Biophysica Acta (BBA) - Bioenergetics* , 1807(4):404–412, 2011.

181. Tan, Y. N., Lee, J. Y., and Wang, D. I. C.: Uncovering the design rules for peptide synthesis of metal nanoparticles. *J. Am. Chem. Soc.* , 132(16):5677–5686, April 2010.

182. Engelbrekt, C., Sørensen, K. H., Zhang, J., Welinder, A. C., Jensen, P. S., and Ulstrup, J.: Green synthesis of gold nanoparticles with starch-glucose and application in bioelectrochemistry. *J. Mater. Chem.* , 19(42):7839–7847, 2009.

183. Eustis, S. and El-Sayed, M. A.: Why gold nanoparticles are more precious than pretty gold: Noble metal surface plasmon resonance and its enhancement of the radiative and nonradiative properties of nanocrystals of different shapes. *Chem. Soc. Rev.* , 35(3):209–217, 2006.

184. Colangelo, E., Chen, Q., Davidson, A. M., Parame lle, D., Sullivan, M. B., Volk, M., and Lévy, R.: Computational and experimental investigation of the structure of peptide monolayers on gold nanoparticles. *Langmuir* , 33(1):438–449, January 2017.

185. Wright, L. B., Rodger, P. M., Corni, S., and Wals h, T. R.: Golp-charmm: First-principles based force fields for the interaction of proteins with au(111) and au(100). *J. Chem. Theory Comput.* , 9(3):1616–1630, March 2013.

186. Iori, F., Di Felice, R., Molinari, E., and Corni, S.: Golp: An atomistic force-field to describe the interaction of proteins with au(111) surfaces in water. *J. Comput. Chem.* , 30(9):1465–1476, July 2009.

187. Micsonai, A., Wien, F., Kernya, L., Lee, Y.-H., Goto, Y., Réfrégiers, M., and Kardos, J.: Accurate secondary structure prediction and fold recognition for circular dichroism spectroscopy. *Proc Natl Acad Sci USA* , 112(24):E3095, June 2015.

188. Lamm, M. S., Rajagopal, K., Schneider, J. P., and Pochan, D. J.: Laminated morphology of nontwisting β-sheet fibrils constructed via peptide self-assembly. *J. Am. Chem. Soc.* , 127(47):16692–16700, November 2005.

189. Bolisetty, S., Vallooran, J. J., Adamcik, J., Handschin, S., Gramm, F., and Mezzenga, R.: Amyloid-mediated synthesis of giant, fluorescent, gold single crys tals and their hybrid sandwiched composites driven by liquid crystalline interac tions. *Journal of Colloid and Interface Science* , 361(1):90–96, 2011.

190. Millstone, J. E., Hurst, S. J., Métraux, G. S., Cutler, J. I., and Mirkin, C. A.: Colloidal gold and silver triangular nanoprisms. *Small* , 5(6):646–664, March 2009.

191. Vaney, M. C., Maignan, S., Riès-Kautt, M., and Ducruix, A.: High-resolution structure (1.33 å) of a hew lysozyme tetragonal crystal grown in the apcf apparatus. data and structural comparison with a crystal grown under microgravity from spacehab-01 mission. *Acta Cryst. D* , 52(3):505–517, 1996.

192. Hill, J. P., Jin, W., Kosaka, A., Fukushima, T., Ichihara, H., Shimomura, T., Ito, K., Hashizume, T., Ishii, N., and Aida, T.: Self-assembled hexa-peri-hexabenzocoronene graphitic nanotube. *Science* , 304(5676):1481, June 2004.

193. Jin, W., Yamamoto, Y., Fukushima, T., Ishii, N., Kim, J., Kato, K., Takata, M., and Aida, T.: Systematic studies on structural parameters for nanotubular assembly of hexa-peri-hexabenzocoronenes. *J. Am. Chem. Soc.* , 130(29):9434–9440, July 2008.

194. Krieg, E., Bastings, M. M. C., Besenius, P., and Rybtchinski, B.: Supramolecular polymers in aqueous media. *Chem. Rev.* , 116(4):2414–2477, February 2016.

195. Beingessner, R. L., Fan, Y., and Fenniri, H.: Molecular and supramolecular chemistry of rosette nanotubes. *RSC Adv.* , 6(79):75820–75838, 2016.

196. Shimizu, T., Masuda, M., and Minamikawa, H.: Supramolecular nanotube architectures based on amphiphilic molecules. *Chem. Rev.* , 105(4):1401–1444, April 2005.

197. Bong, D. T., Clark, T. D., Granja, J. R., and Ghadiri, M. R.: Self-assembling organic nanotubes. *Angew. Chem. Int. Ed.* , 40(6):988–1011, March 2001.

198. Kameta, N., Minamikawa, H., and Masuda, M.: Supramolecular organic nanotubes: how to utilize the inner nanospace and the outer space. *Soft Matter* , 7(10):4539–4561, 2011.

199. Barclay, T. G., Constantopoulos, K., and Matisons, J. n.: Nanotubes self-assembled from amphiphilic molecules via helical i ntermediates. *Chem. Rev.* , 114(20):10217–10291, October 2014.

200. Eisele, D. M., Arias, D. H., Fu, X., Bloemsma, E. A., Steiner, C. P., Jensen, R. A., Rebentrost, P., Eisele, H., Tokmakoff, A., Lloyd, S., Nelson, K. A., Nicastro, D., Knoester, J., and Bawendi, M. G.: Robust excitons inhabit soft supramolecular nanotubes. *Proc Natl Acad Sci USA* , 111(33):E3367, August 2014.

201. Kim, H.-J., Kang, S.-K., Lee, Y.-K., Seok, C., Lee, J.-K., Zin, W.-C., and Lee, M.: Self-dissociating tubules from helical stacking of noncovalent macrocycles. *Angew. Chem. Int. Ed.* , 49(45):8471–8475, November 2010.

202. Liu, Z., Liu, G., Wu, Y., Cao, D., Sun, J., Schneebeli, S. T., Nassar, M. S., Mirkin, C. A., and Stoddart, J. F.: Assembly of supramolecular nanotubes from molecular triangles and 1,2-dihalohydrocarbons. *J. Am. Chem. Soc.* , 136(47):16651–16660, November 2014.

203. Ponnuswamy, N., Pantoş, G. D., Smulders, M. M. J., and Sanders, J. K. M.: Thermodynamics of supramolecular naphthalenediimide nanotube formation: The influence of solvents, side chains, and guest templates. *J. Am. Chem. Soc.* , 134(1):566–573, January 2012.

204. Tian, Z., Li, H., Wang, M., Zhang, A., and Feng, Z.-G.: Vesicular and tubular structures prepared from self-assembly of novel amphiphilic aba triblock copolymers in aqueous solutions. *J. Polym. Sci. A Polym. Chem.* , 46(3):1042–1050, February 2008.

205. Guo, C., Luo, Y., Zhou, R., and Wei, G.: Probing the self-assembly mechanism of diphenylalanine-based pept ide nanovesicles and nanotubes. *ACS Nano* , 6(5):3907–3918, May 2012.

206. Valéry, C., Artzner, F., and Paternostre, M.: Peptide nanotubes: molecular organisations, self-assembly mechanisms and applications. *Soft Matter* , 7(20):9583–9594, 2011.

207. Krieg, E., Shirman, E., Weissman, H., Shimoni, E., Wolf, S. G., Pinkas, I., and Rybtchinski, B.: Supramolecular gel based on a perylene diimide dye: Multiple stim uli responsiveness, robustness, and photofunction. *J. Am. Chem. Soc.* , 131(40):14365–14373, October 2009.

208. Ustinov, A., Weissman, H., Shirman, E., Pinkas, I., Zuo, X., and Rybtchinski, B.: Supramolecular polymers in aqueous medium: Rational design based on directional hydrophobic interactions. *J. Am. Chem. Soc.* , 133(40):16201–16211, October 2011.

209. Percec, V., Wilson, D. A., Leowanawat, P., Wilson, C. J., Hughes, A. D., Kaucher, M. S., Hammer, D. A., Levine, D. H., Kim, A. J., Bates, F. S., Davis, K. P., Lodge, T. P., Klein, M. L., DeVane, R. H., Aqad, E., Rosen, B. M., Argintaru, A. O., Sienkowska, M. J., Rissanen, K., Nummelin, S., and Ropponen, J.: Self-assembly of janus dendrimers into uniform dendrimersomes and other complex architectures. *Science* , 328(5981):1009, May 2010.

210. Shahar, C., Dutta, S., Weissman, H., Shimon, L. J. W., Ott, H., and Rybtchinski, B.: Precrystalline aggregates enable control over organic crystallization in solution. *Angew. Chem. Int. Ed.* , 55(1):179–182, January 2016.

211. Tidhar, Y., Weissman, H., Wolf, S. G., Gulino, A., and Rybtchinski, B.: Pathway-dependent self-assembly of perylene diimide/peptide conju gates in aqueous medium. *Chem. Eur. J.* , 17(22):6068–6075, May 2011.

212. Gillissen, M. A. J., Koenigs, M. M. E., Spiering, J. J. H., Vekemans, J. A. J. M., Palmans, A. R. A., Voets, I. K., and Meijer, E. W.: Triple helix formation in amphiphilic discotics: Demystifying solvent effects in supramolecular self-assembly. *J. Am. Chem. Soc.* , 136(1):336–343, January 2014.

213. Besenius, P.: Controlling supramolecular polymerization through multicomponent self-assembly. *J. Polym. Sci. Part A: Polym. Chem.* , 55(1):34–78, January 2017.

214. Charmm general force field (cgenff)charmm general force field (cgenff). accessed November 4, 2016.

215. Belandria, V., Mohammadi, A. H., and Richon, D.: Volumetric properties of the (tetrahydrofuran+water) and (tetra-n-butyl ammonium bromide+water) systems: Experimental measurements and correlations. *The Journal of Chemical Thermodynamics* , 41(12):1382–1386, 2009.

216. Vukovic, L., Madriaga, A., Kuzmis, A., Ban erjee, A., Tang, A., Tao, K., Shah, N., Kral, P., and On yuksel, H.: Solubilization of therapeutic agents in micellar nanomedicines. *Langmuir* , 29(51):15747–15754, 2013.

217. Vukovic, L., Khatib, F. A., Drake, S. P., Madriaga, A., Brandenburg, K. S., Kral, P., and Onyuksel, H.: Structure and dynamics of highly peg-ylated sterically stabilized micelles in aqueous media. *Journal of the American Chemical Society* , 133(34):13481–13488, 2011.

218. Hermans, T. M., Broeren, M. A. C., Gomopoulos, N. o., van der Schoot, P., van Genderen, M. H. P., Sommerdijk, N. A. J. M., Fytas, G., and Meijer, E. W.: Self-assembly of soft nanoparticles with tunable patchiness. *Nature Nanotechnology* , 4(11):721–726, 2009.

219. Hartgerink, J. D., Beniash, E., and Stupp, S. I.: Self-assembly and mineralization of peptide-amphiphile nanofibers. *Science* , 294(5547):1684, November 2001.

220. Marsden, H. R., Korobko, A. V., van Leeuwen, E. N. M., Pouget, E. M., Veen, S. J., Sommerdijk, N. A. J. M., and Kros, A.: Noncovalent triblock copolymers based on a coiled-coil peptide motif. *J. Am. Chem. Soc.* , 130(29):9386–9393, July 2008.

221. Brunsveld, L., Folmer, B. J. B., Meijer, E. W., and Sijbesma, R. P.: Supramolecular polymers. *Chemical Reviews (Washington, D. C.)* , 101(12):4071–4097, 2001.

222. Sosso, G. C., Chen, J., Cox, S. J., Fitzner, M., Pedevilla, P., Zen, A., and Michaelides, A.: Crystal nucleation in liquids: Open questions and future challenges in molecular dynamics simulations. *Chemical Reviews (Washington, DC, United States)* , 116(12):7078–7116, 2016.

223. Mammen, M., Chio, S.-K., and Whitesides, G. M.: Polyvalent interactions in biological systems: implications for d esign and use of multivalent ligands and inhibitors. *Angewandte Chemie, International Edition* , 37(20):2755–2794, 1998.

224. Kiessling, L. L., Gestwicki, J. E., and Strong, L. E.: Synthetic multivalent ligands as probes of signal transduction. *Angewandte Chemie International Edition* , 45(15):2348–2368, April 2006.

225. Jones, L. H.: Recent advances in the molecular design of synthetic vaccines. *Nature Chemistry* , 7(12):952–960, 2015.

226. Yvon, C., Surman, A. J., Hutin, M., Alex, J. n., Smith, B. O., Long, D.-L., and Cronin, L.: Polyoxometalate clusters integrated into peptide chains and as in organic amino acids: Solution- and solid-phase approaches. *Angew. Chem. Int. Ed.* , 53(13):3336–3341, March 2014.

227. Lachkar, D., Vilona, D., Dumont, E., Lelli, M., and Lacôte, E.: Grafting of secondary diolamides onto $[p_2w_{15}v_3o_{62}]^{9-}$ generates hybrid heteropoly acids. *Angew. Chem. Int. Ed.* , 55(20):5961–5965, May 2016.

228. Gouzerh, P. and Proust, A.: Main-group element, organic, and organometallic derivatives of polyoxometalates. *Chem. Rev.* , 98(1):77–112, February 1998.

229. Müller, A. and Gouzerh, P.: From linking of metal-oxide building blocks in a dynamic library to giant clusters with unique properties and towards adaptive chemistry. *Chem. Soc. Rev.* , 41(22):7431–7463, 2012.

230. Li, G., Wang, L., Ni, H., and Pittman, C. U.: Polyhedral oligomeric silsesquioxane (poss) polymers and copolymers: A review. *Journal of Inorganic and Organometallic Polymers* , 11(3):123–154, 2001.

231. Spokoyny, A. M.: New ligand platforms featuring boron-rich clusters as organomimetic substituents. *Pure and Applied Chemistry* , 85(5):903–919.

232. Lee, I. S., Long, J. R., Prusiner, S. B., and Safar, J. G.: Selective precipitation of prions by polyoxometalate complexes. *J. Am. Chem. Soc.* , 127(40):13802–13803, October 2005.

233. Lundeen, A.: The isomerization of trialkylacetic acids in sulfuric acid1. *J. Am. Chem. Soc.* , 82(12):3228–3228, June 1960.

234. Farha, O. K., Julius, R. L., Lee, M. W., Huertas, R. E., Knobler, C. B., and Hawthorne, M. F.: Synthesis of stable dodecaalkoxy derivatives of hypercloso-b12h12. *Journal of the American Chemical Society* , 127(51):18243–51, 2005.

235. Jalisatgi, S. S., Kulkarni, V. S., Tang, B., Houston, Z. H., Lee, M. W., and Hawthorne, M. F.: A convenient route to diversely substituted icosahedral closomer nanoscaffolds. *J. Am. Chem. Soc.* , 133(32):12382–12385, August 2011.

236. Sarma, S. J., Khan, A. A., Goswami, L. N., Jalisatgi, S. S., and Hawthorne, M. F.: A trimodal closomer drug-delivery system tailored with tracing and targeting capabilities. *Chem. Eur. J.* , 22(36):12715–12723, August 2016.

237. Wixtrom, A. I., Shao, Y., Jung, D., Machan, C. W., Kevork, S. N., Qian, E. A., Axtell, J. C., Khan, S. I., Kubiak, C. P., and Spokoyny, A. M.: Rapid synthesis of redox-active dodecaborane b12(or)12 clusters under ambient conditions. *Inorg. Chem. Front.* , 3(5):711–717, 2016.

238. Messina, M. S., Axtell, J. C., Wang, Y., Chong, P., Wixtrom, A. I., Kirlikovali, K. O., Upton, B. M., Hunter, B. M., Shafaat, O. S., Khan, S. I., Winkler, J. R., Gray, H. B., Alexandrova, A. N., Maynard, H. D., and Spokoyny, A. M.: Visible-light-induced olefin activation using 3d aromatic boron-rich cluster photooxidants. *J. Am. Chem. Soc.* , 138(22):6952–6955, June 2016.

239. Haynes, W. M.: *Handbook of Chemistry and Physics* . CRC/Taylor and Francis, 2016.

240. Lundquist, J. J. and Toone, E. J.: The cluster glycoside effect. *Chem. Rev.* , 102(2):555–578, February 2002.

241. Moore, J. S. and Xu, Z.: Synthesis of rigid dendritic macromolecules: enlarging the repeat unit size as a function of generation, permitting growth to continue. *Macromolecules* , 24(21):5893–5894, October 1991.

242. MacLeod, M. J. and Johnson, J. A.: Pegylated n-heterocyclic carbene anchors designed to stabilize go ld nanoparticles in biologically relevant media. *J. Am. Chem. Soc.* , 137(25):7974–7977, July 2015.

243. Daniel, M.-C. and Astruc, D.: Gold nanoparticles: assembly, supramolecular chemistry, quantum-size-related properties, and applications toward biology, catalysis, and nanotechnology. *Chem. Rev.* , 104(1):293–346, January 2004.

244. Hostetler, M. J., Templeton, A. C., and Murray, R. W.: Dynamics of place-exchange reactions on monolayer-protected gold cluster molecules. *Langmuir* , 15(11):3782–3789, May 1999.

245. Wei, G., Su, Z., Reynolds, N. P., Arosio, P., Hamley, I. W., Gazit, E., and Mezzenga, R.: Self-assembling peptide and protein amyloids: from structure to t ailored function in nanotechnology. *Chem. Soc. Rev.* , 46(15):4661–4708, 2017.

246. Sen, S., Han, Y., Rehak, P., and Vuković, Lela a nd Král, P.: Computational studies of micellar and nanoparticle nanomedicines. *Chem. Soc. Rev.* , 47(11):3849–3860, 2018.

247. Sen, S., Vuković, L., and Král, P.: Computational screening of nanoparticles coupling to aβ40 peptides and fibrils. *Scientific reports* , 9(31780663):17804–17804, November 2019.

248. Patra, N., Wang, B., and Král, P.: Nanodroplet activated and guided folding of graphene nanostructures. *Nano Lett.* , 9(11):3766–3771, November 2009.

249. Patra, N., Song, Y., and Král, P.: Self-assembly of graphene nanostructures on nanotubes. *ACS Nano* , 5(3):1798–1804, March 2011.

250. Rajesh, C., Majumder, C., Mizuseki, H. i., and Kawazoe, Y.: A theoretical study on the interaction of aromatic amino acids wi th graphene and single walled carbon nanotube. *J. Chem. Phys.* , 130(12):124911, March 2009.

251. Mallineni, S. S. K., Shannahan, J., Raghavendr a, A. J., Rao, A. M., Brown, J. M., and Podila, R.: Biomolecular interactions and biological responses of emerging tw o-dimensional materials and aromatic amino acid complexes. *ACS Appl. Mater. Interfaces* , 8(26):16604–16611, July 2016.

252. Božinovski, D. M., Petrović, P. V., Belić, M. R., and Zarić, S. D.: Insight into the interactions of amyloid β-sheets with graphene flakes: Scrutinizing the role of aromatic residues in amyloids that interact with graphene. *ChemPhysChem* , 19(10):1226–1233, May 2018.

253. Larijani, H. T., Jahanshahi, M., Ganji, M. D., and Kiani, M. H.: Computational studies on the interactions of glycine amino acid with graphene, h-bn and h-sic monolayers. *Phys. Chem. Chem. Phys.* , 19(3):1896–1908, 2017.

254. Zou, X., Wei, S., Jasensky, J., Xiao, M., Wang, Q., Brooks, C. L., and Chen, Z.: Molecular interactions between graphene and biological molecules. *J. Am. Chem. Soc.* , 139(5):1928–1936, February 2017.

255. Umadevi, D. and Sastry, G. N.: Impact of the chirality and curvature of carbon nanostructures on their interaction with aromatics and amino acids. *ChemPhysChem* , 14(11):2570–2578, August 2013.

256. Tavassoli Larijani, H., Darvish Ganji, M., and Jahanshahi, M.: Trends of amino acid adsorption onto graphene and graphene oxide surfaces: a dispersion corrected dft study. *RSC Adv.* , 5(113):92843–92857, 2015.

257. Ghadari, R.: A study on the interactions of amino acids with nitrogen doped graphene; docking, md simulation, and qm/mm studies. *Phys. Chem. Chem. Phys.* , 18(6):4352–4361, 2016.

258. Umadevi, D., Panigrahi, S., and Sastry, G. N.: Noncovalent interaction of carbon nanostructures. *Acc. Chem. Res.* , 47(8):2574–2581, August 2014.

259. Panigrahi, S., Bhattacharya, A., Banerjee, S., and Bhattacharyya, D.: Interaction of nucleobases with wrinkled graphene surface: Dispersion corrected dft and afm studies. *J. Phys. Chem. C* , 116(7):4374–4379, February 2012.

260. Camden, A. N., Barr, S. A., and Berry, R. J.: Simulations of peptide-graphene interactions in explicit water. *J. Phys. Chem. B* , 117(37):10691–10697, September 2013.

261. Yang, Z., Ge, C., Liu, J., Chong, Y., Gu, Z., Jimenez-Cruz, C. A., Chai, Z., and Zhou, R.: Destruction of amyloid fibrils by graphene through penetration and extraction of peptides. *Nanoscale* , 7(44):18725–18737, 2015.

262. Titov, A. V., Král, P., and Pearson, R.: Sandwiched graphene-membrane superstructures. *ACS Nano* , 4(1):229–234, January 2010.

263. Chan, H. and Král, P.: Nanoparticles self-assembly within lipid bilayers. *ACS Omega* , 3(9):10631–10637, September 2018.

264. Geim, A. K. and Grigorieva, I. V.: Van der waals heterostructures. *Nature* , 499(7459):419–425, 2013.

265. Huebschle, C. B., Messerschmidt, M., and Luger, P.: Crystal structure of dl-tryptophan at 173k. *Crystal Research and Technology* , 39(3):274–278, 2004.

266. Sresht, V., Pádua, A. A. H., and Blankschtein, D.: Liquid-phase exfoliation of phosphorene: Design rules from molecular dynamics simulations. *ACS Nano* , 9(8):8255–8268, August 2015.

267. Jacobson, A. J.: Colloidal dispersions of compounds with layer and chain structures. *Materials Science Forum* , 152-153(Soft Chemistry Routes to New Materials):1–12, 1994.

268. Zhang, L., Chen, D., and Jiao, X.: Monoclinic structured bivo4 nanosheets: hydrothermal preparation , formation mechanism, and coloristic and photocatalytic properties. *J. Phys. Chem. B* , 110(6):2668–2673, February 2006.

269. Penn, R. L. and Banfield, J. F.: Imperfect oriented attachment: Dislocation generation in defect-free nanocrystals. *Science* , 281(5379):969, August 1998.

270. Banfield, J. F., Welch, S. A., Zhang, H., Ebert, T. T., and Penn, R. L.: Aggregation-based crystal growth and microstructure development in natural iron oxyhydroxide biomineralization products. *Science* , 289(5480):751, August 2000.

271. Wang, C., Du, G., Ståhl, K., Huang, H., Zhong, Y., and Jiang, J. Z.: Ultrathin sno2 nanosheets: Oriented attachment mechanism, nonstoichiometric defects, and enhanced lithium-ion battery performances. *J. Phys. Chem. C* , 116(6):4000–4011, February 2012.

272. Shi, Y., Wang, M., Ma, C., Wang, Y., Li, X., and Yu, G.: A conductive self-healing hybrid gel enabled by metal-ligand supramolecule and nanostructured conductive polymer. *Nano Lett.* , 15(9):6276–6281, September 2015.

273. Sutar, P., Suresh, V. M., Jayaramulu, Kolleboyina an d Hazra, A., and Maji, T. K.: Binder driven self-assembly of metal-organic cubes towards functio nal hydrogels. *Nature Communications* , 9(1):3587, 2018.

274. Lu, C., Zhang, M., Tang, D., Yan, X., Zhang, Z., Zhou, Z., Song, B., Wang, H., Li, X., Yin, S., Sepehrpour, H., and Stang, P. J.: Fluorescent metallacage-core supramolecular polymer gel formed by orthogonal metal coordination and host-guest interactions. *J. Am. Chem. Soc.* , 140(24):7674–7680, June 2018.

275. Liu, Y., Shi, B., Wang, H., Shangguan, L., Li, Z., Zhang, M., and Huang, F.: Construction of metallacage-cored supramolecular gel by hierarchi cal self-assembly of metal coordination and pillar[5]arene-based host-guest reco gnition. *Macromol. Rapid Commun.* , 39(24):1800655, December 2018.

276. Ganta, S. and Chand, D. K.: Multi-stimuli-responsive metallogel molded from a pd2l4-type coordination cage: Selective removal of anionic dyes. *Inorg. Chem.* , 57(7):3634–3645, April 2018.

277. Wei, S.-C., Pan, M., Fan, Y.-Z., Liu, H., Zhang, J., and Su, C.-Y.: Creating coordination-based cavities in a multiresponsive supramolecular gel. *Chem. Eur. J.* , 21(20):7418–7427, May 2015.

278. Feng, J., Zeng, L., Chen, K., Fang, H., Zhang, J., Chi, Z., and Su, C.-Y.: Gelation of luminescent supramolecular cages and transformation to crystals with trace-doped-enhancement luminescence. *Langmuir* , 32(46):12184–12189, November 2016.

279. Zhang, Y., Zhou, Q.-F., Huo, G.-F., Yin, G.-Q. n., Zhao, X.-L., Jiang, B., Tan, H., Li, X., and Yang, H. a.-B.: Hierarchical self-assembly of an alkynylplatinum(ll) bzimpy-funct ionalized metallacage via pt−pt and $\pi-\pi$ interactions. *Inorg. Chem.* , 57(7):3516–3520, April 2018.

280. Liu, D., Liu, H., Song, B., Chen, M., Huang, J., Wang, J., Yang, X., Sun, W., Li, X., and Wang, P.: Terpyridine-based metallo-organic cages and supramolecular gelation by coordination-driven self-assembly and host-guest interaction. *Dalton Trans.* , 47(40):14227–14232, 2018.

281. Yin, P., Li, D., and Liu, T.: Solution behaviors and self-assembly of polyoxometalates as models of macroions and amphiphilic polyoxometalate-organic hybrids as novel surfactants. *Chem. Soc. Rev.* , 41(22):7368–7383, 2012.

282. Yang, M., Chan, H., Zhao, G., Bahng, J. H., Zhang, P., Král, P., and Kotov, N. A.: Self-assembly of nanoparticles into biomimetic capsid-like nanoshells. *Nature Chemistry* , 9(3):287–294, 2017.

283. Sanders, J. K. M.: Book review: Chemistry beyond the molecule: Supramolecular chemistr y. concepts and perspectives. by j.-m. lehn. *Angew. Chem. Int. Ed. Engl.* , 34(22):2563–2563, 1995.

284. Chakrabarty, R., Mukherjee, P. S., and Stang, P. r. J.: Supramolecular coordination: Self-assembly of finite two- and thr ee-dimensional ensembles. *Chem. Rev.* , 111(11):6810–6918, November 2011.

285. Fujita, M., Tominaga, M., Hori, A., and Therrien, B.: Coordination assemblies from a pd(ii)-cornered square complex. *Acc. Chem. Res.* , 38(4):369–378, April 2005.

286. Fujita, M.: Metal-directed self-assembly of two- and three-dimensional synthetic receptors. *Chem. Soc. Rev.* , 27(6):417–425, 1998.

287. Leininger, S., Olenyuk, B., and Stang, P. J.: Self-assembly of discrete cyclic nanostructures mediated by transition metals. *Chem. Rev.* , 100(3):853–908, March 2000.

288. Schultz, A., Li, X., Moorefield, C. N., Wesdemiotis, C., and Newkome, G. R.: Self-assembly and characterization of 3d metallamacrocycles: A study of supramolecular constitutional isomers. *Eur. J. Inorg. Chem.* , 2013(14):2492–2497, May 2013.

289. Newkome, G. R. and Moorefield, C. N.: From 1 to 3 dendritic designs to fractal supramacromolecular constructs: understanding the pathway to the sierpiński gasket. *Chem. Soc. Rev.* , 44(12):3954–3967, 2015.

290. Smulders, M. M. J., Riddell, I. A., Browne, C., and Nitschke, J. R.: Building on architectural principles for three-dimensional metallosupramolecular construction. *Chem. Soc. Rev.* , 42(4):1728–1754, 2013.

291. Riddell, I. A., Smulders, M. M. J., Clegg, J. K., Hristova, Y. R., Breiner, B., Thoburn, J. D., and Nitschke, J. R.: Anion-induced reconstitution of a self-assembling system to express a chloride-binding co10l15 pentagonal prism. *Nature Chemistry* , 4(9):751–756, 2012.

292. Machan, C. W., Adelhardt, M., Sarjeant, A. A., Stern, C. L., Sutter, J., Meyer, K., and Mirkin, C. A.: One-pot synthesis of an fe(ii) bis-terpyridine complex with allosterically regulated electronic properties. *J. Am. Chem. Soc.* , 134(41):16921–16924, October 2012.

293. Kennedy, R. D., Machan, C. W., McGuirk, C. M., Rosen, M. S., Stern, C. L., Sarjeant, A. A., and Mirkin, C. A.: General strategy for the synthesis of rigid weak-link approach platinum(ii) complexes: Tweezers, triple-layer complexes, and macrocycles. *Inorg. Chem.* , 52(10):5876–5888, May 2013.

294. Caulder, D. L. and Raymond, K. N.: Supermolecules by design. *Acc. Chem. Res.* , 32(11):975–982, November 1999.

295. Li, H., Xie, T.-Z., Liang, Z., Dahal, D., Shen, Y., Sun, X., Yang, Y., Pang, Y., and Liu, T.: Conformational change due to intramolecular hydrophobic interaction leads to large blue-shifted emission from single molecular cage solutions. *Chem. Commun.* , 55(3):330–333, 2019.

296. Šebesta, F., Sláma, V., Melcr, J., Futera, Z., and Burda, J. V.: Estimation of transition-metal empirical parameters for molecular mechanical force fields. *J. Chem. Theory Comput.* , 12(8):3681–3688, August 2016.

297. Banner, D. J., Firlar, E., Rehak, P., Foroozan, T., Osborn, J. K., SuryaNarayanan, Tahseen, T., Baggia, Y., Král, P., Shokuhfar, T., and Shahbazian-Yassar, R.: In situ liquid-cell tem observation of multiphase classical andnonclassical nucleation of calcium oxalate.

298. Hartl, W. P., Klapper, H., Barbier, B., Ensik at, H. J., Dronskowski, R., Mueller, P., Ostendorp, G. u., Tye, A., Bauer, R., and Barthlott, W.: Diversity of calcium oxalate crystals in cactaceae. *Canadian Journal of Botany* , 85(5):501–517, 2007.

299. Raven, J. A., Griffiths, H., Glidewell, S. M., Preston, T., and Stewart, W. D. P.: The mechanism of oxalate biosynthesis in higher plants: investigations with the stable isotopes 18o and 13c. *Proceedings of the Royal Society of London. Series B. Biological Sciences* , 216(1202):87–101, August 1982.

300. WHITE, P. H. I. L. I. P. J. and BROADLEY, M. A. R. T. I. N. R.: Calcium in plants. *Ann Bot* , 92(4):487–511, October 2003.

301. Grases, F., Millan, A., and Conte, A.: Production of calcium oxalate monohydrate, dihydrate or trihydrate . a comparative study. *Urological research* , 18(1):17–20, 1990.

302. Sheng, X., Ward, M. D., and Wesson, J. A.: Crystal surface adhesion explains the pathological activity of calcium oxalate hydrates in kidney stone formation. *Journal of the American Society of Nephrology* , 16(7):1904–1908, 2005.

303. Heijnen, W., Jellinghaus, W., and Klee, W. E.: Calcium oxalate trihydrate in urinary calculi. *Urological research* , 13(6):281–3, 1985.

304. Franceschi, V. R. and Nakata, P. A.: Calcium oxalate in plants: Formation and function. *Annual Review of Plant Biology* , 56(Copyright (C) 2020 American Chemical Society (ACS). All Rights Reserved.):41–71, 2005.

305. Ihli, J., Wang, Y.-W., Cantaert, B., Kim, Y.-Y. e., Green, D. C., Bomans, P. H. H., and Sommerdijk, Nico A. J. M. an d Meldrum, F. C.: Precipitation of amorphous calcium oxalate in aqueous solution. *Chemistry of Materials* , 27(11):3999–4007, 2015.

306. Gehl, A., Mondeshki, M., Bach, S., Haeger, T., Panthoefer, M., Barton, B., Kolb, U., and Tremel, W.: Anhydrous amorphous calcium oxalate nanoparticles from ionic liquids: Stable crystallization intermediates of the formation of whewellite. *Chemistry - A European Journal* , 21(50):18192–18201, 2015.

307. Hajir, M., Graf, R., and Tremel, W.: Stable amorphous calcium oxalate: synthesis and potential intermediate in biomineralization. *Chemical Communications (Cambridge, United Kingdom)* , 50(49):6534–6536, 2014.

308. Coe, F. L., Evan, A., and Worcester, E.: Kidney stone disease. *Journal of Clinical Investigation* , 115(10):2598–2608, 2005.

309. Kavanagh, J. P., Jones, L., and Rao, P. N.: Calcium oxalate crystallization kinetics studied by oxalate-induce d turbidity in fresh human urine and artificial urine. *Clinical science (London, England : 1979)* , 98(2):151–8, 2000.

310. Kavanagh, J. P., Jones, L., and Rao, P. N.: Calcium oxalate crystallization kinetics at different concentrations of human and artificial urine, with a constant calcium to oxalate ratio. *Urological Research* , 27(4):231–237, 1999.

311. Kavanagh, J. P.: In vitro calcium oxalate crystallisation methods. *Urological research* , 34(2):139–45, 2006.

312. Weber, E., Verch, A., Levy, D., Fitch, A. N., and Pokroy, B.: Amorphous biogenic calcium oxalate. *ChemistrySelect* , 1(2):132–135, 2016.

313. Shebanova, A., Ismagulova, T., Solovchenko, A., Baulina, O., Lobakova, E., Ivanova, A., Moiseenko, A., Shaitan, K., Polshakov, V., Nedbal, L., and Gorelova, O.: Versatility of the green microalga cell vacuole function as revealed by analytical transmission electron microscopy. *Protoplasma* , 254(3):1323–1340, 2017.

314. Lieske, J. C., Swift, H., Martin, T., Patterson, B., and Toback, F. G.: Renal epithelial cells rapidly bind and internalize calcium oxalate monohydrate crystals. *Proceedings of the National Academy of Sciences of the United States of America* , 91(15):6987–91, 1994.

315. Ruiz-Agudo, E., Burgos-Cara, A., Ruiz-Agudo, C., Ibanez-Velasco, A., Colfen, H., and Rodriguez-Navarro, C.: A non-classical view on calcium oxalate precipitation and the role of citrate. *Nature Communications* , 8(1):1–10, 2017.

316. Weber, E., Levy, D., Ben Sasson, M., Fitch, A. N., and Pokroy, B.: Structural analysis of metal-doped calcium oxalate. *RSC Advances* , 5(119):98626–98633, 2015.

317. Weaver, M. L., Qiu, S. R., Hoyer, J. R., Casey, W. H., Nancollas, G. H., and De Yoreo, J. J.: Inhibition of calcium oxalate monohydrate growth by citrate and the effect of the background electrolyte. *Journal of Crystal Growth* , 306(1):135–145, 2007.

318. Qiu, S. R., Wierzbicki, A., Salter, E. A., Zepeda, S., Orme, C. A., Hoyer, J. R., Nancollas, G. H., Cody, A. M., and De Yoreo, J. J.: Modulation of calcium oxalate monohydrate crystallization by citrate through selective binding to atomic steps. *Journal of the American Chemical Society* , 127(25):9036–9044, 2005.

319. Friddle, R. W., Weaver, M. L., Qiu, S. R., Wierzbicki, A., Casey, W. H., and De Yoreo, J. J.: Subnanometer atomic force microscopy of peptide-mineral interactions links clustering and competition to acceleration and catastrophe. *Proceedings of the National Academy of Sciences of the United States of America* , 107(1):11–15, 2010.

320. Cho, K. R., Salter, E. A., De Yoreo, J. J., Wierzbicki, A., Elhadj, S., Huang, Y., and Qiu, S. R.: Growth inhibition of calcium oxalate monohydrate crystal by linear aspartic acid enantiomers investigated by in situ atomic force microscopy. *CrystEngComm* , 15(1):54–64, 2013.

321. Jung, T., Sheng, X., Choi, C. K., Kim, W. o.-S., Wesson, J. A., and Ward, M. D.: Probing crystallization of calcium oxalate monohydrate and the role of macromolecule additives with in situ atomic force microscopy. *Langmuir* , 20(20):8587–8596, 2004.

322. Guo, S., Ward, M. D., and Wesson, J. A.: Direct visualization of calcium oxalate monohydrate crystallization and dissolution with atomic force microscopy and the role of polymeric additives. *Langmuir* , 18(11):4284–4291, 2002.

323. Narayanan, S., Firlar, E., Rasul, M. G., Forooz an, T., Farajpour, N., Covnot, L., Shahbazian-Yassar, R., and Shokuhfar, T.: On the structure and chemistry of iron oxide cores in human heart and human spleen ferritins using graphene liquid cell electron microscopy. *Nanoscale* , 11(36):16868–16878, 2019.

324. Firlar, E., Ouy, M., Bogdanowicz, A., Covnot, L., Song, B., Nadkarni, Y., Shahbazian-Yassar, R., and Shokuhfar, T.: Investigation of the magnetosome biomineralization in magnetotactic bacteria using graphene liquid cell - transmission electron microscopy. *Nanoscale* , 11(2):698–705, 2019.

325. Ghodsi, S. M., Megaridis, C. M., Shahbazian-Yassar, R., and Shokuhfar, T.: Advances in graphene-based liquid cell electron microscopy: Working principles, opportunities, and challenges. *Small Methods* , 3(5):n/a, 2019.

326. Yuk, J. M., Park, J., Ercius, P., Kim, K., Hellebusch, D. J., Crommie, M. F., Lee, J. Y., Zettl, A., and Alivisatos, A. P.: High-resolution em of colloidal nanocrystal growth

using graphene liquid cells. *Science (Washington, DC, United States)* , 336(6077):61–64, 2012.

327. Wang, C., Shokuhfar, T., and Klie, R. F.: Precise in situ modulation of local liquid chemistry via electron irradiation in nanoreactors based on graphene liquid cells. *Advanced Materials (Weinheim, Germany)* , 28(35):7716–7722, 2016.

328. Wang, C., Qiao, Q., Shokuhfar, T., and Klie, R. F.: High-resolution electron microscopy and spectroscopy of ferritin in biocompatible graphene liquid cells and graphene sandwiches. *Advanced Materials (Weinheim, Germany)* , 26(21):3410–3414, 2014.

329. Chen, Q., Smith, J. M., Park, J., Kim, K., Ho, D., Rasool, H. I., Zettl, A., and Alivisatos, A. P.: 3d motion of dna-au nanoconjugates in graphene liquid cell electron microscopy. *Nano Letters* , 13(9):4556–4561, 2013.

330. Kelly, D. J., Zhou, M., Clark, N., Hamer, M. J., Lewis, E. A., Rakowski, A. M., Haigh, S. J., and Gorbachev, R. V.: Nanometer resolution elemental mapping in graphene-based tem liquid cells. *Nano Letters* , 18(2):1168–1174, 2018.

331. Liu, Z., Zhang, Z., Wang, Z., Jin, B., Li, D., Tao, J., Tang, R., and De Yoreo, J. J.: Shape-preserving amorphous-to-crystalline transformation of caco3 revealed by in situ tem. *Proceedings of the National Academy of Sciences of the United States of America* , 117(7):3397–3404, 2020.

332. Kok, D. J., Papapoulos, S. E., Blomen, L. J. M. J., and Bijvoet, O. L. M.: Modulation of calcium oxalate monohydrate crystallization kinetics in vitro. *Kidney International* , 34(3):346–50, 1988.

333. Lopez-Fontal, E., Grochmal, A., Foran, T., Milanes i, L., and Tomas, S.: Ship in a bottle: confinement-promoted self-assembly. *Chemical Science* , 9(7):1760–1768, 2018.

334. Kroger, R. and Verch, A.: Liquid cell transmission electron microscopy and the impact of confinement on the precipitation from supersaturated solutions. *Minerals (Basel, Switzerland)* , 8(1):21/1–21/9, 2018.

335. Zhao, W., Xia, B., Lin, L., Xiao, X., Liu, P., Lin, X., Peng, H., Zhu, Y., Yu, R., Lei, P., Wang, J., Zhang, L., Xu, Y., Zhao, M., Peng, L., Li, Q., Duan, W., Liu, Z., and Fan, Shoushan an d Jiang, K.: Low-energy transmission electron diffraction and imaging of large -area graphene. *Science Advances* , 3(9):e1603231/1–e1603231/8, 2017.

336. Li, J., Wang, X.-Y., Liu, X.-R., Jin, Z., Wa ng, D., and Wan, L.-J.: Facile growth of centimeter-sized single-crystal graphene on copper foil at atmospheric pressure. *Journal of Materials Chemistry C: Materials for Optical and Electronic Devices* , 3(15):3530–3535, 2015.

337. Tazzoli, V. and Domeneghetti, C.: The crystal structures of whewellite and weddellite: re-examination and comparison. *American Mineralogist* , 65(3-4):327–34, 1980.

338. Jorgensen, W. L., Chandrasekhar, J., Madura, J. D., Impey, R. W., and Klein, M. L.: Comparison of simple potential functions for simulating liquid water. *Journal of Chemical Physics* , 79(2):926–35, 1983.

339. Beglov, D. and Roux, B.: Finite representation of an infinite bulk system: solvent boundary potential for computer simulations. *Journal of Chemical Physics* , 100(12):9050–63, 1994.

340. Khestanova, E., Guinea, F., Fumagalli, L., Geim, A. K., and Grigorieva, I. V.: Universal shape and pressure inside bubbles appearing in van der waals heterostructures. *Nature Communications* , 7(Copyright (C) 2020 American Chemical Society (ACS). All Rights Reserved.):12587, 2016.

341. Chung, J., Granja, I., Taylor, M. G., Mpour mpakis, G., Asplin, J. R., and Rimer, J. D.: Molecular modifiers reveal a mechanism of pathological crystal gr owth inhibition. *Nature (London, United Kingdom)* , 536(7617):446–450, 2016.

342. Wang, L., De Yoreo, J. J., Guan, X., Qiu, S. R., Hoyer, J. R., and Nancollas, G. H.: Constant composition studies verify the utility of the cabrera-vermilyea (c-v) model in explaining mechanisms of calcium oxalate monohydrate crystallization. *Crystal Growth & Design* , 6(8):1769–1775, 2006.

343. Audette, G. F., van Schaik, E. J., Hazes, B., and Ir vin, R. T.: Dna-binding protein nanotubes: Learning from nature's nanotech ex amples. *Nano Letters* , 4(10):1897–1902, 2004.

344. Gravelle, S., Joly, L., Detcheverry, F., Ybert, C., Cottin-Bizonne, C., and Bocquet, L.: Optimizing water permeability through the hourglass shape of aquaporins. *Proceedings of the National Academy of Sciences of the United States of America* , 110(41):16367–16372,S16367/1–S16367/2, 2013.

345. Rasaiah, J. C., Garde, S., and Hummer, G.: Water in nonpolar confinement: from nanotubes to proteins and beyond. *Annual Review of Physical Chemistry* , 59(Copyright (C) 2020 American Chemical Society (ACS). All Rights Reserved.):713–740, 2008.

346. Israelachvili, J. N. and Pashley, R. M.: Molecular layering of water at surfaces and origin of repulsive hydration forces. *Nature (London, United Kingdom)* , 306(5940):249–50, 1983.

347. Ghodsi, S. M., Anand, S., Shahbazian-Yassar, R., Shokuhfar, T., and Megaridis, C. M.: In situ study of molecular structure of water and ice entrapped in graphene nanovessels. *ACS Nano* , 13(4):4677–4685, 2019.

348. Lim, C. H. Y. X., Sorkin, A., Bao, Q., Li, A., Zhang, K., Nesladek, M., and Loh, K. P.: A hydrothermal anvil made of graphene nanobubbles on diamond. *Nature communications* , 4(Copyright (C) 2020 U.S. National Library of Medicine.):1556, 2013.

349. Zhou, W., Yin, K., Wang, C., Zhang, Y., Xu, T., Borisevich, A., Sun, L., Idrobo, J. C., Chisholm, M. F., Pantelides, S. T., Klie, R. F., and Lupini, A. R.: The observation of square ice in graphene questioned. *Nature (London, United Kingdom)* , 528(7583):E1–E2, 2015.

350. Algara-Siller, G., Lehtinen, O., Wang, F. C., Nair, R. R. ., Kaiser, U., Wu, H. A., Geim, A. K., and Grigorieva, I. V.: Square ice in graphene nanocapillaries. *Nature (London, United Kingdom)* , 519(7544):443–445, 2015.

351. Zangi, R.: Water confined to a slab geometry: a review of recent computer simulation studies. *Journal of Physics: Condensed Matter* , 16(45):S5371–S5388, 2004.

352. Johnston, J. C., Kastelowitz, N., and Molinero, V.: Liquid to quasicrystal transition in bilayer water. *Journal of Chemical Physics* , 133(15):154516/1–154516/8, 2010.

353. Feng, X., Maier, S., and Salmeron, M.: Water splits epitaxial graphene and intercalates. *Journal of the American Chemical Society* , 134(12):5662–5668, 2012.

354. He, K. T., Wood, J. D., Doidge, G. P., Pop, E., and Lyding, J. W.: Scanning tunneling microscopy study and nanomanipulation of graphene-coated water on mica. *Nano Letters* , 12(6):2665–2672, 2012.

355. Wu, J., Gao, W., Yang, H., and Zuo, J.-M.: Dissolution kinetics of oxidative etching of cubic and icosahedra l platinum nanoparticles revealed by in situ liquid transmission electron micros copy. *ACS Nano* , 11(2):1696–1703, 2017.

356. Cheong, J. Y., Chang, J. H., Seo, H. K., Yuk, J. M., Shin, J. W., Lee, J. Y., and Kim, I.-D.: Growth dynamics of solid electrolyte interphase layer on sno2 nanotubes realized by graphene liquid cell electron microscopy. *Nano Energy* , 25(Copyright (C) 2020 American Chemical Society (ACS). All Rights Reserved.):154–160, 2016.

357. Patterson, J. P., Parent, L. R., Cantlon, J., Eickhoff, H., Bared, G., Evans, J. E., and Gianneschi, N. C.: Picoliter drop-on-demand dispensing for multiplex liquid cell transmission electron microscopy. *Microscopy and Microanalysis* , 22(3):507–514, 2016.

358. Tanase, M., Winterstein, J., Sharma, R., Aksyuk, V., Holland, G., and Liddle, J. A.: High-resolution imaging and spectroscopy at high pressure: A novel liquid cell for the transmission electron microscope. *Microscopy and Microanalysis* , 21(6):1629–1638, 2015.

359. Kell, G. S.: Density, thermal expansivity, and compressibility of liquid water from 0.deg. to 150.deg.. correlations and tables for atmospheric pressure and saturation reviewed and expressed on 1968 temperature scale. *Journal of Chemical and Engineering Data* , 20(1):97–105, 1975.

360. Vasu, K. S., Abraham, J., Geim, A. K., Nair, R. R., Prestat, E., Haigh, S. J., Dix, J., Carbone, P., Kashtiban, R. J., Sloan, J., Beheshtian, J., and Neek-Amal, M.: Van der waals pressure and its effect on trapped interlayer molecules. *Nature communications* , 7(Copyright (C) 2020 U.S. National Library of Medicine.):12168, 2016.

361. Zamborlini, G., Imam, M., Patera, L. L., M entes, T. O., Stojic, N., Africh, C., Sala, Alessandro a nd Binggeli, N., Comelli, G., and Locatelli, A.: Nanobubbles at gpa pressure under graphene. *Nano Letters* , 15(9):6162–6169, 2015.

362. Shin, D., Park, J. B., Kim, S. J., Kang, J. H., Lee, B., Kim, Y.-J., Cho, S.-P., Hong, B. H., and Novoselov, K. S.: Growth dynamics and gas transport mechanism of nanobubbles in graphene liquid cells. *Nature communications* , 6(Copyright (C) 2020 U.S. National Library of Medicine.):6068, 2015.

363. Bunch, J. S., Verbridge, S. S., Alden, J. S., van der Zande, A. M., Parpia, J. M., Craighead, H. G., and McEuen, P. L.: Impermeable atomic membranes from graphene sheets. *Nano Letters* , 8(8):2458–2462, 2008.

364. Chiou, Y.-C., Olukan, T. A., Almahri, Mariam Ali a nd Apostoleris, H., Chiu, C. H., Lai, C.-Y., Lu, Jin-You an d Santos, S., Almansouri, I., and Chiesa, M.: Direct measurement of the magnitude of the van der waals interacti on of single and multilayer graphene. *Langmuir* , 34(41):12335–12343, 2018.

365. Peng, T., Peng, K., and Li, Q.: Methodology for disjoining pressure of free water nanofilms. *Journal of Physical Chemistry C* , 119(25):14273–14280, 2015.

366. Lee, C., Wei, X., Kysar, J. W., and Hone, J.: Measurement of the elastic properties and intrinsic strength of monolayer graphene. *Science (Washington, DC, United States)* , 321(5887):385–388, 2008.

367. Ruiz-Vargas, C. S., Zhuang, H. L., Huang, P. Y., van der Zande, A. M., Garg, S., McEuen, P. L., Muller, D. A., Hennig, R. G., and Park, J.: Softened elastic response and unzipping in chemical vapor deposition graphene membranes. *Nano Letters* , 11(6):2259–2263, 2011.

368. Nicholl, R. J. T., Conley, H. J., Lavrik, N. V., Vlassiouk, I., Puzyrev, Y. S., Sreenivas, V. P., Pantelides, S. T., and Bolotin, K. I.: The effect of intrinsic crumpling on the mechanics of free-standing graphene. *Nature Communications* , 6(Copyright (C) 2020 American Chemical Society (ACS). All Rights Reserved.):8789, 2015.

369. Pendse, A., Cetindag, S., Rehak, P., Behura, S., Gao, H., Nguyen, N., Wang, T., Berry, V., Král, P., Shan, J., and Kim*, S.: Highly efficient osmotic energy harvesting in charged boron-nitride-nanopore membranes.

370. Yip, N. Y. and Elimelech, M.: Comparison of energy efficiency and power density in pressure reta rded osmosis and reverse electrodialysis. *Environmental Science & Technology* , 48(18):11002–11012, 2014.

371. Jia, Z., Wang, B., Song, S., and Fan, Y.: Blue energy: Current technologies for sustainable power generation from water salinity gradient. *Renewable and Sustainable Energy Reviews* , 31:91–100, 2014.

372. Kim, D.-K., Duan, C., Chen, Y.-F., and Majumdar, A.: Power generation from concentration gradient by reverse electrodialysis in ion-selective nanochannels. *Microfluidics and Nanofluidics* , 9(6):1215–1224, 2010.

373. Hwang, J., Kataoka, S., Endo, A., and Daiguji, H.: Enhanced energy harvesting by concentration gradient-driven ion transport in sba-15 mesoporous silica thin films. *Lab on a Chip* , 16(19):3824–3832, 2016.

374. Esfandiar, A., Radha, B., Wang, F. C., Yang, Q., Hu, S., Garaj, S., Nair, R. R., Geim, A. K., and Gopinadhan, K.: Size effect in ion transport through angstrom-scale slits. *Science (Washington, DC, United States)* , 358(6362):511–513, 2017.

375. Siria, A., Poncharal, P., Biance, A.-L., Fulcrand, R., Blase, X., Purcell, S. T., and Bocquet, L.: Giant osmotic energy conversion measured in a single transmembrane boron nitride nanotube. *Nature (London, United Kingdom)* , 494(7438):455–458, 2013.

376. Turek, M. and Bandura, B.: Renewable energy by reverse electrodialysis. *Desalination* , 205(1-3):67–74, 2007.

377. Behura, S., Nguyen, P., Che, S., Debbarma, R. u., and Berry, V.: Large-area, transfer-free, oxide-assisted synthesis of hexagonal b oron nitride films and their heterostructures with mos2 and ws2. *Journal of the American Chemical Society* , 137(40):13060–13065, 2015.

378. Kong, J.: Synthesis of monolayer hexagonal boron nitride on cu foil using chemical vapor deposition. *Nano Letters* , 12(1):161–166, 2012.

379. Weinstein, J. N. and Leitz, F. B.: Electric power from differences in salinity: the dialytic battery. *Science (Washington, DC, United States)* , 191(4227):557–9, 1976.

380. Stein, D., Kruithof, M., and Dekker, C.: Surface-charge-governed ion transport in nanofluidic channels. *Physical Review Letters* , 93(3):035901/1–035901/4, 2004.

381. Hernandez, A., Martinez, F., Martin, A., and Pradanos, P.: Porous structure and surface charge density on the walls of microp orous alumina membranes. *Journal of Colloid and Interface Science* , 173(2):284–96, 1995.

382. Seshadri, K. S., Selvaraj, M., Kesavamoorthy, R., Srinivasan, M. P., Varatharajan, K., Lal, K. B., and Krishnasamy, V.: Estimation and comparison of pore charge on titania and zirconia membranes prepared by sol-gel route using zeta potential measurement. *Journal of Sol-Gel Science and Technology* , 28(3):327–333, 2003.

383. Gao, H., Shi, Q., Rao, D., Zhang, Y., Su, J. e., Liu, Y., Wang, Y., Deng, K., and Lu, R.: Rational design and strain engineering of nanoporous boron nitride n anosheet membranes for water desalination. *Journal of Physical Chemistry C* , 121(40):22105–22113, 2017.

384. Won, C. Y. and Aluru, N. R.: Water permeation through a subnanometer boron nitride nanotube. *Journal of the American Chemical Society* , 129(10):2748–2749, 2007.

385. Bloch, J. M. and Yun, W.: Condensation of monovalent and divalent metal ions on a langmuir mo nolayer. *Physical Review A: Atomic, Molecular, and Optical Physics* , 41(2):844–62, 1990.

386. Anderson, J. L.: Colloid transport by interfacial forces. *Annu. Rev. Fluid Mech.* , 21(1):61–99, January 1989.

387. Schroeder, T. B. H., Guha, A., Lamoureux, A., Van Renterghem, G., Sept, D., Shtein, M., Yang, J., and Mayer, M.: An electric eel-inspired soft power source from stacked hydrogels. *Nature (London, United Kingdom)* , 552(7684):214–218, 2017.

388. Lee, W., Ji, R., Goesele, U., and Nielsch, K.: Fast fabrication of long-range ordered porous alumina membranes by hard anodization. *Nature Materials* , 5(9):741–747, 2006.

JOHN WILEY AND SONS LICENSE
TERMS AND CONDITIONS

Dec 14, 2020

This Agreement between University of Illinois at Chicago -- Pavel Rehak ("You") and John Wiley and Sons ("John Wiley and Sons") consists of your license details and the terms and conditions provided by John Wiley and Sons and Copyright Clearance Center.

License Number	4965000250277
License date	Dec 09, 2020
Licensed Content Publisher	John Wiley and Sons
Licensed Content Publication	Israel Journal of Chemistry
Licensed Content Title	Formation of Apoptosis-Inducing Amyloid Fibrils by Tryptophan
Licensed Content Author	Shira Shaham-Niv, Pavel Rehak, Lela Vuković, et al
Licensed Content Date	Nov 16, 2016
Licensed Content Volume	57
Licensed Content Issue	7-8
Licensed Content Pages	9
Type of use	Dissertation/Thesis
Requestor type	Author of this Wiley article

Format	Electronic
Portion	Full article
Will you be translating?	No
Title	Molecular Dynamics Simulations of Material Assembly, Growth, and Transport
Institution name	University of Illinois at Chicago
Expected presentation date	Dec 2020
Requestor Location	University of Illinois at Chicago 1826 Meadow Glen Dr. LIVERMORE, CA 94551 United States Attn: University of Illinois at Chicago
Publisher Tax ID	EU826007151
Total	0.00 USD

Terms and Conditions

TERMS AND CONDITIONS

This copyrighted material is owned by or exclusively licensed to John Wiley & Sons, Inc. or one of its group companies (each a"Wiley Company") or handled on behalf of a society with which a Wiley Company has exclusive publishing rights in relation to a particular work (collectively "WILEY"). By clicking "accept" in connection with completing this licensing transaction, you agree that the following terms and conditions apply to this transaction (along with the billing and payment terms and conditions established by the Copyright Clearance Center Inc., ("CCC's Billing and Payment terms and conditions"), at the time that you opened your RightsLink account (these are available at any time at http://myaccount.copyright.com).

Terms and Conditions

- The materials you have requested permission to reproduce or reuse (the "Wiley Materials") are protected by copyright.

- You are hereby granted a personal, non-exclusive, non-sub licensable (on a stand-alone basis), non-transferable, worldwide, limited license to reproduce the Wiley Materials for the purpose specified in the licensing process. This license, **and any CONTENT (PDF or image file) purchased as part of your order,** is for a one-time use only and limited to any maximum distribution number specified in the license. The first instance of republication or reuse granted by this license must be completed within two years of the date of the grant of this license (although copies prepared before the end date may be distributed thereafter). The Wiley Materials shall not be used in any other manner or for any other purpose, beyond what is granted in the license. Permission is granted subject to an appropriate acknowledgement given to the author, title of the material/book/journal and the publisher. You shall also duplicate the copyright notice that appears in the Wiley publication in your use of the Wiley Material. Permission is also granted on the understanding that nowhere in the text is a previously published source acknowledged for all or part of this Wiley Material. Any third party content is expressly excluded from this permission.

- With respect to the Wiley Materials, all rights are reserved. Except as expressly granted by the terms of the license, no part of the Wiley Materials may be copied, modified, adapted (except for minor reformatting required by the new Publication), translated, reproduced, transferred or distributed, in any form or by any means, and no derivative works may be made based on the Wiley Materials without the prior permission of the respective copyright owner.**For STM Signatory Publishers clearing permission under the terms of the STM Permissions Guidelines only, the terms of the license are extended to include subsequent editions and for editions in other languages, provided such editions are for the work as a whole in situ and does not involve the separate exploitation of the permitted figures or extracts,** You may not alter, remove or suppress in any manner any copyright, trademark or other notices displayed by the Wiley Materials. You may not license, rent, sell, loan, lease, pledge, offer as security, transfer or assign the Wiley Materials on a stand-alone basis, or any of the rights granted to you hereunder to any other person.

- The Wiley Materials and all of the intellectual property rights therein shall at all times remain the exclusive property of John Wiley & Sons Inc, the Wiley Companies, or their respective licensors, and your interest therein is only that of having possession of and the right to reproduce the Wiley Materials pursuant to Section 2 herein during the continuance of this Agreement. You agree that you own no right, title or interest in or to the Wiley Materials or any of the intellectual property rights therein. You shall have no rights hereunder other than the license as provided for above in Section 2. No right, license or interest to any trademark, trade name, service mark or other branding ("Marks") of WILEY or its licensors is granted hereunder, and you agree that you shall not assert any such right, license or interest with respect thereto

- NEITHER WILEY NOR ITS LICENSORS MAKES ANY WARRANTY OR REPRESENTATION OF ANY KIND TO YOU OR ANY THIRD PARTY, EXPRESS, IMPLIED OR STATUTORY, WITH RESPECT TO THE MATERIALS OR THE ACCURACY OF ANY INFORMATION CONTAINED IN THE MATERIALS, INCLUDING, WITHOUT LIMITATION, ANY IMPLIED WARRANTY OF MERCHANTABILITY, ACCURACY, SATISFACTORY QUALITY, FITNESS FOR A PARTICULAR PURPOSE, USABILITY, INTEGRATION OR NON-INFRINGEMENT AND ALL SUCH WARRANTIES ARE HEREBY EXCLUDED BY WILEY AND ITS LICENSORS AND WAIVED

BY YOU.

- WILEY shall have the right to terminate this Agreement immediately upon breach of this Agreement by you.

- You shall indemnify, defend and hold harmless WILEY, its Licensors and their respective directors, officers, agents and employees, from and against any actual or threatened claims, demands, causes of action or proceedings arising from any breach of this Agreement by you.

- IN NO EVENT SHALL WILEY OR ITS LICENSORS BE LIABLE TO YOU OR ANY OTHER PARTY OR ANY OTHER PERSON OR ENTITY FOR ANY SPECIAL, CONSEQUENTIAL, INCIDENTAL, INDIRECT, EXEMPLARY OR PUNITIVE DAMAGES, HOWEVER CAUSED, ARISING OUT OF OR IN CONNECTION WITH THE DOWNLOADING, PROVISIONING, VIEWING OR USE OF THE MATERIALS REGARDLESS OF THE FORM OF ACTION, WHETHER FOR BREACH OF CONTRACT, BREACH OF WARRANTY, TORT, NEGLIGENCE, INFRINGEMENT OR OTHERWISE (INCLUDING, WITHOUT LIMITATION, DAMAGES BASED ON LOSS OF PROFITS, DATA, FILES, USE, BUSINESS OPPORTUNITY OR CLAIMS OF THIRD PARTIES), AND WHETHER OR NOT THE PARTY HAS BEEN ADVISED OF THE POSSIBILITY OF SUCH DAMAGES. THIS LIMITATION SHALL APPLY NOTWITHSTANDING ANY FAILURE OF ESSENTIAL PURPOSE OF ANY LIMITED REMEDY PROVIDED HEREIN.

- Should any provision of this Agreement be held by a court of competent jurisdiction to be illegal, invalid, or unenforceable, that provision shall be deemed amended to achieve as nearly as possible the same economic effect as the original provision, and the legality, validity and enforceability of the remaining provisions of this Agreement shall not be affected or impaired thereby.

- The failure of either party to enforce any term or condition of this Agreement shall not constitute a waiver of either party's right to enforce each and every term and condition of this Agreement. No breach under this agreement shall be deemed waived or excused by either party unless such waiver or consent is in writing signed by the party granting such waiver or consent. The waiver by or consent of a party to a breach of any provision of this Agreement shall not operate or be construed as a waiver of or consent to any other or subsequent breach by such other party.

- This Agreement may not be assigned (including by operation of law or otherwise) by you without WILEY's prior written consent.

- Any fee required for this permission shall be non-refundable after thirty (30) days from receipt by the CCC.

- These terms and conditions together with CCC's Billing and Payment terms and conditions (which are incorporated herein) form the entire agreement between you and WILEY concerning this licensing transaction and (in the absence of fraud) supersedes all prior agreements and representations of the parties, oral or written. This Agreement may not be amended except in writing signed by both parties. This Agreement shall be binding upon and inure to the benefit of the parties' successors, legal representatives, and authorized assigns.

- In the event of any conflict between your obligations established by these terms and conditions and those established by CCC's Billing and Payment terms and conditions, these terms and conditions shall prevail.

- WILEY expressly reserves all rights not specifically granted in the combination of (i) the license details provided by you and accepted in the course of this licensing transaction, (ii) these terms and conditions and (iii) CCC's Billing and Payment terms and conditions.

- This Agreement will be void if the Type of Use, Format, Circulation, or Requestor Type was misrepresented during the licensing process.

- This Agreement shall be governed by and construed in accordance with the laws of the State of New York, USA, without regards to such state's conflict of law rules. Any legal action, suit or proceeding arising out of or relating to these Terms and Conditions or the breach thereof shall be instituted in a court of competent jurisdiction in New York County in the State of New York in the United States of America and each party hereby consents and submits to the personal jurisdiction of such court, waives any objection to venue in such court and consents to service of process by registered or certified mail, return receipt requested, at the last known address of such party.

WILEY OPEN ACCESS TERMS AND CONDITIONS

Wiley Publishes Open Access Articles in fully Open Access Journals and in Subscription journals offering Online Open. Although most of the fully Open Access journals publish open access articles under the terms of the Creative Commons Attribution (CC BY) License only, the subscription journals and a few of the Open Access Journals offer a choice of Creative Commons Licenses. The license type is clearly identified on the article.

The Creative Commons Attribution License

The Creative Commons Attribution License (CC-BY) allows users to copy, distribute and transmit an article, adapt the article and make commercial use of the article. The CC-BY license permits commercial and non-

Creative Commons Attribution Non-Commercial License

The Creative Commons Attribution Non-Commercial (CC-BY-NC)License permits use, distribution and reproduction in any medium, provided the original work is properly cited and is not used for commercial purposes.(see below)

Creative Commons Attribution-Non-Commercial-NoDerivs License

The Creative Commons Attribution Non-Commercial-NoDerivs License (CC-BY-NC-ND) permits use, distribution and reproduction in any medium, provided the original work is properly cited, is not used for commercial purposes and no modifications or adaptations are made. (see below)

Use by commercial "for-profit" organizations

Use of Wiley Open Access articles for commercial, promotional, or marketing purposes requires further explicit permission from Wiley and will be subject to a fee.

Further details can be found on Wiley Online Library
http://olabout.wiley.com/WileyCDA/Section/id-410895.html

Other Terms and Conditions:

v1.10 Last updated September 2015

Questions? customercare@copyright.com or +1-855-239-3415 (toll free in the US) or +1-978-646-2777.

JOHN WILEY AND SONS LICENSE
TERMS AND CONDITIONS

Dec 14, 2020

This Agreement between University of Illinois at Chicago -- Pavel Rehak ("You") and John Wiley and Sons ("John Wiley and Sons") consists of your license details and the terms and conditions provided by John Wiley and Sons and Copyright Clearance Center.

License Number	4964991089444
License date	Dec 09, 2020
Licensed Content Publisher	John Wiley and Sons
Licensed Content Publication	Advanced Materials
Licensed Content Title	Electrical Conductivity, Selective Adhesion, and Biocompatibility in Bacteria-Inspired Peptide–Metal Self-Supporting Nanocomposites
Licensed Content Author	Ehud Gazit, Allon I. Hochbaum, Tal Dvir, et al
Licensed Content Date	Jan 15, 2019
Licensed Content Volume	31
Licensed Content Issue	10
Licensed	9

Content Pages	
Type of use	Dissertation/Thesis
Requestor type	Author of this Wiley article
Format	Print
Portion	Full article
Will you be translating?	No
Title	Molecular Dynamics Simulations of Material Assembly, Growth, and Transport
Institution name	University of Illinois at Chicago
Expected presentation date	Dec 2020
Requestor Location	University of Illinois at Chicago 1826 Meadow Glen Dr. LIVERMORE, CA 94551 United States Attn: University of Illinois at Chicago
Publisher Tax ID	EU826007151
Total	0.00 USD

Terms and Conditions

TERMS AND CONDITIONS

This copyrighted material is owned by or exclusively licensed to John Wiley & Sons, Inc. or one of its group companies (each a"Wiley Company") or handled on behalf of a society with

which a Wiley Company has exclusive publishing rights in relation to a particular work (collectively "WILEY"). By clicking "accept" in connection with completing this licensing transaction, you agree that the following terms and conditions apply to this transaction (along with the billing and payment terms and conditions established by the Copyright Clearance Center Inc., ("CCC's Billing and Payment terms and conditions"), at the time that you opened your RightsLink account (these are available at any time at http://myaccount.copyright.com).

Terms and Conditions

- The materials you have requested permission to reproduce or reuse (the "Wiley Materials") are protected by copyright.

- You are hereby granted a personal, non-exclusive, non-sub licensable (on a stand-alone basis), non-transferable, worldwide, limited license to reproduce the Wiley Materials for the purpose specified in the licensing process. This license, **and any CONTENT (PDF or image file) purchased as part of your order,** is for a one-time use only and limited to any maximum distribution number specified in the license. The first instance of republication or reuse granted by this license must be completed within two years of the date of the grant of this license (although copies prepared before the end date may be distributed thereafter). The Wiley Materials shall not be used in any other manner or for any other purpose, beyond what is granted in the license. Permission is granted subject to an appropriate acknowledgement given to the author, title of the material/book/journal and the publisher. You shall also duplicate the copyright notice that appears in the Wiley publication in your use of the Wiley Material. Permission is also granted on the understanding that nowhere in the text is a previously published source acknowledged for all or part of this Wiley Material. Any third party content is expressly excluded from this permission.

- With respect to the Wiley Materials, all rights are reserved. Except as expressly granted by the terms of the license, no part of the Wiley Materials may be copied, modified, adapted (except for minor reformatting required by the new Publication), translated, reproduced, transferred or distributed, in any form or by any means, and no derivative works may be made based on the Wiley Materials without the prior permission of the respective copyright owner.**For STM Signatory Publishers clearing permission under the terms of the STM Permissions Guidelines only, the terms of the license are extended to include subsequent editions and for editions in other languages, provided such editions are for the work as a whole in situ and does not involve the separate exploitation of the permitted figures or extracts,** You may not alter, remove or suppress in any manner any copyright, trademark or other notices displayed by the Wiley Materials. You may not license, rent, sell, loan, lease, pledge, offer as security, transfer or assign the Wiley Materials on a stand-alone basis, or any of the rights granted to you hereunder to any other person.

- The Wiley Materials and all of the intellectual property rights therein shall at all times remain the exclusive property of John Wiley & Sons Inc, the Wiley Companies, or their respective licensors, and your interest therein is only that of having possession of and the right to reproduce the Wiley Materials pursuant to Section 2 herein during the continuance of this Agreement. You agree that you own no right, title or interest in or to the Wiley Materials or any of the intellectual property rights therein. You shall have no rights hereunder other than the license as provided for above in Section 2. No right, license or interest to any trademark, trade name, service mark or other branding ("Marks") of WILEY or its licensors is granted hereunder, and you agree that you

shall not assert any such right, license or interest with respect thereto

- NEITHER WILEY NOR ITS LICENSORS MAKES ANY WARRANTY OR REPRESENTATION OF ANY KIND TO YOU OR ANY THIRD PARTY, EXPRESS, IMPLIED OR STATUTORY, WITH RESPECT TO THE MATERIALS OR THE ACCURACY OF ANY INFORMATION CONTAINED IN THE MATERIALS, INCLUDING, WITHOUT LIMITATION, ANY IMPLIED WARRANTY OF MERCHANTABILITY, ACCURACY, SATISFACTORY QUALITY, FITNESS FOR A PARTICULAR PURPOSE, USABILITY, INTEGRATION OR NON-INFRINGEMENT AND ALL SUCH WARRANTIES ARE HEREBY EXCLUDED BY WILEY AND ITS LICENSORS AND WAIVED BY YOU.

- WILEY shall have the right to terminate this Agreement immediately upon breach of this Agreement by you.

- You shall indemnify, defend and hold harmless WILEY, its Licensors and their respective directors, officers, agents and employees, from and against any actual or threatened claims, demands, causes of action or proceedings arising from any breach of this Agreement by you.

- IN NO EVENT SHALL WILEY OR ITS LICENSORS BE LIABLE TO YOU OR ANY OTHER PARTY OR ANY OTHER PERSON OR ENTITY FOR ANY SPECIAL, CONSEQUENTIAL, INCIDENTAL, INDIRECT, EXEMPLARY OR PUNITIVE DAMAGES, HOWEVER CAUSED, ARISING OUT OF OR IN CONNECTION WITH THE DOWNLOADING, PROVISIONING, VIEWING OR USE OF THE MATERIALS REGARDLESS OF THE FORM OF ACTION, WHETHER FOR BREACH OF CONTRACT, BREACH OF WARRANTY, TORT, NEGLIGENCE, INFRINGEMENT OR OTHERWISE (INCLUDING, WITHOUT LIMITATION, DAMAGES BASED ON LOSS OF PROFITS, DATA, FILES, USE, BUSINESS OPPORTUNITY OR CLAIMS OF THIRD PARTIES), AND WHETHER OR NOT THE PARTY HAS BEEN ADVISED OF THE POSSIBILITY OF SUCH DAMAGES. THIS LIMITATION SHALL APPLY NOTWITHSTANDING ANY FAILURE OF ESSENTIAL PURPOSE OF ANY LIMITED REMEDY PROVIDED HEREIN.

- Should any provision of this Agreement be held by a court of competent jurisdiction to be illegal, invalid, or unenforceable, that provision shall be deemed amended to achieve as nearly as possible the same economic effect as the original provision, and the legality, validity and enforceability of the remaining provisions of this Agreement shall not be affected or impaired thereby.

- The failure of either party to enforce any term or condition of this Agreement shall not constitute a waiver of either party's right to enforce each and every term and condition of this Agreement. No breach under this agreement shall be deemed waived or excused by either party unless such waiver or consent is in writing signed by the party granting such waiver or consent. The waiver by or consent of a party to a breach of any provision of this Agreement shall not operate or be construed as a waiver of or consent to any other or subsequent breach by such other party.

- This Agreement may not be assigned (including by operation of law or otherwise) by you without WILEY's prior written consent.

- Any fee required for this permission shall be non-refundable after thirty (30) days from receipt by the CCC.

- These terms and conditions together with CCC's Billing and Payment terms and conditions (which are incorporated herein) form the entire agreement between you and WILEY concerning this licensing transaction and (in the absence of fraud) supersedes all prior agreements and representations of the parties, oral or written. This Agreement may not be amended except in writing signed by both parties. This Agreement shall be binding upon and inure to the benefit of the parties' successors, legal representatives, and authorized assigns.

- In the event of any conflict between your obligations established by these terms and conditions and those established by CCC's Billing and Payment terms and conditions, these terms and conditions shall prevail.

- WILEY expressly reserves all rights not specifically granted in the combination of (i) the license details provided by you and accepted in the course of this licensing transaction, (ii) these terms and conditions and (iii) CCC's Billing and Payment terms and conditions.

- This Agreement will be void if the Type of Use, Format, Circulation, or Requestor Type was misrepresented during the licensing process.

- This Agreement shall be governed by and construed in accordance with the laws of the State of New York, USA, without regards to such state's conflict of law rules. Any legal action, suit or proceeding arising out of or relating to these Terms and Conditions or the breach thereof shall be instituted in a court of competent jurisdiction in New York County in the State of New York in the United States of America and each party hereby consents and submits to the personal jurisdiction of such court, waives any objection to venue in such court and consents to service of process by registered or certified mail, return receipt requested, at the last known address of such party.

WILEY OPEN ACCESS TERMS AND CONDITIONS

Wiley Publishes Open Access Articles in fully Open Access Journals and in Subscription journals offering Online Open. Although most of the fully Open Access journals publish open access articles under the terms of the Creative Commons Attribution (CC BY) License only, the subscription journals and a few of the Open Access Journals offer a choice of Creative Commons Licenses. The license type is clearly identified on the article.

The Creative Commons Attribution License

The Creative Commons Attribution License (CC-BY) allows users to copy, distribute and transmit an article, adapt the article and make commercial use of the article. The CC-BY license permits commercial and non-

Creative Commons Attribution Non-Commercial License

The Creative Commons Attribution Non-Commercial (CC-BY-NC)License permits use, distribution and reproduction in any medium, provided the original work is properly cited and is not used for commercial purposes.(see below)

Creative Commons Attribution-Non-Commercial-NoDerivs License

JOHN WILEY AND SONS LICENSE
TERMS AND CONDITIONS

Dec 14, 2020

This Agreement between University of Illinois at Chicago -- Pavel Rehak ("You") and John Wiley and Sons ("John Wiley and Sons") consists of your license details and the terms and conditions provided by John Wiley and Sons and Copyright Clearance Center.

License Number	4964980228994
License date	Dec 09, 2020
Licensed Content Publisher	John Wiley and Sons
Licensed Content Publication	Advanced Materials Interfaces
Licensed Content Title	Assessment of Pressure and Density of Confined Water in Graphene Liquid Cells
Licensed Content Author	Seyed Mohammadreza Ghodsi, Soroosh Sharifi-Asl, Pavel Rehak, et al
Licensed Content Date	May 10, 2020
Licensed Content Volume	7
Licensed Content Issue	12
Licensed Content Pages	10
Type of use	Dissertation/Thesis

Requestor type	Author of this Wiley article
Format	Electronic
Portion	Full article
Will you be translating?	No
Title	Molecular Dynamics Simulations of Material Assembly, Growth, and Transport
Institution name	University of Illinois at Chicago
Expected presentation date	Dec 2020
Requestor Location	University of Illinois at Chicago 1826 Meadow Glen Dr. LIVERMORE, CA 94551 United States Attn: University of Illinois at Chicago
Publisher Tax ID	EU826007151
Total	0.00 USD
Terms and Conditions	

TERMS AND CONDITIONS

This copyrighted material is owned by or exclusively licensed to John Wiley & Sons, Inc. or one of its group companies (each a"Wiley Company") or handled on behalf of a society with which a Wiley Company has exclusive publishing rights in relation to a particular work (collectively "WILEY"). By clicking "accept" in connection with completing this licensing transaction, you agree that the following terms and conditions apply to this transaction (along with the billing and payment terms and conditions established by the Copyright Clearance Center Inc., ("CCC's Billing and Payment terms and conditions"), at the time that you opened your RightsLink account (these are available at any time at http://myaccount.copyright.com).

Terms and Conditions

- The materials you have requested permission to reproduce or reuse (the "Wiley Materials") are protected by copyright.

- You are hereby granted a personal, non-exclusive, non-sub licensable (on a stand-alone basis), non-transferable, worldwide, limited license to reproduce the Wiley Materials for the purpose specified in the licensing process. This license, **and any CONTENT (PDF or image file) purchased as part of your order,** is for a one-time use only and limited to any maximum distribution number specified in the license. The first instance of republication or reuse granted by this license must be completed within two years of the date of the grant of this license (although copies prepared before the end date may be distributed thereafter). The Wiley Materials shall not be used in any other manner or for any other purpose, beyond what is granted in the license. Permission is granted subject to an appropriate acknowledgement given to the author, title of the material/book/journal and the publisher. You shall also duplicate the copyright notice that appears in the Wiley publication in your use of the Wiley Material. Permission is also granted on the understanding that nowhere in the text is a previously published source acknowledged for all or part of this Wiley Material. Any third party content is expressly excluded from this permission.

- With respect to the Wiley Materials, all rights are reserved. Except as expressly granted by the terms of the license, no part of the Wiley Materials may be copied, modified, adapted (except for minor reformatting required by the new Publication), translated, reproduced, transferred or distributed, in any form or by any means, and no derivative works may be made based on the Wiley Materials without the prior permission of the respective copyright owner.**For STM Signatory Publishers clearing permission under the terms of the STM Permissions Guidelines only, the terms of the license are extended to include subsequent editions and for editions in other languages, provided such editions are for the work as a whole in situ and does not involve the separate exploitation of the permitted figures or extracts,** You may not alter, remove or suppress in any manner any copyright, trademark or other notices displayed by the Wiley Materials. You may not license, rent, sell, loan, lease, pledge, offer as security, transfer or assign the Wiley Materials on a stand-alone basis, or any of the rights granted to you hereunder to any other person.

- The Wiley Materials and all of the intellectual property rights therein shall at all times remain the exclusive property of John Wiley & Sons Inc, the Wiley Companies, or their respective licensors, and your interest therein is only that of having possession of and the right to reproduce the Wiley Materials pursuant to Section 2 herein during the continuance of this Agreement. You agree that you own no right, title or interest in or to the Wiley Materials or any of the intellectual property rights therein. You shall have no rights hereunder other than the license as provided for above in Section 2. No right, license or interest to any trademark, trade name, service mark or other branding ("Marks") of WILEY or its licensors is granted hereunder, and you agree that you shall not assert any such right, license or interest with respect thereto

- NEITHER WILEY NOR ITS LICENSORS MAKES ANY WARRANTY OR REPRESENTATION OF ANY KIND TO YOU OR ANY THIRD PARTY, EXPRESS, IMPLIED OR STATUTORY, WITH RESPECT TO THE MATERIALS OR THE ACCURACY OF ANY INFORMATION CONTAINED IN THE MATERIALS, INCLUDING, WITHOUT LIMITATION, ANY IMPLIED WARRANTY OF MERCHANTABILITY, ACCURACY, SATISFACTORY

QUALITY, FITNESS FOR A PARTICULAR PURPOSE, USABILITY, INTEGRATION OR NON-INFRINGEMENT AND ALL SUCH WARRANTIES ARE HEREBY EXCLUDED BY WILEY AND ITS LICENSORS AND WAIVED BY YOU.

- WILEY shall have the right to terminate this Agreement immediately upon breach of this Agreement by you.

- You shall indemnify, defend and hold harmless WILEY, its Licensors and their respective directors, officers, agents and employees, from and against any actual or threatened claims, demands, causes of action or proceedings arising from any breach of this Agreement by you.

- IN NO EVENT SHALL WILEY OR ITS LICENSORS BE LIABLE TO YOU OR ANY OTHER PARTY OR ANY OTHER PERSON OR ENTITY FOR ANY SPECIAL, CONSEQUENTIAL, INCIDENTAL, INDIRECT, EXEMPLARY OR PUNITIVE DAMAGES, HOWEVER CAUSED, ARISING OUT OF OR IN CONNECTION WITH THE DOWNLOADING, PROVISIONING, VIEWING OR USE OF THE MATERIALS REGARDLESS OF THE FORM OF ACTION, WHETHER FOR BREACH OF CONTRACT, BREACH OF WARRANTY, TORT, NEGLIGENCE, INFRINGEMENT OR OTHERWISE (INCLUDING, WITHOUT LIMITATION, DAMAGES BASED ON LOSS OF PROFITS, DATA, FILES, USE, BUSINESS OPPORTUNITY OR CLAIMS OF THIRD PARTIES), AND WHETHER OR NOT THE PARTY HAS BEEN ADVISED OF THE POSSIBILITY OF SUCH DAMAGES. THIS LIMITATION SHALL APPLY NOTWITHSTANDING ANY FAILURE OF ESSENTIAL PURPOSE OF ANY LIMITED REMEDY PROVIDED HEREIN.

- Should any provision of this Agreement be held by a court of competent jurisdiction to be illegal, invalid, or unenforceable, that provision shall be deemed amended to achieve as nearly as possible the same economic effect as the original provision, and the legality, validity and enforceability of the remaining provisions of this Agreement shall not be affected or impaired thereby.

- The failure of either party to enforce any term or condition of this Agreement shall not constitute a waiver of either party's right to enforce each and every term and condition of this Agreement. No breach under this agreement shall be deemed waived or excused by either party unless such waiver or consent is in writing signed by the party granting such waiver or consent. The waiver by or consent of a party to a breach of any provision of this Agreement shall not operate or be construed as a waiver of or consent to any other or subsequent breach by such other party.

- This Agreement may not be assigned (including by operation of law or otherwise) by you without WILEY's prior written consent.

- Any fee required for this permission shall be non-refundable after thirty (30) days from receipt by the CCC.

- These terms and conditions together with CCC's Billing and Payment terms and conditions (which are incorporated herein) form the entire agreement between you and WILEY concerning this licensing transaction and (in the absence of fraud) supersedes all prior agreements and representations of the parties, oral or written. This Agreement may not be amended except in writing signed by both parties. This Agreement shall be binding upon and inure to the benefit of the parties' successors, legal representatives,

and authorized assigns.

- In the event of any conflict between your obligations established by these terms and conditions and those established by CCC's Billing and Payment terms and conditions, these terms and conditions shall prevail.
- WILEY expressly reserves all rights not specifically granted in the combination of (i) the license details provided by you and accepted in the course of this licensing transaction, (ii) these terms and conditions and (iii) CCC's Billing and Payment terms and conditions.
- This Agreement will be void if the Type of Use, Format, Circulation, or Requestor Type was misrepresented during the licensing process.
- This Agreement shall be governed by and construed in accordance with the laws of the State of New York, USA, without regards to such state's conflict of law rules. Any legal action, suit or proceeding arising out of or relating to these Terms and Conditions or the breach thereof shall be instituted in a court of competent jurisdiction in New York County in the State of New York in the United States of America and each party hereby consents and submits to the personal jurisdiction of such court, waives any objection to venue in such court and consents to service of process by registered or certified mail, return receipt requested, at the last known address of such party.

WILEY OPEN ACCESS TERMS AND CONDITIONS

Wiley Publishes Open Access Articles in fully Open Access Journals and in Subscription journals offering Online Open. Although most of the fully Open Access journals publish open access articles under the terms of the Creative Commons Attribution (CC BY) License only, the subscription journals and a few of the Open Access Journals offer a choice of Creative Commons Licenses. The license type is clearly identified on the article.

The Creative Commons Attribution License

The Creative Commons Attribution License (CC-BY) allows users to copy, distribute and transmit an article, adapt the article and make commercial use of the article. The CC-BY license permits commercial and non-

Creative Commons Attribution Non-Commercial License

The Creative Commons Attribution Non-Commercial (CC-BY-NC)License permits use, distribution and reproduction in any medium, provided the original work is properly cited and is not used for commercial purposes.(see below)

Creative Commons Attribution-Non-Commercial-NoDerivs License

The Creative Commons Attribution Non-Commercial-NoDerivs License (CC-BY-NC-ND) permits use, distribution and reproduction in any medium, provided the original work is properly cited, is not used for commercial purposes and no modifications or adaptations are made. (see below)

Use by commercial "for-profit" organizations

Use of Wiley Open Access articles for commercial, promotional, or marketing purposes requires further explicit permission from Wiley and will be subject to a fee.

Further details can be found on Wiley Online Library
http://olabout.wiley.com/WileyCDA/Section/id-410895.html

Other Terms and Conditions:

v1.10 Last updated September 2015

Questions? customercare@copyright.com or +1-855-239-3415 (toll free in the US) or +1-978-646-2777.